In vitro investigation of human tissues and definition of their mechanical material models

K 116189

Final report

2020

I. Ophthalmological analysis

Table of Contents

1 Introduction

Globally, in 2015 an estimated 36 million people were blind, and 216.6 million people had moderate to severe visual impairment (MVI and SVI) [1]. Among individuals in the global population who were blind in 2015, the leading cause was cataract, and cataract was the second cause among the population with MVI or SVI [2]. The burden of this eye disease is especially high in developing countries. Although proportions of blindness due to cataract decreased from 1990 to 2010 worldwide [3-9], globally it will remain the major cause of blindness in 2020 [2].

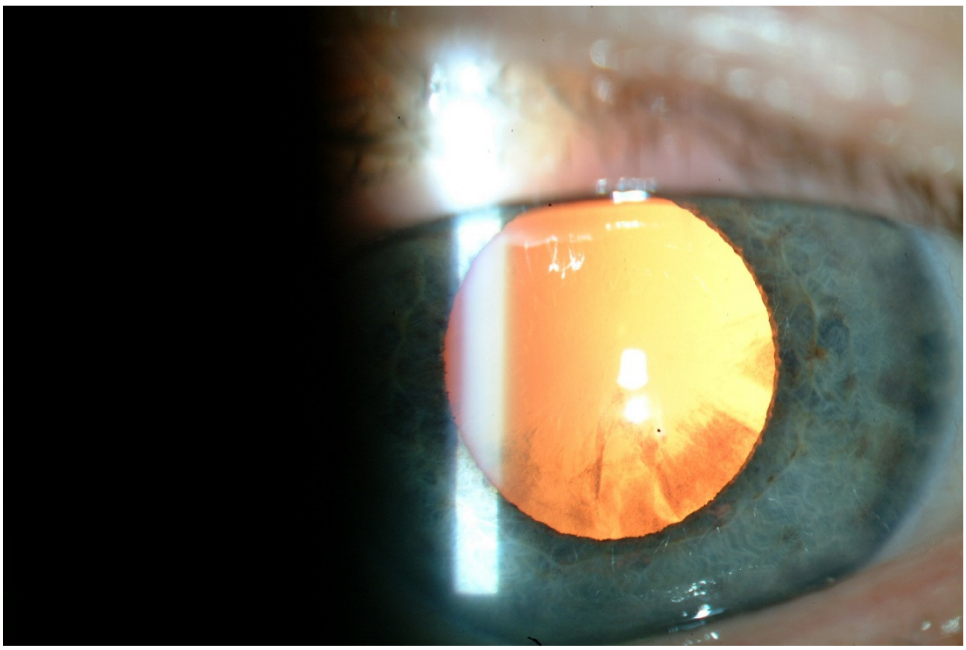

Cataract (The photograph was taken via retroillumination based on the red fundus reflex)

The only way to treat cataract is surgery. Cataract surgery with implantation of an intraocular lens (IOL) is the most common ophthalmic surgery procedure, with approximately 19.5 million procedures being performed worldwide in 2011.

The procedure usually involves making a small incision in the cornea to open the anterior lens capsule (continuous curvilinear capsulotomy or capsulorhexis), followed by ultrasonic emulsification (i.e.: phacoemulsification) and removal of the lens and insertion of the IOL.
Although cataract surgery is generally safe and effective, the outcome is dependent to a large extent on the anterior capsular opening, therefore performing a precise anterior capsulorhexis (CCC) is a key part of cataract surgery. An ideal rhexis is circular, well-centered, and its edge is intact and free from weak points. These factors help to maintain the correct IOL position within the capsular bag as well as help minimize the incidence of radial tears of the anterior capsule. The opening must withstand the stress of maneuvers during surgery because a radial tear can occur at any stage of operation. An anterior capsule tear disrupts the integrity of the capsular bag thus the appropriate position of the IOL may be compromised.

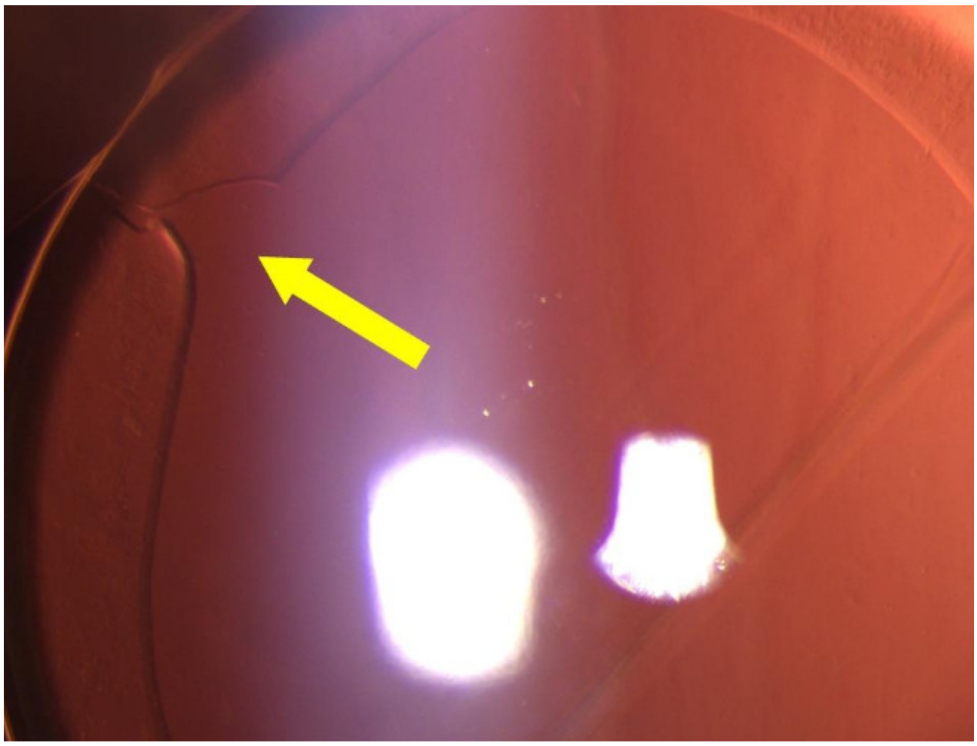

Anterior capsule tear

As patient demands have increased, the importance of a predictable position of the IOL has increased dramatically. Aspheric, toric, and multifocal IOLs have also driven the need for improved position. Furthermore, one of the most feared complications of surgery is posterior capsule rupture, often requiring an anterior vitrectomy or resulting in a vision threatening complication.

Thus, creation of CCC is a crucial step of extracapsular cataract surgery. During this process, visualization of the anterior capsule is based on an adequate red fundus reflex and is therefore more challenging when the red reflex is poor (e.g.: due to a mature cataract).

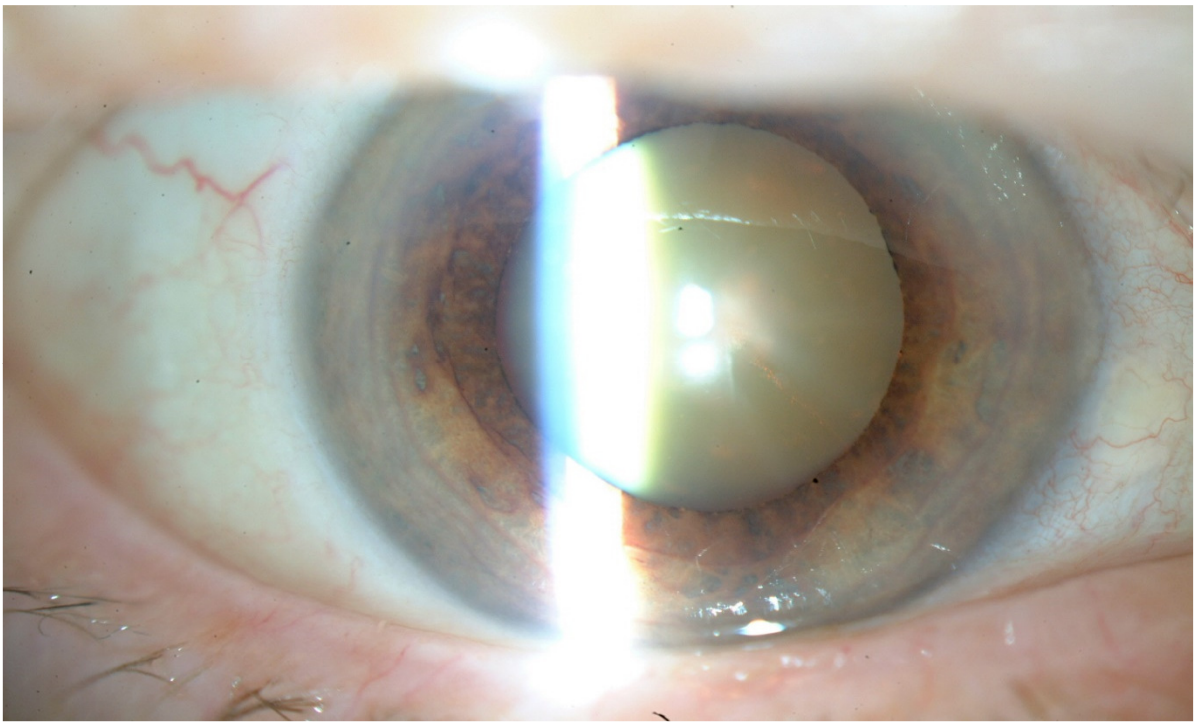

Mature cataract (Due to the grey, mature cataract retroillumination photoraph was not possible to take because the red fundus reflex was lacking)

In these challenging cases, vital dye and novel capsulotomy devices are available to help the surgeon to better visualization. However, after the biomechanical resistance following staining and capsulotomy devices are unknown.

Therefore, understanding the mechanical properties of the anterior lens capsule is essential. Investigations are warranted to evaluate the mechanical behaviour of this unique tissue to reduce the complication rates of cataract surgery and make better the postoperative results.

2 Our research question and the expected benefits of this research

1. How can be evaluated the mechanical properties of the anterior lens capsule?
2. What kind of mechanical properties can be determined by laboratory tests?

Expected benefits of research:

- The developed tissue preparation method and mechanical test may be suitable to evaluate the capsular opening following staining and novel capsulotomy methods.
- The experimental results should be considered in the clinical practice thus the safety of the surgery may improve, and post-operative refractive results may be also improved.

3 Annual work plans

3.1 September 2015 – August 2016

The work plan in the first year of the study:

1/1 Preparation the literature review based on scientific publications related to the lens capsule from a medical and mechanical point of view
1/2 Development of the sample preparation method to harvest the anterior lens capsule in porcine eye model
1/3 Development of the mechanical testing equipment on porcine samples
1/4 Evaluation of the results of the tests
1/5 Statistical assessment of the results and drawing conclusions
1/6 Investigation of the effect of the storage circumstances of the samples

3.2 September 2016 – August 2017

The work plan in the second year of the study:

2/1 Performing mechanical tests on the capsular samples on human samples
2/2 Development a new biaxial test method for the analysis of the mechanical properties of the anterior lens capsule in a porcine eye model

3.3 September 2017 – August 2018

The work plan in the third year of the study:

3/1 Evaluation and comparison of the mechanical resistance to tear of anterior capsule opening following trypan blue staining with different concentrations

We conducted the evaluation of our clumping test method. We found that the former applied method was not suitable for additional calculations. The causes: the clamped boundary condition at the edge of the test procedure was not fully insured. The complex stress distribution under the needle caused unwanted failure mechanism. These effects prevented the clear repetition of the test.

Therefore, we planned to use our novel biaxial test method to investigate an important clinical issue in cataract surgery. The creation of anterior capsulorhexis is a crucial step of extracapsular cataract surgery. During this process, visualization of the anterior capsule is based on an adequate red fundus reflex and is therefore more challenging when the red reflex is poor (e.g., due to a mature cataract). Furthermore, especially in such cases, a strong capsular rim is needed to support the possible stress load during the surgical procedure.

Trypan blue is a dye that is commonly used to facilitate visualization of the anterior lens capsule during creation of the anterior capsulorhexis [10]. The purpose of our current study was to evaluate and compare the mechanical resistance to tear of anterior capsule opening

following trypan blue staining with different concentrations in ex vivo porcine lens capsule specimens using the novel biaxial test method developed by our study group at this year.

3.4 September 2018 – August 2019

The work plan in the fourth year of the study:

4/1 Development of a uniaxial test method
4/2 Development of a preparation method to assess the ultrastructure of the capsular opening via scanning electron microscope (SEM)
4/3 Evaluation of the capsule rim ultrastructure following Precision Pulse Capsulotomy (PPC) via SEM
4/4 Evaluation of the capsule rim ultrastructure following PPC

Based on our experiences harvested last year, we plan to evaluate the capsule rim stability after Precision Pulse Capsulotomy (PPC). PPC is a new, promising method to automate consistent creation of a perfectly circular anterior capsulotomy [11]. This is the newest clinically available capsulotomy device therefore mechanical studies are needed to analyze the advantages and limitations of this method.

4 Completion of the annual work plan

4.1 September 2015 – August 2016

1/1 Preparation the literature review based on scientific publications related to the lens capsule from a medical and mechanical point of view

The results of relevant national and international publications were collected and assessed from a medical and mechanical viewpont.

1/2 Development of the sample preparation method to harvest the anterior lens capsule in porcine eye model

Fresh porcine eyes were obtained immediately following slaughter from a local abattoir. The workflow (transport, storage, etc.) was developed successfully.

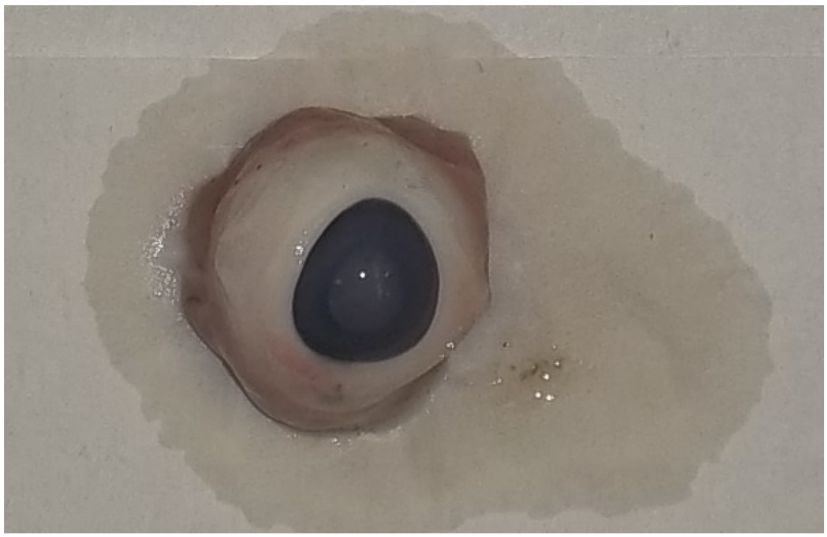

Fresh porcine eye

In the laboratory under surgical microscope the cornea and iris were removed with forceps and cystotome, permitting free access to the anterior capsule. CCC was performed with a cystotome and rhexis forceps. The goal was to perform a well-centered, circular capsular opening with an intended diameter of 5 mm, thus we got a disk-shaped capsular specimen. The rest anterior capsule was cut using micro-scissors around the equator, resulting in a ring-shaped capsule specimen. During the whole process, ophthalmic viscosurgical device (OVD) was used to prevent the tissues.

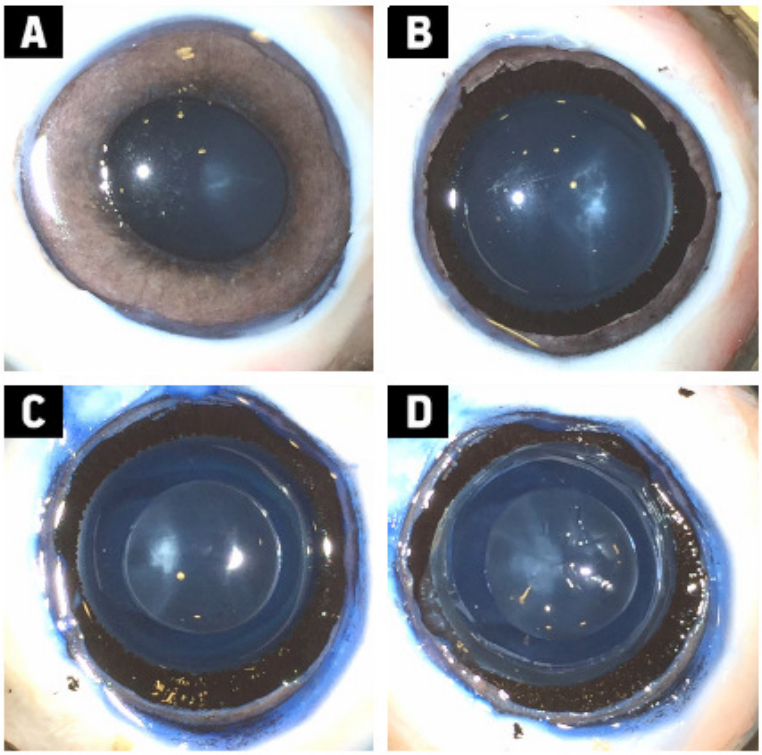

A: Sample after removal of the cornea. B: Sample after removal of the iris. C: State after removal of the central disk-shaped capsule specimen. D: The ring-shaped capsule specimen.

All specimens were inspected via light microscopy (BX 51M, Olympus Co., Tokyo, Japan) to ensure geometrical uniformity of the samples. Specimens with unacceptable shape or size were excluded from the study. Specimens with visible irregularity at the rim of the opening were also discarded.

1/3 Development of the mechanical testing equipment on porcine samples

The custom-made specimen support produced by 3D printing technology consisted of two ring-shaped plastic parts. The capsule specimen was carefully clamped between the two rings. A needle connected to a force transducer, was pushed through the holes of the rings by a stepping motor at a constant speed until the capsule membrane punctured. Mechanical testing was carried out with universal testing equipment (Zwick Z005, Zwick GmbH & Co. KG, Ulm, Germany). The force required for stretching as well as the displacement of the moving pin were recorded continuously with the manufacturer's software (testXpert, Zwick GmbH & Co. KG, Ulm, Germany)

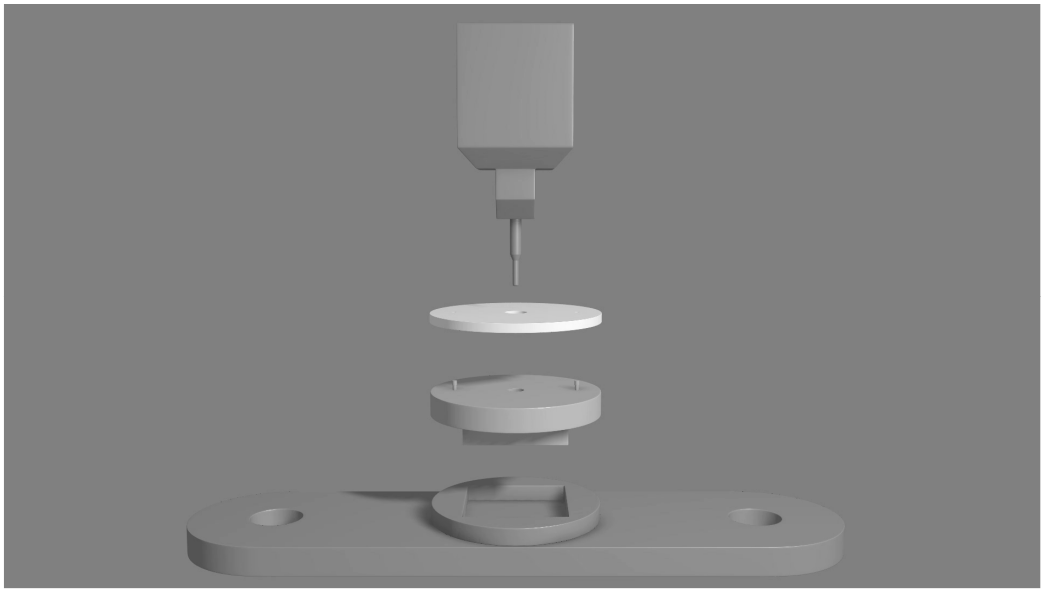

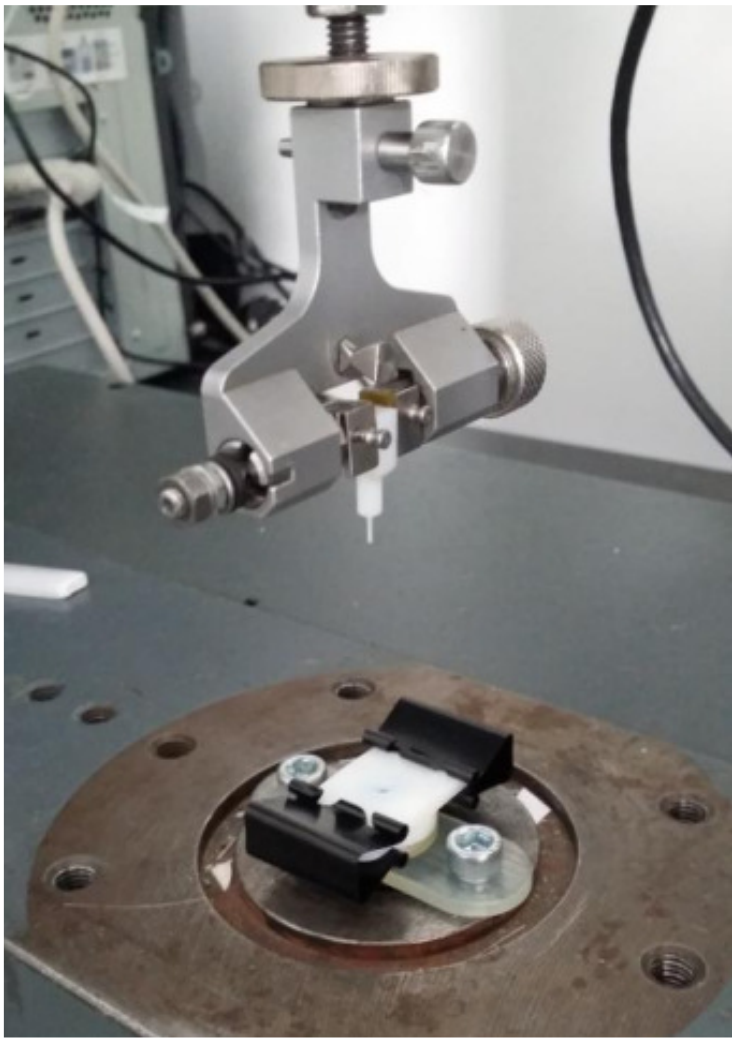

The sample holder and the needle connected to the Zwick universal testing equipment

1/4 Evaluation of the results of the tests

We had opportunity to make pre-test with the prototype tools. Based on the results from the pilot tests we could constantly improve the tool and the process too. After optimizing the tools and the process we measured the load force and the displacement on 14 porcine samples.

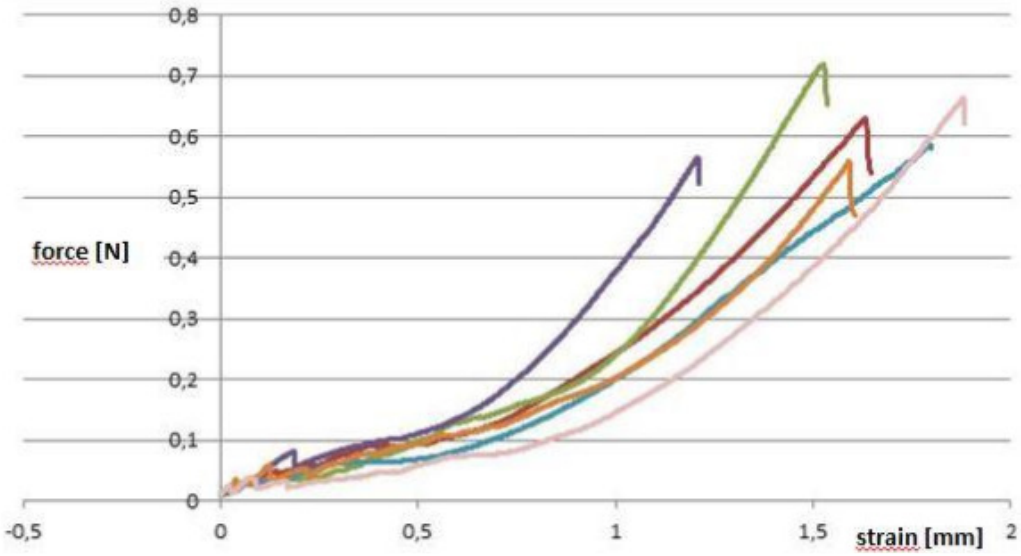

Typical force-displacement diagrams recorded during the test

The maximum deformation of the lens capsule was 2.1 +/- 1.1 mm, and the force were 0.45 +/- 0.17 N in the experiment.

1/5 Statistical assessment of the results and drawing conclusions

As next step, we validated the measurement method. We used 45 anterior capsule samples taken from porcine eyeballs and we tested their elasticity and durability. The outcomes were slightly different, so we looked into the effect of the samples' storage method had on the measurement process. The average force at the break point was: 0.45+/-0.15 N, and the strain of the penetrating instrument was 1.57+/-0.41 mm (after coming in touch with the sample's surface).

1/6 Investigation of the effect of the storage circumstances of the samples

Analysing the results in a statistic way shows that on each experimental measurement day both the force and the strain values assumed a normal distribution, however comparing the results obtained from different days we experienced significant differences in the averages, however the reason was unknown.

In the first year of the study, István Karakas and Flóra Kecskés got their BSc thesis in the topic mentioned above.

4.2 September 2016 – August 2017

2/1 Performing mechanical tests on the capsular samples on human samples

We had started perforation tests on capsular bags recovered from human cadavers, however our preliminary tests did not yield any major result as the provided capsular bag samples

turned out to be thinner than the capsular bags recovered from porcine eyes. Furthermore, other samples that were recovered during cataract surgery on live patients disintegrated into small pieces. We plan to solve these problems using a clamping device with refined geometry.

2/2 Development a new biaxial test method for the analysis of the mechanical properties of the anterior lens capsule in a porcine eye model

We were developed successfully the biaxial test method on porcine samples. The specimen support comprised four polished metal pins, each with a radius of 0.4 mm. Two pair of holders were placed, perpendicular to each other. The ring-shaped specimen was carefully slipped over the four pins, which were lubricated with methylcellulose to reduce friction.

The specimen support was submerged in Balanced Salt Solution at room temperature to ensure an appropriate hydration level during the test. The four pins were separated from each other by four stepping motors, which operated at a speed of 10 mm/min until the capsule ring was torn. The force required to stretch and displace the pins was recorded continuously using a computer.

The unscretched circumference (Cus) and stretched circumference (Cs) of the opening could be calculated based on the relative position of the pins, where the strain reached a small preload and the ring was torn. The circumference stretching ratio (CSR) between the stretched and unstretched circumferences could be expressed as a percentage based on the following formula: CSR = (Cs/Cun) × 100%. The rupture force (RF), CSR, shape of elasticity curves, and secant modulus at 10 mN (SM10mN) and 50 mN (SM50mN) could be evaluated.

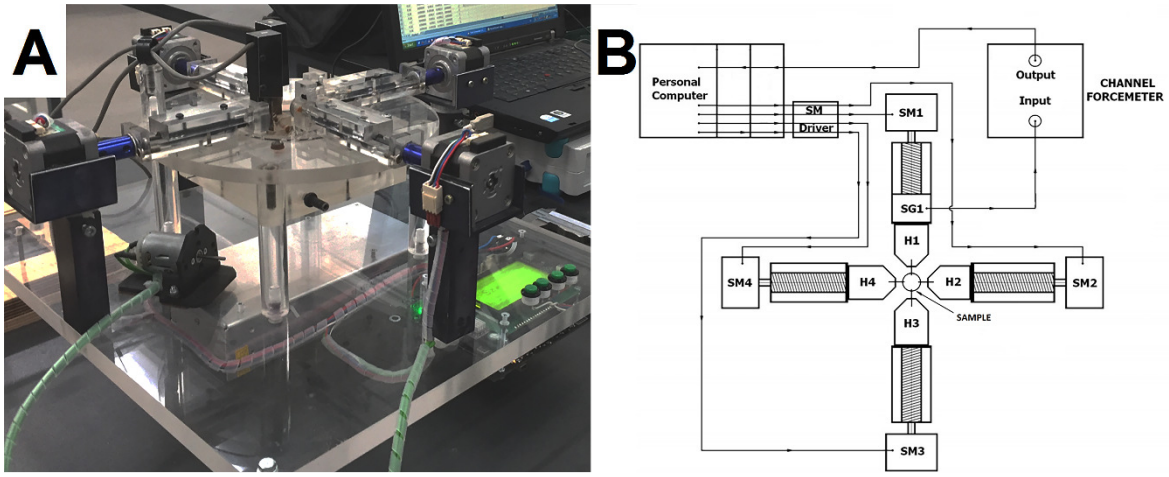

Photograph of the capsule stretching apparatus (A) and simplified diagram of the mechanical test arrangement (B). (SM=stepping motor, H=holder, SG=strain gauge)

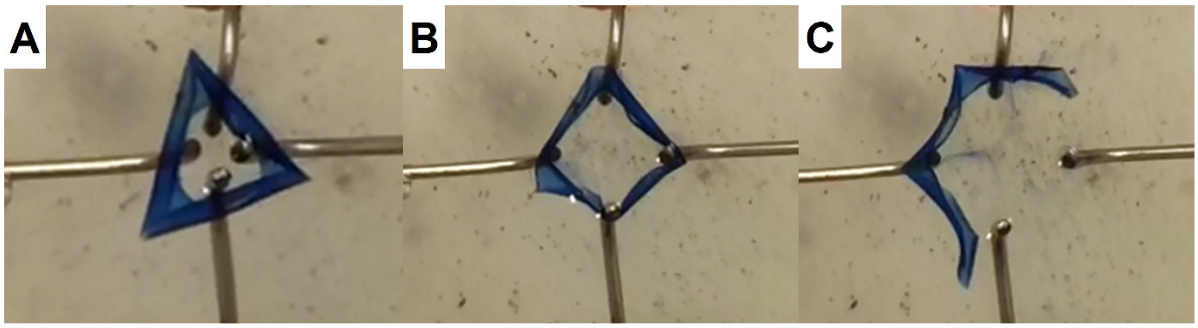

The phases of the stretching process: A ring-shaped specimen (with rolled margin) stained with trypan blue was slipped over four pins (A); the specimen was stretched (B); and the capsule ring was torn (C)

4.3 September 2017 – August 2018

3/1 Evaluation and comparison of the mechanical resistance to tear of anterior capsule opening following trypan blue staining with different concentrations

Fresh porcine eyes were transported from a local abattoir immediately after slaughter and were randomly divided into three groups. Under an operating microscope, the cornea and iris were removed. In the Control Group (C Group), the anterior lens capsule was unstained. Conversely, in the Stained 1 Group (S1 Group), 0.06% trypan blue was used to stain the capsule for 1 minute; 0.1% trypan blue was used to stain the capsule in a similar manner in the Stained 2 Group (S2 Group).

Subsequently, the dye was removed by irrigation with balanced salt solution (BSS). In all groups, continuous curvilinear capsulorhexis (CCC) was performed with a cystotome and forceps. A custom-designed, three-dimensionally printed marker (5.5 mm in diameter) was used to ensure uniform, well-centred, appropriately sized, circular capsular openings. Subsequently, the anterior capsule was cut around the equator, using a pair of micro-scissors to obtain a ring-shaped capsule specimen. All specimens were checked for uniformity via light microscopy (BX 51M, Olympus Co., Tokyo, Japan). Specimens with unacceptable shape, size, or an irregularity at the rim of the opening were excluded. In total, 75 eyes (25 eyes in each group) met the study inclusion criteria.

The rupture force (RF), CSR, shape of elasticity curves, and secant modulus at 10 mN ($SM10_{mN}$) and 50 mN ($SM50_{mN}$) were evaluated.

We found that the RF in each group was as follows: C Group: 108 ± 20 mN, S1 Group: 105 ± 32 mN, and S2 Group: 104 ± 23 mN. The CSR in each group was as follows: C Group: 148 ± 7%, S1 Group: 148 ± 6%, and S2 Group: 150 ± 5%.

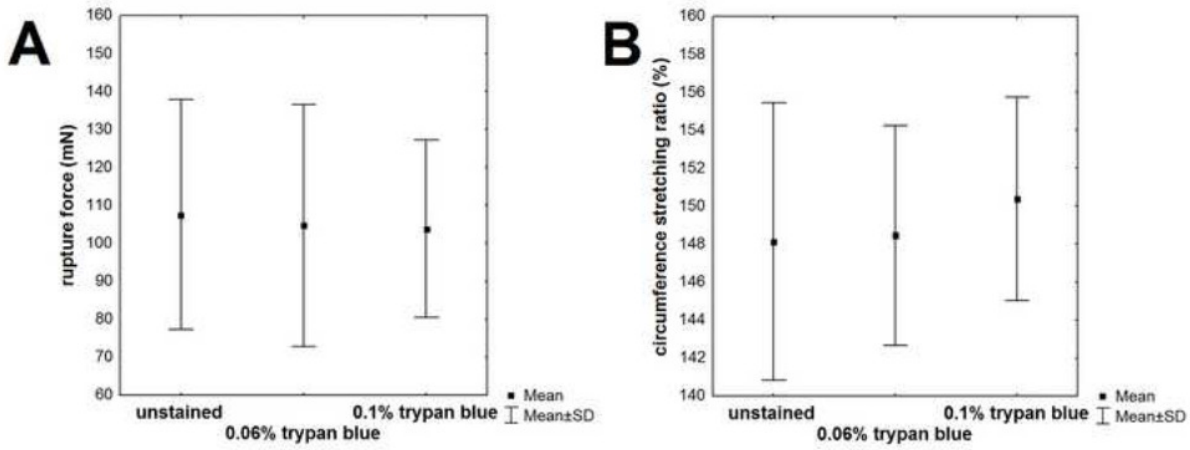

Rupture force (A) and circumference stretching ratio (B) in the study groups.

There were no statistically significant differences in RF (p = .8924) or CSR (p = .3876) among the groups.

The elasticity curves, which represent the force required for stretching as a function of the displacement of the pins for each group. As illustrated by the figures, the force-displacement relation was similar in all groups.

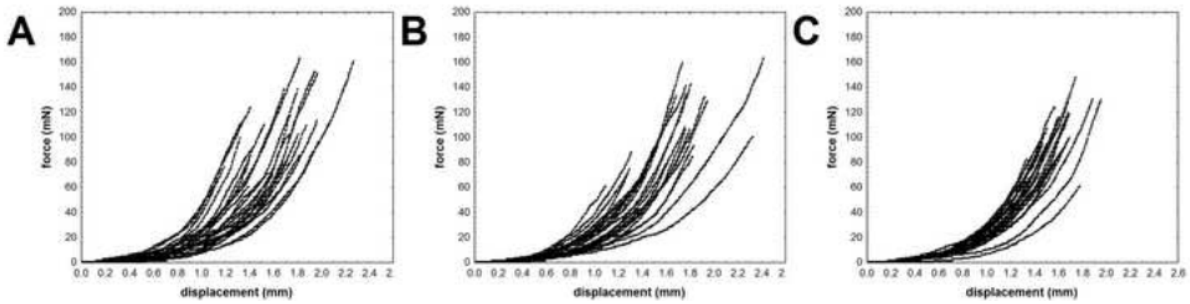

Elasticity curves in the Control Group (A), Stained 1 Group (B) and Stained 2 Group (C).

The $SM10_{mN}$ was 13 ± 2 mN/mm for C Group, 13 ± 2 mN/mm for S1 Group, and 14 ± 2 mN/mm for S2 Group. The $SM50_{mN}$ was 38 ± 6 mN/mm for C Group, 38 ± 5 mN/mm for S1 Group, and 39 ± 3 mN/mm for S2 Group. There were no statistically significant differences among the groups (p = .8215 and p = .4184). The shape of the curves was similar in all groups: the increase in force was rapid, and a steep decline occurred at the point indicating tearing of the specimen.

According to our results in a porcine eye model trypan blue dye has no influence on the mechanical resistance to tearing of the anterior lens capsule. This is a useful result from an experimental viewpoint because the handle of the tissue is easier during the mechanical test, however the results may be the same. It is a useful result from a surgical viewpoint, because the use of trypan blue do not alter the mechanical properties of the capsular rim, therefore it is a safe method to enhance better visualisation during surgery.

In the third year of the study an e-poster abstract was presented in the XXXV Congress of the European Society of cataract and Refractive Surgeons, Lisbon, 2017, Oct. 7-11. (ZOLTÁN KISS,

GÁBOR L. SÁNDOR, ZOLTÁN I. BOCSKAI, ZOLTÁN Z. NAGY. A new laboratory test method to investigate the biomechanical behaviour of the anterior lens capsule)

4.4 September 2018 – August 2019

4/1 Development of a uniaxial test method

Mechanical testing was carried out with universal testing equipment (Zwick Z005, Zwick GmbH & Co. KG, Ulm, Germany). The specimen support consisted of two polished metal pins (r=0.4 mm). The ring-shaped specimen was carefully slipped over the two pins, which were lubricated with methylcellulose to reduce friction.

During the test, the specimen support was submerged in balanced salt solution at room temperature to prevent the dehydration of tissue. The lower pin was fixed. The upper pin, connected to a force transducer (sensitivity 0.01 mN), was separated from the fixed one by a stepping motor at a speed of 10 mm/min until the capsule ring tore. The force required for stretching as well as the displacement of the moving pin were recorded continuously with the manufacturer's software (testXpert, Zwick GmbH & Co. KG, Ulm, Germany).

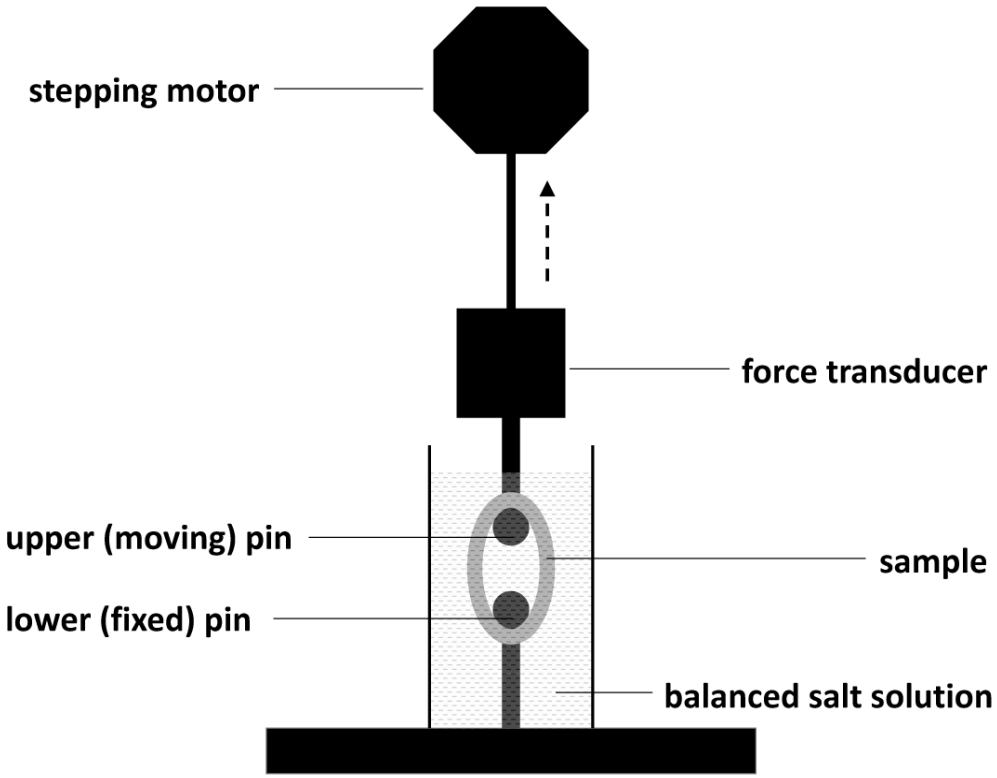

The mechanical test arrangement.

The CSR, the shape of elasticity curves, the secant modulus at 10 mN (SM_{10mN}) and 50 mN ($SM50_{mN}$) and the rupture force (RF) were evaluated.

4/2 Development of a preparation method to assess the ultrastructure of the capsular opening via scanning electron microscope (SEM)

The disk-shaped anterior lens capsule specimens obtained during sample preparation were fixed for scanning electron microscopy in freshly-prepared 1% glutaraldehyde and 1% paraformaldehyde in 0.1 mol/L sodium cacodylate buffer (pH 7.2). The fixed samples were dehydrated in a series of ethanol dilutions (20%-96% vol/vol), 1:1 mixture of 96% (vol/vol) ethanol/acetone, and pure acetone followed by vacuum-drying. The specimens were mounted on adhesive carbon discs, sputter coated with gold, and images taken with SEM JSM 6380LA (JEOL, Ltd., Tokyo, Japan).

4/3 Evaluation of the capsule rim ultrastructure following Precision Pulse Capsulotomy (PPC)

The data were evaluated, the statistical analysis are under process.

4/4 Evaluation of the capsule rim ultrastructure following PPC

SEM revealed a functional edge of PCC specimens. This working edge was regular and smooth. The anatomical edge was everted. The edge of CCC specimens was also regular and the regular lamellar arrangement of collagen fibrils was clearly visible. In the case of incomplete PPC specimen the unique edge was distorted: the everted functional edge was inverted and a focal irregularity was visible.

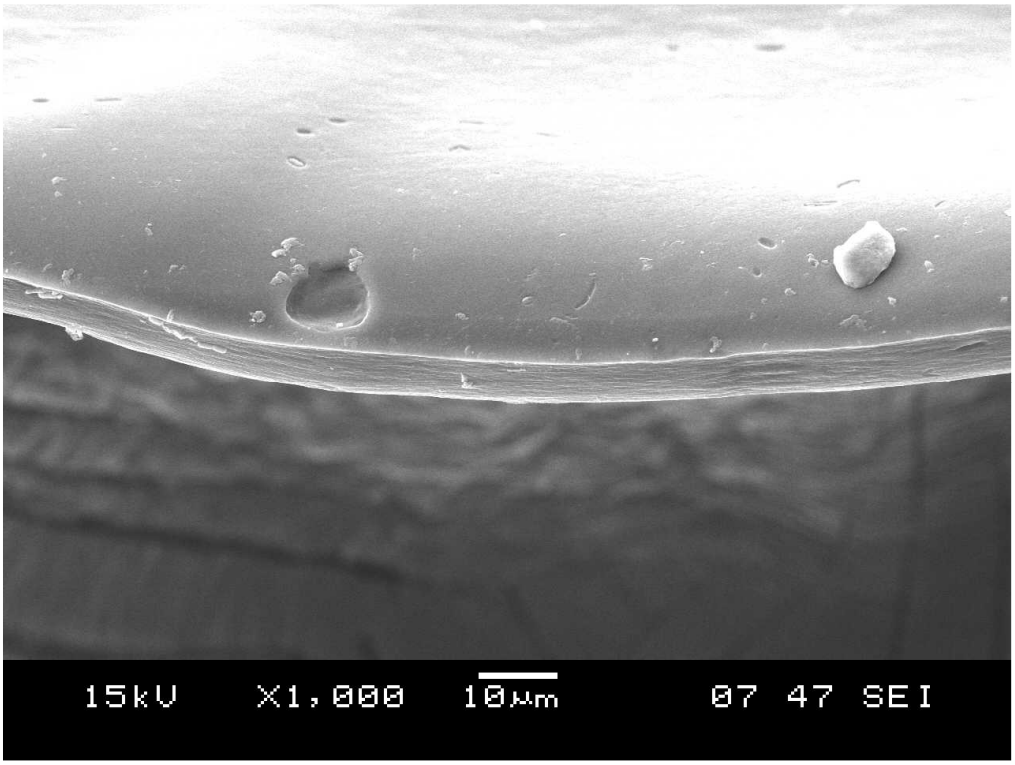

Ultrastructure of the capsule edge following CCC

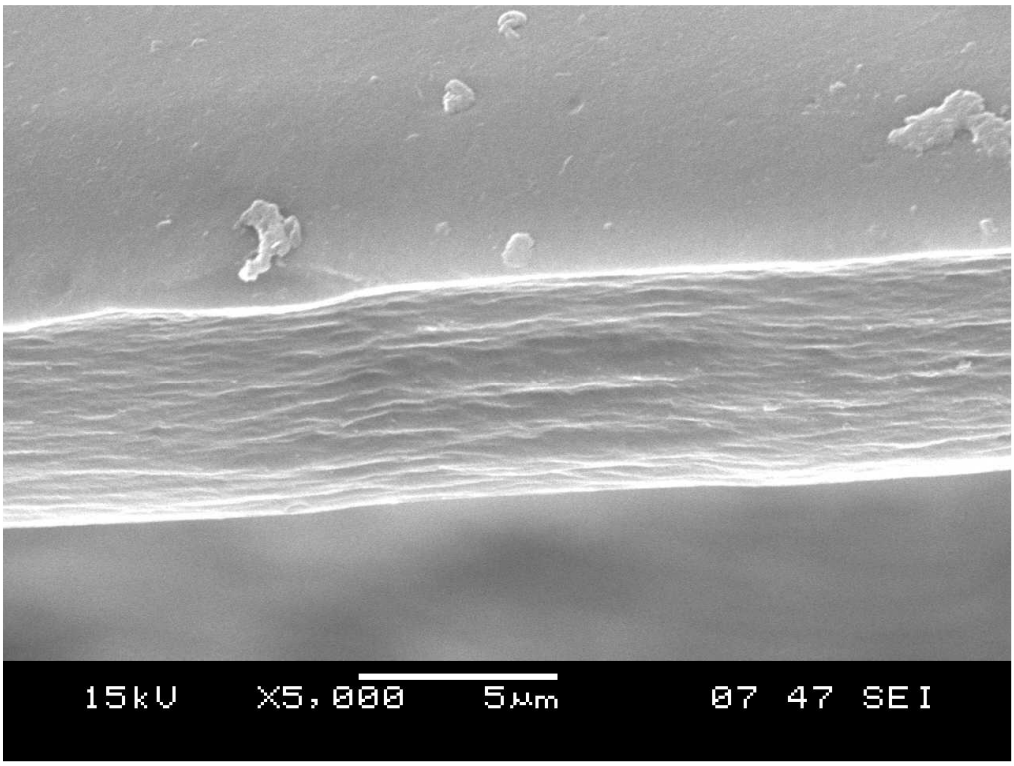

Ultrastructure of the capsule edge following CCC at high magnification

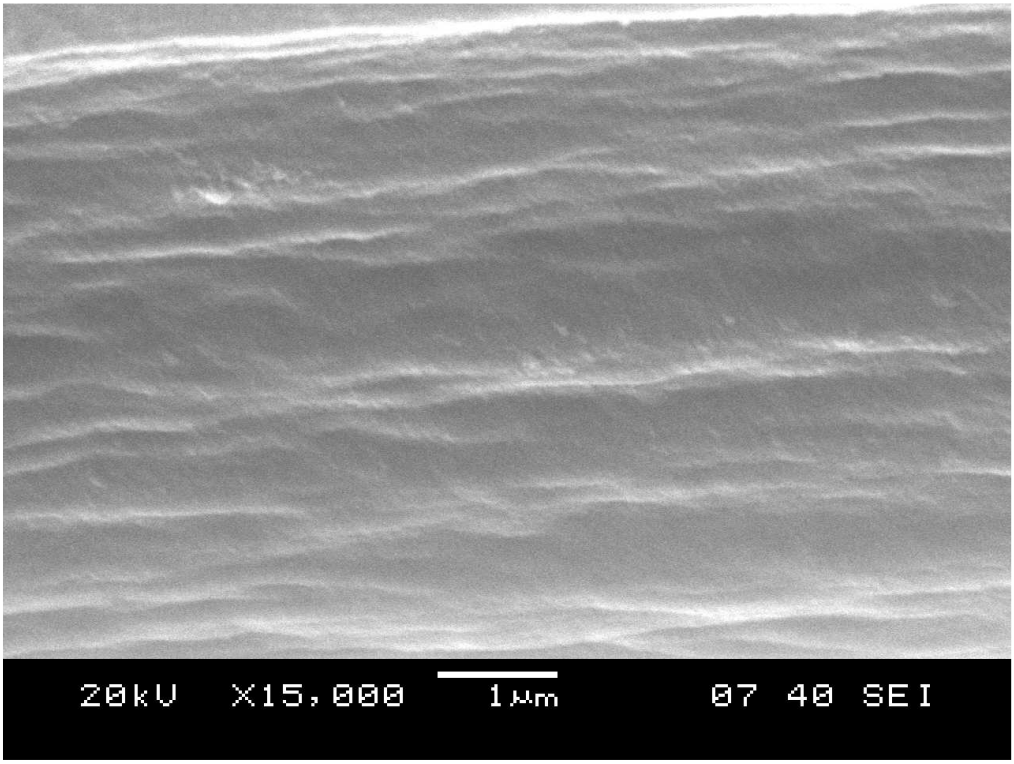

Ultrastructure of the capsule edge following CCC at extreme high magnification

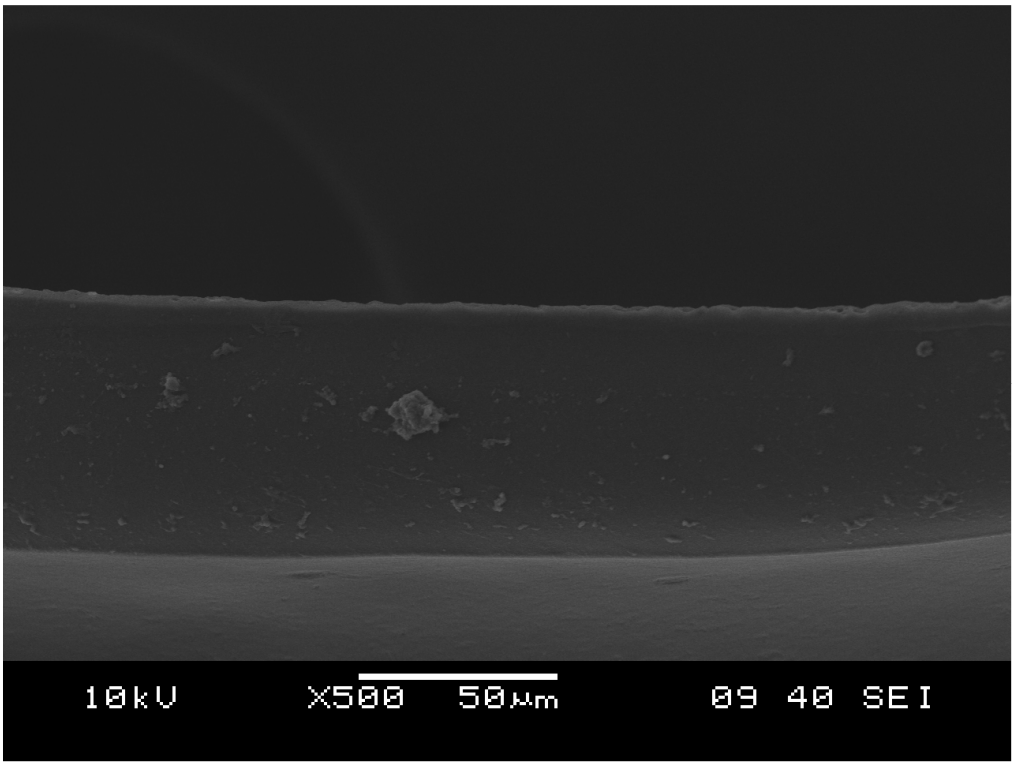

Ultrastructure of the capsule edge following PPC

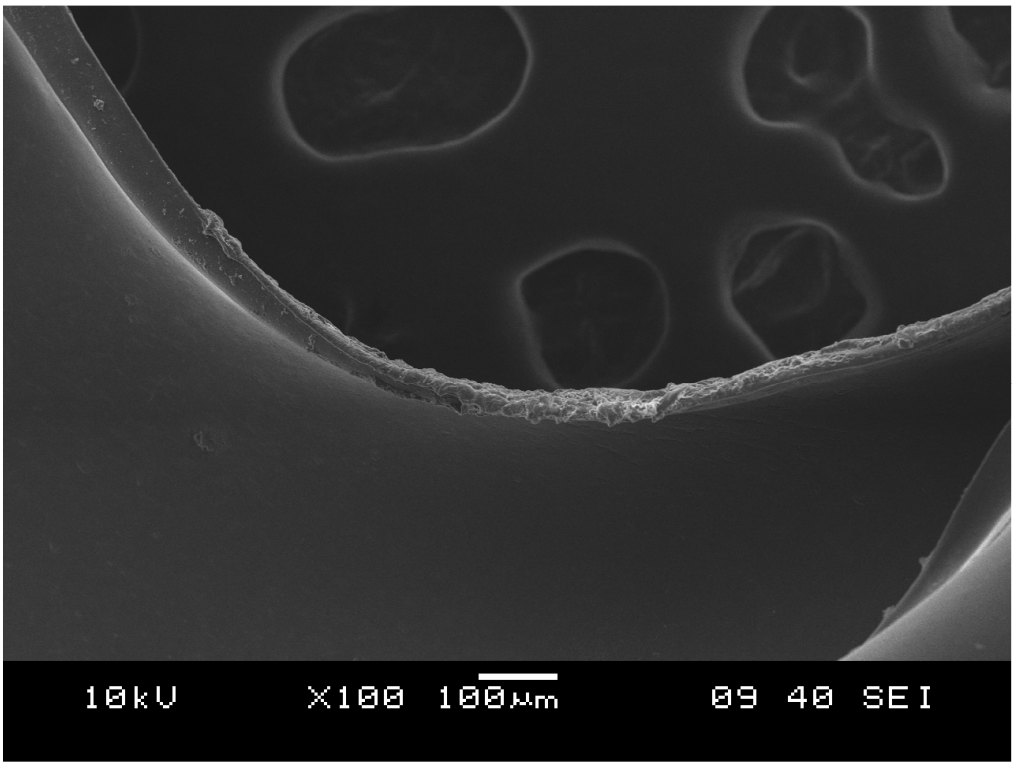

Ultrastructure of the capsule edge following PCC

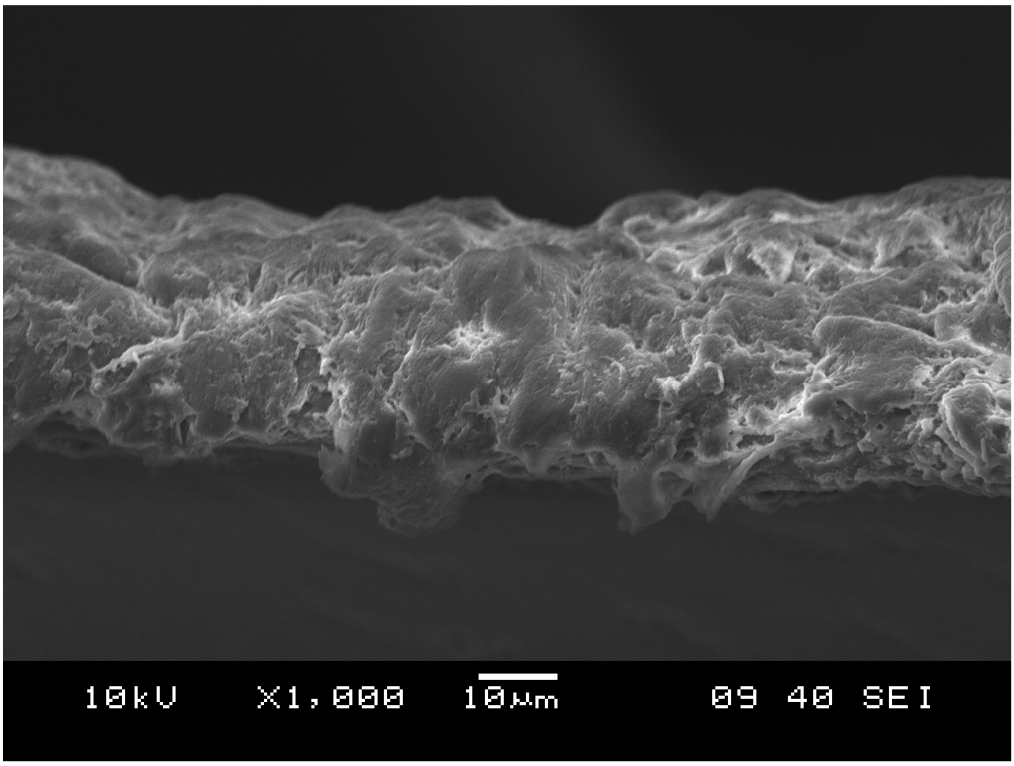

Ultrastructure of the capsule edge following PPC at high magnification

In the 4th year of the study our results were published in the Journal of Cataract and Refractive Surgey **(IF=2,689).** (Gábor L Sándor, Zoltán Kiss, Zoltán I Bocskai, Gábor Tóth, Tamás Temesi, Zoltán Z Nagy, Evaluation of mechanical resistance to tearing of the anterior lens capsule after staining with different concentrations of trypan blue. J Cataract Refract Surg. 2020 Feb;46(2):293-297. doi: 10.1097/j.jcrs.0000000000000017)).

After statistical analysis we plan to submit our results regarding to PPC to the British Journal of Ophthalmology **(IF= 3,611).**

5 Answers to our research questions and the expected benefits of research

1. **How can be evaluate the mechanical properties of the anterior lens capsule?**

Both uniaxial and biaxial test methods devised by our study group are suitable to evaluate the mechanical properties of the anterior lens capsule.

2. **What kind of mechanical properties can be determined by laboratory tests?**

The rupture force, the circumference stretching ratio, the shape of elasticity curve, and secant modulus can be evaluated using our method.

References

1 Bourne RRA, Flaxman SR, Braithwaite T, Cicinelli MV, Das A, Jonas JB, Keeffe J, Kempen JH, Leasher J, Limburg H, Naidoo K, Pesudovs K, Resnikoff S, Silvester A, Stevens GA, Tahhan N, Wong TY, Taylor HR. Magnitude, temporal trends, and projections of the global prevalence of blindness and distance and near vision impairment: a systematic review and meta-analysis. *Lancet Glob Health* 2017; 5(9): 888-897.

2 Flaxman SR, Bourne RRA, Resnikoff S, Ackland P, Braithwaite T, Cicinelli MV, Das A, Jonas JB, Keeffe J, Kempen JH, Leasher J, Limburg H, Naidoo K, Pesudovs K, Silvester A, Stevens GA, Tahhan N, Wong TY, Taylor HR. Global causes of blindness and distance vision impairment 1990-2020: a systematic review and meta-analysis. *Lancet Glob Health* 2017; 5(12): 1221-1234.

3 Bourne RR, Jonas JB, Flaxman SR, Keeffe J, Leasher J, Naidoo K, Parodi MB, Pesudovs K, Price H, White RA, Wong TY, Resnikoff S, Taylor HR. Prevalence and causes of vision loss in high-income countries and in Eastern and Central Europe: 1990-2010. *Br J Ophthalmol* 2014; 98(5): 629-638.

4 Jonas JB, George R, Asokan R, Flaxman SR, Keeffe J, Leasher J, Naidoo K, Pesudovs K, Price H, Vijaya L, White RA, Wong TY, Resnikoff S, Taylor HR, Bourne RR. Prevalence and causes of vision loss in Central and South Asia: 1990-2010. *Br J Ophthalmol* 2014; 98(5): 592-598.

5 Keeffe J, Taylor HR, Fotis K, Pesudovs K, Flaxman SR, Jonas JB, Leasher J, Naidoo K, Price H, White RA, Wong TY, Resnikoff S, Bourne RR. Prevalence and causes of vision loss in Southeast Asia and Oceania: 1990-2010. *Br J Ophthalmol* 2014; 98(5): 586-591.

6 Khairallah M, Kahloun R, Flaxman SR, Jonas JB, Keeffe J, Leasher J, Naidoo K, Pesudovs K, Price H, White RA, Wong TY, Resnikoff S, Taylor HR, Bourne RR. Prevalence and causes of vision loss in North Africa and the Middle East: 1990-2010. *Br J Ophthalmol* 2014; 98(5): 605-611.

7 Leasher JL, Lansingh V, Flaxman SR, Jonas JB, Keeffe J, Naidoo K, Pesudovs K, Price H, Silva JC, White RA, Wong TY, Resnikoff S, Taylor HR, Bourne RR. Prevalence and causes of vision loss in Latin America and the Caribbean: 1990-2010. *Br J Ophthalmol* 2014; 98(5): 619-628.

8 Naidoo K, Gichuhi S, Basanez MG, Flaxman SR, Jonas JB, Keeffe J, Leasher JL, Pesudovs K, Price H, Smith JL, Turner HC, White RA, Wong TY, Resnikoff S, Taylor HR, Bourne RR. Prevalence and causes of vision loss in sub-Saharan Africa: 1990-2010. *Br J Ophthalmol* 2014; 98(5): 612-618.

9 Wong TY, Zheng Y, Jonas JB, Flaxman SR, Keeffe J, Leasher J, Naidoo K, Pesudovs K, Price H, White RA, Resnikoff S, Taylor HR, Bourne RR. Prevalence and causes of vision loss in East Asia: 1990-2010. *Br J Ophthalmol* 2014; 98(5): 599-604.

10 Melles GR, de Waard PW, Pameyer JH, Houdijn Beekhuis W. Trypan blue capsule staining to visualize the capsulorhexis in cataract surgery. *J Cataract Refract Surg* 1999; 25: 7-9.

11 Chang D. Zepto precision pulse capsulotomy: A new automated and disposable capsulotomy technology. *Indian J Ophthalmol* 2017; 65(12): 1411-1414.

II. Analysis of the facial nerve

Table of Contents

1 Introduction

Palsy of the facial nerves occurs in two thirds of the cases as an idiopathic pathology, nowadays considered as result of herpetic infection. In some cases it is caused by certain diseases (such as otitis media, tuberculosis, HIV infection, tumour) or accidents [1].
After the medical examination, determination the underlying disease causing the palsy, the expert physician decides whether the disease (and its consequences) can be treated medically or surgically, and in addition, facial nerve palsy should be treated with medication [2].
In some cases - such as Bell's palsy - facial palsy develops with no detectable cause. In most cases, this nerve palsy heals relatively quickly within a few weeks. However, in some severe cases, it worsens and due to the developing oedema the nerve is under permanent pressure in its narrow duct. In these cases, lesion of the fibres may occur. In these cases, the healing process may last for several months with permanent deficit. If a reduction in nerve fiber function is detected in the early stages of palsy, as measured by certain electrodiagnostic tests, surgical exploration of the facial nerve may be required /early decompression surgery/. In some cases, when no improvement is seen within 5-6 months, surgery may also be required /delayed decompression surgery/ [1].
During surgery, the primary goal of physicians is to eliminate the cause of the disease and palsy and, ideally, to restore the original function of the nerve. They should also ensure protection of the sensitive nerves of the face during the procedure. This is the area where engineering and medicine are linked.

The research idea 'Analysis of the facial nerve' was raised by Róbert Késmárszky MD, head and neck surgeon. The study was undertaken following approval from the ethical committee (Semmelweis University, Regional and Institutional Committee of Science and Research Ethics; TUKEB No. 127/2014) and in accordance with the declaration of Helsinki.

2 Our research questions and the expected benefits of this research

1 What range of load values can be applied to the facial nerves while guaranteeing that no injury occurs?
2 What tools are needed to perform the relevant laboratory measurements?
3 What 'material properties' can be determined by laboratory tests?
Expected benefits of research:

- The expected result of the research is a measuring and evaluation system suitable for laboratory examination of facial nerves, which is suitable for determining the behaviour of individual facial nerves against tensile load.
- There will be objective measurement results which can be used later in clinical practice.
- Preparation of the design and functional properties of a medical device for use in clinical practice. Reduce the risk of facial nerve interventions.

3 Annual work plan

3.1 September 2015 – August 2016

Definition of each element of our test program:
1/1 Preparation of a literature review based on scientific publications related to the facial nerve (medical and engineering aspects)
1/2 Selection of facial nerves

1/3 Defining removal methods (from a medical point of view)
1/4 Development of storage method and transport of facial nerves
1/5 Design and manufacture of special instruments for testing (e.g. in-house developed clamps)
1/6 Preparation of a test protocol using the experience of previously performed (10 cadavers) measurements
1/7 Development of destructive and non-destructive testing methods
1/8 Purchase of unique tools and equipment for autopsy and measurements

3.2 September 2016 – August 2017

2/1 Applying the test protocol developed in the first phase of work on 10 facial nerves removed from cadavers
2/2 Evaluate the results of the previous tests
2/3 Statistical evaluation of results
2/4 Reviewing individual tools and making any changes
2/5 Determine a load range based on the measurement results
2/6 Further investigation – Relaxation studies
2/7 Further investigation – Invested work

3.3 September 2017 – August 2018

3/1 Laboratory examination of 10 more facial nerve samples
3/2 Demonstration of the applicability of the determined measurement technique with new facial nerve samples

3.4 September 2018 – August 2019

4/1 Comparison of measurement results of different facial nerve samples
4/2 Summarizing the relevant results for technical and clinical practice

4 Completion of the annual work plan

4.1 September 2015 – August 2016

1/1 Preparation of a literature review based on scientific publications related to the facial nerve (medical and engineering aspects)

The results of relevant national and international publications were collected. Both engineering and medical aspects were considered. In the review of the literature, special attention was given to the difficulties encountered in clinical practice, their possible solution, and in the light of these, the properties of the nerves to be examined were formulated.

1/2 Selection of facial nerves

Based on the analysis of the literature and medical considerations, our study was based on the VII. cranial nerve, and the recurrent laryngeal nerve which is one of the vagal nerve's (X. cranial nerve) branches.

The VII. cerebral nerve is the facial nerve providing motor innervation of the facial muscles. After the extratemporal bifurcation the nerve has five group of branches.

During our research, three extracranial branches of the nerve were investigated: zygomatic, buccal and marginal [3].

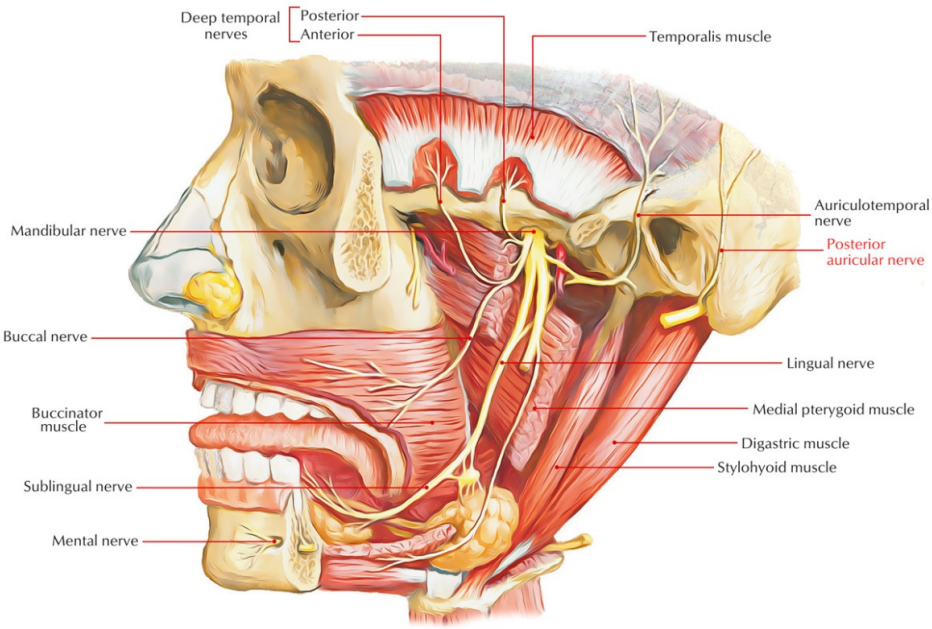

Location of facial nerves [4]

Lesions of the extratemporal facial nerve may lead to devastating aesthetic, psychosocial and functional problems, impacting quality of life [5].

Despite its protective factors, the extratemporal facial nerve is the most frequently injured cranial nerve by mechanical forces [6]. In the case of head trauma, mostly through traffic accidents, palsy occurs in 5.04%, with spontaneous total recovery in 30% of cases [7]. The location of the injury strongly influences the outcome [8]. Facial palsy may be present in live newborns with an overall incidence of 0.2% [9]. The frequency is much higher in adults, even in cases where only the extratemporal portion is affected.

Although Bell's palsy represents 60–75% of all peripheric palsies, its mechanical causes are an important etiological group, with iatrogeny in 5.6%–7% of patients, namely, patients undergoing oral and maxillofacial procedures (40%), resections of head and neck lesions, parotidectomies (25%), otologic procedures (17%), cosmetic surgery (11%) and others (7%) [10] [11] [12].

The ramification, position and depth of the different branches are highly diverse, even in the two hemispheres of the same patient [13] [14] [15].

The marginal mandibular nerve is double or single in 95.9% of cases, and interconnections with other branches occur in less than 15%, while interconnections may be as high as 70% in the zygomatic and buccal branches [16] [17]. Because marginal mandibular nerve is the most frequently dissected branch, injuries are more likely to be symptomatic [18].

The X. cranial nerve -vagal nerve-, is the motor nerve of the pharynx and the soft muscles, the lower two-thirds of the pharyngeal muscles, the laryngeal muscles and the esophagus [3].

The human recurrent laryngeal nerve (HRLN) gives both motor and sensory fibers to the larynx, innervating all intrinsic muscles except the cricothyroid. It also provides the sensation in the glottic and subglottic areas [19].

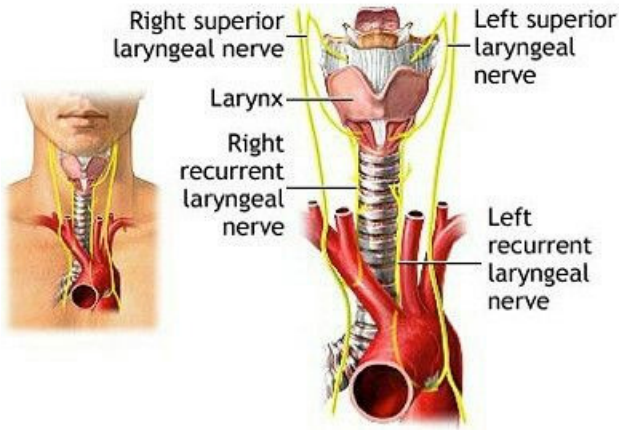

Recurrent laryngeal nerve [20]

Its pathologies may lead to uni- or bilateral vocal fold palsy (VFP). The complex anatomy, biomechanically active ambiance, and the variety of possible pathologies make VFP a diagnostic and therapeutic challenge; it represents the major group of all vocal fold immobility (VFI) cases [21]. Its incidence is higher in adults, However, age dependent etiological differences exist [22] [23] [24] [25].

The consequences may manifest as difficulties of phonation, deglutition, and respiration, all of which impact the quality of life [26].

The anatomical situation, course, relationships, surgical landmarks and ramifications of the HRLN were widely studied. The length, the small number of its branches, the rarity of anastomosis, the physiology of the innervated structures make traumas more likely to be symptomatic [27] [28].

The standard anatomical landmarks may help to identify the nerve, but variations of its course and those of the branching patterns must be considered [29] [30] [31].

The main anatomical difference between the two sides, is their unequal length; this is due to their level of origin from the vagal nerve, followed by looping around the aortic arch on the left, and the subclavian artery on the right [32] [33]. Due to its more important length and biomechanical activity of the surrounding tissues, mostly generated by the proximity of the aorta, the left HRLN is more often a victim of palsy [34] [35]. Mechanical harm is a leading cause of VFP, caused by surgery, intubation, trauma, and tumoral displacement. In the area of the neck, surgeries of the thyroid gland, carotid artery, and the cervical spine are most frequently complicated by VFP [36]. Protective factors which include: epi- and perineural sheets, collagen content, vessels, the tracheoesophageal groove, and fat tissue may only diminish the consequences of trauma [37].

The experience of the surgeon, or presence of a senior tutor by the side of the operating resident, the applied technique, nerve monitoring, and instrumentation are all contributing factors of avoiding VFP [38] [39] [40] [41] [42] [43].

Proved by animal experiments, the acting forces and the provoked elongation may influence the functional recovery if any [44] [45] [46].

1/3 Defining removal methods (from a medical point of view)

For the removal of the nerves, we determined which tools and incisions should be used. The minimum length required was determined too, which is a key element of research work. The nerves were removed unharmed with their epineurium.

The postmortem transfer to the Semmelweis University's 1st Department of Pathology and Experimental Cancer Research was immediate, and the dissection was achieved usually in 24 hours, never later than 3 days.
At the Institute of Pathology, the bodies were autopsied after storage at 6 ° C. The autopsy was performed at a room temperature of 22 ° C.

1/4 Development of storage method and transport of facial nerves

Specimens were stored and transported in 'containers' suitable for clinical specimen tissue. They were stored in 3 different liquids: physiological saline, 5% formaldehyde and 20% formaldehyde. Storage of samples was determined at 0-9 day intervals.
In order to preserve the biomechanical properties of the samples, in most cases, they were transported in physiological saline without any additional solution. The samples were identified in physiological saline at room temperature in order to prevent their drying out.
The storage time influenced the result of the measurement. Among the samples stored for a shorter period (0-2 days), the number of evaluable samples was higher than the samples stored for 5-9 days (93.8% > 68.4%). In case of the evaluable samples that were stored for a short time, 21% were ruptured whilst for others this number was 7% (see diagram).

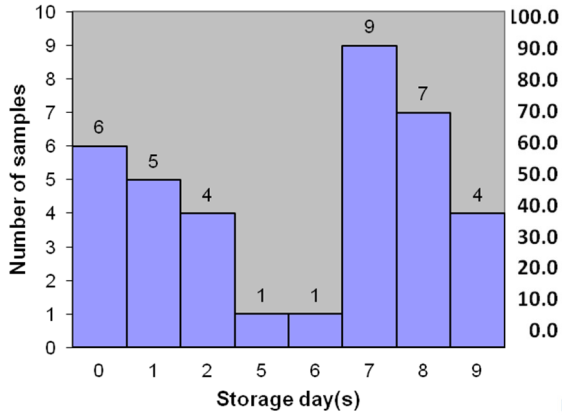

Distribution of samples' storage day(s)

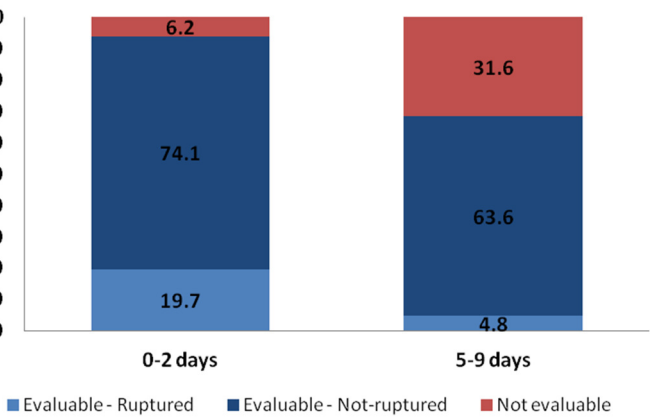

Distribution of samples' evaluable

The time between the death and tensile test influenced the load of the nerve. The nerves became less resistant with the increasing number of days; but there was no significant difference. So, when the tensile test of the nerve was started before the starting point of decomposition, the nerve was more durable.
Comparing the method of storage, we have found, that those samples that were stored in 5% formaldehyde had slightly lower evaluated sample rate than in case of physiological saline and 20% formaldehyde (see diagram). In case of 5% formaldehyde, the evaluable samples ruptured in 20.8%, in case of 20% formaldehyde it was 13%, and in case of physiological saline it was 0% (see diagram).

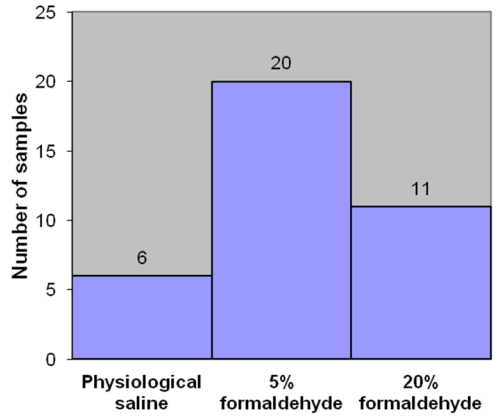

Distribution of samples' storage mode

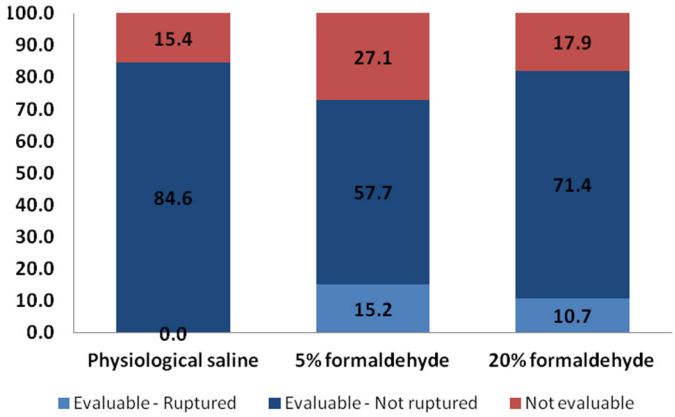

Distribution of samples' evaluable

The first step was to identify the precise the anatomy and branching pattern of the nerve on both sides (right and left side of the cadaver). The nerves were spread all over them. In the case of facial nerves, the identification of the examined 3 branches of the nerve - marginal, buccal, zygomatic - was achieved (see Figures).

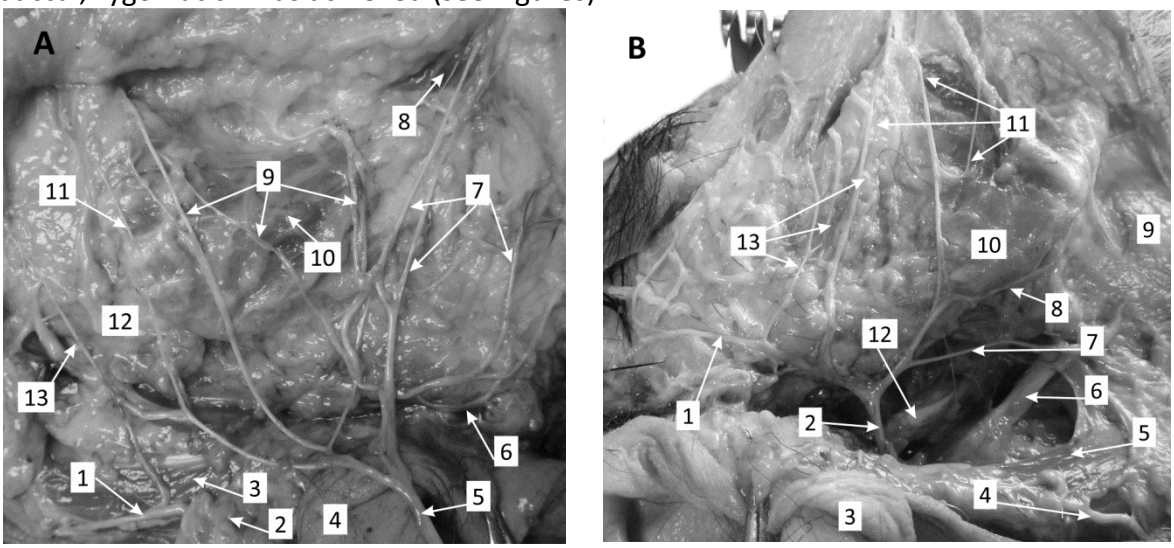

Extratemporal facial nerve, preparation; (a) left side, after liberation at the stylomastoid foramen; (b) right side with the trunk leaving the skull-base.

(a) 1 – great auricular nerve 2 –displaced inferior pole of the parotid 3 – sternocleidomastoid muscle 4 – ear lobe 5 – trunk 6 – temporal branch 7 – zygomatic branches 8 – orbicular oculi muscle 9 – buccal branches 10 – masseter muscle 11 – marginal mandibular branch 12 – mandibular angle 13 – cervical branch

(b) 1 – temporal branch 2 – trunk 3 – ear lobe 4 – great auricular nerve 5 – sternocleidomastoid muscle 6 – posterior belly of the digastric muscle 7 – cervical branch 8 – marginal mandibular branch 9 –submandibular gland 10 – mandibular angle 11 – buccal branches 12 – styloid process 13 – zygomatic branches

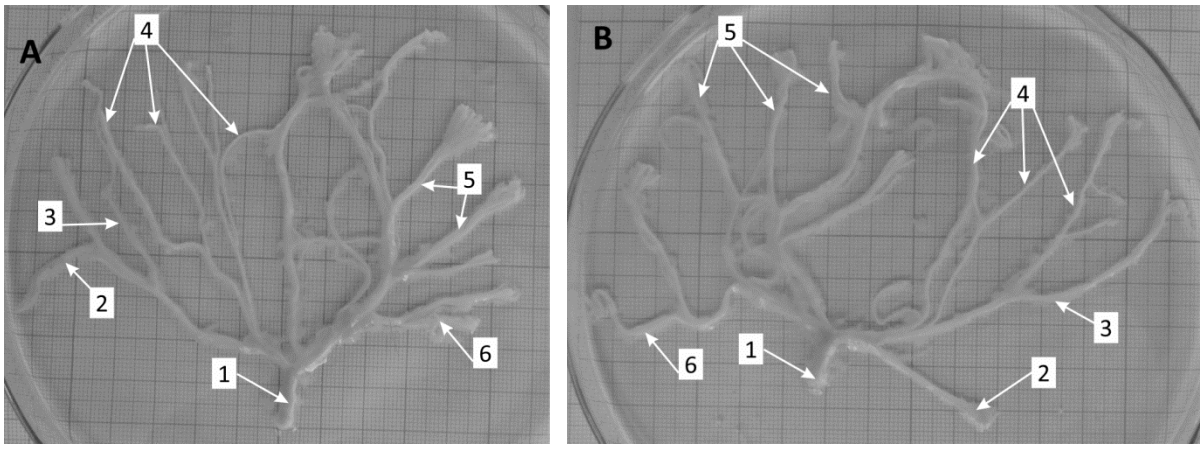

(a) Left and (b) right extratemporal facial nerve in the recipient
1 – trunk 2 – cervical branch 3 – marginal mandibular branch 4 – buccal branches 5 – zygomatic branches 6 – temporal branch

1/5 Design and manufacture of special instruments for testing (e.g. in-house developed clamps)

Individually designed and manufactured clamps were made for nerve clamping (see below). The relaxation tests were performed in liquid. The test apparatus is provided with a unique liquid storage container in which the above-mentioned clamp can be fixed.

Design criteria for clamps:

- As similar as possible to surgical interventions.
- Avoid sliding of the nerve during the tensile test
- To minimize the damage to the nerve caused by the clamp
- Easy manufacturing
- It should be reusable

Polymer Ring Clamp

Aluminium Ring Clamp

Short samples represented a difficulty, wrapping around being impossible. Further modifications were necessary to accommodate shorter samples.

Advanced Aluminium Ring Clamp

Square Aluminium Plate Clamp

Double-blade Aluminium Ring Clamp

Single Ring Double Clamp

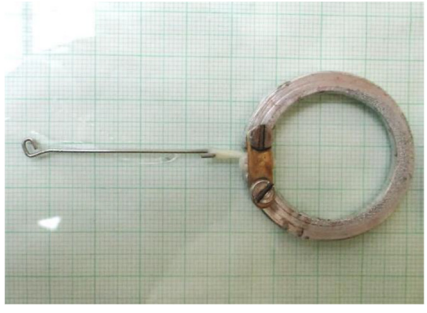

1/6 Preparation of a protocol using the experience of previously performed (10 cadavers) measurements

We have developed a protocol that includes the identification, storage and transport of nerve removed at autopsy, as well as optical and mechanical testing under laboratory conditions.

Elements of the protocol include systematization and processing of data from sample measurements, and statistical analysis and evaluation.
Steps of the test protocol:

- Removal of facial nerves
- Spreading and marking of facial nerves
- Stereomicroscopy before tensile test (see Figure)
- Taking photos when captured in tensile machine (see Figure)
- Tensile test
- Stereomicroscopy after tensile test (see Figure)
- Summary and evaluation of results

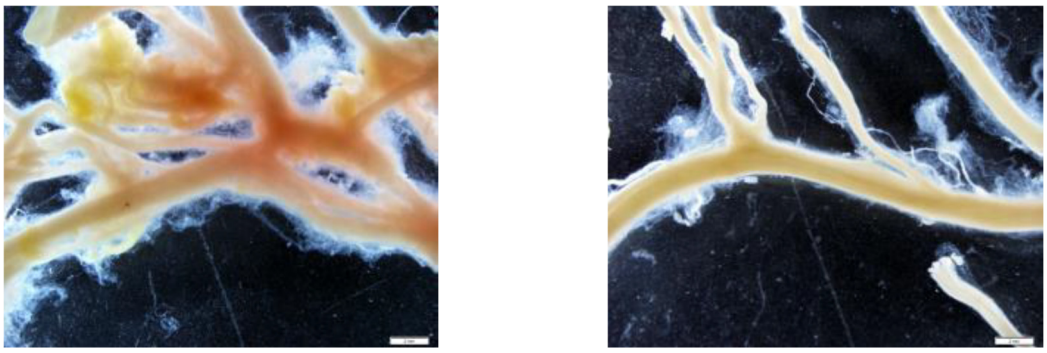

Stereomicroscopic images before tensile test (zygomatic branch and buccal branch)

Macro photos of the captured nerve before and after the tensile test

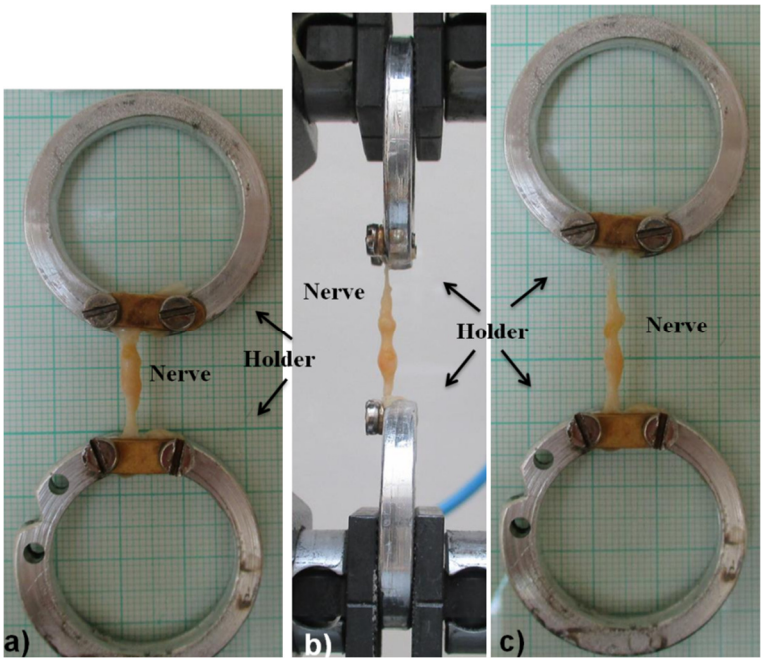

Nerve before (a), during (b) and after (c) the tensile test

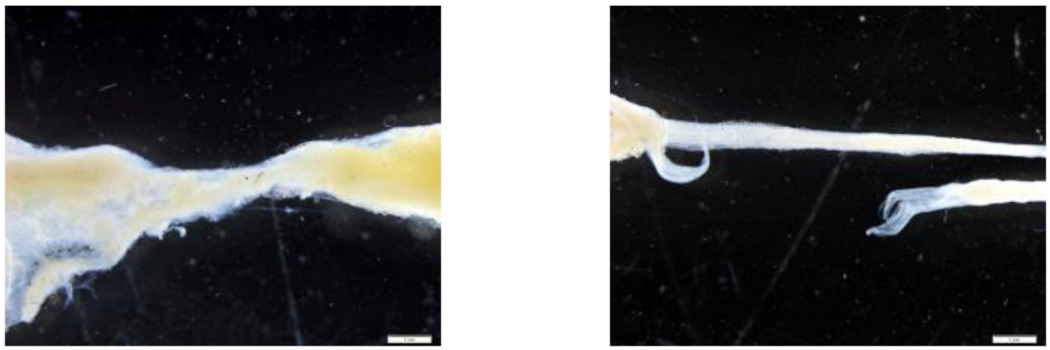
Stereomicroscopic images after tensile test (zygomatic branch and buccal branch)

1/7 Development of destructive and non-destructive testing methods

For the development of the nerve examination methodology, we considered occurring loads in clinical practice as well as the non-destructive and destructive examination methods used in the technical practice. The nerves were analyzed by macro-, microscopic, tensile and tear tests.

1/8 Purchase of unique tools and equipment for autopsy and measurements

The unique facilities for the autopsy, the storage and transport vessels, and the fluids used to store the specimens were provided by the Semmelweis University's 1st Department of Pathology and Experimental Cancer Research. The individual tools necessary for the measurements were provided by the persons involved in the implementation of the professional program.

Further results – Publications

[1] Róbert Késmárszky, Péter, Nagy Tamás Micsik, Gergely Rácz, Liza Pelyhe, Bettina Pogácsás, Réka Potsubay, Eszter Bognár: Applied anatomy of the facial nerve in view of head and neck surgery, II. Triangle Symposium of the Poland-Hungary-Japan Surgical Society, Lublin, Poland, 19-21 June 2016.

[2] Róbert Késmárszky, Péter, Nagy Tamás Micsik, Gergely Rácz, Liza Pelyhe, Bettina Pogácsás, Réka Potsubay, Eszter Bognár: Anatomical and Biomechanical Analysis of the Human

Recurrent Laryngeal Nerve, UEP 2016, Bilbao, Spain; 29 September-01 October 2016, International faculty.
[3] R. Késmárszky, P. Nagy , T. Micsik, G. Rácz , L. Pelyhe, B. Pogácsás, R. Potsubay, E. Bognár: Anatomia e biomeccanica del nervo mandibolare marginale come fattori di rischio chirurgici. 41st Congresso Conventus Societas ORL Latina, Torino, Italy, 2016
[4] R. Késmárszky, P. Nagy , T. Micsik, G. Rácz , L. Pelyhe, B. Pogácsás, R. Potsubay, E. Bognár: El nervio marginal mandibular: un factor de riesgo en la cirugia cervico-facial. 35th Panamerican ENT Congress, La Habanna, Cuba, 2016, International faculty.
[5] R. Késmárszky, P. Nagy , T. Micsik, G. Rácz , L. Pelyhe, B. Pogácsás, R. Potsubay, E. Bognár: Marginal mandibular nerve anatomy and its practical aspects in facial surgery. 8th World Congress of Facial Plastic Surgery, International faculty, Rio de Janeiro, Brasil, 2016, International faculty.
[6] R. Késmárszky, P. Nagy , T. Micsik, G. Rácz , L. Pelyhe, B. Pogácsás, R. Potsubay, E. Bognár: The marginal mandibular nerve to be considered in case of neck dissections due to rhinological malignancies. 3rd International Conference of Rhinology and Otology, Dubai, 2016, International faculty, Key-note lecture.
[7] R. Késmárszky, P. Nagy , T. Micsik, G. Rácz , L. Pelyhe, B. Pogácsás, R. Potsubay, E. Bognár: The applications of the facial nerve's anatomy in sports medicine based on experimental dissections. 50th Congress of the Hungarian Society of Sports Medicine, Budapest, Hungary, 2016.
[8] R. Késmárszky, P. Nagy , T. Micsik, G. Rácz , L. Pelyhe, B. Pogácsás, R. Potsubay, E. Bognár: Psychiatric applications of the macroscopic neuroanatomy of the facial nerve- a look around the facial expressivity. Divan sur la Danube 2016, Budapest, Hungary, 2016.
[9] Róbert KÉSMÁRSZKY, Péter NAGY, Tamás MICSIK, Gergely RÁCZ, Ágnes BOKÁNYI, Bettina POGÁCSÁS, Eszter BOGNÁR : Anatomical and Biomechanical Analysis of the Human Recurrent Laryngeal Nerve, International Federation of ENT Societies (IFOS), Paris, 2017.

4.2 September 2016 – August 2017

2/1 Applying the test protocol developed in the first phase of work on 10 facial nerves removed from cadavers

According to the examination protocol, worked out during the previous year, ten extratemporal facial nerves, including their epineural envelopes, were prepared from five adult cadavers with no systemic disease or local findings that modified the ability to analyse their biomechanical characteristics a standardized fashion. Stereomicroscopy before and after the tensile tests of the marginal mandibular branches provided information about the structure, diameter (thickness) and morphology of the extratemporal facial nerves. The elongation and maximal load were determined.

2/2 Evaluate the results of the previous tests

The nerves were dissected in their integrity. During the tensile test, proportionally important elongations happened at the maximal tolerable load, causing disruption. A mean maximal load value was established. The diameter of the nerves and the age, weight and height of the patients did not show correlation with the value of the maximal load. The elasticity and resistance show differences to biomechanical forces.

Factors like the number and structure of the constructing fibres, the amount of the protective connective tissue, the collagen content and the related vascular network are supposed to explain this heterogeneity. The observations may help to understand surgical activity, trauma and tumoral displacement related transformations of the nerve.

2/3 Statistical evaluation of results

In our study, there was no correlation between the diameter, age, weight and height and maximal load value; the nerve can tolerate a relatively large elongation before its disruption, and the maximum elongation length is not related to its macroscopic characteristics.

2/4 Reviewing individual tools and making any changes

There was no need to modify the clamps.

2/5 Determine a load range based on the measurement results

Regardless of the side, disruption occurred within a maximal force range of 1–13 N.

2/6 Further investigation – Relaxation studies

The relaxation studies were made on 11 human recurrent laryngeal nerves from the left side of 11 cadavers. The relaxation tests were performed in 5% formaldehyde at room temperature.

There were 5 sample from women and 6 from man. The average age was 73 years. The average 'mean thickness' of the investigated nerves was 1.5±0.3 mm without epineurium and 1.7±0.4 mm with epineurium before the relaxation test. There were no any significant differences in the age and the mean thickness of the nerve related to sex (see below).

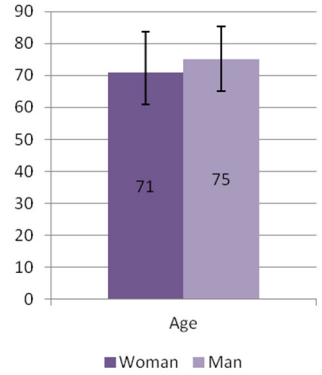

p=0.272

Comparison of age by sex

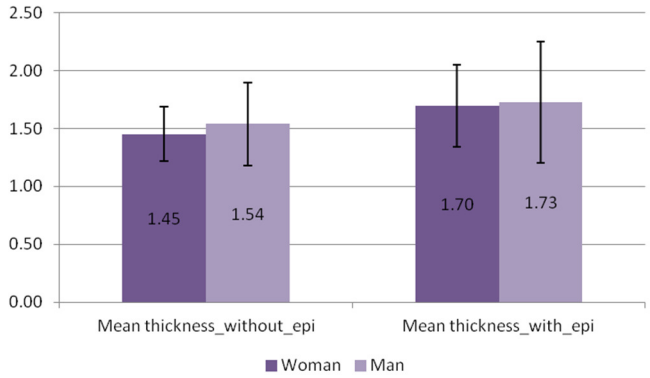

p=0.465 p=0.927

Comparison of average mean thickness by sex

During the relaxation test (Instron 5965, Instron, Norwood, MA, USA), a constant speed of 2 mm/min was used. Disruption was considered to be the state when the loading force was less than 1 N. The preload value was 0.1 N. The measurement started after an extension of 2 mm. The measurement time was approximately 600 sec (approximately 750 sec with rise time).

The resulting curves are shown in the figures below. Two curves had high maximal load, therefore these are shown separately due to the oppression of the others.

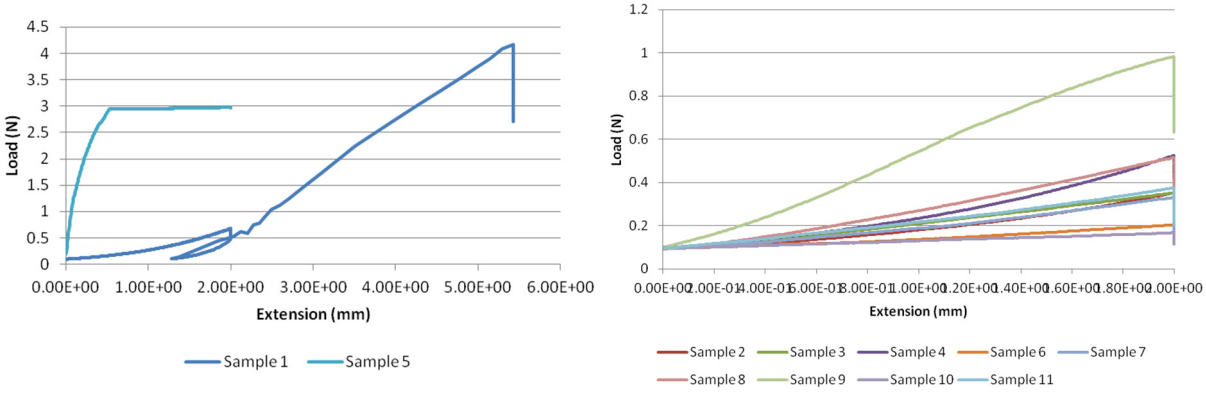

Load – extension curves with (a) high and (b) lower maximal load

There was moderate correlation between the age and diameter decreasing in case of mean thickness without epineurium, and there was weak negative correlation between the age and maximal load. In the other cases, there was no correlation either. There was no significant correlation (see in Table below).

Correlations

		Age	Change in length	Diameter decreasing (without epi.)	Diameter decreasing (with epi.)	Max Load	Sex
Age	Pearson Correlation	1	,252	,503	,313	-,448	-,200
	Sig. (2-tailed)		,454	,115	,348	,167	,555
	N	11	11	11	11	11	11
Change in length	Pearson Correlation	,252	1	,148	,260	,162	-,346
	Sig. (2-tailed)	,454		,664	,440	,634	,297
	N	11	11	11	11	11	11
Diameter decreasing (without epi.)	Pearson Correlation	,503	,148	1	,080	-,073	-,358
	Sig. (2-tailed)	,115	,664		,814	,831	,280
	N	11	11	11	11	11	11
Diameter decreasing (with epi.)	Pearson Correlation	,313	,260	,080	1	,047	-,259
	Sig. (2-tailed)	,348	,440	,814		,890	,442
	N	11	11	11	11	11	11
MaxLoad	Pearson Correlation	-,448	,162	-,073	,047	1	,082
	Sig. (2-tailed)	,167	,634	,831	,890		,810
	N	11	11	11	11	11	11
Sex	Pearson Correlation	-,200	-,346	-,358	-,259	,082	1
	Sig. (2-tailed)	,555	,297	,280	,442	,810	
	N	11	11	11	11	11	11

The sex did not influence significantly the age, the change in length, the diameter decreasing with and without epineurium and the maximal load.

2/7 Further investigation – Invested work

The invested work was measured from the values of load and extension. The number of individuals was 56. The distribution of the range of invested work by different properties is shown on the diagrams below.

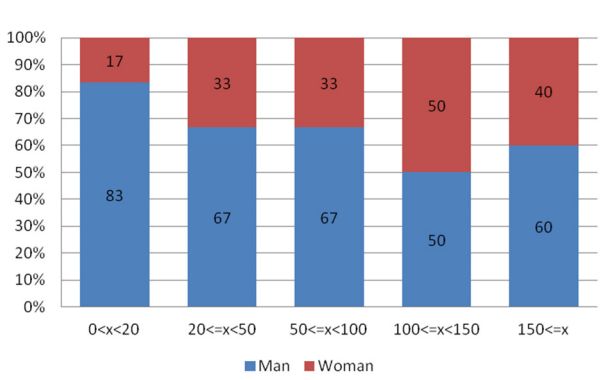

Distribution of invested work by sex

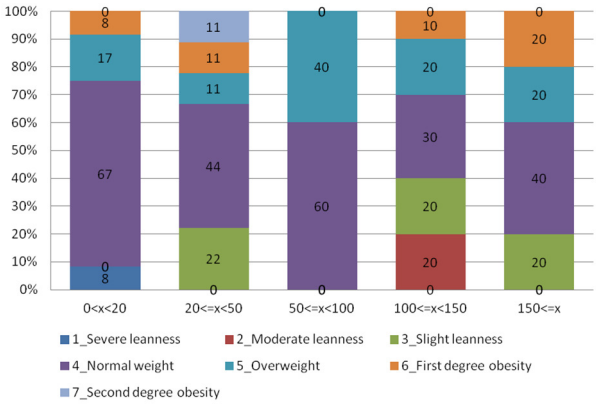

Distribution of invested work by BMI

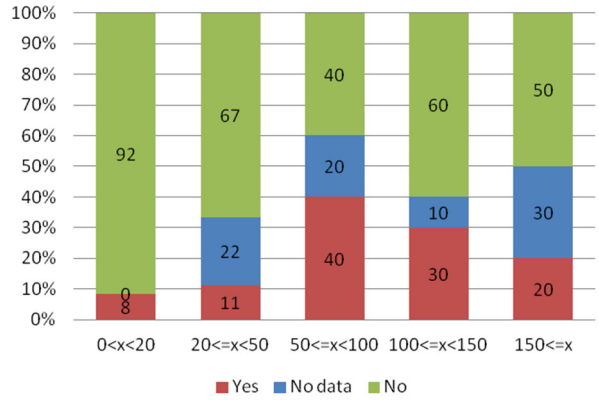

Distribution of invested work by diabetes

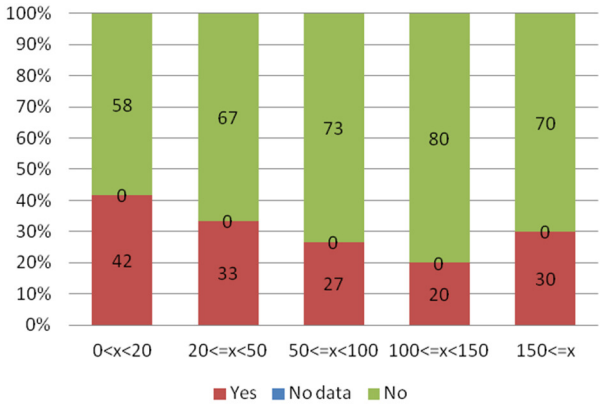

Distribution of invested work by smoking

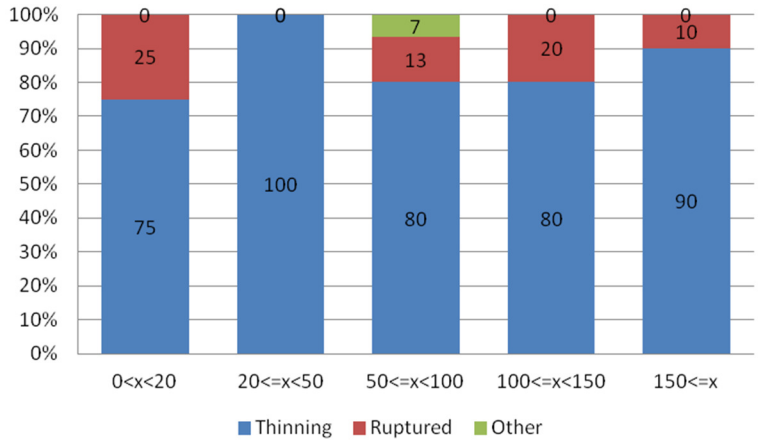

Distribution of invested work by condition of nerve after tensile test

The invested work for nerves from man was between 0-20 Nmm, and this range was 100-150 Nmm in case of woman. The invested work by nominal weight was 0-20 or 50-100 Nmm. Be noted that in the range of 50-100 Nmm there were only the normal and the overweight BMI. It cannot be said that the highest BMI had the highest investigated work.

The invested work when analysing specimens of diabetic patients was higher than without diabetes. In case of smoking, the invested work was lower than without smoking. In case of total rupture, the invested work was not lower than in case of thinning.

Further results – Publications

[1] R Késmárszky, B Pogácsás, P Nagy, T Micsik, G Rácz, Á Bokányi, E Bognár: An Ex-vivo Biomechanical Study of the Human Marginal Mandibular Nerve, 13th International Facial Nerve Symposium, Hollywood, California, August 3-6, 2017; oral presentation

[2] R Késmárszky, P Nagy, T Micsik, G Rácz, Á Bokányi, B Pogácsás, E Bognár: Analysis of the Anatomy and Biomechanics of the Human Recurrent Laryngeal Nerve in View of its Resistance to Mechanical Trauma. 21st IFOS ENT World Congress, International Federation of Oto-Rhino-Laryngologycal Societies, E-Poster, 2017, Paris 2017 June 24-28.

[3] R Késmárszky: Anatomy of the Facial Nerve and its Clinical Aspects. Semmelweis Medical School, Budapest, public lecture in English, 2017 March

[4] R Késmárszky R: Az Arcideg Anatómiája es Klinikai Aspektusai. Semmelweis Egyetem, Anatómiai Intézet, Budapest, tantermi előadás. 2017 március, magyarul

[5] R Késmárszky, P Nagy, T Micsik, G Rácz, L Pelyhe, B Pogácsás, E Bognár: Anatomy and psychology of the facial palsies. Kerekasztalban /moderator: R. Késmárszky/, Divan sur la Danube, Budapest, Hungary, 2017

[6] Késmárszky R, Nagy P, Micsik T, Pogácsás B, Bokányi-Tóth Á, Bognár E: A statisztikai elemzések szerepe a sérülések megelőzésében a perifériás arcidegi ágak területén végzett műtétek kapcsán hazai populációban. ÉRTÉKMENTÉS és INNOVÁCIÓ a TUDOMÁNYBAN konferencia sorozat, STATISZTIKA a TUDOMÁNYOK, a TECHNIKA és az ORVOSLÁS KÖRÉBEN. V. KLINIKUM, OKTATÁSI FELADATOK, STATISZTIKA szekció. Abstract, előadás. 2017. November 16-17., Budapest

[7] Róbert Késmárszky, Péter Nagy, Imre Kientzl, Liza Pelyhe, Tamás Micsik, Gergely Rácz, Tareg Ben Naser, Ágnes Bokányi-Tóth, Bettina Pogácsás, Eszter Bognár: The biomechanical characteristics of the human recurrent laryngeal nerve: An ex-vivo neuromechanical study. European Annals of Otorhinolaryngology, Head and Neck Diseases, invited paper to their special issue, article in progress.

4.3 September 2017 – August 2018

3/1 Laboratory examination of 10 more facial nerve samples

Damage to the human facial nerve may lead to palsy. Damage to the human recurrent laryngeal nerve (HRLN) may lead to vocal fold palsy. It is important to understand their responses to mechanical forces. No objective biomechanical studies were available that could serve as a basis to explain the consequences of mechanical forces, which led to this ex-vivo studies.

Five pairs of the extratemporal facial nerve, and five pairs, representing 10 specimens of the human recurrent laryngeal nerve including their epineural sheaths were prepared from adult cadavers with no systemic disease or local findings that could have modified the ability to analyze their biomechanical characteristics.

3/2 Demonstration of the applicability of the determined measurement technique with new facial nerve samples

A standardized tensile test was used to simulate uniaxial forces (see Figure). The maximal load leading to disruption and the corresponding elongation were measured. The structure, thickness, and morphology were examined by stereomicroscopy before and after the exposure.

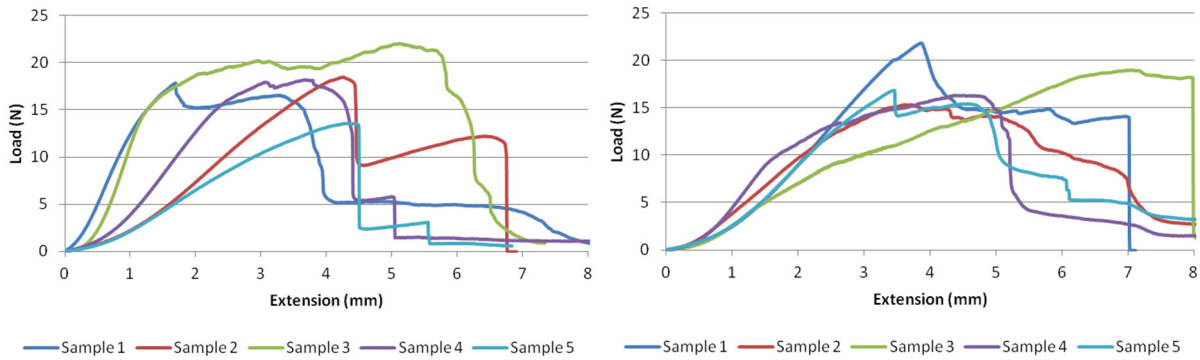

Load-extension curves of (a) left and (b) right HRLN

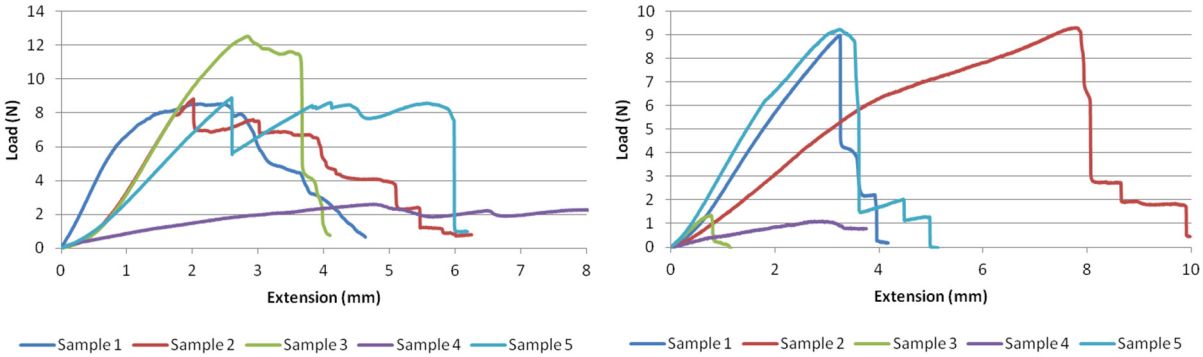

Load-extension curves of (a) left and (b) facial nerve

In case of human facial nerve, the length and thickness of the specimens from the two sides were similar. The maximal load values and percentage elongation were very volatile both side. The ultimate tensile strength was very volatile on both sides too without significant differences. There was no strong correlation between the mean thickness and the percentage elongation of the two sides. Biomechanical differences of the elasticity and resistance cannot be predicted by the biometric characteristics of the patients and the nerves; the macroscopic appearance of the nerve does not correlate with its vulnerability.

In case of human recurrent laryngeal nerve, the length and thickness of specimens from the two sides were similar. The maximal load values were very heterogenic both sides. The percentage elongation was very heterogenic or very volatile; the elongation on the left being significantly more important. The ultimate tensile strength was very volatile on both sides without significant differences between them (see Figures). There was no strong correlation between the mean thickness and the percentage elongation on the two sides. The elongation during the tensile test was proportionally important at the maximal tolerable load that caused disruption. During exposure to mechanical forces, currently obtainable data does not permit predicting the morphological and the related physiological answers of the nerve. Other than the meticulous surgery and knowledge of the anatomy, understanding the relationship of the mean maximal load and elongation may help to reduce the incidence of iatrogenic vocal fold palsy and promote the efficacy of nerve reconstructions.

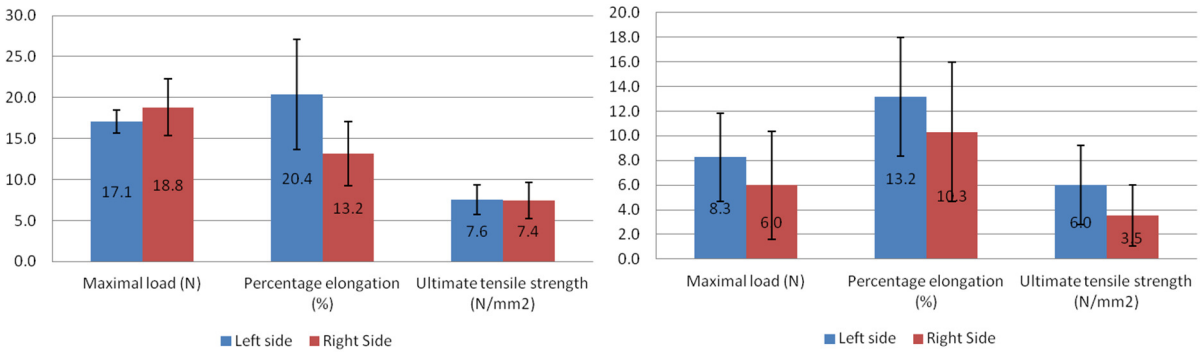

Comparison of important features of (a) HRLN and (b) facial nerve by side

The expected result of these two researches is a measurement and evaluation system suitable for the examination of the facial nerve in laboratory conditions, which is suitable for determining the behaviour of the individual facial nerve against the tensile force. Preparing the design and functional properties of a medical device for clinical use to reduce the risk of facial nerve interventions.

4.4 September 2018 – August 2019

4/1 Comparison of measurement results on different facial nerve samples

In this period, our aim was the determination of effect of the mean thickness, the maximal load, the elongation and the percentage elongation of the ultimate tensile strength in case of the human recurrent laryngeal nerve and in case of the human facial nerve. In case of the human recurrent laryngeal nerve, these variables or one part of these rather heavily influenced the ultimate tensile strength.

In the next step, the inclusion of different explanatory variables was investigated in the model using the significance level. Out of these, they had no influence on the 'elongation' and 'percentage elongation' variables; their significance was above 0.05 (see Table).

Coefficients[a]						
Model		Unstandardized Coefficients		Standardized Coefficients	t	Sig.
		B	Std. Error	Beta		
1	(Constant)	13,040	1,856		7,025	,001
	Mean thickness	-7,331	,893	-,998	-8,205	,000
	Maximal load	,421	,070	,702	6,009	,002
	Elongation	,217	,276	,255	,787	,467
	Percentage elongation	-,102	,121	-,266	-,843	,438
a. Dependent Variable: Ultimate tensile strength						

The mean thickness and maximal load significantly influenced the ultimate tensile strength; they explained 94% of the differences in ultimate tensile strength. The strength of the relationship between outcome variables and explanatory variables was quite strong. For example, ceteris paribus unit change in maximal load resulted +0.43 change in the rate of ultimate tensile strength (see Table below).

Coefficients[a]					
Model	Unstandardized Coefficients		Standardized Coefficients	t	Sig.
	B	Std. Error	Beta		

1	(Constant)	13,262	1,306		10,154	,000
	Mean thickness	-7,448	,746	-1,014	-9,990	,000
	Maximal load	,431	,061	,718	7,077	,000
a. Dependent Variable: Ultimate tensile strength						

In case of the facial nerve, the ‘elongation' and 'percentage elongation' did not significantly influence the ultimate tensile strength (similar as in case of human recurrent laryngeal nerve), but the mean thickness and maximal load significantly influenced it (see Table below).

Coefficients[a]						
Model		Unstandardized Coefficients		Standardized Coefficients	t	Sig.
		B	Std. Error	Beta		
1	(Constant)	7,849	3,491		2,248	,074
	Mean thickness	-6,506	1,106	-,911	-5,884	,002
	Maximal load	,827	,087	1,041	9,466	,000
	Elongation	,017	,252	,010	,067	,949
	Percentage elongation	,015	,064	,025	,234	,824
a. Dependent Variable: Ultimate tensile strength						

The strength of the relationship between outcome variables and explanatory variables was quite strong. The mean thickness and maximal load explained 96% of the differences in ultimate tensile strength. For example, ceteris paribus unit change in maximal load resulted +0.83 change in the rate of ultimate tensile strength (see Table below).

Coefficients[a]						
Model		Unstandardized Coefficients		Standardized Coefficients	t	Sig.
		B	Std. Error	Beta		
1	(Constant)	8,253	,838		9,847	,000
	Mean thickness	-6,596	,657	-,924	-10,044	,000
	Maximal load	,830	,073	1,044	11,346	,000
a. Dependent Variable: Ultimate tensile strength						

Altogether, it was found that the mean thickness and maximal load strongly influenced the ultimate tensile strength regardless of the nerve type. However, the ceteris paribus unit change in maximal load resulted different change in the rate of ultimate tensile strength.

4/2 Summarizing the relevant results for technical and clinical practice

The Table and Figure below contains the force-interval of the nerves determined by our research. By following these values, damage of nerves can be avoided.

Branch	Marginalis		Buccalis		Zygomaticus		HRLN	
Side	Left	Right	Left	Right	Left	Right	Left	Right
Safety interval (N)	0-2.10	0-1.10	0-0.95	0-1.88	0-0.61	0-0.50	0-4.11	0-6.89

Safety interval (N) by nerve by side

The mean thickness and maximal load strongly influenced the ultimate tensile strength regardless of the nerve type. The increasing of the nerve thickness increased the load uptake. Compared the investigation of longitudinal and transverse rupture, in the case of transverse rupture, the nerves could attain greater load during the rupture. This result was encouraging as this type of load is most common during surgeries.

The tolerance of the nerve depended on the tensile test speed; the load values were higher in case of higher tensile test speed.

4/3 Summary of the studies in numbers

There were 37 cadavers in the investigation. Their distributions of various characteristics are shown in the following figures.

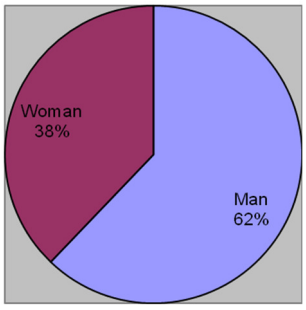

Distribution by sex

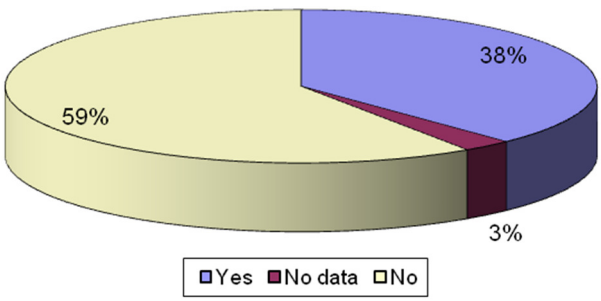

Distribution by smoking

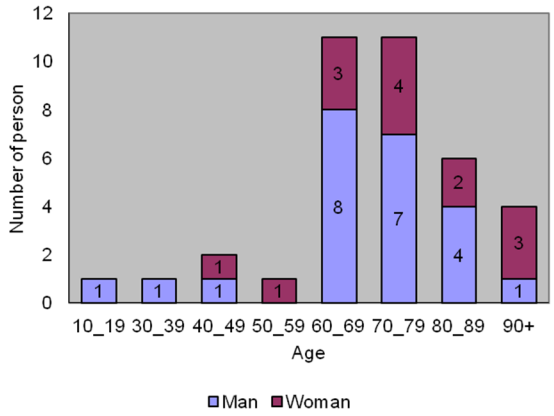

Distribution by age and sex

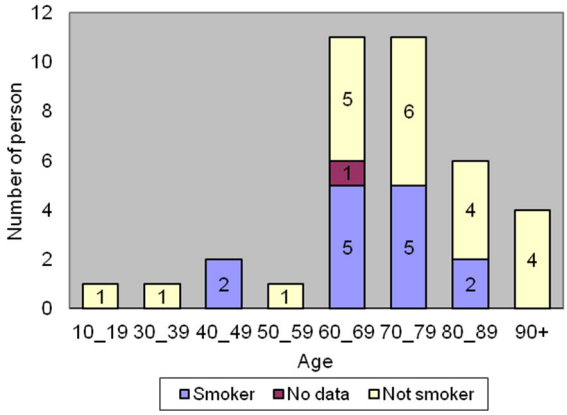

Distribution by smoking and age

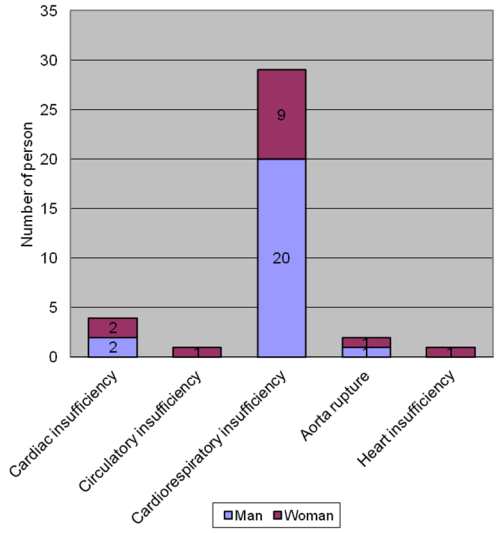

Distribution by known disease and sex

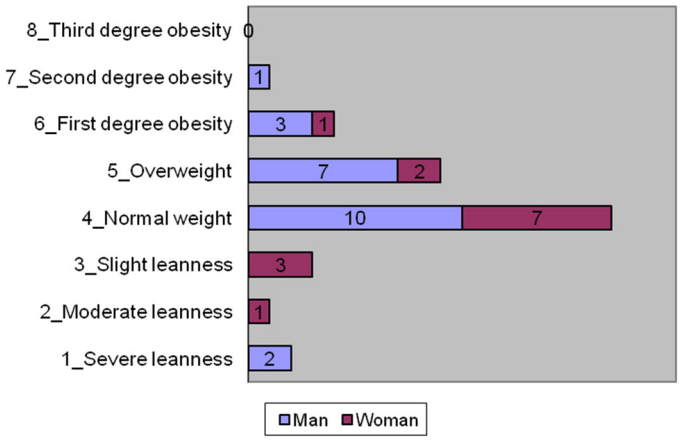

Distribution by BMI and sex

7 cadavers had diabetes (see diagram), their number of samples were 16. Among these, the number of evaluable samples was higher than the others (see diagram).

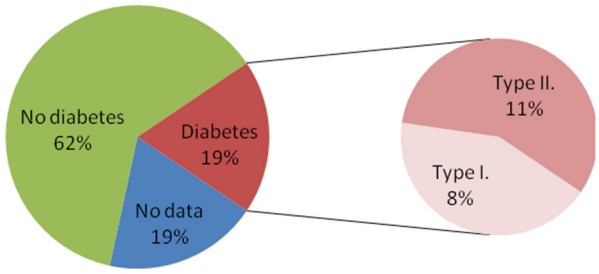

Diabetes ratio

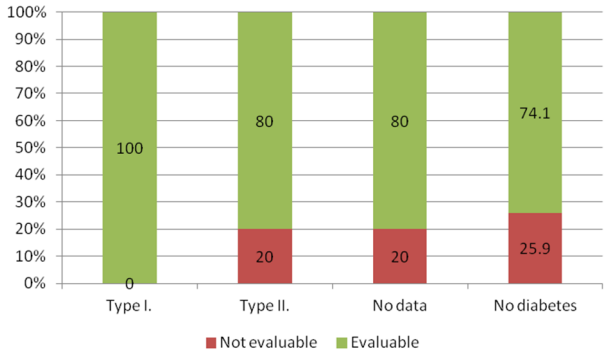

Evaluable ratio by diabetes

A total of 89 tensile tests were performed, of which 20 could not be evaluated, 11 were Relax tests and the other 58 were successful tensile test (see diagram).

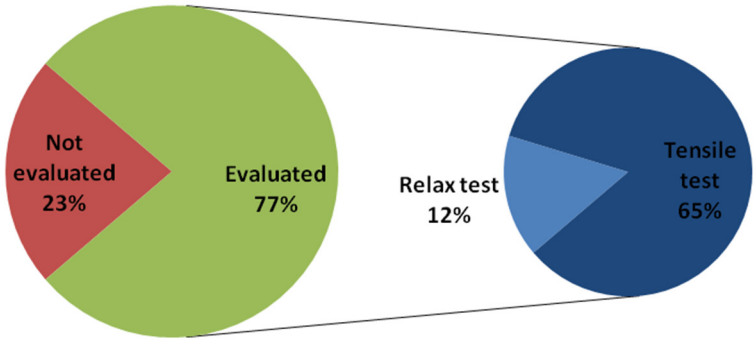

Tensile test ratio

There was a larger ratio of left-sided nerves that could be evaluated (see diagram). On the other hand, ruptures were twice as high in the left samples (21.7%) than in the right samples (10.7%) (see diagram).

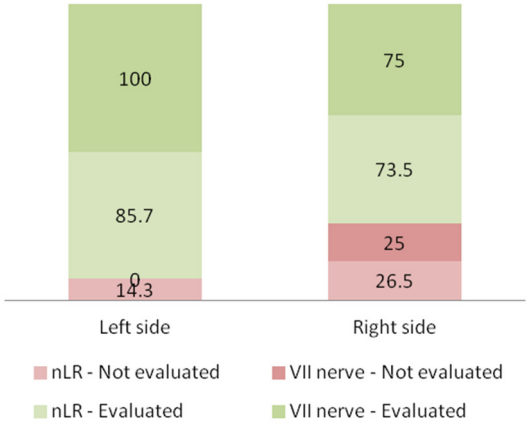

Comparison of nerve side usability by side

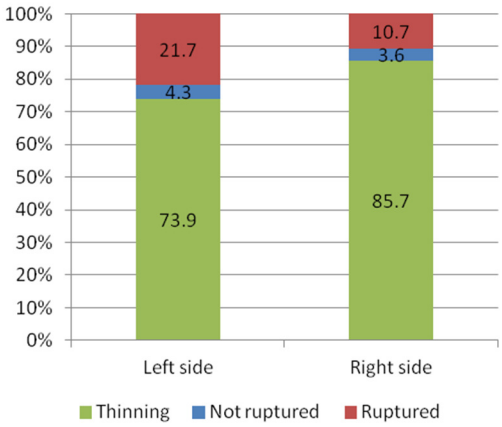

Comparison of rupture ratio by side

Women had a slightly higher number (in proportion) of evaluable samples and, to a lesser extent, a higher rate of rupture (see diagram).

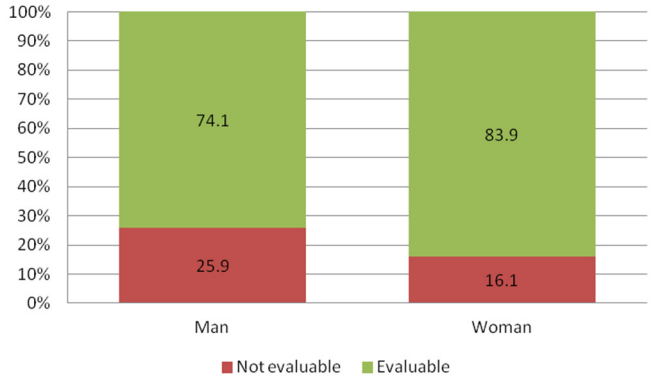

Comparison of evaluable ratio by sex

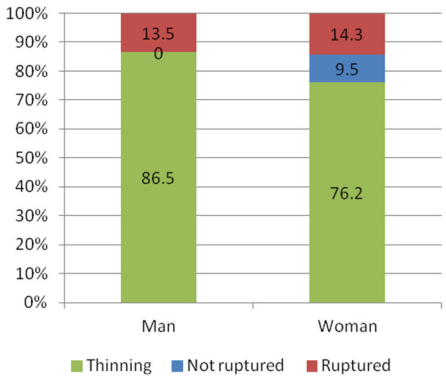

Comparison of rupture ratio by side

There was no rupture in case of less than 60 years, but between 80 and 89 years was exceptionally high, 45.5% (see diagram).

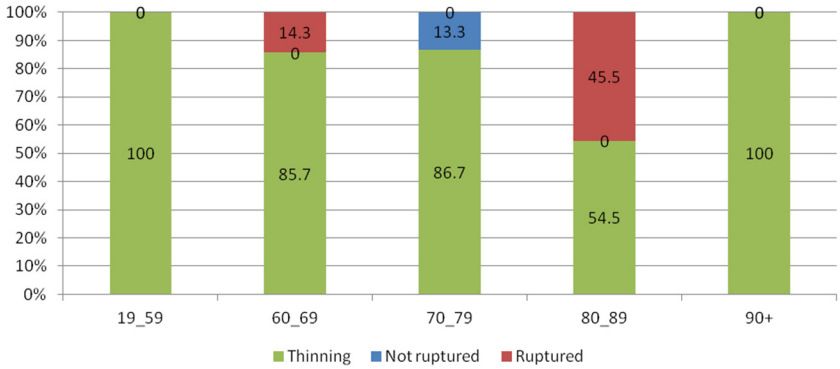

Rupture ratio by age

The rupture ratio by BMI is shown on diagram below. There was total rupture in case of slight leanness, normal weight and overweight BMI.

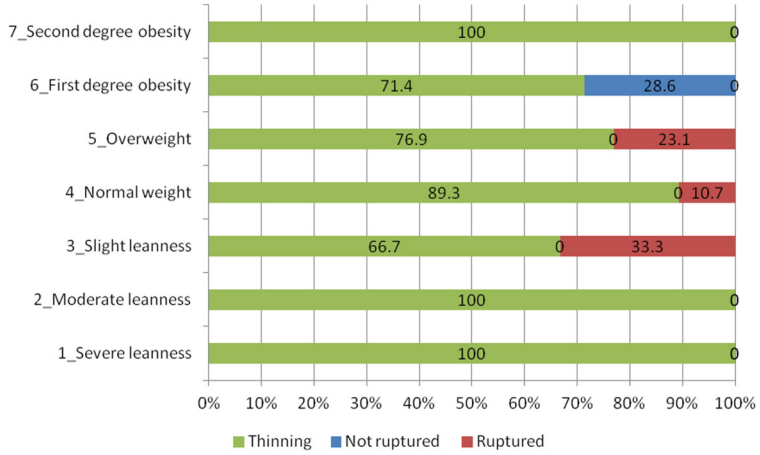

Rupture ratio by BMI

5 Answers to our research questions and the expected benefits of research

1. What range of load values can be applied to the facial nerves while guaranteeing their non-injury?

The Figure below contains the force-interval of the nerves determined by our research. By following these values, damage of nerves can be avoided.

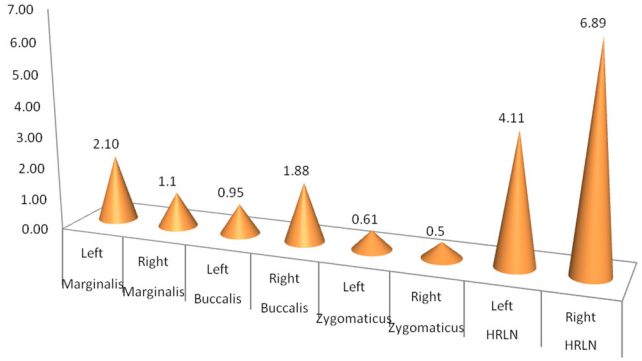

2. What tools are needed to perform the relevant laboratory measurements?

- Digital camera for digital documentation (in our case: Canon ixus 145)
- Tensile Testing Machine with low kN load cell and jaw face (in our case: Instron 5965 Dual Column Tabletop Testing Systems with 5 kN load cell and 2kN jaw face)
- Special clamp for nerve clamping

- Stereomicroscope (in our case: Olympus SZX16)
- Other little things: plotting paper, ruler

3. What 'material properties' can be determined by laboratory tests?

- Elongation from the initial length and the length after the tensile or relaxation test
- Percentage elongation (%) from the initial length and the length after the tensile or relaxation test
- Change of mean thickness from the initial mean thickness and the mean thickness after the tensile or relaxation test
- Maximal load from the tensile or relaxation test
- Investigated work from the load and extension
- Ultimate tensile strength from the maximal load and cross-section area

References

[1] R. Késmárszky, Writer, *Arcidegek biomechanikaja disszekcios modelleken [Biomechanics of facial nerves in dissection models].* [Performance]. BUTE, Department of Materials Science and Technology, 2014.

[2] FlorHosp, "Arcideg műtéti feltárása arcidegbénulás esetén (Nervus facialis decompressio)," Pest Megyei Flór Ferenc Kórház, [Online]. Available: https://florhosp.hu/wp-content/uploads/2015/09/08_arcideg.pdf. [Accessed 06 02 2020].

[3] M. Réthelyi and J. Szentágothai, "A környéki idegrendszer," in *Funkcionális anatómia III.*, Budapest, Medicina Könyvkiadó Zrt., 2002.

[4] J. H. Volker, "Posterior Auricular Nerve," Earthslab, 08 08 2018. [Online]. Available: https://www.earthslab.com/anatomy/posterior-auricular-nerve/. [Accessed 14 02 2020].

[5] L. A. Ho, A. M. Scott, F. A. Klassen, J. S. Cano, L. A. Pusic and N. Van Laeken, "Measuring quality of life and patient satisfaction in facial paralysis patients: a systematic review of patient-reported outcome measures.," *Plast Reconstr Surg,* vol. 130, pp. 91-99, 2012.

[6] L. J. Kampshoff, H. T. Cogbill, A. M. Mathiason, J. K. Kallies and T. L. Martin, "Cranial nerve injuries are associated with specific craniofacial fractures after blunt trauma," *Am Surg,* vol. 76, p. 1223–7, 2010.

[7] O. T. Odebode and E. F. Ologe, "Facial nerve palsy after head injury: Case incidence, causes, clinical profile and outcome," *J Trauma,* vol. 6, p. 388–91, 2006.

[8] N. Sharma, K. Cunningham, G. R. Porter, J. S. Marzo, J. K. Jones and M. E. Foecking, "Comparison of extratemporal and intratemporal facial nerve injury models," *Laryngoscope,* vol. 119, pp. 2324-30, 2009.

[9] A. N. Falco and E. Eriksson, "Facial nerve palsy in the newborn: incidence and outcome," *Plast Reconstr Surg,* vol. 85, pp. 1-4, 1990.

[10] M. May and R. S. Klein, "Differential diagnosis of facial nerve palsy," *Otolaryngol Clin North Am,* vol. 24, p. 613–45, 1991.

[11] H. M. Hohman and A. T. Hadlock, "Etiology, diagnosis and management of facial palsy: 2000 patients in a facial nerve center," *Laryngoscope,* vol. 124, pp. 283-93, 2014.

[12] H. M. Hohmann, K. P. Bhama and A. T. Hadlock, “Epidemiology of iatrogenic facial nerve injury: a decade of experience,” *Laryngoscope,* vol. 124, pp. 260-65, 2014.

[13] M. J. Stuzin, J. T. Baker and L. H. Gordon, “The relationship of the superficial and deep facial fascias: relevance to rhydectomy and aging,” *Plast Reconstr Surg,* vol. 89, pp. 441-9, 1992.

[14] K. Tzafetta and K. J. Terzis, “Essays ont he facial nerve: Part I. Microanatomy,” *Plast Reconstr Surg,* vol. 125, pp. 879-89, 2010.

[15] R. M. Farahvash, A. Yaghoobi, B. Farahvash, Y. Farahvash and S. Hadid Abivaneh, “The extratemporal facial nerve and its branches: analysis of 42 hemifacial dissections in fresh Persian (Iranian) cadavers,” *Aesthet Surg J,* vol. 33, pp. 201-8, 2013.

[16] A. T. Liu, H. Jiang, Z. Y. Zhao, Z. D. Yu, S. R. Dang, F. Y. Zhang and L. J. Zhang, “Anatomy of buccal and marginal mandibular branches of facial nerve and its clinical significance,” *Zhonghua Zheng Xing Wai Ke Za Zhi,* vol. 23, pp. 434-7, 2007.

[17] K. A. Gosain, “Surgical anatomy of the facial nerve,” *Clin Plast Surg,* vol. 22, pp. 241-51, 1995.

[18] R. Hazani, S. Chowdhry, A. Mowlavi and J. B. Wilhelmi, “Bony anatomic landmarks to avoid injury to the marginal mandibular nerve,” *Aesthet Surg J,* vol. 31, pp. 286-9, 2011.

[19] M. Old, S. Oh, E. Feldman and N. Hogikyan, “Novel model to assess laryngeal function, innervation, and reinnervation,” *Ann Otol Rhinol Laryngol,* vol. 120, pp. 331-338, 2011.

[20] Pinterest, “Pinterest,” Pinterest, [Online]. Available: https://www.pinterest.com/pin/165085142575980184/. [Accessed 14 02 2020].

[21] H. L. Rosenthal, S. M. Benninger and H. R. Deeb, “Vocal fold immobility: a longitudinal analysis of etiology over 20 years,” *Laryngoscope,* vol. 117, pp. 1864-1870, 2007.

[22] O. Laccourreye, F. J. Papon, R. Kania, M. Ménard, D. Brasnu and S. Hans, “Unilateral laryngeal paralyses: epidemiological data and therapeutic progress [in French],” *Presse Med,* vol. 32, pp. 781-786, 2003.

[23] C. Lee, H. B. Su, C. H. Lin, C. Tsai, D. D. Lin and W. T. Lin, “Outcome of vocal cord paralysis in infants,” *Acta Paediatr Taiwan,* vol. 45, pp. 278-281, 2004.

[24] A. S. Nouraei, E. S. Middleton, R. C. Butler and S. G. Sandhu, “An estimation of the population incidence of adult unilateral vocal fold mobility impairment in England,” *Logoped Phoniatr Vocol,* vol. 21, pp. 1-2, 2014.

[25] I. R. Zbar and J. R. Smith, “Vocal fold paralysis in infants twelve months of age and younger,” *Otolaryngol Head Neck Surg,* vol. 114, pp. 18-21, 1996.

[26] O. D. Francis, E. M. McKiever, G. C. Garrett, B. Jacobson and F. D. Penson, “Assessment of patient experience with unilateral vocal fold immobility: a preliminary study,” *J Voice,* vol. 28, pp. 636-643, 2014.

[27] B. Campos and P. Henriques, “Relationship between the recurrent laryngeal nerve and the inferior thyroid artery: a study in corpses,” *Rev Hosp Clin Fac Med,* vol. 55, pp. 195-200, 2000.

[28] W. Tang, S. Sun, X. Wang, Y. Sun and H. Huang, “An applied anatomical study on the recurrent laryngeal nerve and inferior thyroid artery,” *Surg Radiol Anat,* vol. 34, pp. 325-332, 2012.

[29] O. B. Cakir, I. Ercan, B. Sam and S. Turgut, “Reliable surgical landmarks for the identification of the recurrent laryngeal nerve,” *Otolaryngol Head Neck Surg,* vol. 135, pp. 299-302, 2006.

[30] S. Liu, Y. Chou and S. WF, “A rapid and accurate technique for the identification of the recurrent laryngeal nerve,” *Ann Otol Rhinol Laryngol,* vol. 123, pp. 805-810, 2014.

[31] Z. Pisko-Dubiensky, “A rapid method of finding recurrent laryngeal nerves safely during thyroidectomy,” *Ir J Med Sci,* vol. 409, pp. 40-44, 1960.

[32] G. Jotz, D. de Campos, M. Rodrigues and L. Xavier, “Histological asymmetry of the human recurrent laryngeal nerve,” *J Voice,* vol. 25, pp. 8-14, 2011.

[33] J. Prades, M. Dubois, J. Dumollard, L. Tordella, J. Rigail, A. Timoshenko and M. Peoc'h, “Morphological and functional asymmetry of the human recurrent laryngeal nerve,” *Surg Radiol Anat,* vol. 34, pp. 903-908, 2012.

[34] M. Williams, A. Ayylasomayajula, R. Behkam, A. Bierhals, M. Jacobs, J. Edgar, R. Paniello, J. Barkmeier-Kraemer and J. Vande Geest, “A computational study of the role of the aortic arch in idiopathic unilateral vocal-fold paralysis,” *J Appl Physiol,* vol. 118, pp. 465-474, 2015.

[35] M. Williams, U. Utzinger, J. Barkmeier-Kraemer and J. Vande Geest, “Differences in the microstructure and biomechanical properties of the recurrent laryngeal nerve as a function of age and location,” *J Biomech Eng,* vol. 136, 2014.

[36] E. Spataro, D. Grindler and R. Paniello, “Etiology and Time to Presentation of Unilateral Vocal Fold Paralysis,” *Otolaryngol Head Neck Surg,* vol. 151, pp. 286-293, 2014.

[37] M. Alexander, J. Barkmeier-Kraemer and J. Vande Geest, “Biomechanical properties of recurrent laryngeal nerve in the piglet,” *Ann Biomed Eng,* vol. 38, pp. 2553-2562, 2010.

[38] Z. Acun, A. Cihan, S. Ulukent, M. Comert, B. Ucan, G. Cakmak and A. Cesur, “A randomized prospective study of complications between general surgery residents and attending surgeons in near-total thyroidectomies,” *Surg Today,* vol. 34, pp. 997-1001, 2004.

[39] F. Chiang, I. Lu, W. Kuo, K. Lee, N. Chang and C. Wu, “The mechanism of recurrent laryngeal nerve injury during thyroid surgery--the application of intraoperative neuromonitoring,” *Surgery,* vol. 143, pp. 743-749, 2008.

[40] F. Chiang, I. Lu, C. Tsai, P. Hsiao, C. Hsu and C. Wu, “Does extensive dissection of recurrent laryngeal nerve during thyroid operation increase the risk of nerve injury? Evidence from the application of intraoperative neuromonitoring,” *Am J Otolaryngol,* vol. 32, pp. 499-503, 2011.

[41] S. Manolidis, M. Takashima, M. Kirby and M. Scarlett, “Thyroid surgery: a comparison of outcomes between experts and surgeons in training,” *Otolaryngol Head Neck Surg,* vol. 125, pp. 30-33, 2001.

[42] I. Petrakis, N. Kogerakis, K. Lasithiotakis, N. Vrachassotakis and G. Chalkiadakis, “LigaSure versus clamp-and-tie thyroidectomy for benign nodular disease,” *Head Neck,* vol. 26, pp. 903-909, 2004.

[43] B. Veyseller, F. Aksoy, Y. Yildirim, A. Karatas and O. Ozturan, “Effect of recurrent laryngeal nerve identification technique in thyroidectomy on recurrent laryngeal nerve paralysis and hypoparathyroidism,” *Arch Otolaryngol Head Neck Surg,* vol. 137, pp. 897-900, 2011.

[44] J. Haftek, “Stretch injury of peripheral nerve. Acute effects of stretching on rabbit nerve,” *Bone Joint Surg Br,* vol. 52, p. 354–365, 1970.

[45] D. Spiegel, A. Seaber, L. Chen and J. Urbaniak, “Recovery following stretch injury to the sciatic nerve of the rat: an in vivo study,” *J Reconstr Microsurg,* vol. 9, pp. 69-74, 1993.

[46] E. Wall, J. Massie, M. Kwan, B. Rydevik, R. Myers and S. Garfin, “Experimental stretch neuropathy changes in nerve conduction under tension,” *J Bone Joint Surg ,* vol. 74, pp. 126-9, 1992.

III. Mechanical testing of human ligaments and bones

Table of Contents

1 Introduction

The aim of our studies in this subtopic was to investigate and properly characterize the mechanical properties of human tendons with the help of the cutting-edge DIC system and to investigate the possibility of similar measurement of intricately structured bones with special mechanical loadings. The main output, the mechanical properties created in this subtopic were used as an input for subtopic 4, the modelling of the biomaterials.

The demand for anterior cruciate ligament (ACL) allografts (knee ligament replacements sourced from different patients) has changed in the last years [1], and the postoperative results are promising. Its increased availability made the allograft tissue an appealing alternative to autograft (where the ligament to replace the damaged ligament is sourced from the same patient's body) for primary ACL reconstruction, especially for ACL revision [2]. The use of musculoskeletal graft allograft grew continuously in recent years. The American Academy of Orthopaedic Surgeons estimates that nowadays, approximately 60,000 allografts are used in knee reconstruction procedures [3, 4]. However, 27% of primary ACL reconstruction operations and 57% of ACL revisions used allografts [5].

The tendons are usually stored deep-frozen (-80 °C). In practice, there is no significant change in the mechanical properties of the tendons, but it has not been systematically investigated in the literature. Freezing as a method of sterilization is not tested due to storage temperature. Allografts should be sterilized before implantation as they may carry bacterial or viral diseases. [1, 6-7]. In most cases, gamma radiation is used for sterilization. A radio-protectant solution is used to avoid side effects and protect tissues. A lower dose of gamma radiation (10-15 kGy) is bactericidal, whereas higher doses (30-50 kGy) are antiviral. [7-10].

In our previous preliminary study [11] we showed that the effect of radiation depends on the type of tendons. The aim of the study was biomechanical evaluation the changes of mechanical properties in four different types of tendon allografts used in knee ligamentous reconstruction, caused by freezing and gamma irradiation in a higher sample size. The procedure was refined based on a preliminary study so that Achilles tendon was excluded from the tested tendons [11]. Doubled semitendinosus, and gracilis (STG), doubled tibialis anterior (TA), doubled peroneus longus (PL), and quadriceps tendons were involved in the present study. The mechanical properties of the tendons, such as tensile modulus, maximum load, strain at maximum force and fracture strain were determined by the measurement method used previously [12]. We hypothesized that the type of tendons influences the effect of gamma irradiation on mechanical properties. In the present research we have investigated numerous new treatments and a selected group of tendons with the help of the DIC strain measurement system.

2 Our research questions and the expected benefits of this research

1 Can a DIC based strain measurement system be applied for testing of human tissue samples? Can it provide more accurate and reliable results?

2 What is the effect of cyclic loading on different kinds of tendons?

3 What is the effect of constant long term loading on different kinds of tendons?

4 What is the effect of freezing, sterilization by gamma and electron irradiation on different kinds of tendons?

5 How can complex shape bones be properly characterized?

Expected benefits of research:

- Robust measurement methods for mechanical testing of human tendons and bones.

- Fundamental knowledge on the effect of conservation and sterilization techniques on the mechanical properties of tendons.
- Reliable mechanical input parameters for simulation and modelling.

3 Research tasks and results

3.1 Setup of DIC optical measurement system for human tissue measurement

In the project we have purchased a Sobriety Mercury optical DIC full field measurement system which can give us the opportunity to thoroughly investigate the deformation behaviour of the tested human ligaments during mechanical loading. The previously used crosshead displacement based deformation measurement introduced some unwanted phenomena, measurement uncertainties into our deformation results (strain at maximum force, strain at break). In the last reporting period numerous set-up tests were run with the complete system to be able to apply the full field DIC measurement for the very problematic measurement of the human cadaver tendons. The results of the set up tests are:

- The amount of dry ice had to be lowered to avoid the fogging effect provided by the melting.
- Polarized filters had to be applied to minimize the mirroring/glimmer effect of the wet tendon surface.
- Accurate perpendicularity setup has to be performed before each measurement due to the uneven surface of the tendons.

With the completion of these requirements, several full field measurements were performed on different types of tendons in the four-year course of the project to evaluate the efficiency of the method. Our publication in Applied Sciences journal presented the results of the tendon tests with the application of the DIC strain measurement system.

The DIC software has the option to process images from external sources. Successful trials were run to investigate the possibility to extend the measurement to the eye tissue and aneurysm measurements, from which the micrographic images were used for the measurements.

One of the key advantages of the application of the DIC system was the possibility to also use it for cross-section measurement (Figure 3.1.)

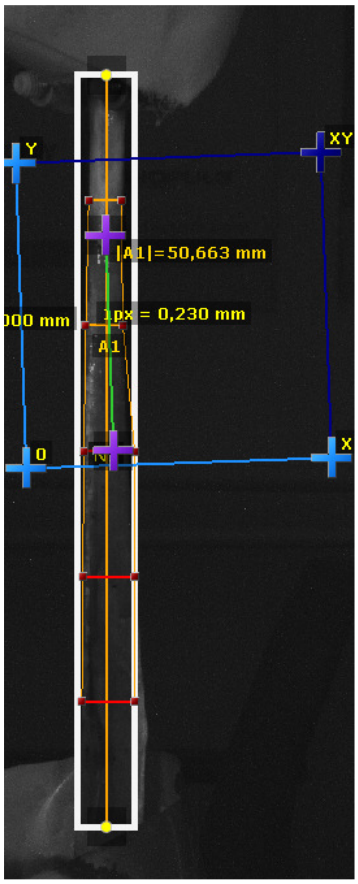

Figure 3.1: DIC cross section measurement example of human tendon

In addition, the application of the DIC system for the measurements has given us the opportunity to more thoroughly investigate the failure process of a ligament, as depicted in Figure 3.2 below.

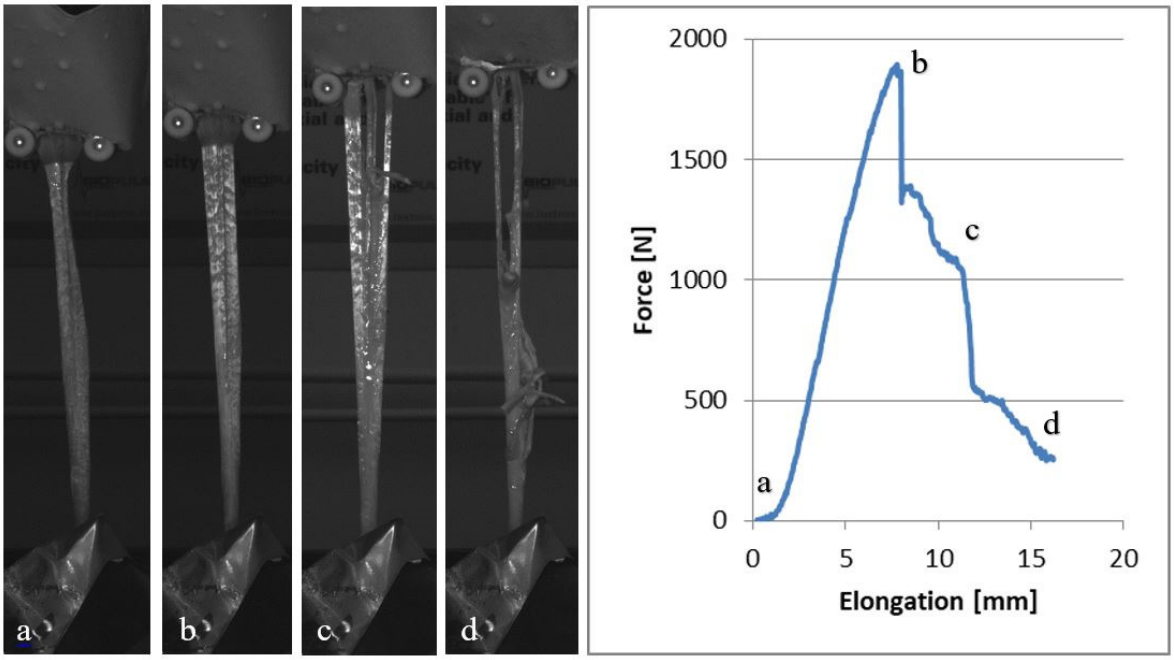

Figure 3.2: DIC images and force-elongation curve of a tested tendon with the different failure phases (a-d, note the formation of fracture and disbanding of the fibrous structure)

3.2 Investigation of the effect of different conservation methods of human tendons

In the present study, 268 tendons from 35 human cadavers were examined. From every cadaver, the following types of tendon were harvested: 67-67 pieces quadriceps and peroneus longus (PL), 69 pieces semitendinosus + gracilis (STG) and 65 pieces tibialis anterior (TA) tendons. The types of tendon grafts were collected from human cadavers within 24 hours post-mortem. All tendons were visually inspected before mechanical testing, and the cortex of the dead were also examined.

Each graft was soaked in a radioprotective solution for 4 hours at 40 °C with agitation and then for 24 hours at 4 °C, according to [13], to help prevent the harmful effects of sterilization and storage on the tissue. The solution contained 2.7% D-mannitol, 3.8% D-trehalose, 16.7% 1,2-propanediol and 24.2% dimethyl-sulfoxide (all w/w, manufacturer: Sigma-Aldrich, Saint Louis, USA). Each specimen was labeled in a separate container.

The grafts were then divided into three groups. Group A contained 63 fresh specimens (16 quadriceps, 17 semitendinosus + gracilis, 14 tibialis anterior, 16 peroneus longus, the average age of the donors was 78.4 ± 15.69 years). The other groups of tendons were frozen slowly to −80 °C. Group B (22 quadriceps, 22 semitendinosus + gracilis, 22 tibialis anterior, 22 peroneus longus, the average age of donors was 85.2 ± 15.31 years) were sterilized with a bactericidal dose (target dose: 21 kGy, dose range: 18–24 kGy). Group C contained the rest 117 tendons (29 quadriceps, 30 semitendinosus + gracilis, 29 tibialis anterior, 29 peroneus longus, the average age of donors was 77.8 ± 20.61 years) sterilized with a virucidal dose (target dose: 42 kGy, dose range: 38–46 kGy).

According to the results of a preliminary study [11] the freezing, the irradiation, and thawing were unified at all graft types. Irradiation was performed on frozen grafts, with the same method at all grafts. Before the test, the tendons were thawed at 37 °C for 20 minutes. Prior to the start of the test, the cross-section of the tendons and the length of the clamp were measured with a micrometric calipers.

For the endurance tests, we used an Instron 8872 servohydraulic load frame (Instron Ltd., High Wycombe, UK) equipped with an Instron Dynacell load cell with a 25 kN load capacity and an Instron Fasttrack 8800 control unit and a freezer clamp structure at the accredited materials testing laboratory of the Budapest University of Technology and Economics Biomechanical Research Center. The strain characteristics of the specimens were also investigated by a Mercury Monet (Sobriety, Kurim, Czech Republic) optical digital image correlation (DIC) machine. During the preliminary tests, three minutes of freezing was used for proper fixation and for preventing the freezing of the grafts at the gauge length [12]. Based on our previous result [12], the effect of frost had a negligible effect on the measuring length because the thermal conductivity of the tissue is weak. The force-elongation curve was determined after 1000 cycles at a frequency of 2 Hz between 50 N and 250 N. The method of the load-to-failure test is summarized in [12]. The cross-section of the specimen was measured by a digital caliper, the strain (crosshead displacement), and force was measured by the tensile tester for the calculation of the presented results. The tests were authorized by the Research Ethics Committee of Uzsoki utcai and Péterffy Sándor Hospital (license number: 03/2009).

Statistical analysis was performed with Statsoft Statistica 13.3 (Statsoft Inc., Tulsa, OK, USA). The median with the corresponding interquartile range (25% and 75% percentile) is displayed for each calculated parameter. The variables were compared in groups by using the Kruskal-Wallis test. Multiple comparisons of mean ranks for all groups were applied for post hoc analyses. As statistical significance, a p-value of less than 0.05 was accepted.

Firstly, we investigated the tendon's fracture behavior. The typical force – elongation curves of each type of tendon are presented in Figure 3.3.

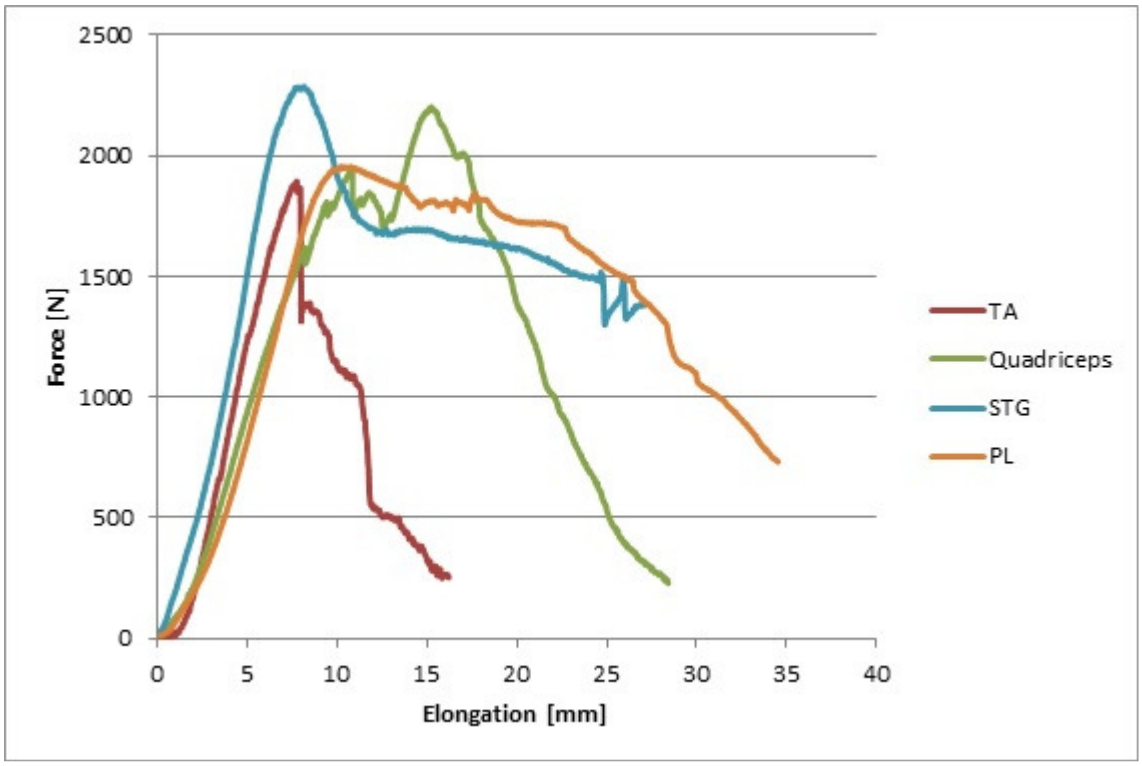

Figure 3.3: Typical force – elongation curves recorded during the tensile tests of the tendons

The investigation of the failure process showed, that in most of the tests, longitudinal fractures formed in the tendons during the elongation, so the co-working of the adjacent fiber bundles was hindered, the modulus of elasticity (slope of the curve) has decreased after every fracture step. When comparing different tendons, the main failure process is the same; only the severity of each force-drop is different. Some differences can also be seen, which can be connected to crack propagation. While in the curve of STG presented in Figure 3.3, ductile failure with quasi-plastic deformation occurs, for example, in the case of the Quadriceps tendon's curve, the cracks and partial fractures are more severe. In the case of the Quadriceps tendon, the process is also worth investigating: irreversible damage progresses even from relatively low elongation, the loss of connection between the fiber bundles is not so critical, the force required to elongate the tendon further is still increasing.

In Table 3.1, the numerical data of tensile modulus, maximum load, strain at maximum force and fracture strain were summarized and compared.

Table 3.1. Results of biomechanical tests of the tendons

Tendon types and mechanical properties	Group A			Group B			Group C		
	Median	25%	75%	Median	25%	75%	Median	25%	75%
Quadriceps									
Tensile modulus (MPa)	191,31	138,13	292,42	120,24	90,13	299,29	83,20	30,65	137,05
Maximum load (N)	1939,75	1121,97	2727,15	2803,68	1653,26	3591,97	2564,77	1835,38	3265,92
Strain at maximum force (-)	0,1540	0,1340	0,2485	0,1841	0,1467	0,2299	0,2729	0,1949	0,3472
Fracture strain (-)	0,3370	0,2766	0,6090	0,3231	0,2481	0,4885	0,4392	0,3574	0,5909
Semitendinosus + gracilis (STG)									
Tensile modulus (MPa)	186,46	142,82	229,26	210,28	137,08	244,11	222,66	128,59	255,73
Maximum load (N)	1922,96	1501,00	2374,84	2171,41	1330,37	2414,74	2357,61	1827,42	2670,83
Strain at maximum force (-)	0,1300	0,0980	0,1864	0,1346	0,0985	0,1540	0,1631	0,1315	0,1895
Fracture strain (-)	0,2460	0,1500	0,2850	0,1924	0,1685	0,2248	0,2220	0,1991	0,2815
Tibialis anterior (TA)									
Tensile modulus (MPa)	343,24	308,25	383,33	432,55	393,64	538,25	318,85	257,63	347,66
Maximum load (N)	2582,22	2236,38	2784,23	2552,10	2322,61	3176,63	3063,90	2603,71	3416,14
Strain at maximum force (-)	0,1041	0,0831	0,1543	0,1476	0,1285	0,1630	0,1482	0,1225	0,1618
Fracture strain (-)	0,1580	0,1099	0,2131	0,1656	0,1473	0,2021	0,1781	0,1611	0,1922
Peroneus longus (PL)									
Tensile modulus (MPa)	250,33	166,58	309,85	267,83	212,43	329,96	256,55	203,47	277,46
Maximum load (N)	2490,82	1657,51	3083,02	2398,30	2166,18	3092,63	2339,75	2111,68	2773,67
Strain at maximum force (-)	0,1402	0,1049	0,1790	0,1489	0,1269	0,1690	0,1420	0,1108	0,1675
Fracture strain (-)	0,1947	0,1266	0,4440	0,1827	0,1487	0,2186	0,1660	0,1417	0,1930

In group A (no freezing, no irradiation), we found no difference in maximum loads, strain at maximum force and tensile modulus among the tendons (Table 3.1, Figures 3.4-3.7). Fracture strain of the quadriceps tendons was significantly inferior to the TA ($p=0.0016$) tendons in this respect.

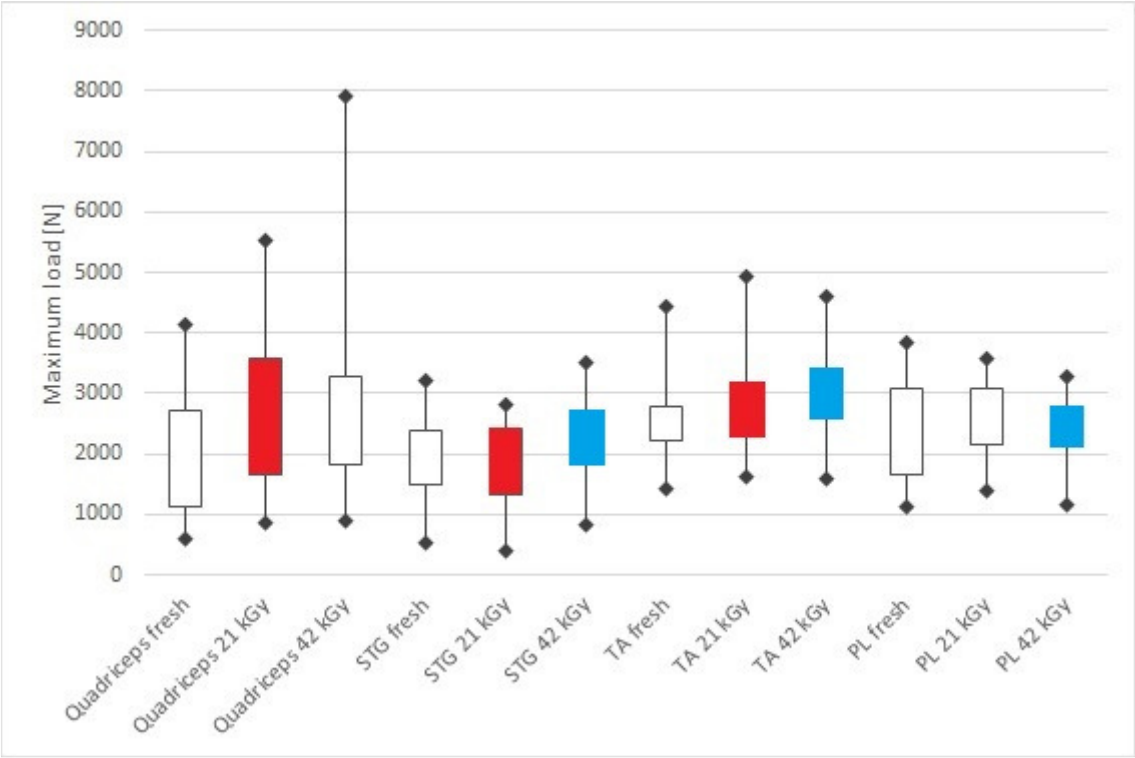

Figure 3.4: Minimum, maximum, median, 25 and 75% percentile values of maximum load

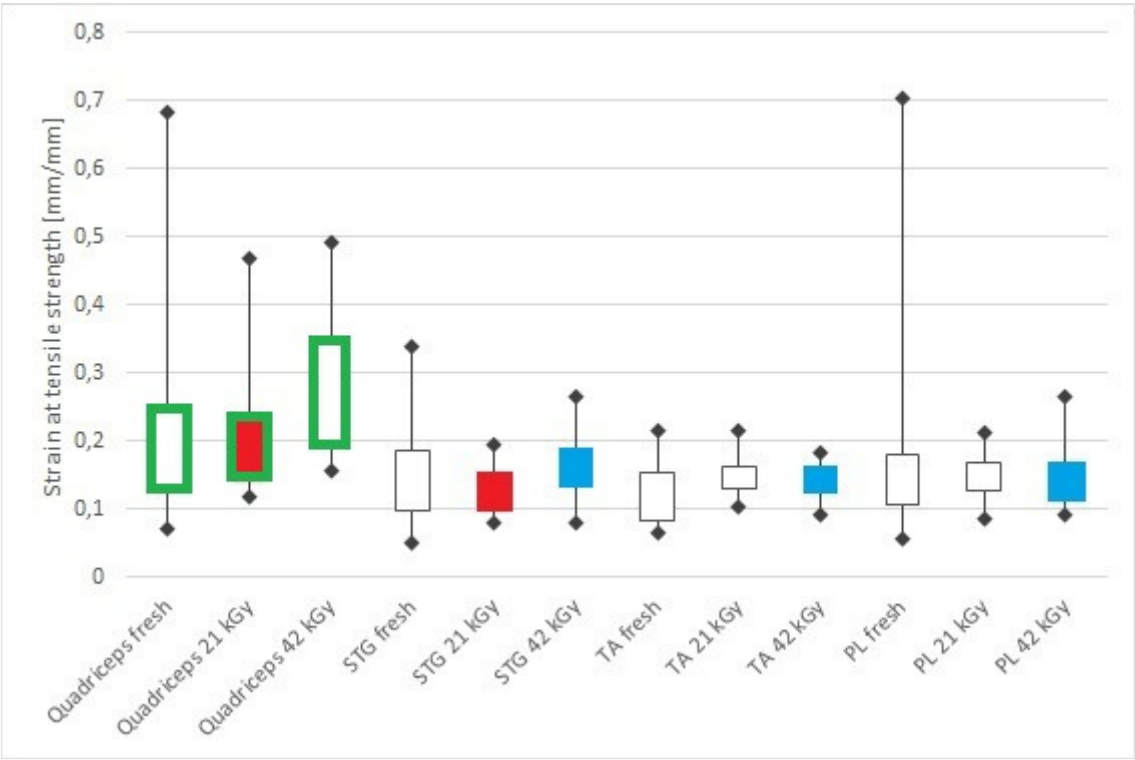

Figure 3.5: Minimum, maximum, median, 25 and 75% percentile values of strain at maximum force

In group B (frozen and irradiated with 21 kGy), the maximum loads of the STG tendons were significantly lower compared to the maximum loads of the quadriceps (p=0.0193) and TA tendons (p=0.0272). The strain at maximum force of the quadriceps tendons were inferior compared to the STG

tendons (p=0.0022). The tensile modulus of the quadriceps tendons was significantly inferior to that of the TA (p=0.0313) and PL tendons (p=0.0201). The fracture strain of the quadriceps tendons was worse than that of the STG (p=0.0001), the TA (p=0.00001), and the PL tendons (p=0.00001).

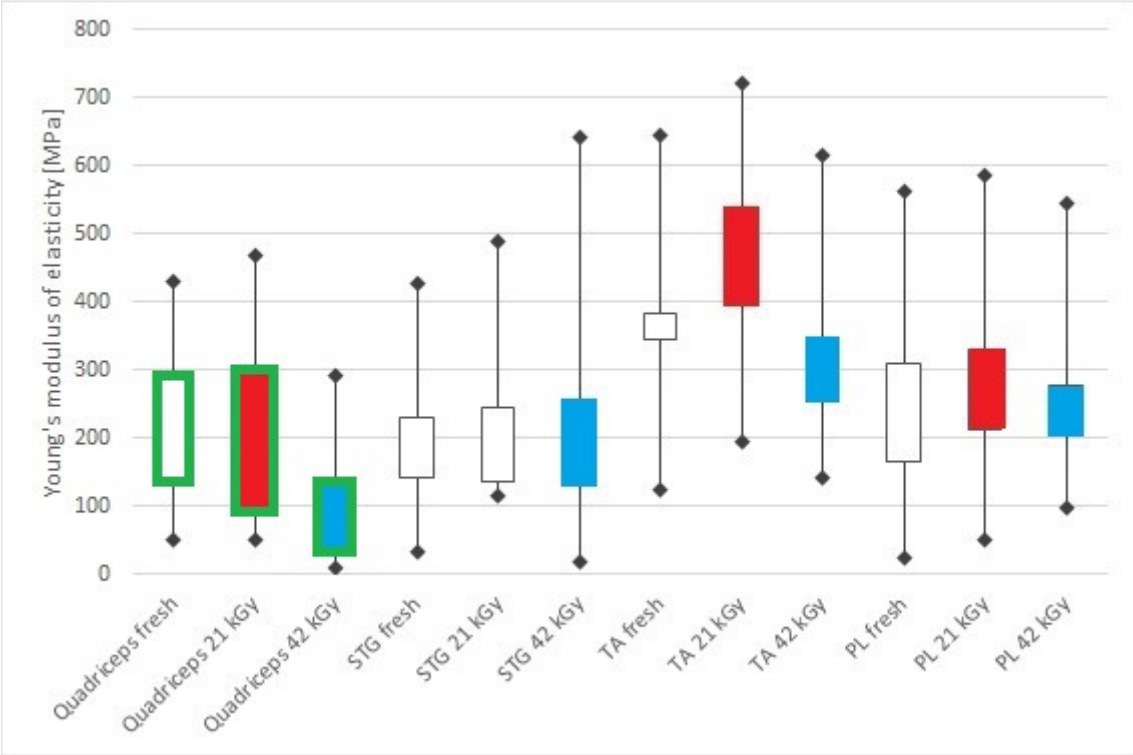

Figure 3.6: Minimum, maximum, median, 25 and 75% percentile values of tensile moduli

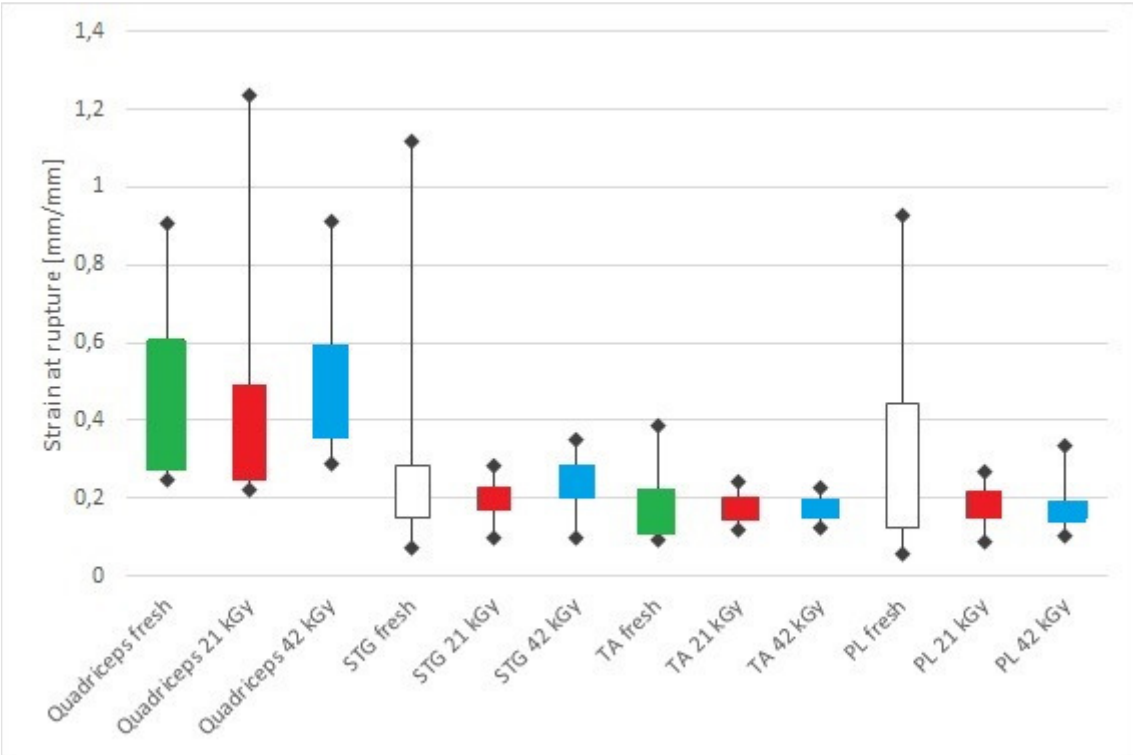

Figure 3.7: Minimum, maximum, median, 25 and 75% percentile values of fracture strain

In group C (frozen and irradiated with 42 kGy), we compared the maximum loads and found that TA tendons showed a significantly higher maximum load than the STG (p=0.0014) and the PL tendons (p=0.0122). The strain at maximum force of the quadriceps tendons performed better than the STG (p=0.00001), the TA (p=0.0006), and the PL tendons (p=0.0020). The tensile modulus of the quadriceps tendons showed lower than the STG (p=0.0046), the TA (p=0.000001), and the PL tendons (p=0.00001). The fracture strain of the quadriceps tendons was significantly inferior to that of the STG (p=0.0000), TA (p=0.0034), and PL tendons (p=0.0042).

A higher gamma irradiation dose reduced the strain at maximum force of the quadriceps tendons (p=0.0005-0.0237) more significantly than that of the other two groups. The strain at maximum force of the STG, the TA, and the PL tendons was similar in all groups. In the case of the quadriceps tendons (p=0.0151); however, the higher dose of gamma irradiation significantly decreased tensile modulus (group D). Fracture strain was not affected by freezing and gamma irradiation; we found no difference in the results of any of the tendons.

The replacement of autografts with allografts from organ banks in ligament reconstruction is a hot topic in medicine [14, 15]. In our work, we have combined engineering and medical knowledge to check the feasibility of safe transplantation after freezing and irradiation treatment using different doses aimed for the disinfection of the ligaments, which are necessary for long term bank storage and transportation. Our method can provide better accuracy for strain measurement and fracture analysis of the ligaments, make the whole measurement more robust and give deeper insight into the behaviour of and the differences between the tendon types, as it is based on digital image correlation. Four types of allografts for potential ligamentous reconstruction were evaluated in this study. The allografts were subjected to either freezing and 21 kGy dose gamma irradiation or freezing and 42 kGy dose of gamma irradiation. Four main mechanical parameters were evaluated and compared: tensile modulus, which represents the elasticity of the materials, maximum load, which is the limiting factor for each ligaments strength, strain at maximum force, which shows the specific strain at the maximum load and fracture strain which is the ultimate limiting strain. These parameters give a good overview of material characteristics, which is useful for the selection of the right replacement by doctors and also for simulation and modelling purposes for engineers.

In this study, the doubled tibialis anterior and peroneus longus tendons performed best in general. They were the stiffest, showing the highest tensile modulus. Strain at maximum force and fracture strain were better than or equal to those of all other currently tested ACL grafts.

Previous studies [16, 17] reported mixed effects of freezing. In the work of Chen et al., no difference was shown in endurance properties [16]. In contrast, Giannini S. et al. reported decreasing load-bearing capacity and stiffness as a result of freezing [17]. Comparing the native and frozen tendon samples, no significant difference was found in endurance properties. It could be the effect of the cryoprotectant solution.

It was previously well-known, that high doses of gamma irradiation hurt the biomechanical parameters of tendon grafts [18-21]. However, our measured values were significantly higher than those required for walking (303-355N) [22] or aggressive early rehabilitation programs (450 N) [23].

The decrease in maximum load can be the result of gamma irradiation, which was visible in both irradiated groups. This means that the strength of the irradiated tendons has decreased. This may be the reason behind the early failures of the grafts. The other evaluated TA's parameters did not change (Table 1).

The results confirmed the findings of our previous research [11]. The aggregate results of the present and prior studies [11, 12] show that there is a difference in irradiation sensitivity of the examined tendons, which has to be considered before application. The tendons types, which were the most affected by the treatments, were quadriceps grafts. When the donors are properly screened, a gamma irradiation treatment below 21 kGy does no severe damage but can destroy infectious bacteria on the samples without compromising the mechanical integrity of the tendons. Finally, it can be concluded that the tibialis anterior and the peroneus longus are recommended for replacement in ACL reconstruction when gamma radiation is required. The results have shown that the quadriceps tendon,

which is usually used for an autograph, is not suitable for allograft reconstruction after gamma irradiation.
The results of this part of our research was published in Applied Sciences journal. The results were used to create material "cards" for the simulation and modelling.

References

1. Jung, H.J.; Vangipuram, G.; Fisher, M.B.; Yang, G.; Hsu, S.; Bianchi, J.; Ronholdt, C.; Woo, S. L. The effects of multiple freeze-thaw cycles on the biomechanical properties of the human bone-patellar tendon-bone allograft. *J Orthop Res* **2011**, *8*, 1193-1198; DOI: 10.1002/jor.21373.
2. Zaffagnini, S.; di Sarsina, T.R.; Bonanzinga, T.; Nitri, M.; Macchiarola, L. Stefanelli, F.; Lucidi, G.; Grassi, A. Does Donor Age of Nonirradiated Achilles Tendon Allograft Influence Mid-Term Results of Revision ACL Reconstruction? *Joints* **2018**, *6*, 10-15; DOI: 10.1055/s-0038-1626739.
3. Eagan, M.J.; McAllister, D.R. Biology of allograft incorporation. *Clin Sports Med* **2009**, *28*, 203–214; DOI: 10.1016/j.csm.2008.10.009.
4. Wilde, J.; Bedi, A.; Altchek, D.W. Graft selection for revision ACL reconstruction. In *Revision ACL Reconstruction*; Marx, R.G., Ed; Springer, New York, USA, 2014; pp. 75–86; DOI: 10.1007/978-1-4614-0766-9_8.
5. Buda, R.; Ruffilli, A.; Di Caprio, F.; Ferruzzi, A.; Faldini, C.; Cavallo, M.; Vannini, F.; Giannini, S. Allograft salvage procedure in multiple-revision anterior cruciate ligament reconstruction. *Am J Sports Med*, **2013**, *41*, 402–410; DOI: 10.1177/0363546512471025.
6. Kainer, M.A.; Linden, J.V.; Whaley, D.N.; Holmes, H.T.; Jarvis, W.R.; Jernigan, D.B.; Archibald, L.K. Clostridium infections associated with musculoskeletal-tissue allografts. *N Engl J Med*, **2004**, *350*, 2564-2571; DOI: 10.1056/NEJMoa023222.
7. Scheffler, S.U.; Scherler. J.; Pruss, A.; von Versen, R.; Weiler, A. Biomechanical comparison of human bone-patellar tendon-bone grafts after sterilization with peracetic acid ethanol. *Cell Tissue Banking*, **2005**, *6*, 109-115; DOI: 10.1007/s10561-004-6403-z.
8. Greaves, L.L; Hecker, A.T.; Brown Jr., C.H. The effect of donor age and low-dose gamma irradiation on the initial biomechanical properties of human tibialis tendon allografts. *Am J Sports Med*, **2008**, *36*, 1358-1366; DOI: 10.1177/0363546508314394.
9. Ng, K.W.; Wanivenhaus, F.; Chen, T.; Abrams, V.D.; Torzilli, P.A.; Warren, R.F.; Maher, S.A. Differential cross-linking and radio-protective effects of geninpin on mature bovine and patella tendons. *Cell Tissue Banking*, **2013**, *14*, 21-32; DOI: 10.1007/s10561-012-9295-3.
10. Almqvist, K.F.; Jan, H.; Vercruysse, C.; Verbeeck, R.; Verdonk, R. The tibialis tendon as a valuable anterior cruciate ligament allograft substitute: biomechanical properties. *Knee Surg Sports Traumatol Arthrosc*, **2007**, *15*, 1326-1330; DOI: 10.1007/s00167-007-0396-7.
11. Hangody, G.; Szebényi, G.; Abonyi, B.; Kiss, R.; Hangody, L.; Pap, K. Does a different dose of gamma irradiation have the same effect on five different types of tendon allografts? — a biomechanical study. *Int Orthop*, **2017**, *41*, 357–365; DOI: 10.1007/s00264-016-3336-7.
12. Hangody, G.; Pánics, G.; Szebényi, G.; Kiss, R.; Hangody, L.; Pap, K. Pitfalls during biomechanical testing – Evaluation of different fixation methods for measuring tendons endurance properties. *Physio Int*, **2016**, *103*, 86–93; DOI: 10.1556/036.103.2016.1.8.
13. Grieb, T.A.; Forng, R-Y.; Bogdansky, S.; Ronholdt, C.; Parks, B.; Drohan, W.N.; Burgess, W.H.; Lin, J. High-Dose Gamma Irradiation for Soft Tissue Allografts: High Margin of Safety with Biomechanical Integrity. *J Orthop Res*, **2006**, *24*, 1011-1018; DOI: 10.1002/jor.20079.
14. Vyas, D.; Rabuck, S.J.; Harner, C.D. Allograft anterior cruciate ligament reconstruction: Indications, techniques, and outcomes. *J Orthop Sports Phys Therap*, **2012**, *42*, 196-207; DOI: 10.2519/jospt.2012.4083.
15. Zheng, X.; Li, T.; Wang, J.; Dong, J.; Gao, S. Medial collateral ligament reconstruction using bone-patellar tendon-bone allograft for chronic medial knee instability combined with multi-ligament injuries: A new technique. *J Orthop Surg Res*, **2016**, *11*, 85-89; DOI: 10.1186/s13018-016-0416-8.
16. Chen, L.; Wu, Y.; Yu, J.; Jiao, Z.; Ao, Y.; Yu, C.; Wang, J.; Cui, G. Effect of repeated freezing-thawing on the Achilles tendon of rabbits. *Knee Surg Sports Traumatol Arthrosc*, **2011**, *19*, 1028–1034; DOI: 10.1007/s00167-010-1278-y.

17. Giannini, S.; Buda, R.; Di Caprio, F.; Agati, P.; Bigi, A.; De Pasquale, V.; Ruggeri, A. Effects of freezing on the biomechanical and structural properties of human posterior tibial tendons. *Int Orthop*, **2008**, *32*, 145–151; DOI: 10.1007/s00264-006-0297-2.
18. Pearsall, A.W.; Hollis, M.J.; Russel Jr., G.V.; Scheer, Z. A biomechanical comparison of three lower extremity tendons for ligamentous reconstruction about the knee. *Arthroscopy*, **2003**, *19*, 1091-1096; DOI: 10.1016/j.arthro.2003.10.015.
19. Di Matteo, B.; Loibl, M.; Andriolo, L.; Filardo, G.; Zellner, J.; Koch, M.; Angele, P. Biologic agents for anterior cruciate ligament healing: a systematic review. *World J Orthop*, **2016**, *7*, 592-603; DOI: 10.5312/wjo.v7.i9.592.
20. Dong, S.; Huangfu, X.; Xie, G.; Zhang, Y.; Shen, P.; Li, X.; Qi, J.; Zhao, J. Decellularized versus fresh-frozen allografts in anterior cruciate ligament reconstruction: an in vitro study in a rabbit model. *Am J Sports Med*, **2015**, *43*, 1924–1934; DOI: 10.1177/0363546515585314.
21. Conrad, B.P.; Rappé, M.; Horodyski, M.; Farmer, K.W.; Indelicato, P.A. The effect of sterilization on mechanical properties of soft tissue allografts. *Cell Tissue Banking*, **2013**, *14*, 359-366; DOI: 10.1007/s10561-012-9340-2.
22. Nagura, T.; Matsumoto, H.; Kiriyama, Y.; Chaudhari, A.; Andriacchi, T.P. Tibiofemoral joint contact force in deep knee flexion and its consideration in knee osteoarthritis and joint replacement. *J Appl Biomech*, **2006**, *22*, 305-313; DOI: 10.1123/jab.22.4.305.
23. Noyes, F.; Butler, D.; Grood, E.; Zernicke, R.F.; Hefzy, M.S. Biomechanical analysis of human ligament grafts used in knee-ligament repairs and reconstructions. *J Bone Joint Surg Am*, **1985**, *66*, 344-352.
24. Mabe, I.; Hunter, S. Quadriceps tendon allografts as an alternative to Achilles tendon allografts: a biomechanical comparison. *Cell Tissue Banking*, **2014**, *15*, 523-529; DOI: 10.1007/s10561-014-9421-5.

3.3 Investigation of long-term dynamic properties of human tendons

The human tendons are some of the most important parts of our limbs, these help to fix and to move the bones together. The tendons are subjected to a continuous fatigue load during the movement of the body. [1]; [2] In the human body, the knee joint is the largest and the most complicated articulation, furthermore it owns the highest incidence of tendons injury. Several articles have been dealt with the mechanical study of the knee joint. [1]; [3]; [4] After the cyclic tensile loading of the tendons, it can be observed that breaking force and the modulus of elasticity exceeding the pre-load state can be measured, primarily due to the fibrous structure and the orientation of these fibers in the load-bearing orientation. [2]; [5]; [6] Fatigue of the first cross-band of the knee joint represent an increasing proportion in orthopaedic deformations. As a result the surrounding ligaments and muscles become instable, surgical treatment will be necessary. [1]; [4]; [7]; [8]

The efficieny of each new surgical method must be demonstrated by tests performed on in vitro specimens before introduction. The tendons that are potentially usable to replace the first cross-band of the knee joint should be tested. [1], [3], [9] The following tendons are good candidates for substitution: achilles, quadriceps, semintendinosus + gracilis, tibialis anterior, peroneus longus. The question can also be posed as follows: how should tendons be preserved for the in vitro examination of different surgical techniques in order that their mechanical properties resemble the characteristics of live tendons the most. [2]; [4]

Fitzgerald stated that the mechanical properties of bones and ligaments change significantly 5 hours post mortem this particularly applies to tensile strengths. [10]; [11] Linde and Sorensen measured significant decrease in the Young' modulus 24 hours post mortem by compressive tests on trabecular bones extracted from the tibia. [12] There are two recommended methods for storage to identify strength characteristics: cooling and freezing. Both methods of storage can be dry or wet. In the case of storage by freezing, the mechanical properties of human and animal ligaments do not change significantly even after 100 days of storage. One of the best conservative solution media for this method is the radio-cryoprotectant solution, which is slowly cooled to -78 degrees Celsius. [3], [10]; [11]; [12]

The frozen ligaments must be melted correctly before the test. This is done with one of the controlled melting methods so that the mechanical properties of the tendon do not change. Poor melting process can damage the structure. [13]; [14] The most optimal defrost method after freezing with the radio-cryoprotectant solution is to melt the tendons at 37 degrees Celsius for 20 minutes. [13]; [15]
In our research, we investigated the stiffness change of human tendons during strain controlled fatigue loading. Five different tendons were tested as in vitro samples, which have been thawed after freezing. We have investigated the Young's modulus change in several selected cycles. Our goal was to investigate how the stiffness of the tendons changes with the progressing fatigue loading in case of the different tested samples.

In the course of our experiments, potential replacements of the first cross-band of the knee joint were tested: achilles, peroneus longus (PL), quadriceps, semitendinosus + gracilis (STG) and tibialis anterior (TA) were studied with a constant elongation amplitude sinusoidal loading during a fatigue test. We have collected the five types of grafts from 8-8 human cadaver tendons within 24 hours post mortem. The TA, STG, PL tendons were harvested from the musculotendinous junction. All soft tissue including the paratenon was removed from around the tendons. The mid-thirds of the quadriceps and the Achilles tendons were used. We used only the free ends of the grafts, because of the measurement difficulties. All tendons were visually and mechanically screened for degenerative changes. There was no previous history or evidence of injury or disease of the tendons in the patient's documentation. We have removed and placed the grafts in a radio-cryoprotectant solution and slowly cooled and stored them at -78 ° C.
Before the test the ligaments were thawed at 37 ° C for 20 minutes and then advanced for 30 seconds before testing. Using a freezer clamp structure, 1000 cycles of 2 Hz frequency sinusoid waveform fatigue were performed on the ligaments using Instron 8872 computer-controlled servo hydraulic tester equipped with an Instron FastTrack 8800 control/data acquisition unit.
Before starting the load, we have waited for freezing to fix the ligaments. Because of the poor thermal conductivity of the tissue, the freezing effect of the measuring length in the clamps was minimal. Before and during the test, the temperature of the samples was checked using a Flir A325sc infrared (IR) camera. The load was defined as a sinusoid function, the starting values are assigned to a peak load of 250 N and a minimum load of 0 N. Data was recorded with the Instron Fasttrack 8800 data acquisition device in the 2th, 4th, 8th, 16th, 32nd, 64th, 128th, 256th, 515th and 1000th cycle. In the given cycles the whole measured waveform was registered.
An example test setup of the fatigue test is presented in Figure 3.8.

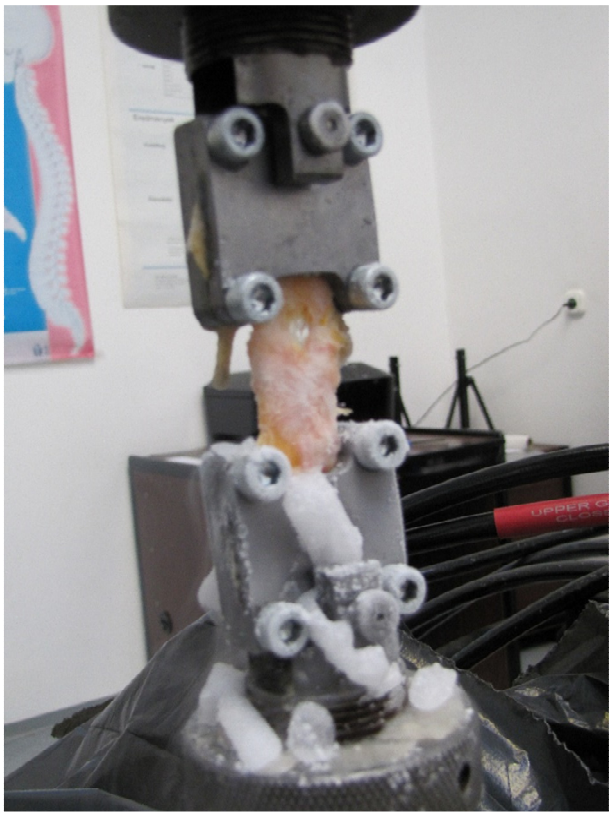

Figure 3.8: Test setup of the fatigue test

To compare the biomechanical behavior of the different tendons the Young's modulus values were evaluated in the 64th, 128th, 256th, 512th and 1000th cycles. An example curve set used for the modulus evaluation is presented in Fig 3.9. In the graph it can be seen that as the number of cycles increases, the maximum force increases, resulting in an increase in the inclination of the sinus curve. The shape of the curves is also worth investigating: while the loading strain excitation waveform is a pure sinusoid, in case of the recorded load curves show an asymmetric shape. The positive peak is a standard sinusoid, but the negative peak corresponding to the unloading of the tendon in each cycle is deformed. This can be caused by the viscoelastic behavior of the tendons: the effect of unloading is damped by the soft material with high loss factor.

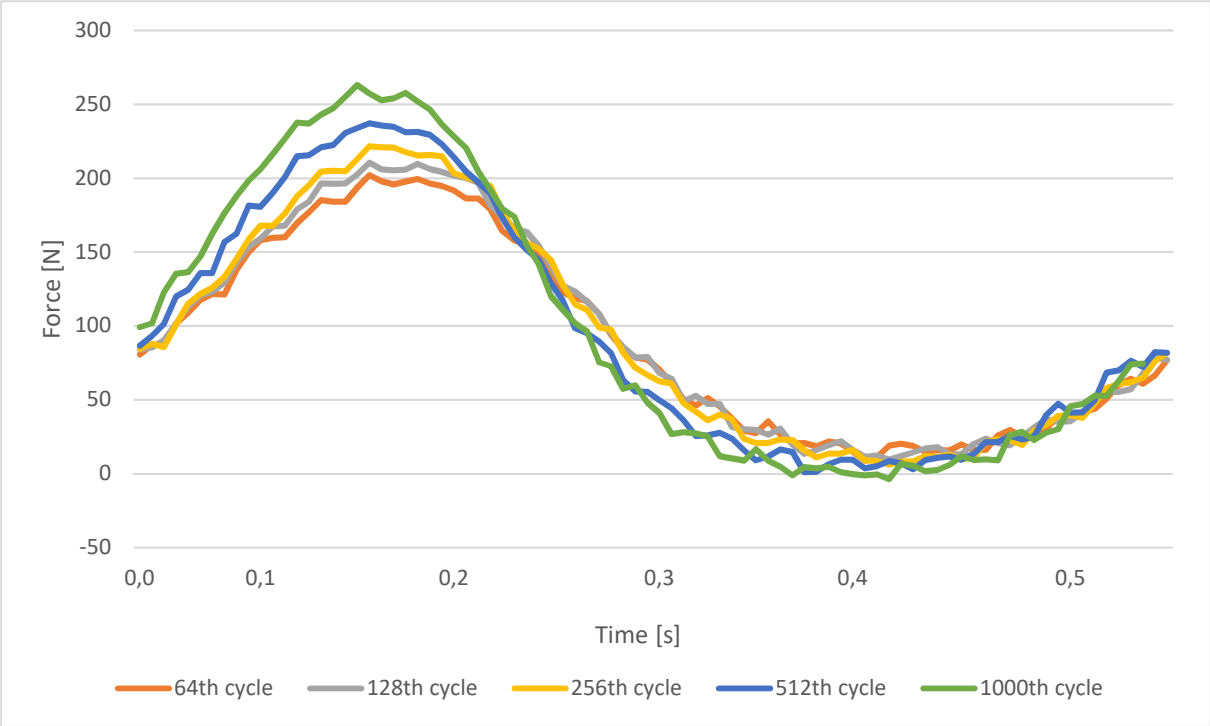

Figure 3.9: Sample sinus curves of an Achilles tendon in the examined cycles

Comparing the different tendons in the same cycles (Figures 3.10-3.11), similar behavior can be observed showing that the basically identical structure results in also similar mechanical behavior.

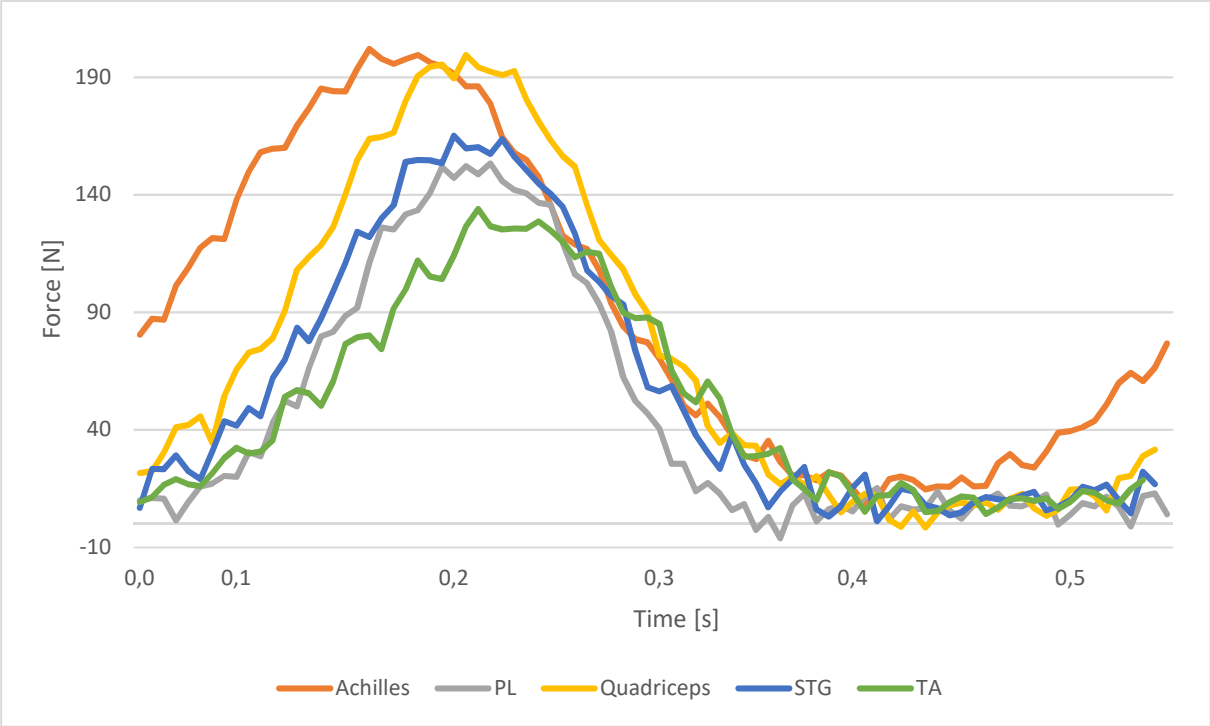

Figure 3.10: Behavior of different tendons in the 64th cycle

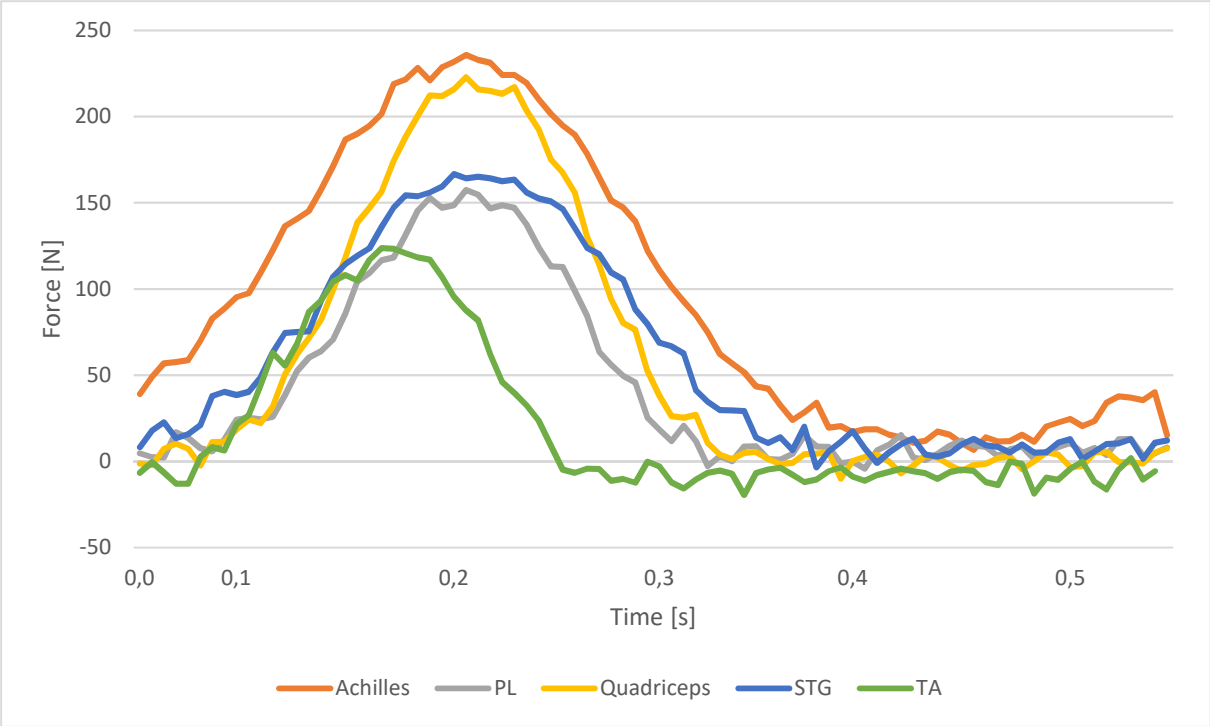

Figure 3.11: Behavior of different tendons in the 1000th cycle

The evaluated Young's moduli in function of the elapsed cycles is presented in Figure 3.12 and Table 3.2. On the summary chart, it can be seen that the orientation of the fibers is clearly present during the fatigue tests. While in case of PL and STG tendons the change is apparently linear in the investigated range, in case of the Achilles, quadriceps and TA tendons there is a region where a significant change in modulus occurs. In case of the Achilles and the quadriceps tendons, which have the largest cross-section this significant increase appears earlier, between the 128th and 256th cycles. In case of the TA tendon this change occurs later, between the 512th and 1000th cycle. This can be probably explained by the differences in the cross-sections of the tested tendons. In case of the wider and thicker tendons with a higher cross-section there are more fiber bundles which can be oriented simultaneously and therefore more easily, providing a more pronounced effect in the increase of the Young's modulus of elasticity. Further investigations with higher cycle number fatigue tests performed on the STG and PL tendons have further supported our assumptions.

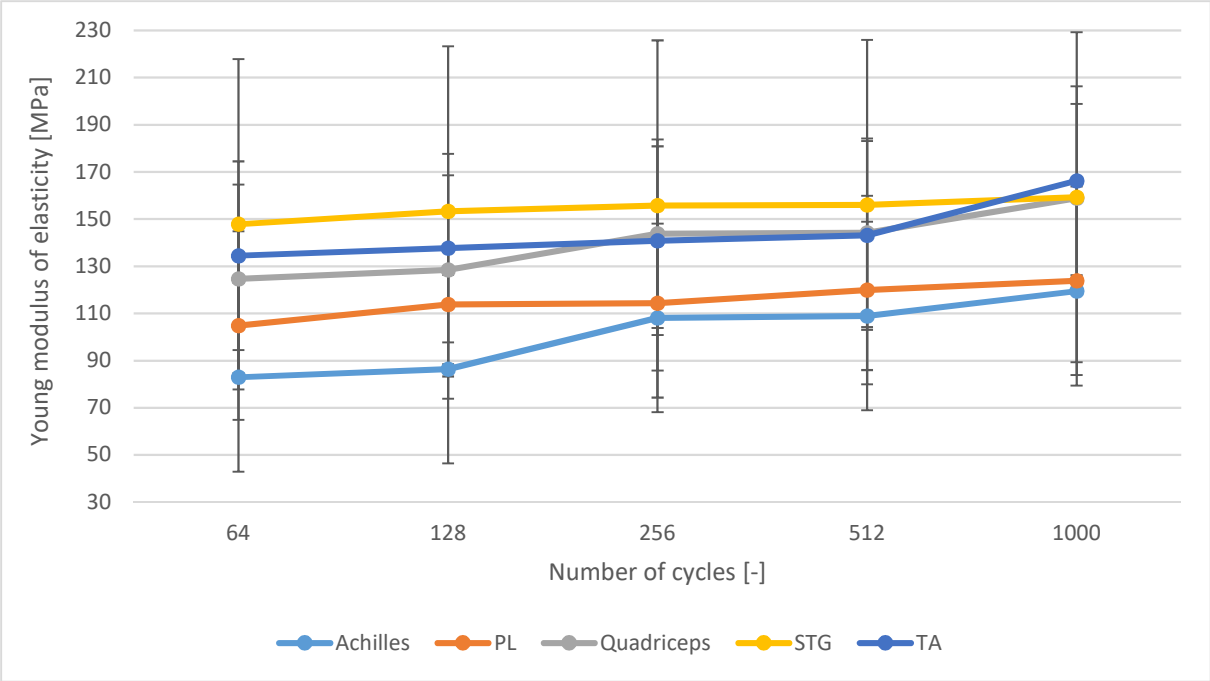

Figure 3.12: Average Young modulus of elasticity evolution in different cycles for all types of tendons

Tendon type	Achilles	Perosneus longus	Quadriceps	Semitendinosus + Gracilis	Tibialis ant
Cycle number	Young's modulus of elasticity [MPa]				
64	36,1	106,0	124,2	195,1	175,9
	88,9	131,3	108,5	297,6	147,6
	155,8	88,0	57,7	87,3	135,2
	96,7	126,0	125,9	118,2	159,1
	64,1	110,5	102,7	134,1	60,9
	32,3	67,6	185,6	88,2	173,3
	89,1	105,2	167,6	114,2	94,1
	100,6	104,4	124,9	147,9	129,9
Average	**82,9**	**104,9**	**124,6**	**147,8**	**134,5**
Deviation	**39,6**	**20,2**	**39,2**	**69,8**	**39,8**
128	34,2	130,3	128,9	219,8	131,0
	107,8	142,5	119,3	289,6	158,8
	154,3	102,2	62,8	87,8	193,1
	112,4	114,0	115,9	124,1	169,2
	75,1	118,5	96,5	140,0	76,7
	34,3	75,6	169,2	83,3	122,1
	82,9	115,2	206,5	127,7	111,5
	90,8	112,5	129,2	154,0	139,0
Average	**86,5**	**113,8**	**128,5**	**153,3**	**137,7**
Deviation	**40,3**	**19,7**	**43,6**	**69,5**	**36,3**
256	43,5	110,2	134,1	220,7	183,2
	120,5	135,8	111,4	293,5	184,7
	173,2	104,3	64,9	85,0	140,6
	120,5	112,4	141,2	127,8	164,8

	173,2	108,5	110,1	136,6	73,4
	120,3	113,8	208,1	95,4	123,6
	77,3	109,8	235,4	126,5	116,6
	36,5	119,8	145,2	160,8	139,9
Average	**108,1**	**114,3**	**143,8**	**155,8**	**140,9**
Deviation	**52,4**	**9,8**	**54,8**	**69,5**	**37,3**
512	33,8	104,5	151,2	223,0	197,3
	141,1	137,8	139,0	287,9	152,5
	213,8	123,1	109,3	96,2	196,6
	132,9	110,7	153,9	127,2	161,1
	89,4	123,5	154,5	123,4	72,5
	40,3	138,5	150,8	100,1	119,4
	97,2	110,2	140,9	125,0	102,8
	123,1	111,2	154,2	165,2	142,8
Average	**109,0**	**119,9**	**144,2**	**156,0**	**143,1**
Deviation	**58,2**	**13,0**	**15,4**	**67,1**	**43,7**
1000	30,2	132,9	157,5	212,9	158,4
	165,8	137,5	114,8	285,6	178,0
	202,8	116,3	82,0	86,4	270,6
	148,1	114,0	169,3	133,9	228,4
	70,2	117,6	137,1	128,9	68,6
	94,8	130,8	349,7	123,8	121,1
	123,6	119,2	134,9	142,5	137,0
	120,2	122,8	125,9	160,2	168,2
Average	**119,5**	**123,9**	**158,9**	**159,3**	**166,3**
Deviation	**54,7**	**8,7**	**81,5**	**62,4**	**62,5**

Table 3.2: Dynamic young modulus of elasticity values in selected cycles for all types of tendons

According to our research, it can be stated that the Young modulus of elasticity of all tendons increased during the cycles by 20-30 MPa, due to the orientation of the fibers. The most significant increase in Achilles was between 128th and 256th cycles, the Quadriceps, PL and STG tendons are increasing continuously, the TA showed the largest modulus increase between 512th and 1000th cycles.
The results of our research was published id Biomechanica Hungarica. The results were used to create material "cards" for the simulation and modelling.

References

1. F. Szakály, I. Bojtár, G. Szebényi: Numerical modelling of human ligaments. Biomechanica Hungarica IX/1.
2. Gunther T. A térdízület biomechanikájának változása az unikompartmentális térdprotézis beültetése során [dissertation]. Budapest (HUN): Semmelweis Univ., 2001.
3. G. Szebényi, P. Görög, Á. Török & R. M. Kiss: Effect of different conservation methods on some mechanical properties of swine bone. Modelling in Medicine and Biology X 2013, Page: 225-233
4. https://link.springer.com/article/10.1007%2Fs00264-016-3336-7
5. Kastelic J, Galeski A, Baer E. Multicomposite structure of tendon. Connective Tissue Research 1978;6(1):11-23
6. Vita, RD. Structural constitutive model for knee Ligaments [dissertation]. Pennsylvania (USA): University of Pittsburgh, 2005.

7. Holzapfel GA. Biomechanics of soft tissue. In: Lemaitre J, editor. Handbook of materials behaviour models 1. New York: Academic Press; 2000. p. 1057-75.
8. Xie F, Yang L, Guo L, Wang Z, Dai G. A Study on construction three-dimensional nonlinear finite element model and stress distribution analysis of anterior cruciate ligament. Journal of Biomechanical Engineering 2009;(13112):121007.
9. Weiss JA, Gardiner JC. Computational modeling of ligament mechanics. Critical Reviews in Biomedical Engineering 2001;29(3):303-71.
10. Fitzgerald, E.R., Dynamic mechanical measurements during the life to death transition in animal tissues. Biorheology, 12, pp. 397–408, 1975.
11. Fitzgerald, E.R., Postmortem transition in the dynamic mechanical properties of bone. Med Phys, 4, pp. 49–53, 1977.
12. Linde, F. and Sorensen, H.C.F., The effect of different storage methods on the mechanical properties of trabecular bone. Journal of Biomechanics, 26, pp. 1249–1252, 1993.
13. https://www.ncbi.nlm.nih.gov/pmc/articles/PMC3968887/
14. Delince P., and Ghafil D. Anterior cruciate ligament tears: conservative or surgical treatment? A critical review of the literature. Knee Surg Sports Traumatol Arthrosc 20**,**48, 2012 [PubMed]
15. Kuo C.K., Marturano J.E., and Tuan R.S. Novel strategies in tendon and ligament tissue engineering: advanced biomaterials and regeneration motifs. Sports Med Arthrosc Rehabil Ther Technol 2**,**20, 2010

3.4 Geometric and mechanical characterization of human carpal bones

Human hand injuries account for a significant number of accidents of young adults (mostly sports injuries) and elderly people. The most vulnerable part of the hand is the wrist, a construct consisting of numerous bones and ligaments. The hand is a complex structure, the mechanical behavior is hard to describe, and also it is sometimes hard to correctly diagnose the injuries. The goal of our research was to create a quickly and inexpensive measurement method to characterize the geometrical and mechanical properties of carpal bones.
The method presented is suitable to properly characterize the intact and damaged geometries of different carpal bones (capitate scaphoid, trapezium, pisiform). 3D models of intact and failed bones are determined by a 3D scanner, mechanical properties are determined with high-speed compression load (700 mm/min), which represents the fracture by falling down.
According to the test results, the 3D scanning technique provided valuable geometrical data for cross-section calculation (scan before the test) and for analysis of the failure mode of the bones (scan after the test). The modulus of elasticity data for finite element simulation can be determined by the high-speed compression tests.

Characterizing the mechanical properties of bone and tissues is fundamental for advances in numerous areas of biomedicine such as diagnostics, forensics, surgical simulations, and injury prediction [1-5]. Various methods have been used to determine the properties of tissues such as tension testing,

compression testing, perfusion, probing, aspiration, and imaging [1], [3], [6], [8].The human hand is often exposed to injury, it dampens falls, raises hard things, but it can also be damaged during sports and play. One of the most important parts of the hand is the wrist, consisting of 8 bones: capitate (os Capitateeum), lunate (os lunatum), triquetrum (os triquetrum), pisiform (os pisiforme), scaphoid (os scaphoid), trapezium (os trapeziodeum), pisiform (os capitatum) and hamate (os hamatum). The carpal bones are bounded by the radius and the ulna from the arm, the fingers and the metacarpale. (Figure

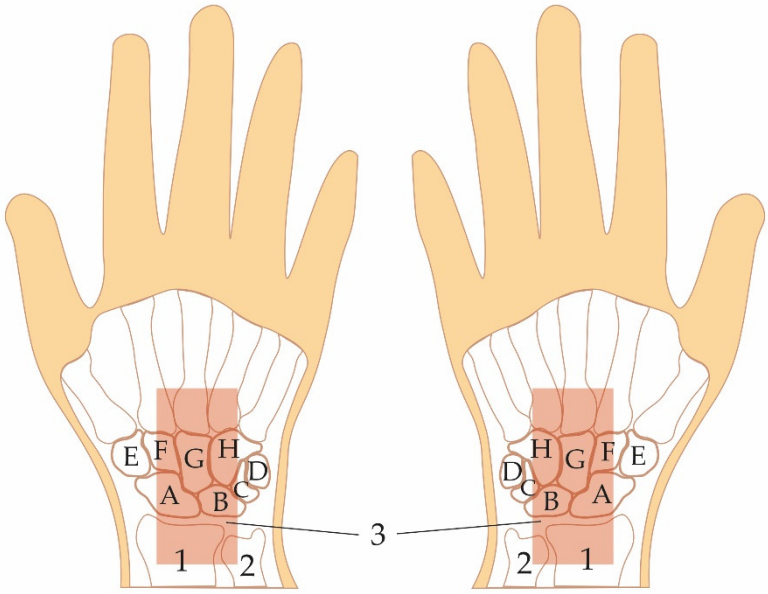

3.13.) [19].

Figure 3.13: Carpal bones and their locations in the hand. A: Capitate, B: Lunate, C: Triquetrum, D: Pisiform, E: Scaphoid, F: Trapezium, G: Pisiform, H: Hamate, 1: Radius, 2: Ulna; 3: carpal tunnel [based on 19]

The radius and the capitate are the two wrist bones that most commonly get fractured. The cause of both capitate and the distal radius fracture is when an individual has fallen onto an outstretched hand in order to break their fall. The capitate is required for stability and coordination. This fracture is mostly seen in young and elderly adults [1], [2]. It often occurs when the hand is breaking during a fall. It is common for capitate fractures to go unrecognized or to be misdiagnosed as a wrist sprain. Such fractures account for roughly about 60% of all carpal fractures. The radius may be damaged in two ways: the distal radius fracture is called the “colles fracture” [1], [3]. The other fracture of the radius is the reverse of colles fracture, that is, the Sminth’s fracture [4], [5]. This fracture occurs when the back of the wrist is the first to break during the fall, forcing the hand under the wrist. If a distal radius fracture is left untreated, it can lead to soft tissue damage and a late development of the carpal tunnel syndrome (CTS), which is a painful condition resulting from the compression of the median nerve[1], [3], [6], [7].

The carpal tunnel is defined as the fibro-osseous tunnel on the palmar side of the wrist; the bony landmarks used to define carpal tunnel volume boundaries are variable. [8] Given that posture-related changes in tunnel volume and shape are partially contingent in individual bone motions, it is essential to consider the positions of all four bony attachments of the transverse carpal ligament. Proximal boundary definitions have included the radiocarpal joint, the distal tip of the radial styloid, the most proximal aspect of the pisiform, and the distal edge of the capitate. [1], [9], [10] Linking changes in carpal tunnel shape to the wrist bones would enable potential errors associated with volume rendering from MRI to be assessed [1], [3], [10], [11].

To be able to describe these failure phenomena, a compression mechanical testing of carpal bones is made, where on the basis of the 3D images of the intact bones and artificially damaged bones their

injuries are evaluated. In the case of middle finger bones, their size permits a twist test, but in this case it is not possible because of the geometry of the carpal bones, which hinders proper gripping [1], [12]–[15]. The tendons which connect the carpal bones have been tested several times, because they are also vulnerable. Researchers investigated the carpal bones system as a whole, but they did not examine them separately [1], [3], [10], [16], [17]. Few literary sources were available; we could not compare the results. They show modelling rather than practical utility [14], [16-17].

In the present study, the behavior of several types of carpal bones were investigated in the case of static compression tests with high speed loading. Before and after the compression test, a 3D scanner was used to create 3D images for the determination of the geometrical properties of the investigated bones. The load and the strain were measured during the mechanical test of different types of carpal bones. The Young's moduli were calculated at an early stage of the graph with deformations between 1 and 2 % [21-23]. The goal of the present research is to create a quick and inexpensive measurement method to characterize the geometrical and mechanical properties of carpal bones. In the four experiments, bones of different geometries were examined, forming part of the carpal bones system.

Materials and methods

The four types of carpal bones were investigated, including capitate, scaphoid, trapezium and pisiform (Figure 3.13.). All 4 pieces of bones were removed from the same human cadaver within 24 hours post

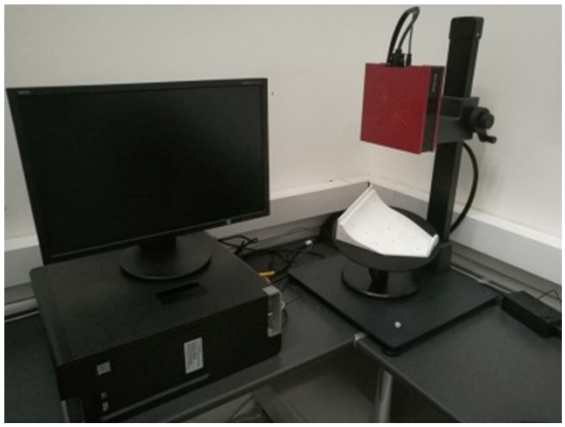

mortem. The bones were placed in a radio-cryoprotectant solution and cooled and stored them at 5°C until mechanical testing (max. 1 week). Before the 3D images are acquired, the bones must be cleaned from the soft tissues with medical tweezers to fit the bone into a stable bone cement base, ensuring exact placement for both geometric and mechanical measurements. After the consolidation of the medical bone cement, a GOM ATOS Core 5M 3D scanner (Gesellschaft für optische Messtechnik GmbH, Germany) was used to make 3D images of the intact bone (Figure 3.14.). The cross-sectional area of the initial samples was measured using 3D software (Autodesk Inventor 2018) based on 3D images.

Figure 3.14: The GOM ATOS Core 5M 3D scanner used for the measurements

The compression test was performed at room temperature using a Zwick Z020 (Zwick GmbH, Ulm, Germany) computer-controlled tensile tester (Figure 3.15.). The static load was defined by 700 mm/min constant crosshead displacement for bones. The high speed represented the fracture by falling.

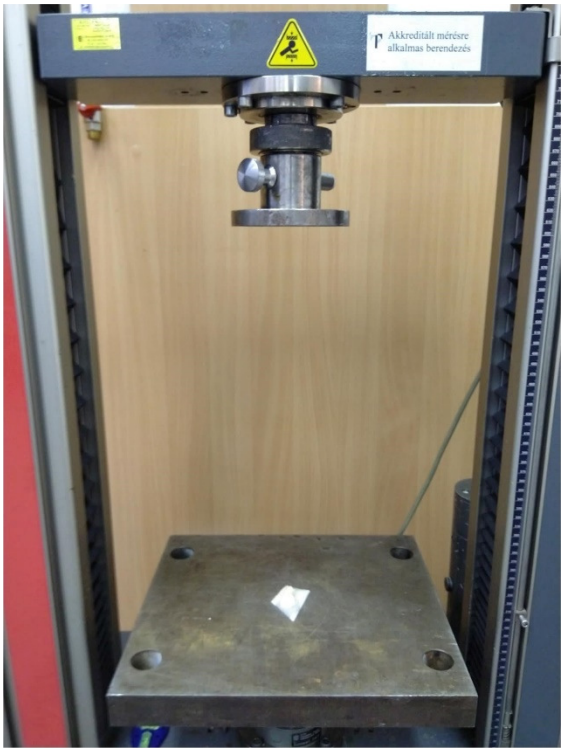

Figure 3.15. ZWICK Z020 tensile tester before the test

The compressive test was continued until complete failure, which was defined at 2 mm displacement. Values of failure load and strain at failure were determined by the computer-controlled material testing machine. The Young's moduli were calculated using the resulting graphs and number results. The Young's moduli were calculated at an early stage of the graph with deformations between 1 and 2 % [21-23].

After the mechanical test, the 3D images of failed bones were produced with a GOM ATOS Core 5M 3D scanner. The cross-sectional area of the failure samples was not measured because the cross-sectional area did not change as bones were embedded in the bone cement. However, the failure mode and failure lines could be determined on the images. The removed bones were placed in a radio-cryoprotectant solution, and cooled and stored at 5°C until the destruction.

In this study, four carpal bones (capitate, scaphoid, trapezium and pisiform) were investigated. 3D images about the intact bones are shown in the subsequent figures below (left sides). The measured cross-sectional areas are summarized in Table 1.

The standard force – strain diagrams for the compressive test are shown in Figures 3.17, 3.19, 3.21 and 3.23. The measured (failure load, strain at failure) and the calculated (Young's modulus of elasticity) results are summarized in Table 3.4.

The 3D images of the damaged bones are shown in the figures below (right sides).

Figure 3.16: 3D images of the capitate bone a) (left) before the compressive test (intact) b) (right) after the compressive test (failed)

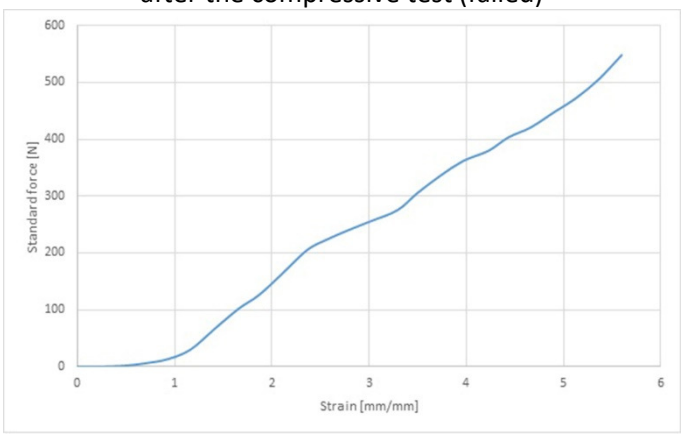

Figure 3.17: Force and strain curve of capitate bone

Figure 3.18: 3D images of the scaphoid bone a) (left) before the compressive test (intact) b) (right) after the compressive test (failed)

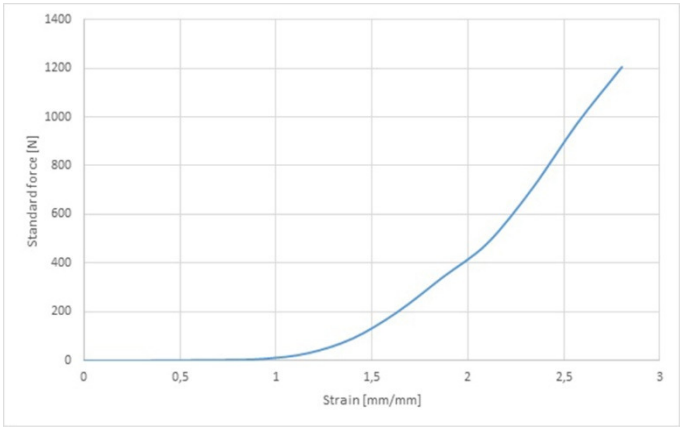

Figure 3.19: Force and strain curve of scaphoid bone

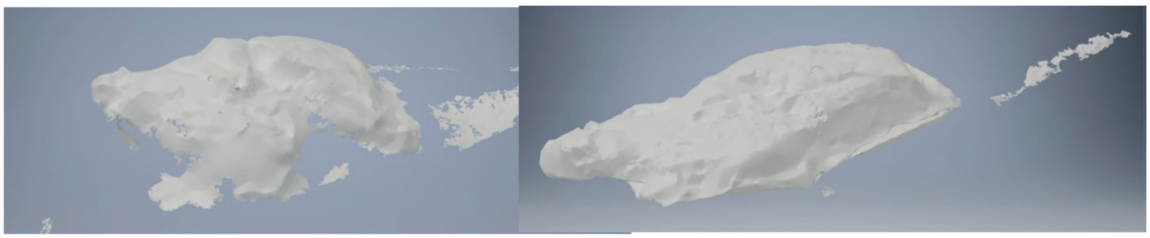

Figure 3.20: 3D images of the trapezium bone a) (left) before the compressive test (intact) b) (right) after the compressive test (failed)

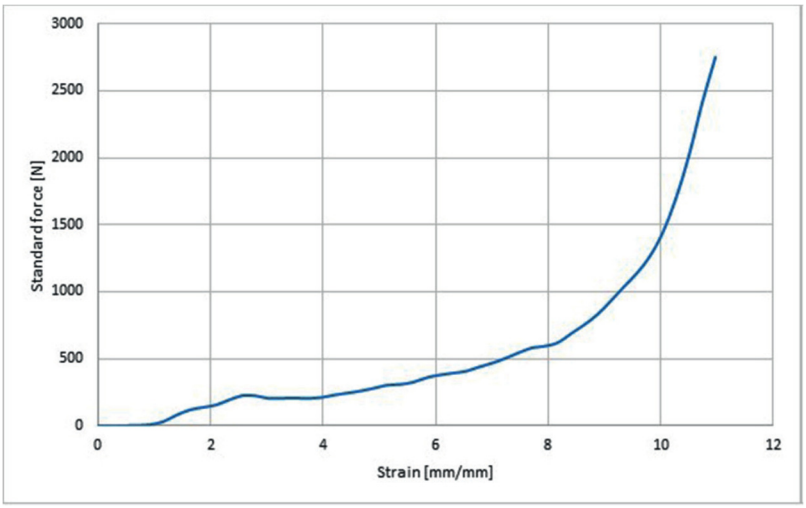

Figure 3.21: Force and strain curve of trapezium bone

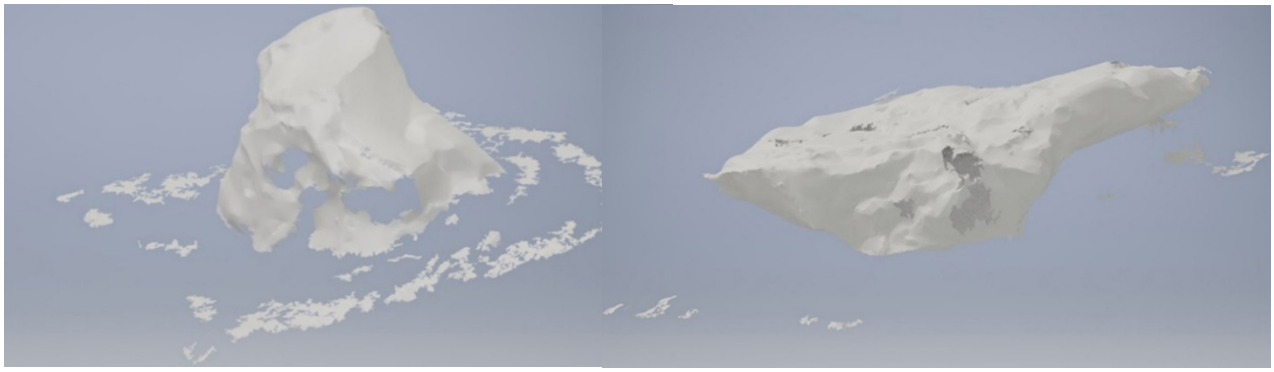

Figure 3.22: 3D images of the pisiform bone a) (left) before the compressive test (intact) b) (right) after the compressive test (failed)

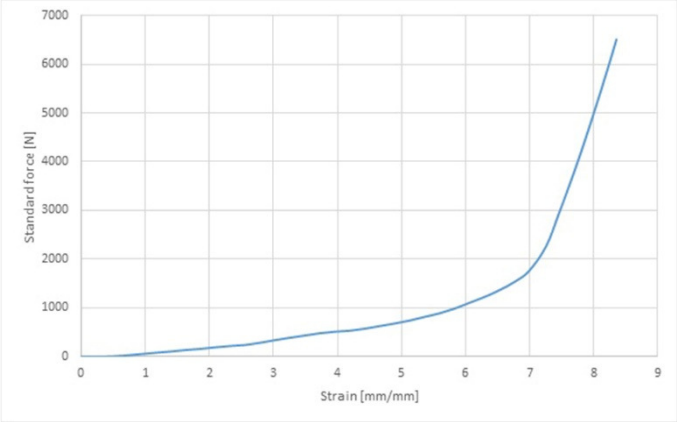

Figure 3.23: Force and strain curve of pisiform bone

	Capitate	Scaphoid	Trapezium	Pisiform
Cross-sectional area [mm^2]	408.42	455.53	383.64	265.49

Table 3.3: Cross-sectional area values of samples

	Capitate	Scaphoid	Trapezium	Pisiform
Failure load [N]	548.15	1204.29	6507.96	2754.03
Failure stress [N/mm^2]	1.34	2.64	16.96	10.37
Strain at failure [mm/mm]	5.61	2.80	8.36	10.97
Young's modulus of elasticity	3.61	21.82	92.09	67.17

Table 3.4: Measured and calculated parameters of compressive test

The results showed that the trapezium bone (failure load: 6507.96 N, failure stress: 16.96 N/mm2) was the strongest bone among the bones measured. It was about 12 times stronger than the weakest capitate bone (failure load: 548.15N, failure stress: 1.34 N/mm2). The Young's moduli of elasticity showed a similar tendency. The biggest deformity was measured at the pisiform bone (10.97%). The smallest deformity was measured at the scaphoid bone (2.80%).

The goal of the present research is to create a quickly and inexpensive measurement method to characterize the geometrical and mechanical properties of carpal bones. The resulting 3D images allow to insert bones into a finite element program for later modelling as input geometrical data and mechanical properties. The novelty of the present research is that the mechanical test has been combined with 3D imaging.

In the examined carpal bones, a large deviation of mechanical and geometrical parameters was observed (Figure 3.24.). The cause of large deviation is that different carpal bones are investigated. In this study, we have defined the measurement layout, the preparation of the measurement, and the measured and calculated mechanical parameters required for the investigation of different carpal bones.

In order to compare the biomechanical behaviour of the different bones, the apparent Young's modulus values were evaluated. In case of Young's moduli an almost 25-fold difference was observed between the strongest and the weakest bones (Table 3.4). The tendency of failure load and failure stress is similar. This phenomenon can be explained by its location in the hand and its size. The shape of the curves is also worth investigating. In the case of the capitate bone, the inclination of the curve is lower than in the other cases. After the maximum load there is no initial and leap failure, which can

be explained by the geometry of the bone. The graph of the capitate bone showed a “saw-tooth character” before the failure. This means that more and more "bone sticks of spongiosa" are failed before the maximum load. It can be explained by the high volume percent of spongiosa in the capitate bone, which can be seen in Fig 3.16b.

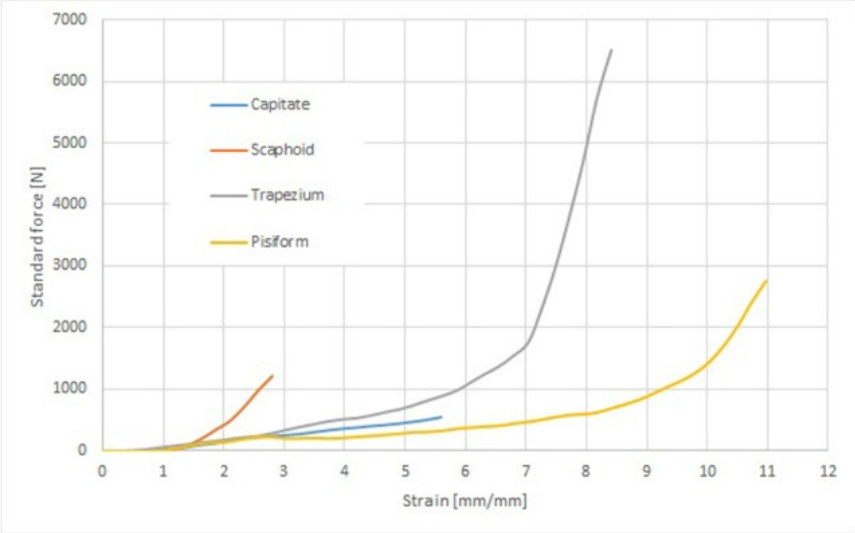

Figure 3.24: The force and strain curves of all bones investigated in the present research.

The limit of the present study is that only one sample of each capital bone was investigated. In further research, the number of samples from each carpal bone should be increased. However, the study and its results have confirmed that the complex method is suitable for the determination of the geometrical and mechanical properties of small bones, such us carpal bones. The results of the new complex method can be used for the modelling and simulation of the failure of carpal bones. It can also be used for the 3D printing of different carpal bones’ replacements.
The results were published in Periodica Polytechnica. The results were used to create material “cards” for the simulation and modelling.

References

[1] B. A. Khader and M. R. Towler, “Common treatments and procedures used for fractures of the distal radius and Capitate: A review,” Mater. Sci. Eng. C, 2016. https://doi.org/10.1016/j.msec.2016.12.038
[2] K. Xiu, J. Kim, and Z. Li, “Clinical Biomechanics Biomechanics of the transverse carpal arch under carpal bone loading,” JCLB, vol. 25, no. 8, pp. 776–780, 2010. https://doi.org/10.1016/j.clinbiomech.2010.05.011
[3] T. M. Moojen, J. G. Snel, M. J. P. F. Ritt, H. W. Venema, J. M. G. Kauer, and K. E. Bos, “In Vivo Analysis of Carpal Kinematics and Comparative Review of the Literature,” pp. 81–87. https://doi.org/10.1053/jhsu.2003.50009
[4] R. N. Kamal, A. Starr, and E. Akelman, “Carpal Kinematics and Kinetics,” J. Hand Surg. Am., pp. 1–7, 2016. https://doi.org/10.1016/j.jhsa.2016.07.105
[5] M. Garcia-elias, K. An, W. P. C. Iii, R. L. Linscheid, and E. Y. S. Chao, “Stability of the transverse carpal arch: An experimental study,” pp. 277–282, 1989. https://doi.org/10.1016/0363-5023(89)90021-X
[6] B. J. Crisco, W. M. R. Heard, R. R. Rich, D. I. Palier, and S. W. Wolfe, “The Mechanical Axes of the Wrist Are Oriented ObHquely to the Anatomical Axes,” pp. 169–178, 2011. https://doi.org/10.2106/JBJS.I.01222

[7] P. Raven, W. P. Cooney, J. H. Dobyns, and R. L. Linscheid, “Arthroscopy of the Wrist: Anatomy and Classification of Carpal Instability,” vol. 6, no. 2, pp. 133–140, 1990. https://doi.org/10.1016/0749-8063(90)90014-5
[8] F. Schuind, W. P. Cooney, R. L. Linscheid, K. N. An, and E. Y. S. Chao, “FORCE AND PRESSURE TRANSMISSION THROUGH THE NORMAL WRIST . A THEORETICAL TWO-DIMENSIONAL STUDY IN THE POSTEROANTERIOR PLANE,” vol. 28, no. 5, 1995. https://doi.org/10.1016/0021-9290(94)00093-J
[9] H. Mitsuyasu, M. Shah, W. L. Buford, and S. F. Viegas, “CAPITATE ANATOMY AND MECHANICS: UPDATE AND REVIEW,” vol. 13, no. 1, pp. 2–10, 2003. https://doi.org/10.1053/otor.2003.36316
[10] J. P. M. Mogk and P. J. Keir, “Clinical Biomechanics The effect of landmarks and bone motion on posture-related changes in carpal tunnel volume,” Clin. Biomech., vol. 24, no. 9, pp. 708–715, 2009. https://doi.org/10.1016/j.clinbiomech.2009.05.012
[11] M. Foumani et al., “The effect of tendon loading on in-vitro carpal kinematics of the wrist joint,” J. Biomech., vol. 43, no. 9, pp. 1799–1805, 2010. https://doi.org/10.1016/j.jbiomech.2010.02.012
[12] K. Márquez-florez, E. Vergara-amador, M. Gavilán-alfonso, and D. Garzón-alvarado, “Load distribution on the radio-carpal joint for carpal arthrodesis,” Comput. Methods Programs Biomed., pp. 1–12, 2016. https://doi.org/10.1016/j.cmpb.2015.12.023
[13] J. J. Crisco et al., “Carpal Bone Postures and Motions Are Abnormal in Both Wrists of Scapholunate Interosseous Ligament Tears,” vol. 5023, no. 03, pp. 926–937, 2003. https://doi.org/10.1016/S0363-5023(03)00422-2
[14] X. Guo, Y. Fan, and Z. Li, “Effects of dividing the transverse carpal ligament on the mechanical behavior of the carpal bones under axial compressive load: A finite element study,” vol. 31, pp. 188–194, 2009. https://doi.org/10.1016/j.medengphy.2008.08.001
[15] P. Varga, P. Schefzig, E. Unger, W. Mayr, P. K. Zysset, and J. Erhart, “Finite element based estimation of contact areas and pressures of the human Capitate in various functional positions of the hand,” J. Biomech., vol. 46, no. 5, pp. 984–990, 2013. https://doi.org/10.1016/j.jbiomech.2012.11.053
[16] J. N. Gabra and Z. Li, “Three-dimensional stiffness of the carpal arch,” J. Biomech., pp. 1–7, 2015. https://doi.org/10.1016/j.jbiomech.2015.11.005
[17] P. Varga, P. K. Zysset, P. Schefzig, E. Unger, W. Mayr, and J. Erhart, “A finite element analysis of two novel screw designs for Capitate waist fractures,” Med. Eng. Phys., vol. 38, no. 2, pp. 131–139, 2016. https://doi.org/10.1016/j.medengphy.2015.11.006
[18] http://www.washington.edu/news/2011/01/03/meet-dermestes-maculatus-the-burke-museums-flesh-eating-volunteers/
[19] https://en.wikipedia.org/wiki/Carpal_bones
[20] http://www.pt.bme.hu/gepadat.php?sorszam=154&l=m
[21] Kurutz, M., Tornyos, A´ ., 2004. Numerical simulation and parameter identification of human lumbar spine segments in traction. In: Bojta´ r, I., (Ed.), Proceedings of the First Hungarian Conference on Biomechanics. Budapest, Hungary, June 10–11, 2004, 254–263, ISBN 963 420 799 5. https://www.researchgate.net/publication/260530824
[22] Kurutz, Marta; Varga, Peter; Jakab, Gabor Prophylactic vertebroplasty versus kyphoplasty in osteoporosis - A comprehensive biomechanical matched-pair study by in vitro compressive testing. MEDICAL ENGINEERING & PHYSICS 65 pp. 46-56. , 11 p. (2019) https://doi.org/10.1016/j.medengphy.2019.01.004
[23] Kurutz, M; Jakab, G ; Varga, P ; Varga, PP Biomechanical evaluation of vertebroplasty and kyphoplasty by uniaxial compressive test BIOMECHANICA HUNGARICA VI : 1 pp. 311-322. , 12 p. (2013) https://doi.org/10.17489/biohun/2013/1/33

IV. Continuum-mechanics based material models and the modification and verification of fibre-bundle-cells models applied to human tissues

László Mihály VAS, Péter TAMÁS, Gábor SZEBÉNYI, Attila BOJTOS, Dénes FARAGÓ

Table of Contents

Introduction

Most human and animal tissues (e.g. tendon, muscle, bone, nerve, vein/artery, and skin, foil, or pellicle tissues) have a fibrous structure [F12, F19]. Similar to artificial fibrous materials, such as textiles or fiber-reinforced composites [F15, F16, F22], presently they are usually examined through the continuum mechanical approach [F10, F15, F16, F22-F25].

The mechanical features of fibrous materials, however, strongly depend on the statistical geometrical and mechanical properties of the building elements like fibrils, fibers, and bundles of them such as macro-fibrils, yarns or rovings, as well as on the connection between the fibers and their environment. Fiber bundles, especially the so-called classic type, have been studied since the first third of the last century [F1, F3-F5, F7, F8, F14, F17, F20, F21, F23, E2-E14] and the results of Daniels [F1], Harlow and Phoenix [F5], and Phoenix [F7], among others, have proved to be of fundamental importance. These researchers focused mainly on strength as a stochastic factor.

The testing and modeling of fibrous structures has got a great tradition at the University BUTE [E1-E14]. Nowadays the application of composites has given a new life to this scientific field. In case of textiles and fiber reinforced composites the mechanical properties of the fibrous structures depend on significantly statistical geometrical and mechanical properties of the fibers as well as frictional and shear effects acting among them and between the fibrous structure and its vicinity. All these are crucial for creating the adequate material model.

The majority of these properties and effects - the deformation and damage behavior of fibrous structures during mechanical tests - can advantageously be modeled with the so-called ***fiber-bundle-cells*** (FBC) method developed by us earlier, where the FBC model is a network consisting of parallel and serial connections of statistical FBCs as model elements, which use ***linear elastic fibers*** [E2-E13, RP2]. These FBCs, such as the E-, EH-, ES-, ET- bundles and their combinations, represent different idealized and typified statistical fiber properties such as fiber shape, state of deformation, connection to their environment (stiff or frictional grip), and the character of damage and the transmission of force.

All the parameters determining the position, state or strength of fibers are random variables. With the aid of the weighted parallel or serial connection of the fiber bundle cells, the mechanical behavior and the measured damage process of real fibrous systems can be modeled or identified from a fiber-bundle-cell model on the basis of measurements, and the structural properties of the systems also can be determined.

A program package named ***FiberSpace*** was developed by the authors in Delphi[1] environment earlier in order help professionals construct a suitable linear FBC model for a given material or study the behavior of model structures where the model fibers were considered linear elastic [E6-E10]. Results of testing and analyzing woven fabric samples showed that instead of linear fiber elements, non-linear elements had to be used for modeling tensile behavior [E14]. The use of such type of bundles can be found in some papers dealing with other structures as well [F14, F17, F20-F23]. We had similar results when testing biological (plant, animal, and human) tissues [RP1-RP3].

The aim of the research has been to develop mechanical material models for describing the mechanical behavior of human tissues based on the concept of the idealized statistical fiber bundle cells and the experiences in their applications. All that needs to investigate the structure and the mechanical properties of the human tissues and their fibril-bundle-like building elements as much as possible. In addition, it has been important to reveal the role and measure

[1]https://www.embarcadero.com/products/delphi

of the frictional and shear effects. After successful testing of simple FBC based material models they can and should be improved in a further development.
According to the concept of the FBC method and the FBC based material models make it possible to describe the total deformation and failure process of human tissue samples subjected to mechanical load without using failure criteria. All that needs to reformulate the mathematical form of the FBC based material models developed on the basis of the mechanical tests of human tissue samples in order to apply them as material model to finite element simulation. This may make possible to model real human tissues and parts of 3D geometry such as tendons and bones subjected to multiaxial mechanical load.

1. Nonlinear Fiber Bundle Cells

1.1. Motivation of Introducing Nonlinear FBCs

The building elements of a FBC model are idealized fiber bundles (Fig.1.1) representing statistical structural and mechanical defects where the fibers, as dominant fiber-like elements of the fibrous structure, are linear elastic (E=Elastic) but break at a random breaking strain. The fibers in an E-bundle are straight, parallel to the tensile load direction, ideally gripped and are not pre-strained. One of these ideal properties is spoilt in the other bundles. The fibers in an EH-bundle may be crimped or pre-strained, or they may be oblique in an ET-bundle or slip out of the gripping in an ES-bundle.

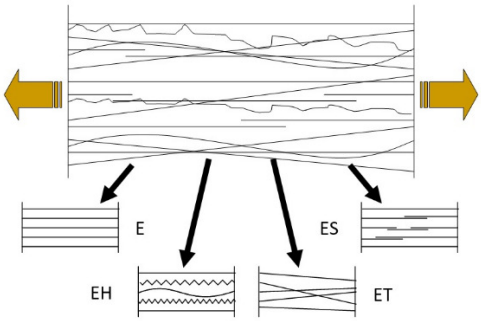

Figure 1.1 Classifying fibers and the structural schemes of the idealized fiber bundle cells

Studying the structure and mechanical properties of textiles (Fig. 1.2) and biological (plant, animal, and human) tissues (Figs. 1.3 and 1.4) has shown that they have a multilevel hierarchical structure where fiber-like building elements, such as different types of fibrils, are formed as the bundles of lower level elements (e.g. a fibril is a bundle of the micro-fibrils) (Figure 1.5) [E2-E14, F10, F12, F19].

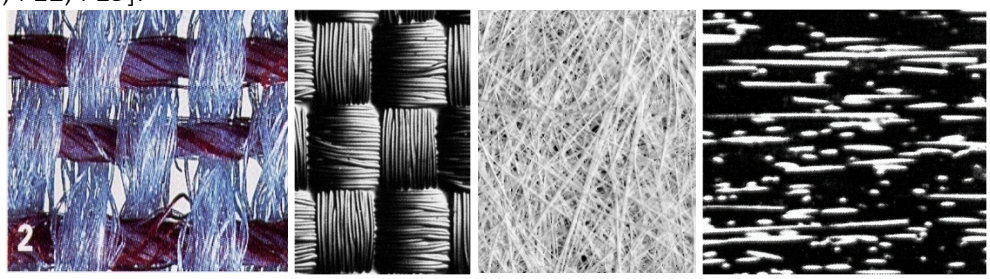

Figure 1.2 Structure of some textiles: woven fabrics made of PP (a) and carbon (b) fibers, glass fiber mat (c), and short glass fiber reinforced UP composite (d)

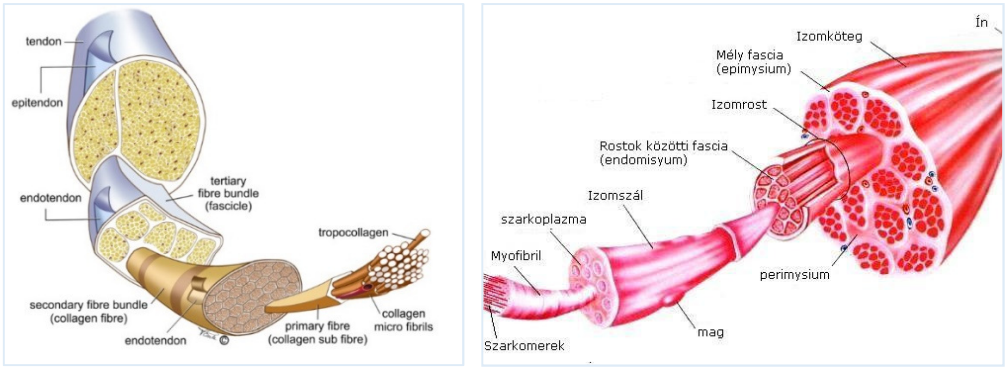

Figure 1.3 Structure of tendons http://vearlemedicalart.com/gallery-2 /structure-of-tendons/ (a) and muscles http://testepites.blog.hu/2011/09/10/csontok_es_izmok_1 (b)

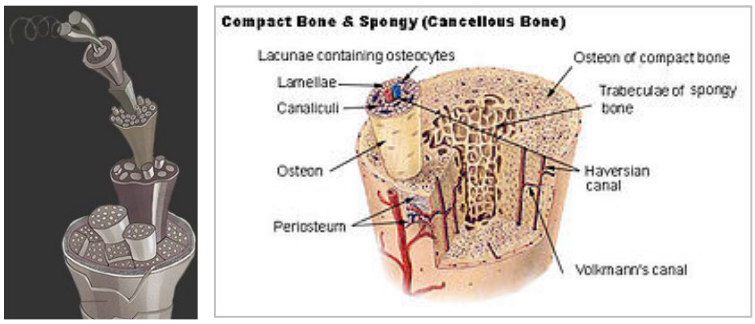

Figure 1.4 Structure of hair or wool fibers http://www.backpackinglight.com/cgi-bin/backpackinglight/ (a) and bones http://hu.wikipedia.org/wiki/Csont (b)

Therefore, even if the elementary fibers of the lowest level are linear elastic, the intermediate fibers, which are bundles of elementary fibers, cannot be modeled as linear, but at least nonlinear hyper-elastic materials, however, the FBCs based modeling offers better solution.

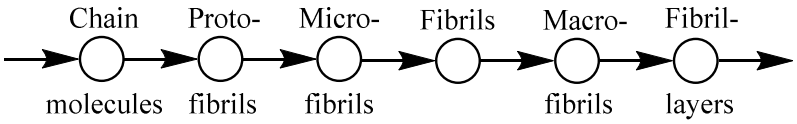

Figure 1.5 Partial structural graph of biological tissues

The analysis of measured data obtained by strain-controlled quasi-static tensile testing of human tissues (face nerves and tendons) has revealed that the initial part of the recorded stress-strain curve has often been convex from below that has been called structural deformation in the case of textiles (Fig. 1.6.a). As shown earlier, the crimping of the fibers may have macro- and micro-components, hence the significant convex initial part may be attributed to the micro- and macro waviness of the fibrils at the dominant structural level (Fig. 1.6.b).

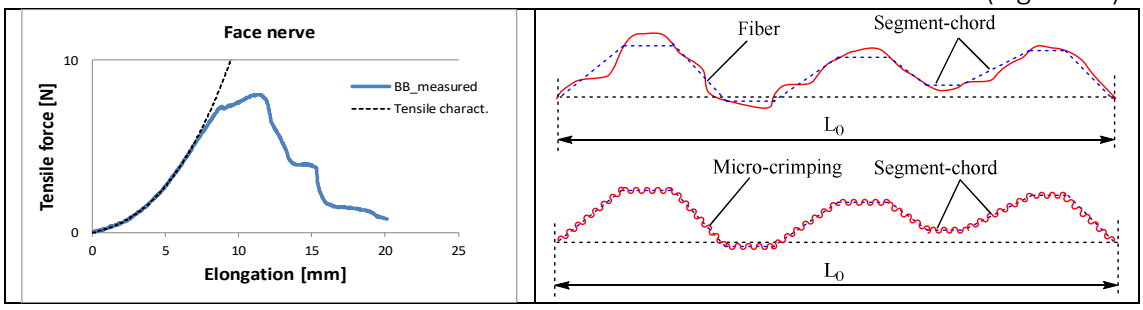

(a) (b)

Figure 1.6 Measured tensile force-elongation curve of a human face nerve (a) and micro- and macro-waves of a fiber and their modeling with a chain of straight and oblique micro-crimped fibers (b)

The modeling of the convex initial part of the measured stress-strain curve can be performed by using primarily the EH-bundle of crimped linear elastic fibers and secondarily the ET-bundle of oblique linear elastic fibers (Fig. 1.7). Fig. 1.7 shows some normalized expected tensile force-strain curves of the linear FBCs modeling the behavior with (Fig. 1.7.a) and without failures (Fig. 1.7.b).

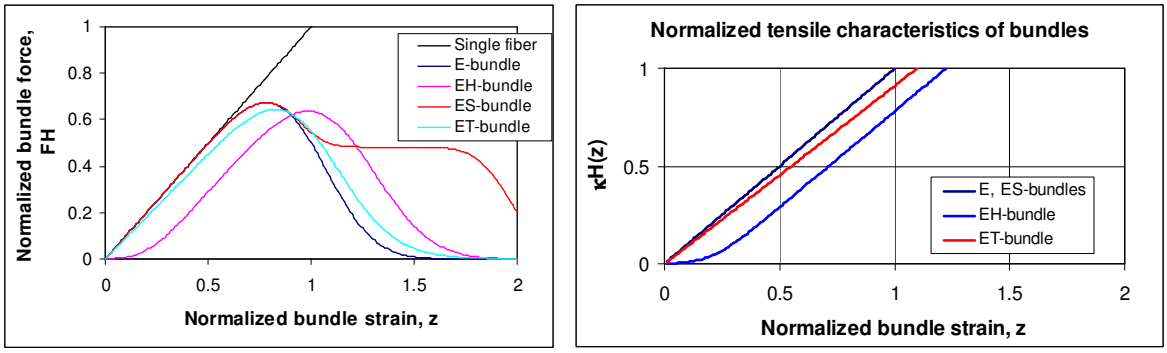

Figure 1.7 Normalized expected tensile process of the different linear FBCs and their weighted sum (composite bundle) (a) and the expected tensile characteristics of the linear FBCs (b) [E7, E12, RP2]

However, as a consequence, the falling part of the model curve provided by linear EH-bundle becomes flatter meaning wider time and strain interval for the failure process, larger than that of the measured one. We have drawn the conclusion that model-fibers of nonlinear tensile characteristics should be applied to eliminate the fitting problems with the rising and damaging parts of the stress-strain curve. Consequently, the parallel connected nonlinear E- and EH bundles can share the problem of modeling the initial part convex from below caused by short and long waves and the situation can be improved by including the nonlinear ES- and ET-bundles as well.

Hence, in order to model the tensile behavior of animal and human tissues, we developed the ***concept of non-linear FBC modeling*** and a ***general approximation method*** based on nonlinear E-bundles. This needed to develop modified formulas to describe the expected tensile force process of the different nonlinear fiber bundles, and to build them into a new version of the FiberSpace software.

It should be mentioned, that the human tissues - besides they have fibrous structures - built up of fiber bundles on different structural levels, they exhibit certain gel-like behavior due to their organic liquid content. Describing this behavior and that observable at cyclic mechanical load with a satisfactory accuracy may need the use of viscoelastic fibers and the development of viscoelastic FBCs.

1.2. Theoretical Relationships

The geometrical and mechanical properties of fibers in practical fibrous materials, such as textiles and composite reinforcements, and those of the structures made of these fibers are of significantly stochastic nature. For modeling these properties and describing the deformation and failure processes we have developed the idealized statistical fiber bundle cells (FBCs), such as the E-, EH-, ES-, ET- bundles and their combinations, and the fundamentals of the related modeling method based on networks of parallel and/or serial connected FBCs. These FBCs as building elements make it possible to model the oblique, crimped, slipping and breaking fibers, the defects in connections, and the stochastic scattering of the strength properties. Hence, when evaluating the results of mechanical tests performed on real fibrous materials and

designing textiles or composite machine parts or constructions, the macroscale effects of these statistical properties can be taken into account.

1.2.1. Definitions of nonlinear FBCs and the force-strain relationships of single fibers

1.2.1.1. Strain of FBC fibers

As mentioned above, fibers of the FBCs subjected to uniaxial tensile strain load (u) (Fig. 1.8) are supposed to be perfectly flexible, non-linearly elastic and to break at a random strain (ε_B). Figure 1.8 shows a crimped fiber enclosed in a cuboid determined by the co-ordinates of the fiber end. The deformation of the fiber is given by the length of its chord vector. In the case of uniaxial tensile load (in x direction) the deformations can be treated as 2 dimensional.

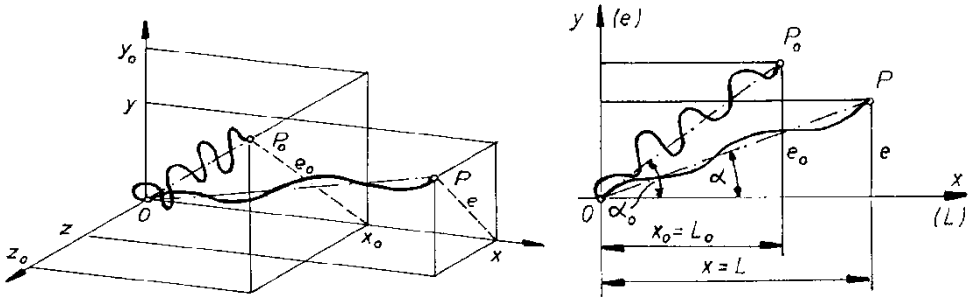

(a) (b)

Figure 1.8 Uniaxial tensile deformation of a fiber enclosed in a cuboid and the Poisson effect in 3D (a) and in 2D (b) [E7, RP2]

Disregarding any possible damage, let $0<l_0$, $-1<\varepsilon_0$, and $0<\lambda_0=1+\varepsilon_0$ denote the unloaded length, the possible initial strain, and the initial extension ratio of the fiber respectively. Consequently, the initial length of the fiber is:

$$l(\varepsilon_0) = \lambda_0 l_0 = (1+\varepsilon_0)l_0 = \|\underline{r}_0\| = \sqrt{x_0^2 + y_0^2 + z_0^2} \tag{1.1}$$

where the length of the chord vector, $\underline{r}_0$, of the fiber is given by the Euclidian norm. In deformed state the length of the fiber chord vector, $\underline{r}$, is l therefore the resultant strain (ε) without any damage or failure that can be calculated by:

$$\varepsilon = \frac{l-l_0}{l_0} = (1+\varepsilon_0)\frac{\|\underline{r}\|}{\|\underline{r}_0\|} - 1 = (1+\varepsilon_0)\frac{\sqrt{x^2+y^2+z^2}}{\sqrt{x_0^2+y_0^2+z_0^2}} - 1 = (1+\varepsilon_0)\frac{\sqrt{x_0^2(1+u)^2+e^2(y,z)}}{\sqrt{x_0^2+e_0^2}} - 1 \tag{1.2}$$

All the parameters of the initial state are stochastic variables. In a constant-rate elongation tensile test, the strain ($\varepsilon(u)$[–]) and the tensile force ($F(u)$) of fibers create stochastic processes as a function of the bundle strain (u[–]$=(x-x_0)/x_0$). The formulas for fiber strain (ε) and the possible crosswise contraction ($W=e/e_0$ Fig. 1.8) of the oblique fibers are as follows [E2, E7, RP2]:

$$\varepsilon(u) = g(u;\varepsilon_0,T_0) = (1+\varepsilon_0)\sqrt{\frac{(1+u)^2+T_0^2W^2(u)}{1+T_0^2}} - 1 \tag{1.3}$$

$$W(u) = \frac{1}{(1+c_a u)^{c_b}} \sim 1 - c_a c_b u \quad (u \to 0) \tag{1.4}$$

where ε_0 is the possible initial strain (if $\varepsilon_0>0$, the fiber is pre-strained, if $\varepsilon_0<0$, the fiber is crimped), $T_0=tg\alpha_0=e_0/x_0$ is the initial obliquity of the fibers (α_0 is the initial orientation angle) and c_a, c_b are contraction constants. According to the asymptotic approximation in Eq. (1.4), the product of constant $c_a c_b$ can be understood as the Poisson's coefficient of the fibrous system in the case of small deformations. For simplicity, all the stochastic parameters and variables are assumed to be independent.

1.2.1.2. Nonlinear tensile characteristics of FBC fibers

We chose the response of a Standard-Solid model [32, 33] to a ramp-type stimulus as the nonlinear tensile characteristic function of the fibers (Fig. 1.9.b). This model is created by the parallel connection of a Maxwell branch and a spring – or its generalized version with several Maxwell branches [E1, F9, F11] (Fig. 1.9.a). The model is often used to describe the mechanical behavior of hyperelastic or viscoelastic materials such as elastomers (soft rubbers). The ramp-type stimulus is realized by the constant rate elongation during tensile tests.

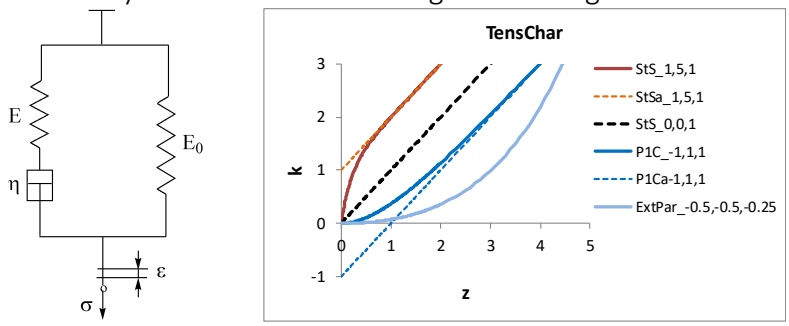

(a) (b)

Figure 1.9 Standard-Solid model (a) and the possible responses to a stimulus of ramp type at different (a, b, c) parameters (b)

This engineering stress response function of the Standard-Solid model is as follows:

$$\sigma(\varepsilon) = E_0\varepsilon + E\varepsilon_0\left(1 - e^{-\frac{\varepsilon}{\varepsilon_0}}\right), \quad \varepsilon_0 = \dot{\varepsilon}_0\tau, \quad \dot{\varepsilon}_0 = \frac{v}{l_0}, \quad \tau = \frac{\eta}{E} \tag{1.5}$$

where E>0 and E_0>0 are the elastic moduli of the springs, η>0 is the dynamic viscosity of the viscous element, the dashpot, and $\varepsilon\geq 0$ and $\sigma\geq 0$, and $\dot{\varepsilon}_0$ are the engineering strain and stress, and the strain rate, respectively (Fig. 1.9.a). *v* is the elongation rate, l_0 is gauge length, and τ is the (relaxation) time constant of the Maxwell branch. As a formal generalization of Eq. (1.5), we denote the constants simply by *a*, *b*, and *c*. Allowing the negative values of *a* makes it possible to obtain not only a linear (*a*=0) or a concave (*a*>0) function shape but a convex (*a*<0) shape as well (Fig. 1.9.b). Moreover, when a large initial curved arc of the force-strain curve is to be modeled, the extension of the parameter domain for the negative *b* values can provide a simple way to describe it (Fig. 1.9.b: Ext.par.). However, it should be noted that in practical processes, the exponential rising is just the initial part of a logistic curve. Consequently, as opposed to the one-parameter (*c*) linear tensile force-strain curves of the single fibers used earlier [17-24], the non-linear curves are described by the next 3-parameter (*a, b, c*) formula [25, 34]:

$$F_f\big(\varepsilon(u)\big) = A_0\sigma\big(\varepsilon(u)\big) = k\big(\varepsilon(u)\big) = c\varepsilon(u) + a\big(1 - e^{-b\varepsilon(u)}\big) \sim \begin{cases} (c+ab)\varepsilon(u), & u \to 0 \\ c\varepsilon(u) + a, & u \to \infty, \ b > 0 \\ -ae^{-b\varepsilon(u)}, & u \to \infty, \ b < 0 \end{cases} \tag{1.6}$$

where the tensile characteristic $k(\varepsilon(u))\geq 0$ and A_0 is the cross-sectional area of the single fibers and $K_0=c+ab$ is the initial tensile stiffness. In general, the parameters, *a*, *b*, and *c* are constant and may depend on the type of the FBC. Obviously, this 3-parameter curve by Eq. (1.6) includes the linear one as well (*c*>0, *a*=0), moreover, when b>0, it is asymptotically linear determined by slope *c* and intercepts *a*. If the fiber breaking strain distribution is known, the expected fiber breaking force can be calculated as follows:

$$\overline{F}_B = E(F_B) = E(k(\varepsilon_B)) = \overline{k(\varepsilon_B)} \tag{1.7}$$

Besides the schematic of the bundles, Figs. 1.11-1.14 show the normalized graphic relationships for the strain ($y=\varepsilon/\varepsilon_B$) and the tensile force ($Y=F/F_B$) of individual flexible and elastic fibers with both linear and non-linear force-strain characteristics as a function the bundle strain ($z=u/\varepsilon_B$). The bundle strain-dependent fiber strain, $\varepsilon(u)$, and the fiber force can be considered as stimulus and response, respectively. On the other hand, the relationship between the fiber and bundle strains, $\varepsilon(u)$, represents and characterizes the mechanical connection between the single fiber and its material environment.

1.2.1.3. Tensile force response of the nonlinear FBC fibers

The fibers of the ***E-bundle*** are straight and parallel to the load direction and they are ideally gripped, meaning that they do not slip out of the grips and do not break in the grips (Fig. 1.10). Therefore, it is often called ideal fiber bundle [14-17]. As a consequence of its properties, the strain of each fiber (ε) in the E-bundle is equal to that of the bundle (u). Yet the overall relationship between the fiber and bundle strains is not linear if breakage is taken into account.

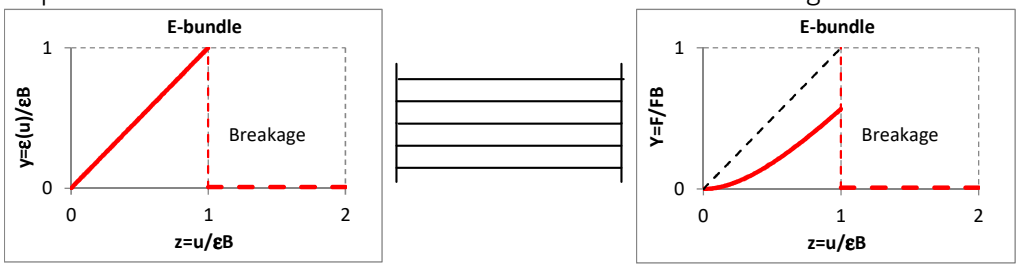

(a) (b) (c)

Figure 1.10 Relationship between the strain (a) and tensile force (c) of single nonlinear fibers and an E-bundle (b) strain

Spoiling the ideal properties of the E-bundle, one by one, leads to three other bundle types which represent statistical behavior in some idealized way. The fibers in the ***EH-bundle*** are ideally gripped but they may be loose ($\varepsilon_o<0$) or pre-tensioned ($\varepsilon_o>0$) [17, 21] (Fig. 1.11).

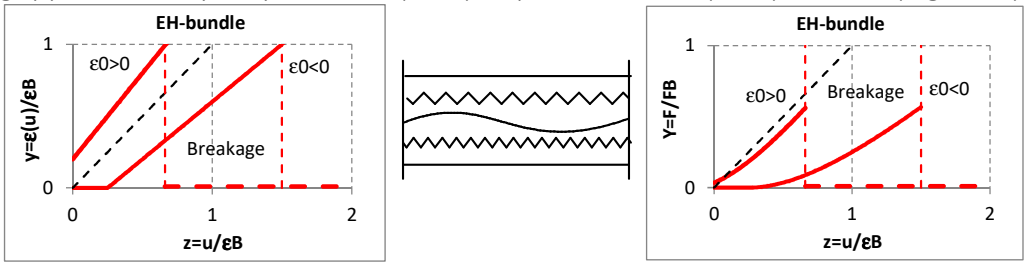

(a) (b) (c)

Figure 1.11 Relationship between the strain (a) and tensile force (c) of single non-linear fibers and an EH-bundle (b) strain

Fibers in the ***ES-bundle*** are straight and parallel but they may slip out of their grip at a strain level (ε_S) or create fiber chains with slipping bonds (Fig. 1.12)..

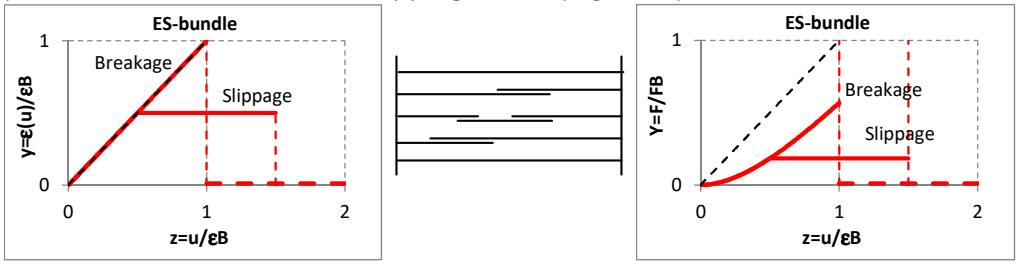

(a) (b) (c)

Figure 1.12 Relationship between the strain (a) and tensile force (c) of single non-linear fibers and an ES-bundle (b) strain

The breaking strain-related slippage length is ε_L and the slippage ends at $\varepsilon_{SL}=\varepsilon_S+\varepsilon_L$. The strain level of slippage is obviously the minimum of those obtained at the two finer ends as well as at the slipping bonds if there is any. Thus, the fibers in the ES-bundle can produce two types of failure depending on their stochastic parameters: slippage if $\varepsilon_S<\varepsilon_B$ or breakage if $\varepsilon_B<\varepsilon_S$. The slippage may model the flow in the fibrous structuresThe fibers are straight and ideally gripped but they may be oblique (the initial fiber angle, α_0, is not zero, so $T_0=\mathrm{tg}\alpha_0\neq 0$) in the ***ET-bundle*** (Fig. 1.13). The orientation angle of fibers may be a stochastic variable. In most cases, the expected value of the orientation angle is zero, meaning scattering about the load direction but a non-zero value means essential obliquity. The extreme case of the latter is when the orientation angle is a non-zero constant, modeling a kind of shearing.

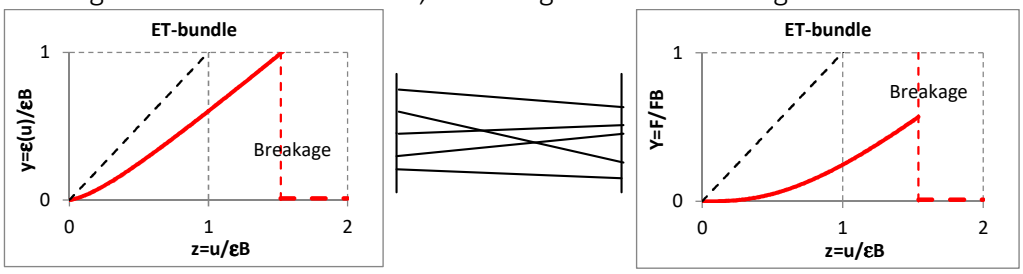

(a) (b) (c)

Figure 1.13 Relationship between the strain (a) and tensile force (c) of single non-linear fibers and ET-bundle (b) strain

Both the shape, position, and strength parameters of fibers are assumed to be independent stochastic variables. Consequently, the strain ($\varepsilon(u)$) and the tensile force ($F(u)$) of both the individual fibers and the bundles create multi-parameter stochastic processes as a function of the bundle strain (u).

1.2.2. Formulas for calculating the expected tensile force process of non-linear FBCs

Knowing the relationship between the bundle (u) and fiber strains (ε), one can calculate the expected value of the tensile force of the FBCs ($E(F)=\overline{F}(u)$) as a sum of the single fiber forces, using the suitable formulas developed [7, 12]. The expected tensile force process of an arbitrary fiber bundle in the load direction is given by the ***fundamental equation of the FBC modeling method*** [E7, RP2]

$$\overline{F}(u)=E[\textstyle\sum_{i=1}^{n}F_i(u)]=nE\left[k_i(u,\underline{\beta_i},\underline{\vartheta_i})cos\alpha_i(u,\underline{\vartheta_i})\chi_i(u,\underline{\vartheta_i},\underline{\gamma_i})\right] \tag{1.8}$$

where k_i, α_i and χ_i are the tensile characteristic, the orientation angle and the stochastic window-function of the ith fiber while $\underline{\beta_i}$, $\underline{\vartheta_i}$, $\underline{\gamma_i}$ are the parameter vectors of the tensile characteristic, the coupling structural parameters and the strength parameters. The factor $k_i\cos\alpha_i$ and the window-function χ_i describe the flawless functioning and the damage/failure process. The introduction of the stochastic window-function is the key for separating the flawless and the damage/failure process that makes the calculations much easier. Every stochastic parameter of the fibers is of the same distribution.

Dividing the expected value by the mean breaking force of fibers, the normalized tensile force of the bundle is calculated as follows:

$$0<FH(z)=\frac{\overline{F}(z\overline{\varepsilon}_B)}{n\overline{F}_B}=\frac{\overline{F1}(z\overline{\varepsilon}_B)}{\overline{F}_B}\leq 1,\qquad z=\frac{u}{\overline{\varepsilon}_B} \tag{1.9}$$

where n, $\overline{F}_B$, and $\overline{\varepsilon}_B$ are the number of fibers, the mean breaking force and the strain of fibers, respectively, and z is the bundle strain normalized by the mean breaking strain of fibers, while

$\overline{F1}$ is the bundle force related to one fiber. Accordingly, normalizing the strain quantities in Equation (1.3) with $\overline{\varepsilon}_B$ defines a new function:

$$h(z;x,y) = g(z\overline{\varepsilon}_B; x\overline{\varepsilon}_B, y) = (1+x\overline{\varepsilon}_B)\sqrt{\frac{(1+z\overline{\varepsilon}_B)^2+y^2W^2(xz_B)}{1+y^2}} - 1 \tag{1.10}$$

Earlier we had developed mathematical formulas for calculating the expected value of the tensile force processes of linear fiber bundles [E2, E7, RP2] and built their numerical realization in the software named FiberSpace [E6, E8-E10, E13]. In this case, the tensile characteristic of fibers was linear, that was $k_i(u)=K_iu$ where Ki was the tensile stiffness. Based on the nonlinear tensile characteristic of fibers, $k_i(u)$, these mathematical relationships were modified. The related shape of the fiber strain by Eq. (1.10) and the normalized version of the formulas are presented subsequently for every FBC.

Non-linear E-bundle

$$\varepsilon(u) = g(u;0,0) = u \tag{1.11}$$

$$FH(z) = \frac{k(z\overline{\varepsilon}_B)}{\overline{k(\varepsilon_B)}}\left(1 - Q_{\varepsilon_B}(z\overline{\varepsilon}_B)\right) \tag{1.12}$$

Non-linear EH-bundle

$$\varepsilon(u) = g(u;\varepsilon_0,0) = (1+\varepsilon_0)(1+u) - 1 \tag{1.13}$$

$$FH(z) = \frac{1}{\overline{k(\varepsilon_B)}}\int_{-1/\overline{\varepsilon}_B}^{\infty} |k(y(z,x))|_+ \left[1 - Q_{\varepsilon_B}(y(z,x))\right] dQ_{\varepsilon_0}(x\overline{\varepsilon}_B) \tag{1.14}$$

where $k(0)=0$ and k is a strictly monotonically increasing function according to Eq. (1.6). Since the fibers are perfectly flexible, they cannot transmit negative (compressive) force, hence the positive part of the tensile characteristic is calculated from the positive part of fiber strain as well:

$$|k(y)|_+ = k(|y|_+) = \begin{cases} k(y), & y > 0 \\ 0, & y \le 0 \end{cases} \tag{1.15}$$

Non-linear ES-bundle

Eq. (1.11) is valid for fiber strain in the ES-bundle as well.

$$FH(z) = \frac{k(z\overline{\varepsilon}_B)}{\overline{k(\varepsilon_B)}}\left(1 - Q_{\varepsilon_B}(z\overline{\varepsilon}_B)\right)\left[1 - Q_{\varepsilon_S}(z\overline{\varepsilon}_B)\right] + \\ + \frac{1}{\overline{k(\varepsilon_B)}}\int_{-\infty}^{z\overline{\varepsilon}_B} k(w\overline{\varepsilon}_B)\left[1 - Q_{\varepsilon_B}(w\overline{\varepsilon}_B)\right]\left[1 - Q_{\varepsilon_{SL}}(z\overline{\varepsilon}_B - w\overline{\varepsilon}_B)\right] dQ_{\varepsilon_S}(w\overline{\varepsilon}_B) \tag{1.16}$$

Non-linear ET-bundle

The initial strain (ε_0) is equal to zero, thus fiber strain is as follows:

$$\varepsilon(u) = g(u;0,T_0) = \sqrt{\frac{(1+u)^2+T_0^2W^2(u)}{1+T_0^2}} - 1 \tag{1.17}$$

The force components in the direction of the tensile load (L) and perpendicular to that (T) are given by

$$FH_L(z) = \frac{1}{\overline{k(\varepsilon_B)}}\int_{-\infty}^{\infty} |k(g(z\overline{\varepsilon}_B;0,x))|_+ \left[1 - Q_{\varepsilon_B}(g(z\overline{\varepsilon}_B;0,x))\right] \frac{(1+z\overline{\varepsilon}_B)dQ_{T_0}(x)}{\sqrt{(1+z\overline{\varepsilon}_B)^2+x^2W^2(z\overline{\varepsilon}_B)}} \tag{1.18}$$

$$FH_T(z) = \frac{1}{\overline{k(\varepsilon_B)}}\int_{-\infty}^{\infty} |k(g(z\overline{\varepsilon}_B;0,x))|_+ \left[1 - Q_{\varepsilon_B}(g(z\overline{\varepsilon}_B;0,x))\right] \frac{xW(z\overline{\varepsilon}_B)dQ_{T_0}(x)}{\sqrt{(1+z\overline{\varepsilon}_B)^2+x^2W^2(z\overline{\varepsilon}_B)}} \tag{1.19}$$

The limit of slippage resistance (ε_S) and the slippage length (ε_L) expressed as relative strains are independent of any other stochastic variables in the ES-bundle, which is well usable for studying different slipping or flow processes in general. However, when the fibers are for example molecule chains built in the crystalline part or micro-fibers of a short fiber-reinforced composite, slippage resistance and slippage length depend on the length of the fibers. In this case, instead of the ES-bundle, its modified versions, the ES1-bundle and the ES2-bundle can be used. In the ES1-bundle, the slipping resistance is constant during slippage, whereas it decreases linearly in the ES2-bundle [E4, E5, E7, RP2]. The linear ES1 and ES2 bundles were

applied to describe the strength of fiber flows and unidirectional short fiber composites. We plan to develop their non-linear versions as a next step.

1.3. FiberSpace Modeling Software as Numerical Realization

We have developed an updated version of the program package named FiberSpace as the numerical realization of the nonlinear FBC-based modeling procedure, in order to assist the construction of a suitable FBC model for a given material or facilitate studying the behavior of model structures [E6, E8-E10]. The identification of the different statistical fiber bundle cells (FBCs) to be applied has been based on the minimization of the squared deviation between the measured force-strain curve and the expected tensile force process of the FBC model, which was created as the parallel connection of number-weighted fiber bundle cells.

1.3.1. Numerical realization of non-linear FBCs by FiberSpace

In Fig. 1.14, the normalized expected tensile force process of a nonlinear E-bundle can be seen together with the window for setting the tensile characteristic parameters of fibers as displayed by the novel version of FiberSpace.

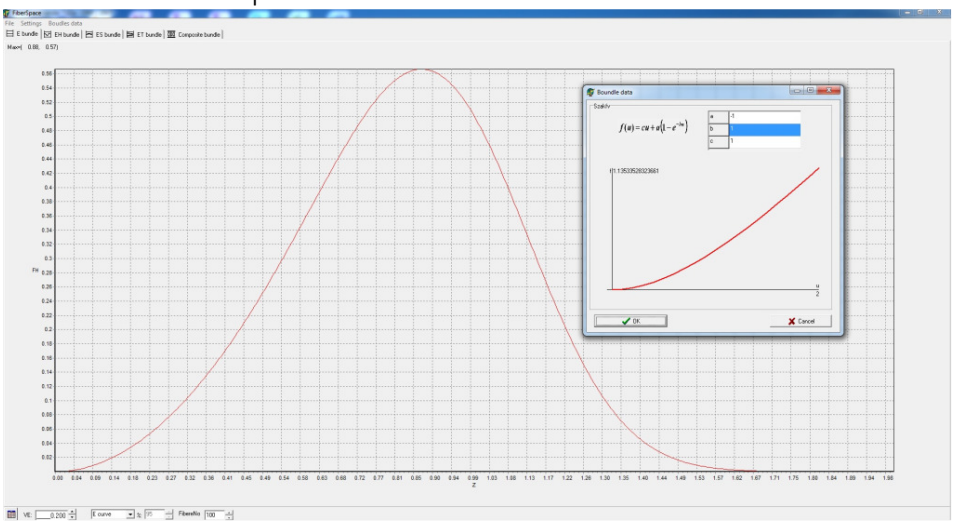

Figure 1.14 The tensile force process of a nonlinear E-bundle and the setting window for the nonlinear fiber characteristic

The parameters (a, b, c) are the same as in Eq. (1.6). The window reveals the shape of the characteristic function as well. In addition, besides the exponential type characteristic by Eq. (1.6), FiberSpace offers two other modes for setting nonlinear fiber characteristic. One of them is a polynomial of maximum degree of 5, the other is a numerical method where the measured data can be imported from MS Excel.

Figs. 1.15 and 1.16 show some typical results of calculating the normalized expected tensile process of the basic linear and non-linear FBCs.

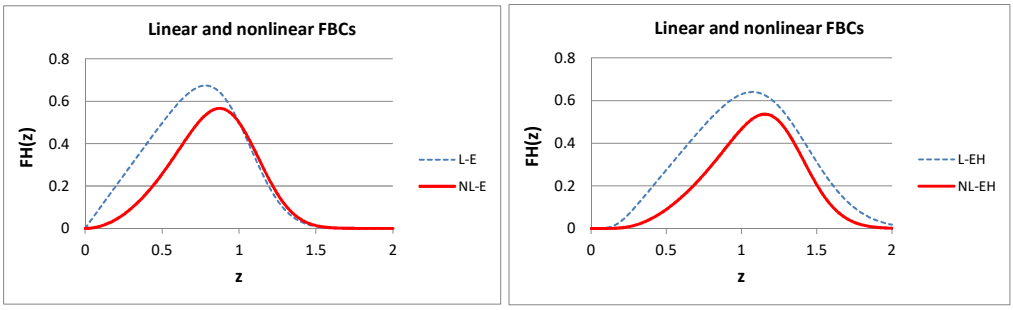

(a) (b)

Figure 1.15 Normalized expected tensile force-strain curves of the E-bundle (AE=1.0; VE=0.2) (a) and EH-bundle (AE=1.0, VE=0.2; EH=-0.15>0 waviness, VH=0.05) (b)

They were calculated with the same model parameters except for those belonging to the fiber tensile characteristic. The parameters of the latter were a=b=0 and c=1 for the linear FBCs while they were a=-1 and b=c=1 for the nonlinear FBCs. The diagrams were created with MS Excel. The short designations of the normalized expected value, E(X), and standard deviation, D(X), of the stochastic variables X∈{ε_B, ε_0, ε_S, ε_L, T_0}, used in FiberSpace are the following: AE=E(ε_B), VE=D(ε_B)/AE; EH=E(ε_0)/AE, VH=D(ε_0)/AE; ES=E(ε_S)/AE, VS=D(ε_S)/AE, EL=E(ε_L)/AE, VL=D(ε_L)/AE; ET=E(T_0), ST=D(T_0), Ca=c_a and Cb=c_b are the contraction parameters, while the parameters of the nonlinear tensile characteristic of fibers are: Ya, Yb, Yc with the FBC code Y∈{E, EH, ES, ET}.

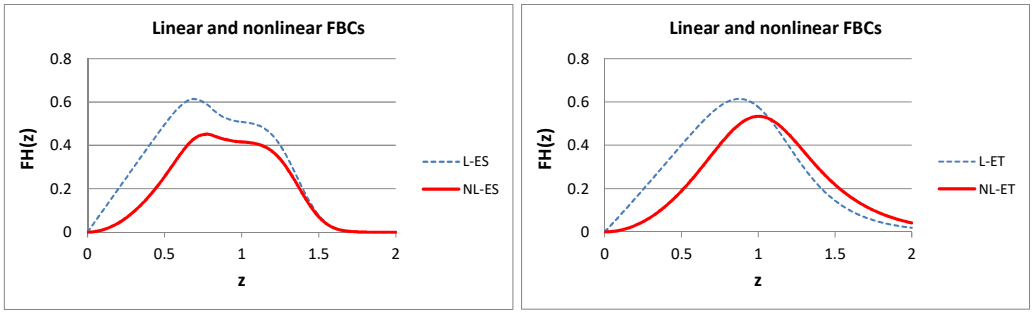

(a) (b)

Figure 1.16 Normalized expected tensile force-strain curve of the ES-bundle (AE=1.0, VE=0.2; ES=0.8, VS=0.1, EL=0.55, VL=0.1) (a) and the ET-bundle (AE=1.0, VE=0.2; ET=0.4, ST=0.35, Ca=Cb=0) (b)

On the basis of Figs. 1.15 and 1.16, one can conclude that, relating to the E-bundle-curve, every stochastic disorder or damage decreases the expected tensile force values on the ascending parts and extends the range of the descending parts. At the same time, the latter effect increases the mechanical reliability of the fiber bundles. On the other hand, in general, the introduction of nonlinear fiber characteristic decreases the tensile force values and modifies the shape of the initial ascending part of the curves while the descending part essentially remains similar to the linear case. However, as can be seen in Fig. 1.15.b, in the case of the EH-bundle, the slope of the descending part increases, which can compensate for the flattening effect of crimping and allows steeper descending. The latter can extend the possibilities of modeling tensile measurement results with FBCs.

1.3.2. The non-linear FBC model – parallel connected FBCs

The analysis of the bundle structure and the identification of the different statistical fiber bundle cells (FBCs) to be applied were based on the minimization of the squared deviation between the measured force-strain curve and the expected tensile force process of the FBC model, which was created as the parallel connection of number-weighted FBCs (Fig. 1.17.a). This latter model is called composite bundle. The expected value process of a composite bundle (Fig. 1.17.a) is calculated as the weighted sum of the components (w_k is the weighting factor, that is, the fiber number ratio of the k-th FBC):

$$FH(z) = \sum_{k=1}^{4} w_k FH_k(z), \quad \sum_{k=1}^{4} w_k = 1 \tag{1.20}$$

Weights can be given by arbitrary non-negative integers *Se*, *Sh*, *Ss*, *St* for the E, EH, ES, ET bundles, respectively (their sum should be positive), and FiberSpace calculates the weighting fraction values w_k, that is, the fiber number fractions, as follows, for example (k=1 can be used instead of k=e):

$$w_1 = w_e = Se/(Se + Sh + Ss + St) \tag{1.21}$$

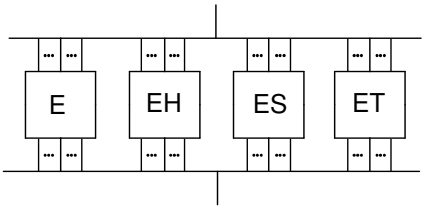

(a)

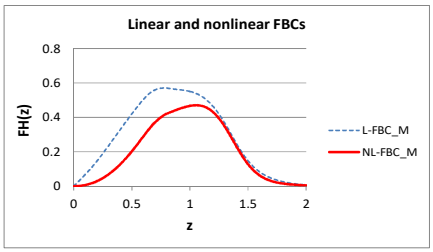

(b)

Figure 1.17 Parallel connection of the FBCs (a) and the resultant expected tensile force process of parallel connected linear (a=0, b=0, c=1) and non-linear (a=-1, b=1, c=1) FBCs with the weights w_e=10%, w_h=30%, w_s=50%, w_t=10% (b)

Fig. 1.17.b presents the weighted sum of the normalized expected tensile force processes of the linear and non-linear FBCs shown in Figs. 1.15 and 1.16.

The curves well demonstrate the possible effect of nonlinearity regarding the tensile characteristic of the fiber. Shifting to nonlinear behavior not only decreases the force values of the onset part of the curve but may change the shape as well. The slightly descending plateau of the ES-bundle becomes slightly ascending while the descending damage part does not become flatter it remains about the same.

The load-strain curve of a real fibrous sample is determined with a tensile test and its normalized form can be imported into FiberSpace from Excel files with the aid of the Microsoft Component Object Model technology[2].

By default, FiberSpace treats the z values between 0 and 2 with an adjustable partition. In the partitioning points, the normalized load-strain curve is calculated by interpolation trigonometrically on the basis of the measured strain values. The measured load-deformation data can be normalized or the normalized result of modeling can be denormalized, respectively.

The 16-model parameters - used in the linear case, such as the 4-component weights and the data of the 12 statistical bundles - are completed with a maximum of 12 non-linearity parameters of the different bundle types (the maximum is for the case when all the FBCs have different tensile fiber characteristics). Consequently, including the mean breaking force of the fibers ($\overline{F}_B$) used for normalization, which may be unknown as well, the functional (Ψ) is to be minimized in order to estimate the structural and mechanical data of the FBC model represented by vector $\underline{p}$. The best approximation of a measured load-deformation curve $F(u)$ can be determined with a fitting procedure based on the least squares method:

$$\Psi\left(\underline{p}\right) = \sum_{i=0}^{N}\left(\frac{F(z_i \cdot A)}{B} - FH(z_i, \underline{p})\right)^2 \rightarrow min! \qquad (1.22)$$

where Z_0 is the limit of the normalized strain domain, and A=AE, B=$n\overline{F}_B$ are the normalizing factors of the measured force-strain curve.

1.3.3. Fourier approximation and the final model parameters

Since the FBC model may use up to 29 parameters, determining them by minimizing the deviation according to Eq. (1.22) needs suitable initial parameter values. The measured and normalized load-strain curve is approximated by non-periodical part of the Fourier regression[3] so that its shape features can be recognized. On the basis of our experiences, the load-strain curves can be well approximated with a Fourier polynomial of 8 terms besides the constant (Fig. 1.18).

[2] https://en.wikipedia.org/wiki/Component_Object_Model
[3] https://en.wikipedia.org/wiki/Fourier_series

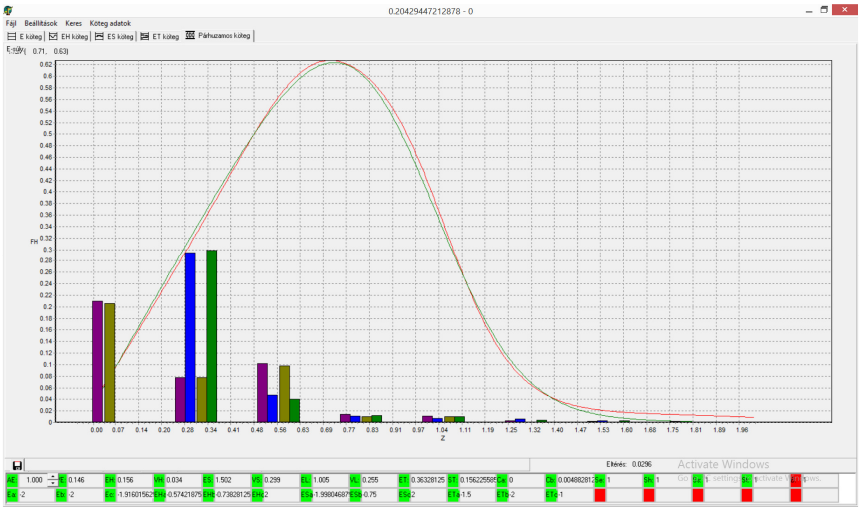

Figure 1.18 Demonstration of FCB modeling by FiberSpace

The FiberSpace system uses the gradient method[4] for seeking the global minimum which depends on the initial values of the model parameters. In order to find the adequate initial position, we built in the so called nearest neighbor searching system [F6]. The already determined Fourier coefficient vectors ($\underline{f}=[a_0, a_1,\ldots, a_n, b_1,\ldots, b_n]^T$) and the related parameter vectors ($\underline{m}\in \mathbf{R}^P$) containing the P=29 FBC model parameters are stored in database Data. The input data of the deducing system are formed by the Fourier coefficient ($\underline{f}$) determined from the normalized measured tensile force-strain curve, FN(z), while the output data are the initial parameters ($\underline{\hat{p}}$) of the model composite bundle. The final model parameters ($\underline{p}$) are obtained by minimizing the expression according to Eq. (1.22):

$$FN(z) \xrightarrow{Fourier} \underline{f} \xrightarrow{Deduction} \underline{\hat{p}} \xrightarrow{FH} FH(z,\underline{\hat{p}}) \xrightarrow{Minimizing} FH(z,\underline{p}) \approx FN(z) \tag{1.23}$$

Finally, when d_1>0, the vector pair ($\underline{f}$, $\underline{p}$) is stored in Data as one record of the training data. This constitutes a step of machine learning. Fig. 1.18 shows an example for demonstrating the results obtained by FiberSpace, where the green and red curves are the measurement and the approximation, respectively, while the colored columns represent the amplitudes of the Fourier polynomial used by the deducing system of the software.

1.4. Modeling with Nonlinear E-bundle Series

Using the FBCs introduced and discussed above leads to a decomposition of the measured tensile force-strain relationship. This gives information on the fiber classes of the fibrous structure tested and represents stochastic structural imperfections, such as wavy, crimped, oblique, pre-stressed fibers, or the possibility of fiber pullout. At the same time, the application of non-linear E-bundles only may be very advantageous when the purpose of decomposition is to determine sub-bundles corresponding to certain known conditions (e.g. damage/failure modes, elements of hierarchic structural levels).

On the other hand, the mechanical behavior of the nonlinear EH, ES, and ET bundles can be decomposed into weighted parallel combinations of nonlinear E-bundles therefore the expected responses of the previous FBCs can be decomposed into the weighted sum of the nonlinear E-bundle-responses ($j\in$ {E,EH,ES,ET}):

$$FH_j(u) \approx \sum_{i=1}^{n_j} w_{ji} FH_{ji}(u) = \sum_{i=1}^{n_j} w_{ji} k_{ji}(u) R_{ji}(u) \tag{1.24}$$

[4] https://en.wikipedia.org/wiki/Gradient_descent

where the R_{ij} reliability functions are the complement distribution functions of the fiber breaking strain, which are of the same two parameter type with different expected values (m_i=E(ε_{Bi})) and standard deviations (s_i=D(ε_{Bi})).

In general, in order to show and analyze the effects of statistical inhomogeneities in the structure, the fibers in different linear or nonlinear FBCs have the same mechanical properties but according to Eq. (1.24), the fibers in a series of E-bundles have different tensile characteristics. This fact makes further analysis possible. Fig. 1.19 shows the approximation of normalized force responses of nonlinear EH- and ES-bundles with a single and two nonlinear E-bundles, respectively. Using the simplest way, the initial arc of the nonlinear EH-response was approximated by a shifted E-bundle response (Fig. 1.19.a; b>0; $FH_E(u-u_0)>0$ if $u>u_0$ and =0 if u_0), however, the exponential rising (b<0) could be used as well.

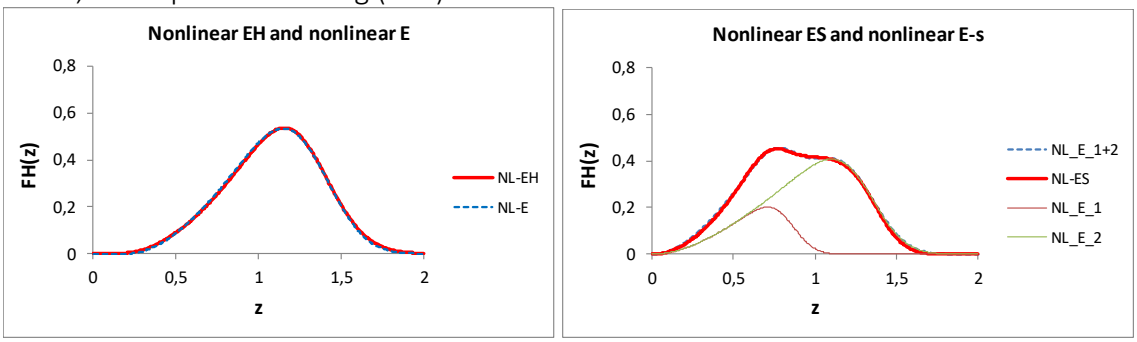

Figure 1.19 Approximating the normalized tensile response of a nonlinear EH-bundle (see Figure 1.15.a) (a) and ES-bundle (see Figure 1.16.a) (b) with parallel-connected nonlinear E-bundles

(a): a shifted E-bundle (a=-1, b=1.5, c=1.5, u0=0.2, m=0.67, s=0.2; RMSE=1.04%, R^2=0.999)

(b): two E-bundles (u0=0; w1=0.4; a1=-0.8, b1=2.125, c1=1.7, m1=0.83, s1=0.11; w2=0.6, a2=-0.55, b2=2.09, c2=1.15; m=1.3, s2=0.17; RMSE=1.67%, R^2=0.998)

Uniting the different approximations, the measured tensile force-strain curve, $F(u)$, can be modelled by the weighted parallel connection of nonlinear E-bundles ($n=\Sigma n_j$), hence it can be approximated with the expected tensile process of the resultant bundle:

$$F(u) \approx \overline{f}(u) = \sum_{i=1}^{n} w_i \overline{f}_i(u) = \sum_{i=1}^{n} w_i k_i(u) R_i(u), \qquad \sum_{i=1}^{n} w_i = 1 \tag{1.25}$$

On the other hand, Equation (1.25) represents the law of total expectation [36], namely:

$$F(u) \approx \overline{f}(u) = \sum_{i=1}^{n} E(f(u)|B_i)P(B_i) = \sum_{i=1}^{n} k_i(u)R_i(u)w_i \le \sum_{i=1}^{n} k_i(u)w_i = \overline{k}(u) \tag{1.26}$$

where $\overline{k}(u)$ is the expected tensile characteristic, hence, the conditional expected value of $f(u)$ and the probability of the condition are given by:

$$E(f(u)|B_i) = k_i(u)R_i(u), \quad P(B_i) = w_i \tag{1.27}$$

respectively, where B_i is the event that an arbitrary fiber belongs to the i^{th} subbundle.

It should be noted that Eq. (1.25) is a finite part of a special function series of product-shaped terms thus the decomposition into nonlinear E-bundles is equivalent to an expansion into series (bundle-expansion). Moreover, taking into consideration that the values - expected values of fiber breaking strain - m_i (i=1,..,n) create a strictly monotonically increasing series

$$m_1 < m_2 < \cdots < m_n \tag{1.28}$$

the sum according to Eq. (1.25) can be converted into an integral form as follows:

$$F(u) \approx \overline{f}(u) = \int_0^{\infty} k(u;m)R(u;m)dW(m) \tag{1.29}$$

where $W(m)$=P(μ<m) is the distribution function of μ, which is the expected fiber breaking strain as a stochastic variable. Taking into consideration that the tensile characteristic, $k(u)$, can be given by the relaxation spectrum, which characterizes the damage-less work of the material,

one can suppose that the density function $w(m)=dW/dm$ and the $s(m)$ standard deviation function can be regarded as damage parameter spectra characterizing the failure process.
Here $s^2(m)$ is a conditional variance of μ, thus it should obviously contain the variance of μ therefore the next expression may be suitable to use:

$$s(m) = \sqrt{s_0^2 + \omega^2(m-M)^2}, \quad E(s^2(\mu)) = s_0^2 + \omega^2 E[(m-M)^2] = s_0^2 + \omega^2 S^2 \tag{1.30}$$

where the standard deviation of the fiber breaking strain, s_0,and weighting factor ω are constants, and $M=E(\mu)$ and $S=D(\mu)$ are the expected value and the standard deviation of μ. This can be decomposed into a sum of such variances:

$$s^2(m) = \sum_{i=1}^{n}[s_{0i}^2 + \omega_i^2(m-M_i)^2] = \sum_{i=1}^{n} s_{0i}^2 + \sum_{i=1}^{n} \omega_i^2(m-M_i)^2 \tag{1.31}$$

Note that the sum is equivalent to a polynomial of 2nd order like in Eq. (1.30) and it is a decomposition of the variance like the ANOVA equation.
The relaxation spectrum determines the deformation behavior in the undamaged state, while the damage parameter spectra characterize the failure process. Fitting the model by Eq. (1.25) and determining the free parameters (a_i, b_i, c_i, m_i, s_i)(i=1,…,n)(see Eq. (1.6) as well) are performed by minimizing the squared deviation according to Eq. (1.22), from the measured data. The series in Eq. (1.25) can be estimated from above by a kind of Prony-series[5] that is the mean tensile characteristic. The Prony-series can be characterized by a so-called discrete relaxation spectrum [E1, F9, F11], {(b_i; a_i, c_i)}, which consists of pair-values; besides that, the original series itself can be a damage or failure parameter spectrum, {(b_i; m_i, s_i)}, which contains double values as well. It can be easily seen that b_i is a kind of "strain-frequency" or relaxation parameter since it can be expressed with the relaxation time, τ_i (see Eqs. (1.5) and (1.6)):

$$\frac{1}{b_i} = \dot{u}_0 \tau_i = \dot{u}_0 \frac{\eta_i}{E_i} \tag{1.32}$$

where $\dot{u}_0$ is the engineering strain rate ($u = \dot{u}_0 t$), and η_i and E_i are the dynamic viscosity and the tensile modulus, respectively, which are the parameters of the Maxwell model used for the tensile characteristic of the model fibers (Fig. 1.9.a). The non-linear E-bundles, as the simplest FBCs, can easily be calculated even in an MS Excel environment, and we used them first for modeling and analyzing the results of tensile and acoustic emission tests [P2].

1.5. FBC Model-based Damage Maps and Reliability Characteristics

The FBC model fitted to tensile test measurements makes it possible to calculate some qualitative characteristics of the material, such as the reliability characteristics and damage maps of different weighting.
According to Eq. (1.20), the resultant normalized expected tensile force of the FBC model is the weighted sum of those of the components. The gradual addition of the components decomposes the resultant curve into ranges which show the weighted fraction of the components and the represented damage modes as a function of the normalized FBC strain (n=1,…,N≤4):

$$FH(z)_n = \sum_{i=1}^{n} w_i FH_i(z) \tag{1.33}$$

where N is the number of components with non-zero weight. The normalized form of Eq. (1.33) is this:

$$fH(z)_n = \frac{\sum_{i=1}^{n} w_i FH_i(z)}{\sum_{i=1}^{N} w_i FH_i(z)} \tag{1.34}$$

[5] https://en.wikipedia.org/wiki/Prony%27s_method

According to Eq. (1.12), the normalized expected tensile characteristic of the E-bundle, $kH_E(z)$, is identical with that of the fibers, consequently, the reliability characteristic equals the complement distribution function of the fiber breaking strain:

$$kH_E(z) = \frac{k(z\bar{\varepsilon}_B)}{k(\varepsilon_B)}, \quad RH_E(z) = 1 - Q_{\varepsilon_B}(z\bar{\varepsilon}_B) \tag{1.35}$$

The normalized expected tensile characteristic of the other FBCs can be obtained by substituting the complement distribution function of the damage variables (ε_B, ε_S, and ε_{BL}) with the unit-step function in Eqs. (1.14), (1.16), and (1.18). For the ES-bundle, this leads to the same function as that of the E-bundle while for the EH- and ET-bundles, we obtain Eqs. (1.36) and (1.37), respectively:

$$kH_{EH}(z) = \frac{1}{k(\varepsilon_B)} \int_{-1/\bar{\varepsilon}_B}^{\infty} |k(y(z,x))|_+ dQ_{\varepsilon_0}(x\bar{\varepsilon}_B) \tag{1.36}$$

$$kH_{ET,L}(z) = \frac{1}{k(\varepsilon_B)} \int_{-\infty}^{\infty} |k(g(z\bar{\varepsilon}_B;0,x))|_+ \frac{1+z\bar{\varepsilon}_B}{\sqrt{(1+z\bar{\varepsilon}_B)^2 + x^2 W^2 (z\bar{\varepsilon}_B)}} dQ_{T_0}(x) \tag{1.37}$$

In this case, $RH_E(z)$ gives the fraction of the fibers intact at the strain considered, hence $RH_E(z)$ is the reliability function of the E-bundle. The reliability characteristic of the i^{th} component, $RH_i(z)$, can be obtained when its expected tensile force, $FH_i(z)$, is divided by the related expected tensile characteristic, $kH_i(z)$, which represents the failure-less behavior of the bundle at any strain load:

$$RH_i(z) = \frac{FH_i(z)}{kH_i(z)} \tag{1.38}$$

Accordingly, in a weighted sense, the reliability characteristic has a similar role concerning the damage and failure of fibers.

The reliability characteristic of the i^{th} component, $RH_i(z)$, can be obtained when its expected tensile force, $FH_i(z)$, is divided by the related expected tensile characteristic, $kH_i(z)$, which represents the failureless behavior of the bundle at any strain load:

$$RH(z) = \frac{FH(z)}{kH(z)} = \sum_{i=1}^{N} w_i \frac{FH_i(z)}{kH(z)} = \sum_{i=1}^{N} \frac{w_i kH_i(z)}{kH(z)} RH_i(z) \tag{1.39}$$

where $kH(z)$ is the resultant expected tensile characteristic of the FBC model:

$$kH(z) = \sum_{i=1}^{N} w_i kH_i(z) \tag{1.40}$$

Similarly to Eq. (1.33), a kind of damage or failure map can be constructed by adding the component reliability characteristics together gradually (n=1,..,N):

$$RH(z)_n = \sum_{i=1}^{n} w_i \frac{FH_i(z)}{kH(z)} \tag{1.41}$$

In the case of modeling the tensile force-extension measurements directly, the suitable formulas can be obtained by denormalizing the equations like Eqs. (1.12)-(1.19) and (1.35)-(1.37).

2. Application to Modeling and Analyzing Woven Reinforcements

Woven fabrics are discrete element structures built up of fibers with at least two structural levels: elementary fibers – yarns as fibers – woven fabric. Hence, this artificial and regular structure is a good base and a first step to study the applicability of the nonlinear FBC method.

2.1. Objectives of FBC Modeling of Woven Reinforcements

The goal of examining the woven fabric samples cut out in warp and diagonal direction was to study the deformation and failure process in such a regular fibrous reinforcement structure and see how to model the effect of crimped yarns of artificial regular waviness. The fibers in the ES-bundle may slip or break but as a default the resistance force during slipping is assumed constant similar to the Coulomb friction up to the end of slipping (Fig. 2.1.a).

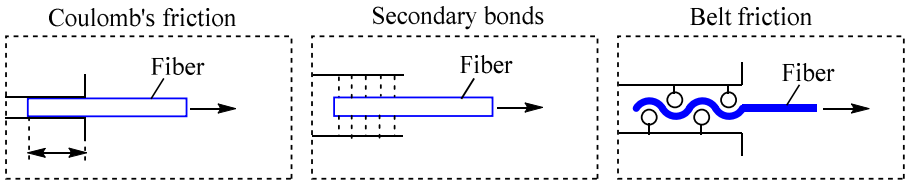

Figure 2.1 Types of resistance against pulling out during fiber slipping

In the ES2-bundle, that is the modified version of the ES-bundle [E4, E5], the resistance of fibers during slipping linearly decreases modeling the slippage of molecule chains bonded to the neighbor molecules regularly by secondary bonds in a crystallite (Fig. 2.1.b). The yarns in a woven fabric are bonded regularly by the crosswise yarns by belt friction effects (Fig. 2.1.c). This latter phenomenon with stochastic nature is assumed to occur in the fibrillary structure of the human tissues therefore it has good reason to study this effect in a regular structure like the woven fabric and create adequate FBC model for that.

2.2. Theoretical Considerations

As in general, the FBC modeling aims at describing both the total deformation and the failure processes during the tensile testing of the woven fabric samples. In this case nonlinear E-bundles are used for creating FBC model for describing the tensile test results. The shear and friction effects can be studied by yarn pulling out tests.

The woven fabric sample cut out in the warp direction is made of warp yarns that are parallel to one another but they are regularly crimped by the crosswise weft yarns. The load is taken up by the warp yarns the weft yarns give crosswise bonds between them. The fibers in the E-bundle are also parallel to the direction of the uniaxial tensile load but they are straight. These are the model fibers (Fig. 2.2) that straight and there is no bond between them but their mechanical properties, given by the tensile characteristic and the breaking strain determined from fitting, can include the effects of crimping, crosswise bonding, and the possible friction. Hence the bundle of them can give a good approximation of the measured stress-strain curve. For a sample cut out in warp direction the model bundle contains 'strong' fibers. On the other hand, the sample cut out in diagonal direction provides an E-bundle of 'weak' fibers because in this case there is not any yarn parallel to the load direction hence the tensile resistance is determined essentially by the shear and friction effects between the crimped and oblique yarns.

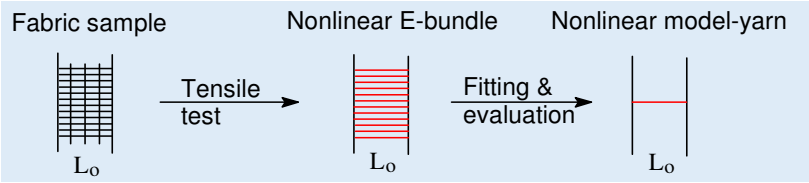

Figure 2.2 Creating FBC model by mapping the fabric structure into the E-bundle model

2.3. Results of Measurements and Modeling

Two woven fabrics made of glass fiber roving yarns and used as composite reinforcement were tested (Fig. 2.3). All their parameters such as area density of the sheets, linear density of the yarns, sizing material, etc. were the same except for their binding structure: one of them was of plain weave and the other was of twill weave.

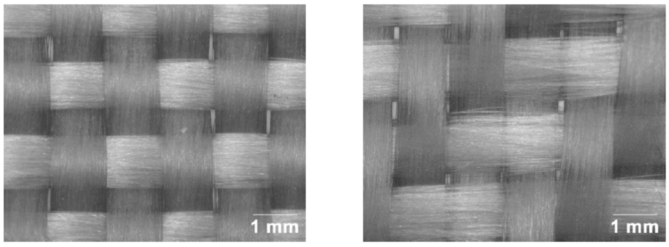

Figure 2.3 Plain (a) and twill (b) woven fabrics

2.3.1. Tensile test results

The measured force-elongation curves obtained by tensile tests, performed at 100 mm gauge length and 25 mm/min rate, and their mean curve calculated by averaging point by point can be seen in Figs. 2.4-2.5 for the samples of 50 mm width cut out in warp and diagonal directions.

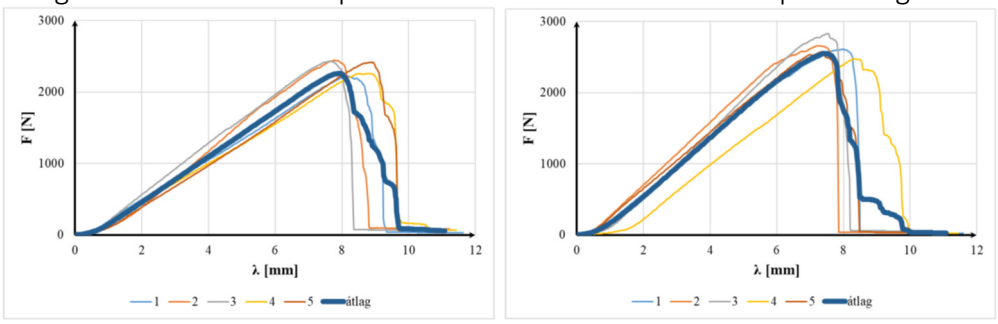

(a) (b)

Figure 2.4 Tensile test results of plain (a) and (b) twill woven fabric samples cut in warp direction (átlag = average)

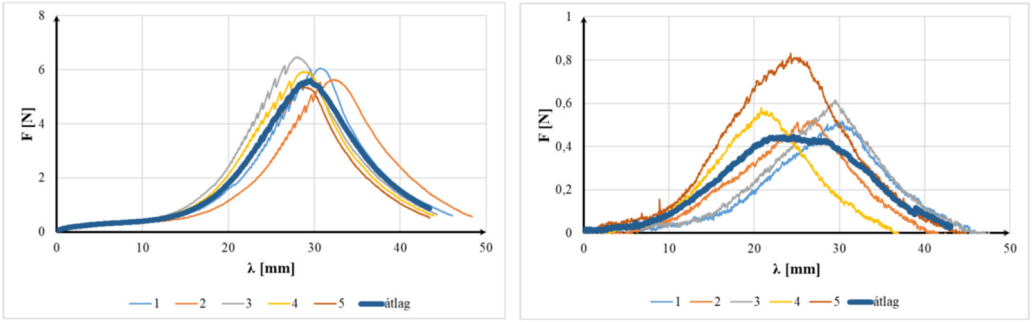

(a) (b)

Figure 2.5 Tensile test results of plain (a) and (b) twill woven fabric samples cut in diagonal direction (átlag = average)

The tensile strength defined by the force peak is larger for the twill sample that the plain one because the entanglements make denser but weaker the fabrics and their number is smaller in the former. On the other hand, corresponding to the theoretical considerations, the resistance force measured on the diagonal samples was by more than two magnitudes smaller than that in warp direction due to the fact that in the lack of yarns in load direction therefore the resistance was provided by shear and friction effects. The diagonal peak force for the plain sample was by one magnitude greater than that for the twill one, which can be attributed to the larger entanglement number.

The results of FBC modeling in Figs. 2.6-2.7, where the relative mean squared error was less than 3.6% in every case, show that the nonlinear E-bundles can effectively be applied to describe the tensile test curves of the woven samples. In the case of the samples cut out of the warp direction a single E-bundle could give satisfactory approximation while the diagonal samples needed two different parallel connected E-bundles for that purpose.

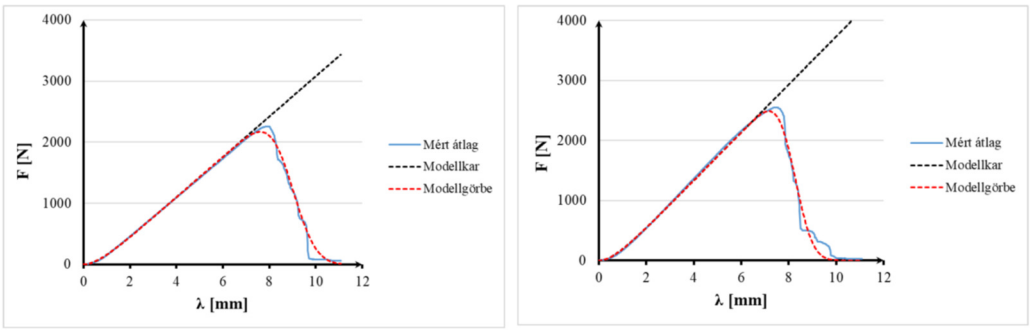

(a) (b)

Figure 2.6 Modeling results for plain (a) and (b) twill woven fabric samples cut in warp direction (Mért átlag = measured average, Modellkar = model characteristic, Modellgörbe = model curve)

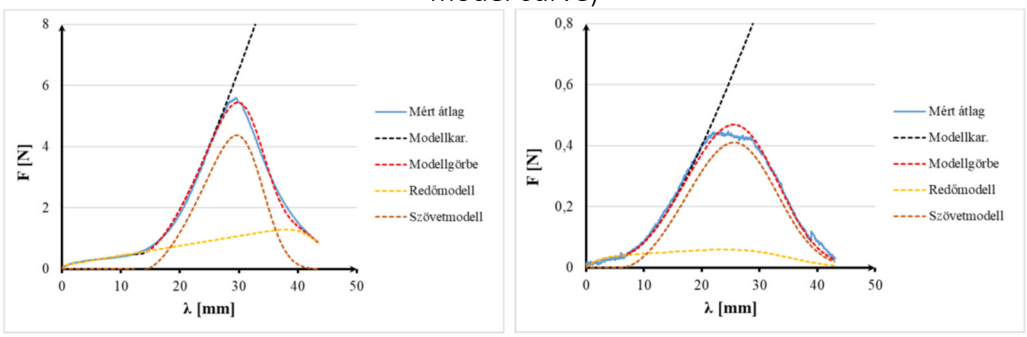

(a) (b)

Figure 2.7 Modeling results for plain (a) and (b) twill woven fabric samples cut in diagonal direction (Mért átlag = measured average, Modellkar = model characteristic, Modellgörbe = model curve)

2.3.2. Yarn pulling out tests

In order to examine the shear and friction effects in a more direct way warp yarn pulling-out tests were carried out using a multifunctional appliance, developed at the Department of Polymer Engineering BUTE, fastened on a tensile tester. The tests were performed on 200x200 mm fabric samples at 100 mm/min test speed where the gripped length of the yarn was 200 mm. The results of the yarn pulling out tests are shown in Fig. 2.8 where the dotted thick blue curves show the average. Regarding their variation, they were analyzed in details in [P6, RP4, RP5].

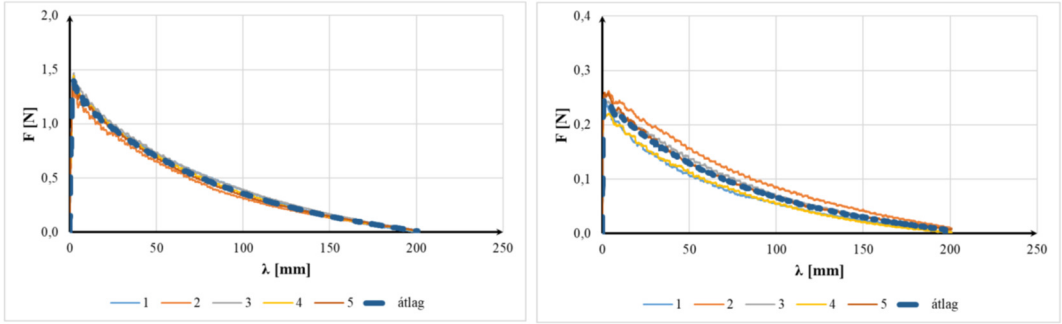

(a) (b)

Figure 2.8 Results of warp yarn pulling-out teste for plain (a) and (b) twill woven fabric samples (átlag = average)

Based on the diagrams in Fig. 2.8 it can be stated that pulling yarn out of the plain sample needs more than 5 times greater resistance force than that of the twill one. This is in accord with the tensile test results obtained in warp direction.

Every curves in Fig. 2.8 shows a decreasing form convex from below that can well be described with exponential function corresponding to the nature of belt friction (Figs. 2.1.c and 2.9) [P6, RP4, RP5]. This needs introducing a new type of ES-bundle denoted by ES3.

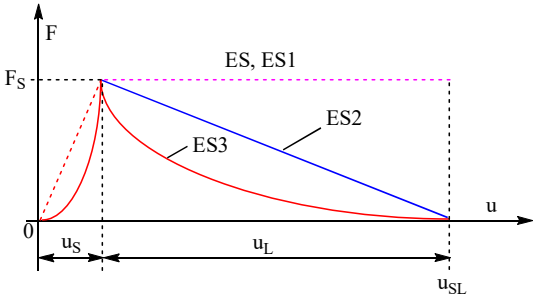

Figure 2.9 Force transmitting during pull-out of a fiber – Friction of Coulomb type: ES, ES1; Resistance of secondary bonds: ES2; Friction of belt type: ES3

2.4. Conclusions

Regarding the results of modeling the tensile test measurements of the woven fabric samples made of glass fiber roving fabrics, it can be stated that the nonlinear E-bundle based FBC models can successfully be used for approximating the measured force-elongation curves including the special convex form of their initial part caused by crimped and/or oblique yarns.
As for the yarn pulling out tests, describing this decreasing exponential process cannot be implemented with the default ES or the special ES1 and ES2 bundles it need to develop a new one denoted by ES3 that has not been found in the FBC set (Fig. 2.9)

Publications: 2 TDK conference papers (2nd and 1st prizes) [P3, P4], 1 MSc Thesis [P6]
Related publications and projects: The results are related to 2 publications [RP4, RP5] and have been utilized by and 1 PhD Thesis project [RP10].

3. Application to Tensile Testing of Composites with Using AE Measurements

Fiber reinforced composites are fibrous materials made of a fibrous reinforcement embedded in a matrix material filling the material space continuously. Therefore, in opposite to the woven fabric studied before, these composites are ***artificial fibrous continuum materials*** hence they are more similar to the human tissues regarding their structure than the unbedded woven fabrics that is a reinforcement only. Consequently, it is worth studying how the nonlinear FBCs can be applied to model the mechanical behavior of composite materials.

3.1. Objectives of FBC Modeling of Tensile Test and AE Measurements

Nowadays one of the most effective non-destructive structural-mechanical tests is the detection and analysis of acoustic emission (AE) signals in materials subjected to mechanical load. The most important objectives of utilizing AE data are to identify, classify, and characterize the different damage or failure modes that can occur e.g. in inhomogeneous materials, such as fiber-reinforced composites and to qualify the fracture mechanical behavior of materials or the structural-mechanical state of machine parts, or health monitoring, as it is usually called.
The AE signal generated by an energy release which is induced by a sudden irreversible local change in mechanically loaded material is a burst type vibration of 30-600 kHz. The local change is usually crazing or micro-cracking. The vibration can be detected with suitable sensors and converted into an electric signal. Based on the data of single AE signals, various statistics can be calculated and plotted, such as the number of hits or cumulative energy versus time, amplitude or energy histograms, or counts versus the amplitude cross-plot.

To detect the different failure modes (crazing, micro-cracking in matrix, debonding between fiber and matrix, pullout or break of fiber, micro-buckling, delamination, propagation of macro-crack), the simplest and conventional method is to analyze changes in the load-deformation relationship obtained by mechanical test and the time domain AE data such as the number of AE events and the maximum amplitude versus time plot and to compare them to each other and to the amplitude histogram and possibly other descriptive statistics.
We developed a statistical fiber-bundle-cells based novel modeling and evaluating method for classifying and characterizing AE signals, which can manage overlaps in histograms or spectrums by the simultaneous decomposition of the stress-strain curve, the cumulative number of AE events and any cumulative statistics of AE descriptors. The fitted FBC model makes it possible to analyze the mechanical reliability of the material and construct a kind of damage map for characterizing the failure behavior. We demonstrate the applicability of this method by evaluating some tensile tests and AE measurements.
Actually, in this case, the aim of FBC modeling is to decompose the measurements corresponding to the different damage modes. This would need different types of nonlinear FBCs but for the sake of simple calculations we used nonlinear E-bundles only.

3.2. Modeling Acoustic Emission Events

3.2.1. Elementary lifetime and the event number process

Le us suppose that the number of the different failure modes such as crazing, microcracking, slippage or breakage of reinforcing fibers and fiber-matrix debonding is r and the material sample can be partitioned in small volume elements belonging to a given failure mode. The total number of volume elements is N. Detection time of the jth AE event of ith type, τ_{ij}, can be regarded as the lifetime of the jth volume element belonging to the ith failure mode (i=1,…,r; j=1,2,…) that is the source of the given AE signal. The detection time values create a stochastic point or event process on the time axis, where the number of AE events in interval (0,t) denoted by $\nu(t)$ is the sum of its components, $\nu_i(t)$ (i=1,…,r), corresponding to the failure modes and this process can be expressed as a cumulative step function determined by the detection times (τ_{ij}). The expected value of the process, $\nu(t)$, can be approximated with the mean ($\bar{n}$) of some (≥1) observed realizations. According to experiences, the mean of this point or event/hit process, Λ(t), changes with increasing strain, which is proportional to the time in the case of a tensile test. In general, in most cases these points signify events, which can be treated as an inhomogeneous Poisson process [F3, E7, RP2]:

$$P(\nu(t) = n) = \frac{\Lambda^n(t)}{n!} e^{-\Lambda(t)} \tag{3.1}$$

where the parameter, $\Lambda(t)$ equals the expected value of $\nu(t)$ and is the integral of the mean point density $\lambda(t)$. In the case of homogenous processes, all the point densities are constant although in general, this does not stand for tensile test measurements of polymers.

3.2.2. Strength characteristics of the failure modes and the event number process

It can be supposed that the sample is built up of N elements, each of which contains a single critical flaw. Ultimate failure occurs when the last still intact element fails determining the lifetime (τ) of the sample subjected to the tensile load. Hence, the lifetime of the sample is determined by the lifetime of elements, which can be identified with the detection times. Their distribution depends on the failure mode. Thus the distribution function of the element lifetime, $Q_{\tau i}(t)$, determines the distribution function of a kind of breaking strain (ε_B) providing the strength characteristics of the i^{th} failure mode and at the same time it gives what fraction

of the volume-elements containing the i^{th} type critical flaws failed in the interval (0,t). Hence the expected value of the number of events can be obtained with by

$$\Lambda_i(t) = E\big(\nu_i(t)\big) = N_i Q_{\tau i}(t) \tag{3.2}$$

Thus, the expected value of the number of AE events is proportional to the weighted sum of the lifetime distribution functions related to the different failure modes. Similarly, the resultant distribution of the signal maximum amplitudes, α_{ij}, can be calculated as a ~~weighted sum defining a~~ mixture of distribution functions $Q_{\alpha i}(x)$ where the weights are $p_i=N_i/N$.

3.3. FBC Model of Damages and Failures

Besides the detected AE signals and the event number process, the recorded stress-strain curve has also got a lot of information about not only deformation behavior but the damage process during the tensile test as well. Based on the relations discussed above, it can be supposed that the stress-strain curve can be decomposed into components corresponding to the failure modes.

It was assumed above that the sample is built up of elements containing critical flaws that fail during the tensile test. The number of such elements is *N* and the ultimate failure of the sample occurs when the last intact element fails. These elements can be regarded as fibers and the interruption of their tensile force transfer caused by fiber break can model the elementary failure that generates an AE signal. Disregarding the last one, an elementary failure does not cause the total failure of the sample, therefore these model-fibers are parallel connected, creating a fiber bundle (Fig. 3.1.a).

Consequently, with the use of the fiber-bundle-cells modeling method, every flaw population can be modeled with a special fiber bundle corresponding to the nature of damage (e.g. fiber breakage: E-bundle, fiber pull-out: ES-bundle, etc.) and the sample can be considered as the parallel connection of these fiber bundles in which the number fractions of the bundle fibers are equal to those of the failure populations (Fig. 3.1.b). In this sense, the measured stress-strain curve is a realization of the stochastic tensile force process.

For simplicity, non-linear E-bundles according can be used, therefore the expected tensile force-load time (the strain or elongation, u, is proportional to the load time, t: $u=vt$; v is the extension rate) curve
was calculated instead of the tensile force-strain one.

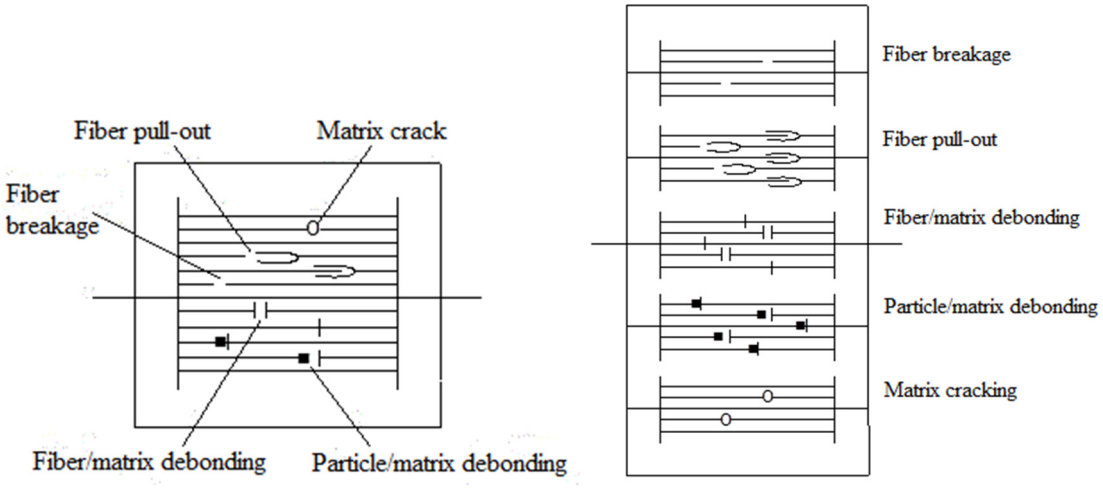

(a) (b)

Figure 3.1 Bundle of fibers representing different failure modes (a) FBC model of fibrous structures for describing deformation and the damage process (b)

3.4. Determining the FBC Parameters

For the decomposition of the AE number and the tensile force processes, the parameters of the component processes corresponding to the failure modes have to be determined. They can be obtained by minimizing the squared deviation between the measured and model processes:

$$\Psi_n^2 = \int_0^T \left[\frac{\bar{n}(t)}{\bar{n}(T)} - \sum_{i=1}^r p_i Q_{\tau i}(t; b_i)\right]^2 dt \to min \tag{3.3}$$

$$\Psi_F^2 = \int_0^T [\bar{F}(t) - \sum_{i=1}^r p_i \kappa_i(t; c_i)(1 - Q_{\tau i}(t; b_i))]^2 dt \to min \tag{3.4}$$

$$\Psi_w^2 = \int_0^W \left[\hat{Q}_w(x) - \sum_{i=1}^r p_i Q_{wi}(x; d_i)\right]^2 dx \to min \tag{3.5}$$

where $\bar{n}(t)$, $\bar{F}(t)$, and $\hat{Q}_w(x)$ are the measured event-number, the tensile force and the amplitude or energy histogram, while p_i, $Q_{\tau i}$, κ_i, Q_{wi} are the weight, the life-time distribution function, the tensile characteristic, and the amplitude or energy histogram of the i^{th} bundle, respectively, and b_i, c_i, d_i are parameter vectors to be determined from fitting. It should be noted that in general, it may be important to recognize the known sequence of the possible failure modes as a condition for fitting, which can be formulated as a series of relation for the expected value of the life times (or strength):

$$E(\tau_1) \le E(\tau_2) \dots \le E(\tau_r) \tag{3.6}$$

A linear combination of a homogeneous linear function and a finite exponential function can be applied to the mathematical form of the tensile characteristics of components. It has only three parameters, yet it can model tensile characteristics with a convex or concave initial part as well.

In general, the damage or failure processes are governed by the minimum strength properties of the building elements, hence the Weibull type of two parameters (b_{1i}>0, b_{2i}≥1) can be used as the distribution function of the lifetime (τ_{ij}).

3.5. Analysis by Reliability Relations and Damage Maps

In the knowledge of the components, some very informative diagrams can be plotted that characterize the reliability and the damage and failure process of the fiber-reinforced or filled sample.

The partial weighted sums of the component lifetime distributions (Q_{τ}) show the number fraction of failures of different types detected as AE hits at a given time or time-proportional strain load (k=1,2,…,r):

$$0 \le Q_{\tau k}(t; B_k) = \sum_{i=1}^k p_i Q_{\tau i}(t; b_i) \underset{t\to\infty}{\longrightarrow} 1 \tag{3.7}$$

where B_k is the parameter matrix created from parameter vectors b_1,…,b_k. Anyway, $Q_{\tau}(t;B_r)$ can be considered the distribution of the general lifetime (τ) of the sample. The plot of the curves $Q_{\tau}(t;B_r)$ determines time-dependent ranges the vertical section of which gives the number fraction of the failed model fibers at a certain load. A similar plot can be obtained if the partial weighted sums of the component reliability functions (R_i)(k=1,…,r) are calculated:

$$1 \ge R_k(t; B_k) = \sum_{i=1}^k p_i R_i(t; b_i) = \sum_{i=1}^k p_i [1 - Q_{\tau i}(t; b_i)] \underset{t\to\infty}{\longrightarrow} 0 \tag{3.8}$$

Hence $R_r(t;B_r)$ is the general reliability function that provides the number fraction of i^{th}-type fibers intact at the given load.

Besides the number of the intact fibers, their resistance force is taken into account as well, as the component tensile force-time relationships are applied as follows (k=1,…,r):

$$0 \le F_k(t; B_k) = \sum_{i=1}^k p_i F_i(t; b_i, c_i) = \sum_{i=1}^k p_i \kappa_i(t; c_i)(1 - Q_{\tau i}(t; b_i)) \underset{t\to\infty}{\longrightarrow} 0 \tag{3.9}$$

Eq. (3.7) can be normalized with the total sum of the components when k=r. This ratio is the estimation of the fractions of the AE event number in the model, which characterizes the damage modes (k=1,…,r):

$$0 \le P_k(t;B_k) = \frac{\sum_{i=1}^{k} p_i Q_{\tau i}(t;b_i)}{\sum_{i=1}^{r} p_i Q_{\tau i}(t;b_i)} \underset{t\to\infty}{\longrightarrow} 0 \tag{3.10}$$

The normalization of Eq. (3.9) by the resultant tensile force gives the ratio of the tensile force components as a fraction of the resultant force at the current time (strain load). (k=1,…,r):

$$0 \le P_{Fk}(t;B_k) = \frac{\sum_{i=1}^{k} p_i F_i(t;b_i,c_i)}{\sum_{i=1}^{r} p_i F_i(t;b_i,c_i)} = \frac{\sum_{i=1}^{k} p_i \kappa_i(t;c_i)(1-Q_{\tau i}(t;b_i))}{\sum_{i=1}^{r} p_i \kappa_i(t;c_i)(1-Q_{\tau i}(t;b_i))} \underset{t\to\infty}{\longrightarrow} 1 \tag{3.11}$$

P_{Fk} characterizes both the current resistance of the sample and the failure process as well because it expresses the tensile force fraction of the fibers intact at the current time.

The curve families create a kind of failure map where the ranges between the curves characterize the participation of the components and the failure processes represented by them. This is vividly descriptive when the curves R_k, P_{Fk} or P_k (k=1,…,r), providing percentages are used.

3.6. Application to Glass Fiber Reinforced PP Composites

Figure 3.2 shows the results of the tensile test and AE measurements, which are the tensile force vs. time (vertical blue dotted line indicates the force peak) and the AE event number vs. time records.

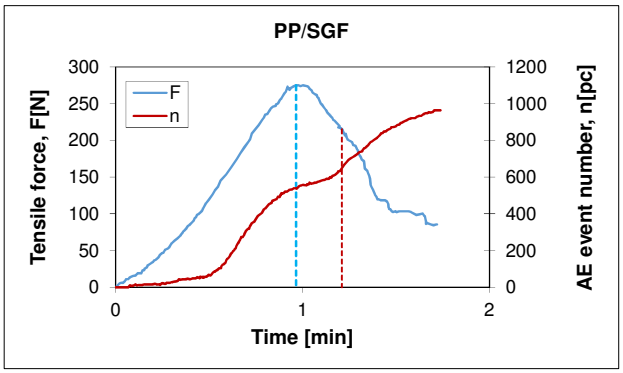

Figure 3.2. Measured tensile force-time curve and cumulative event number process of PP composite reinforced with short glass fibers

The results of the decomposition of the AE event number (n) and the tensile force (F) vs. time (t) processes can be seen in Fig. 3.3. The relative mean squared error (MSE) was less than 4.3% in every case regarding both the event number (MSE(n)) and the tensile force (MSE(F)).

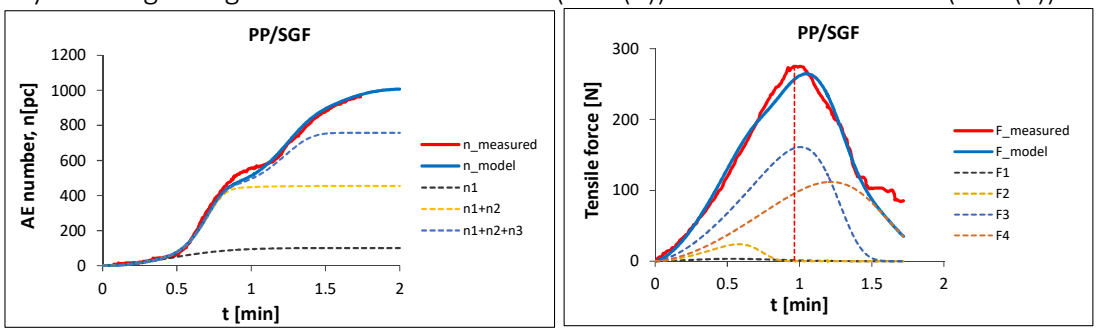

(a) (b)

Figure 3.3 The measured and modeled cumulative event number process (a) and tensile force-time curve (b) of the PP/SGF composite

Fig. 3.4 shows the reliability function and its components belonging to the four damage modes (D1,…,D4) at different load times calculated by using Eq. (3.8).

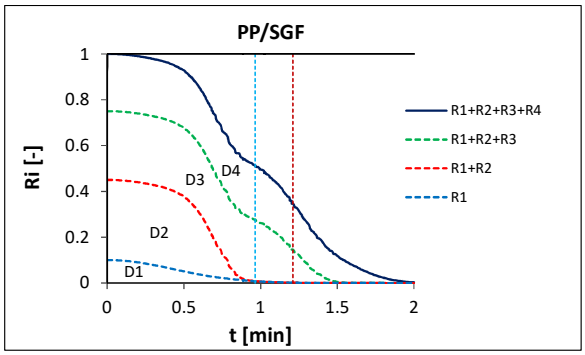

Figure 3.4 The component and resultant reliability functions of the PP/SGF composite sample belonging to different damage modes (D*i*) as a function of load time

Fig. 3.5.a shows the calculated fractions of the AE events given by Eq. (3.10) while Fig. 3.5.b shows the fractions of the component and resultant force resistances according to Eq. (3.11) provided by the intact model fibers belonging to the different damage modes.

It is observable in Fig. 3.5 that although the damage of fibers of D1 and D2 types (matrix failures and debonding) lasts during the test (Fig. 3.5.a), their resistance becomes essentially negligible beyond the peak time related to that of fibers of D3 and D4 types representing the slippage and breakage of fibers (Fig. 3.5.b).

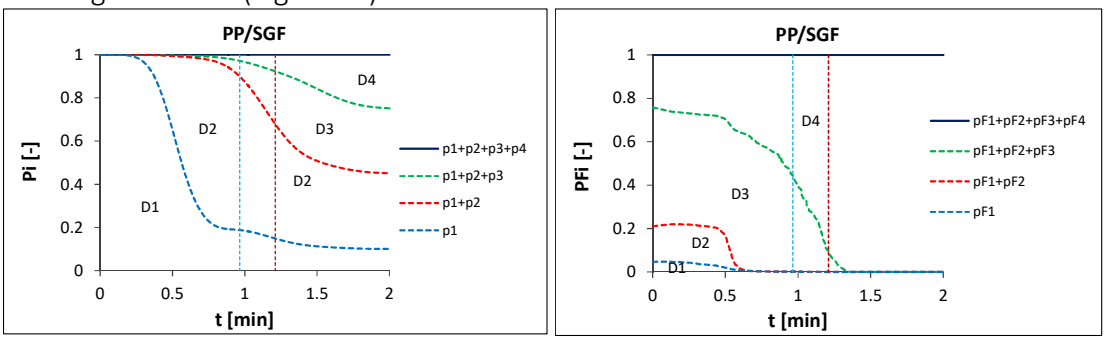

(a) (b)

Figure 3.5 Fraction of AE event number (a) and force resistance (b) belonging to different damage modes (Di) as a function of the load time

Probability distributions of signal amplitude and energy are characterized by the frequency histograms in Fig. 3.6 measured up to the time t_{AE}=0.7·T (beyond the force peak) and the probability density function of the fitted components in Fig. 3.7.

Fitting could be carried out with small relative mean squared error (MSE<2.3%) and according to the khi-squared test, the agreement between the measured and modeled histograms is highly acceptable (amplitude: p-value=0.411, energy: p-value=0.810) (Figs. 3.6, 3.7).

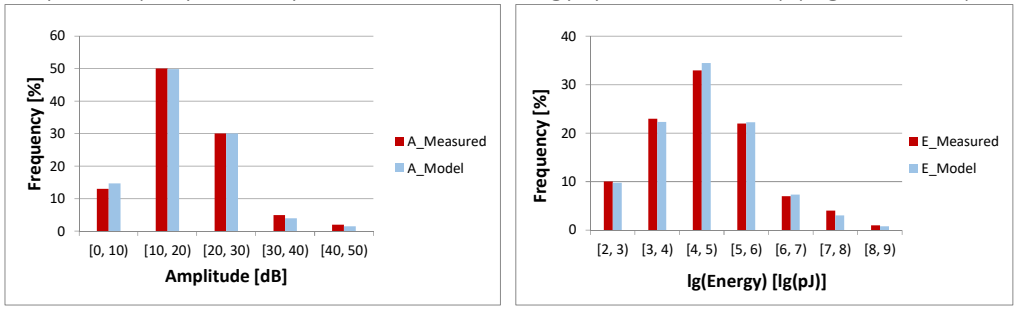

(a) (b)

Figure 3.6 Signal amplitude (a) and energy (b) histograms measured and modeled for the PP/SGF composite

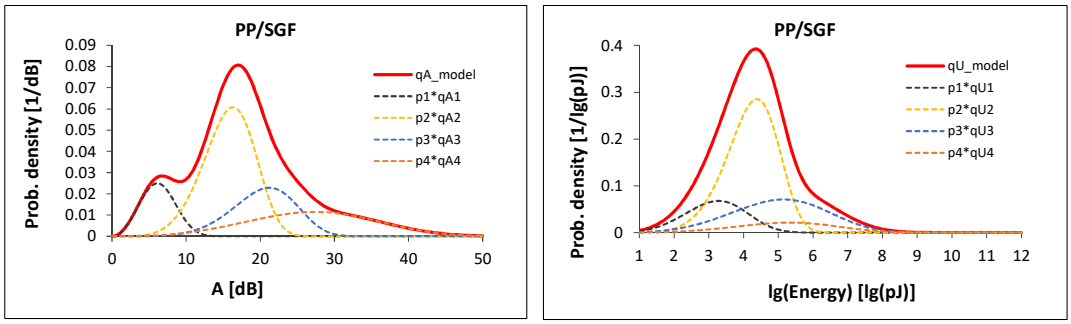

(a) (b)

Figure 3.7 Fitted probability density functions of the signal amplitude (a) and energy (b) and their components for the PP/SGF composite

3.7. Application to Wood Fiber Reinforced PP Composites

Injection molded wood fiber reinforced PP composites, without and with a coupling agent were tested under tensile load and simultaneously AE measurement data were recorded and the results can be seen in Fig. 3.8. In this case, the number of the components representing different damage modes was five (r=5) because the expected value process of the FBC model used represents continuous damage and the measured tensile force vs. time curves with a broken end indicating a sudden fracture need a closing part realized by the fifth component (Figs. 3.9 and 3.10).

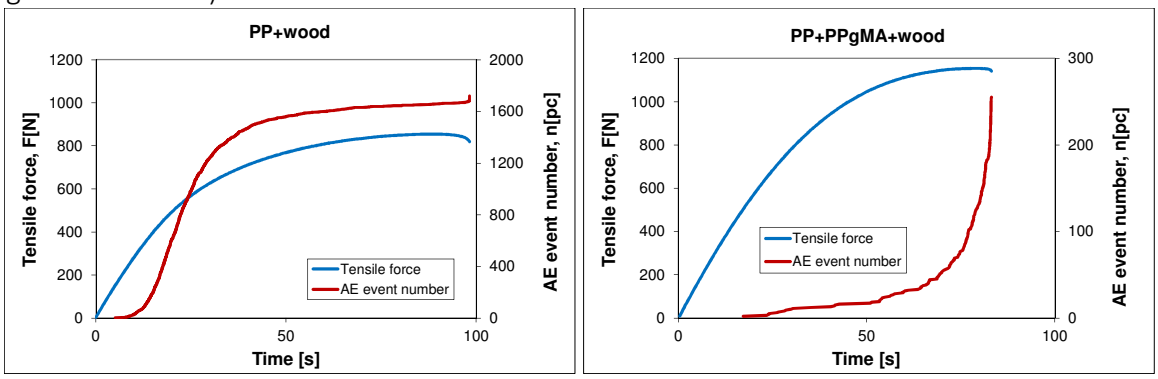

(a) (b)

Figure 3.8 Tensile force-load time curve and cumulative event number process of PP/wood composite without (a) and with a coupling agent (b)

Otherwise, linear tensile characteristics were used for the force components (c_{1i}>0, c_{2i}=c_{3i}=0, i=1,…,5 in Eq. (1.6)) since the initial part of the force-time curves could be approximated with a homogeneous linear relationship.

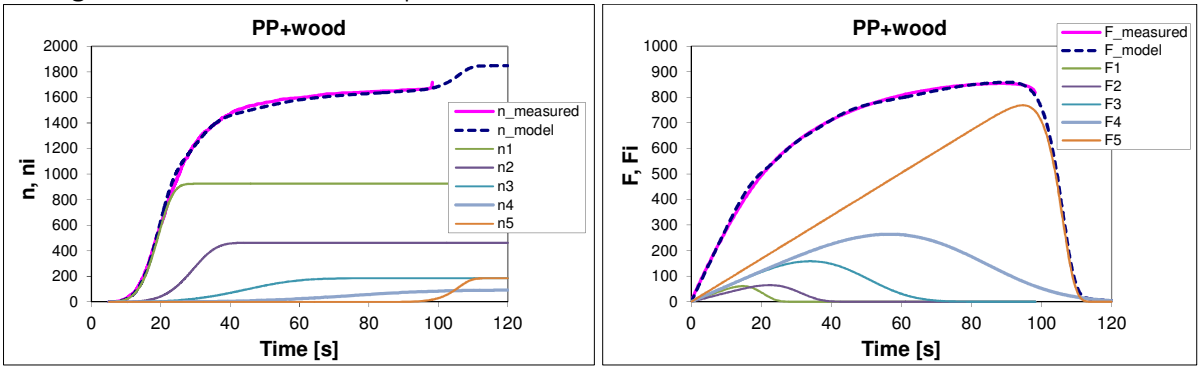

(a) (b)

Figure 3.9 Measured and modeled cumulative event number process (a) and tensile force-time curve (b) of PP/wood composite without a coupling agent

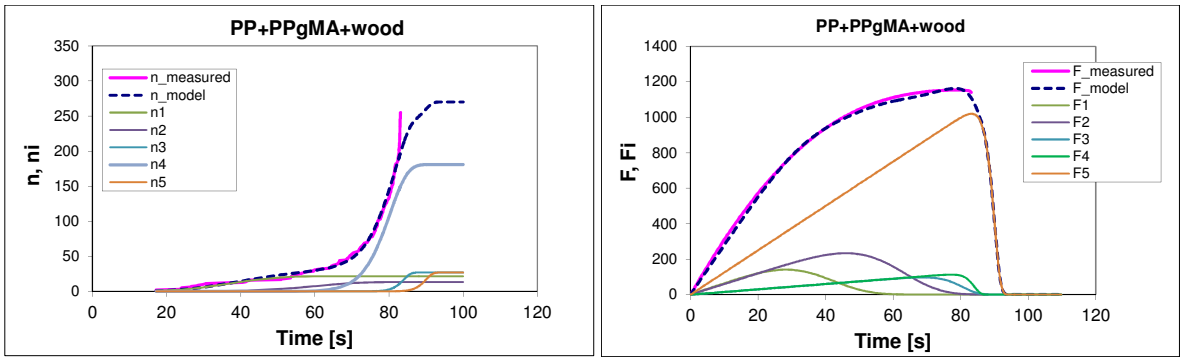

(a) (b)

Figure 3.10 Measured and modeled cumulative event number process (a) and tensile force-time curve (b) of PP/WF composite with a coupling agent (PPgMA)

The relative mean squared error of the FBC model fitting was less than 1.7% in three cases while it was ~4% in the fourth case, where the AE event number increased suddenly at the end of measurement, closed by a sudden breakage, which was not modeled since it was just a single phenomenon to be averaged for the expected value model used (Fig. 3.10.a).

The comparison of the mechanical behavior of the two composites is performed by calculating the components and the resultant of the reliability functions (Fig. 3.11) and weighted resistant forces (Fig. 3.12). The vertical dotted black lines in Figs. 3.11 and 2.12 indicate the peak value of the measured tensile force (t^*). In the composite sample without a coupling agent (Fig. 3.11.a), at lower loads the matrix damages (D11) and debonding (D12) determine the damage process, then the reliability, which is the number of the intact elements (model fibers), quickly decreases while at higher load the slippage (D13) and breakage (D14) of fibers dominate before ultimate failure. As opposed to that, in the case of the composite treated with a coupling agent (Fig. 3.11.b), fiber-based damage (D23-D25) governs the whole deformation and damage process producing far higher reliability.

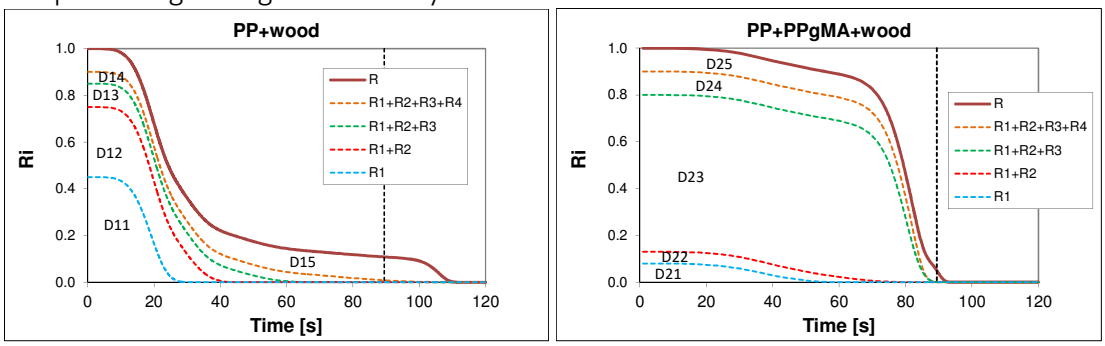

(a) (b)

Figure 3.11 The fraction of different damage modes (D*ji*) vs. the time of PP/WF composites without (a; *j*=1) and with (b; *j*=2) a coupling agent (PPgMA)

Fig. 3.12 shows the variation of the component fraction of the AE event numbers as a function of load time according to Eq. (3.10), confirming the statements above. The component fraction of the AE event number can also show in itself the difference in the mechanical behavior of the two composites since, as Fig. 3.12 indicates, in the case of the composite without a coupling agent (Fig. 3.12.a), there are four significant damage modes (D11-D14) before the force peak, while the use of this agent (Fig. 3.12.b) decreases the number to three (D21-D23), although in the latter case the third damage mode (D23) dominates the AE event process around the force peak. In both cases, the fifth component (D15, D25) modeling the ultimate failure of the remaining intact part of the sample plays a virtual role appearing beyond the force peak only.

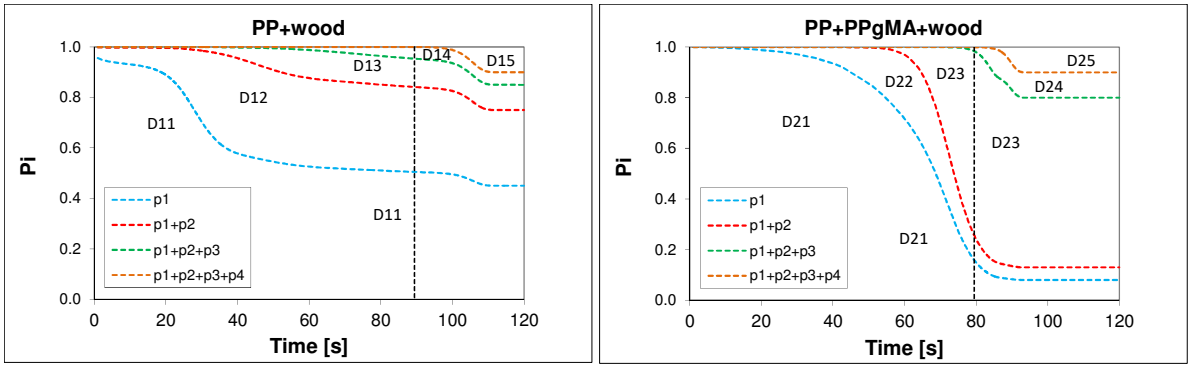

(a) (b)

Figure 3.12 The fraction of different damage modes (D*ji*) vs. the time of PP/WF composites without (a; *j*=1) and with (b; *j*=2) a coupling agent (PPgMA)

3.8. Conclusions

In general, the main objective of AE assisted mechanical tests is to identify and determine the strength properties of the different failure modes characterizing the material and the loading mode.

The presented fiber-bundle-cells (FBC) based modeling method can evaluate a simultaneous tensile test and AE measurements. It makes it possible to decompose the measured tensile force and AE event number processes and to determine the number fraction of the components obtained and the distributions of their strength, that is, the load levels where the micro-failures occur, and the amplitude and energy of the AE signals generated by the micro-failures. In addition, the number fraction of the AE events generated by different failure modes can be calculated as a function of the load time, providing a failure map characterizing the mechanical behavior and the load bearing ability of the material tested.

All this was demonstrated by the compact tension (CT) testing of short fiber reinforced VERTON PP sheets as well as injection molded wood fiber reinforced PP composites, without and with a coupling agent and the results proved the applicability of the FBC modeling and evaluation method proposed. The reliability functions and the failure maps seem to give important and comprehensive information on the mechanical behavior and the damage process of the samples subjected to tensile load.

Evaluation can be improved with the use of multivariate statistical methods, such as cluster analysis, to assess the number of significant damage modes without performing structural investigation on the samples at different tensile loads or after fracture.

Publications: 1 paper in impact factor periodical JCM [P2]

Related publications and projects: The results have been utilized by 3 PhD Thesis projects [RP8-RP10].

4. Application to Testing Human Tissues

4.1. Introduction

In order to demonstrate the applicability of the modeling and evaluation methods, samples of human facial nerves and tendons were tested, modeled and analyzed by decomposing single

measurements by slicing the load-strain curve and modeling by nonlinear E-bundles. The concept of breaking strain or lifetime spectrum was introduced.

4.2. Materials and Tensile Test Results

Human facial nerve samples

The tensile tests were performed with a Zwick Z005 computer-controlled tensile tester with custom grips, where the nerves were rigidly fixed on steel slit rods. Test speed was 10 mm/min. In Fig. 4.1.a, the arrangement of the tensile test of some facial nerves (Tab. 4.1) of a 59-year-old man (Fig. 4.1.a) can be seen, while Fig. 4.1.b shows the results. Tab. 4.2 contains the geometrical and mechanical data of the specimens.

Code	Explanation
VII	Nervus facalis
VII_LS_TB	VII, left side, temporal branch
VII_LS_ZB	VII, left side, zygomatic branches
VII_LS_BB	VII, left side, buccal branches
VII_LS_MB	VII, left side, mandibular branches
VII_LS_CB	VII, left side, cervical branch

Table 4.1 Identity codes of facial nerves tested

Type of nerve	Short code	L [mm]	l_0 [mm]	l_1 [mm]	t_0 [mm]	T_0 [mm]	t_1 [mm]	T_1 [mm]	F_{max} [N]
Left side VII_LS	TB	32	8	17	2.90	4.50	2.31	2.42	1.23
	ZB	24	4	24	1.46	2.69	1.06	1.11	0.06
	BB	48	24	38	1.37	2.64	0.65	0.77	8.01
	MB	40	11	37	1.93	3.17	0.98	2.07	0.23
	CB	34	6	12	0.98	1.70	0.62	0.68	1.21

Table 4.2 Geometrical and tensile test data of the left side facial nerves (nervus facialis) (L: length of the nerve, l_0: gauge length, l_1: length after test measured in the grips; t_0 and t_1: mean thickness without epineurium before and after test, T_0 and T_1: mean thickness with epineurium before and after test; F_{max}: maximum tensile force)

The force-elongation curves in Fig. 4.1.b are significantly different, hence averaging them point by point would not give a reasonably usable result for modeling or analyzing. Therefore, both their evaluation and modeling are to be performed on the individual measurements.

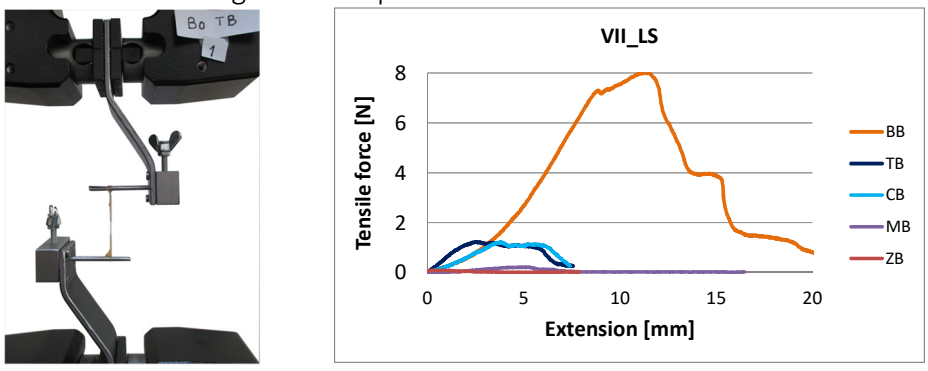

(a) (b)

Figure 4.1 Arrangement of the tensile test of human facial nerves (a) and the results (b)

For modeling and analysis, the facial nerve sample Code BB was selected because of its large bent initial part convex from below and structured failure process containing interesting peaks and drops.

Tendon samples

Before tensile testing, the prepared human cadaver tendon samples (harvested within a maximum of 24 hours post mortem, stored at -80°C in a radio-protectant solution and subjected to 42 kGy dose virucidal gamma irradiation) were subjected firstly to a static load of 50 N for 30 seconds and after that, a fatigue load of 2000 tensile cycles. The applied waveform was sinusoidal, with a force between 50 N and 250 N, and at a frequency of 2 Hz. The tensile testing of the samples was performed on an INSTRON 8872 servo-hydraulic tester (maximum load 25 kN, gripping mode: freezing jaws) with a constant extension rate of 20 mm/min. Before the test, the samples were pre-tensioned by a tensile load of 150 N at this rate, in order to eliminate possible gripping errors. In Fig. 4.2, the arrangement of testing and the graphical results of the tensile test of some tendons after fatigue are depicted while the numerical data can be found in Tab. 4.3. Similarly, as above, the tensile force-elongation curves are significantly different, thus it is reasonable to carry out modeling on single measurements.

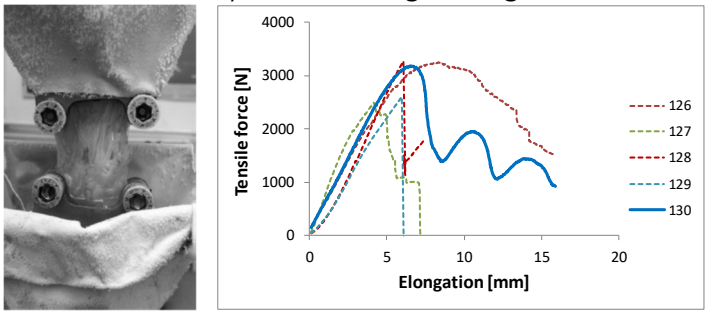

Figure 4.2 Arrangement of the tensile test of tendons (a) and the results (b)

Code	Type	Width [mm]	Thick-ness [mm]	Gauge length [mm]	Fmax [N]	Elong. at Fmax [mm]	Tensile stiffness [N/mm]	Breaking elong. [mm]
126	Quadriceps	15	2	50	3251	8.5	564	15.8
127	Semit.+Grac.	9	3		2487	4.2	830	7.2
128	Tibialis ant.	9	3		3268	6.1	654	7.4
129	Perosn. long.	9	3		2598	6.0	536	6.1
130	Achilles	16	2		3179	6.6	562	15.9

Table 4.3 Geometrical and tensile test data of the human tendons tested (Semit.+Grac.=Semitendinosus + Gracilis, ant.=anterior, Perosn. long.=Perosneus longus)

For modeling and analysis, tendon sample Code 130 was selected because of its specially structured failure process showing three large separated peaks.

4.3. FBC Modeling of the Test Results

Two modeling methods were used based on fiber bundles. One included parallel-connected nonlinear FBCs of different types (E, EH, ES, and ET) and the other was the parallel connection of a series of nonlinear E-bundles. In modeling, the elongation or strain at break was assumed to be of normal distribution. The goodness of approximation was characterized by the absolute squared error (denoted as Difference in FiberSpace) or the relative mean squared error (RMSE) and the determination coefficient (R^2). RMSE is the square root of mean difference related to the maximum measured force at the given scaling, while R^2 is the squared value of the linear correlation coefficient between the modeled and measured force values.

4.4.1 Modeling the tensile behavior of a human facial nerve

4.4.1.1. Decomposition into nonlinear FBCs

As mentioned above, the tensile test result of the left side facial nerve code BB was modeled and analyzed with the aid of the FiberSpace software.

The first step before creating an FBC model is the normalization of the measured force-elongation curve, which needs the normalizing parameters. For example, they can be estimated by fitting a simple shifted linear E-bundle to the measured data, as shown in Fig. 4.3, where the tensile characteristic was approximated by the inflection tangent of the rising part (its equation is y=4.65+1.3(x-6.61)). From fitting the linear E-bundle (a=0), we obtained that E(ε_B)≈ε_N=12.80 mm and the tangent gave at this place that E(F_B)≈F_N=12.69 N, hence the shifting of the E-bundle response came at about 3.03 mm.

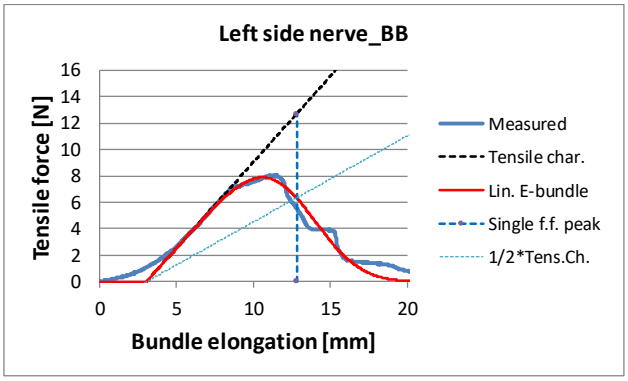

Figure 4.3 Tensile force vs. bundle strain curve of the facial nerve modeled by shifted linear (a) and nonlinear (b) E-bundles

Fig. 4.4 shows the final approximation (red) of the measured and normalized force-elongation relationship (green) obtained by FBC modeling in the FiberSpace environment, together with the sine and cosine Fourier amplitudes as parameters (olive and green columns of the measured sample, and purple and blue columns of the approximating FBC), which were stored in the learning process of the software. The goodness properties of approximation were RMSE=3.39% and R^2=0.988.

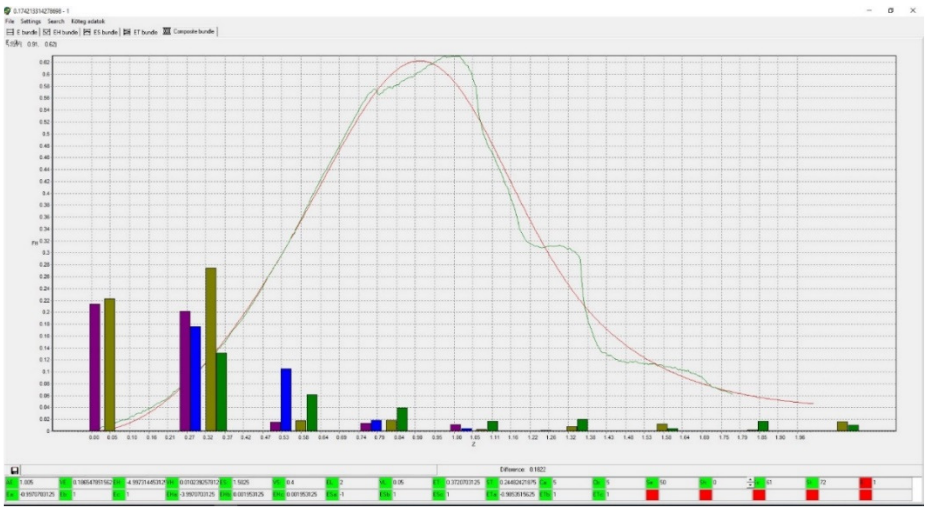

Figure 4.4 The result of seeking the best approximation by FiberSpace: the normalized measured (green) and modeled (red) curves

Fig. 4.5 shows the component curves belonging to FBCs and the parameters are summarized in Tab. 4.4. The tensile characteristic parameters of all the fibers were the same (a=-1, b=1, c=1) while ET contraction parameters were Ca=Cb=5, meaning a very strong contraction by the reduction of the free volume among fibers. An ideal normalization leads to AE=1.0. Here a bit

of correction was carried out by FiberSpace (Tab. 4.4). In this case, the fiber tensile characteristics found by fitting have a large initial curved part (b<0), hence the EH-bundle, which models the effect of the crimped or loose fibers, was not needed, therefore FiberSpace cancelled it by giving it zero weight. According to the results in Table 4.4, only about 27% of the fibrils creating the facial nerve behave like well-aligned and ideally gripped fibers (E-bundle), while 73% can be considered oblique (ET-bundle) or not ideally gripped (ES-bundle) fibers. Moreover, mean obliquity is not zero (ET=0.37), meaning that the oblique fibers may be aligned following a kind of spiral.

Regarding the ES-fibers, both the mean slippage threshold (ES=1.5) and the mean slippage length (EL=2.0) are high, hence the majority of this type of fibers break.

FBC code	w%	AE	VE	ES	VS	EL	VL	ET	ST
E	27.3								
ES	33.3	1.01	0.19	1.50	0.40	2.00	0.05		
ET	39.4							0.37	0.25

Table 4.4 Parameters of the nonlinear FBC model of the facial nerve BB

In Fig. 4.5.a, the weighted component curves can be seen, while in Fig. 4.5.b, their sum gives a map regarding their participation in the resultant resistance force. Fig. 4.6 shows the reliability map of the components and their sum computed with Eq. (3.8), which shows a division similar to that in Fig. 4.5.b.

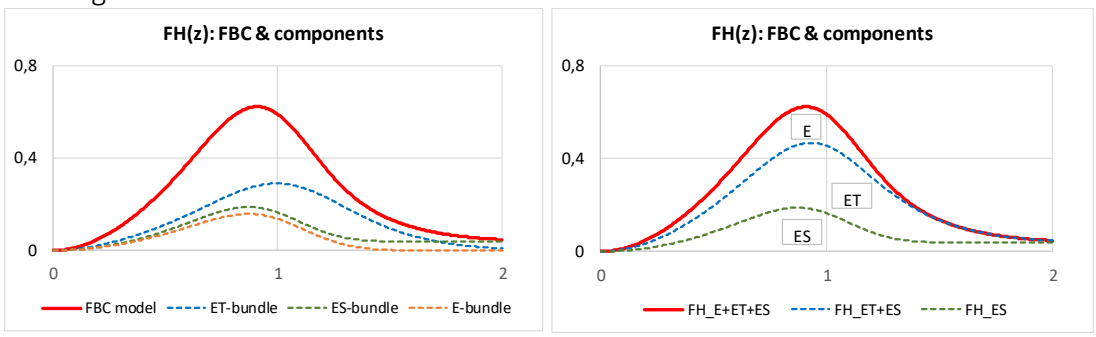

a) (b)

Figure 4.5 Normalized results of modeling the facial nerve BB: FBC components (a), and the map obtained by adding them (b)

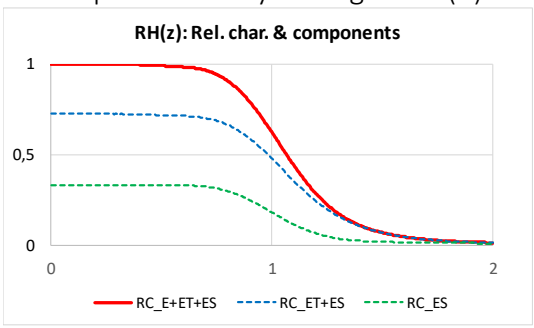

Figure 4.6 Reliability characteristic of the facial nerve BB and its components

On the basis of Fig. 4.5, it can be stated that the fraction (27, 33, 40%) and role of the FBCs as subbundles created by ideal (E), oblique (ET) and slipping (ES) fibers in the force response are essentially similar considering the resistance force and so is their role regarding reliability (Fig. 4.6). Yet, the overall significant role of the oblique fibers should be stressed, except for very large deformations, where the slipping fibers of the ES-bundle dominate mechanical behavior.

4.4.1.2. Decomposition into a series of nonlinear E-bundles

According to Fig. 4.4, the FBC model curve gives a rather good mean profile, but it does not follow the strongly structured failure process of such a single measurement. Based on the

parallel connection of a series of E-bundles, the force response of which is in a simple product form as it is discussed in Chapter 1.4, the measured force-elongation curve can be approximated with the sum of the component responses (Fig. 4.7.a). All this results in a decomposition of the measured profile into small parts as well as the area below the measured curve into 'slices' bounded by the tensile characteristics of the E-bundle components (Fig. 4.7.b). Hence, this operation is a kind of slicing and layering decomposition, where sectioning and layering can follow both the different arcs in the rising part and the peaks and drops in the falling part of the measured single curve.

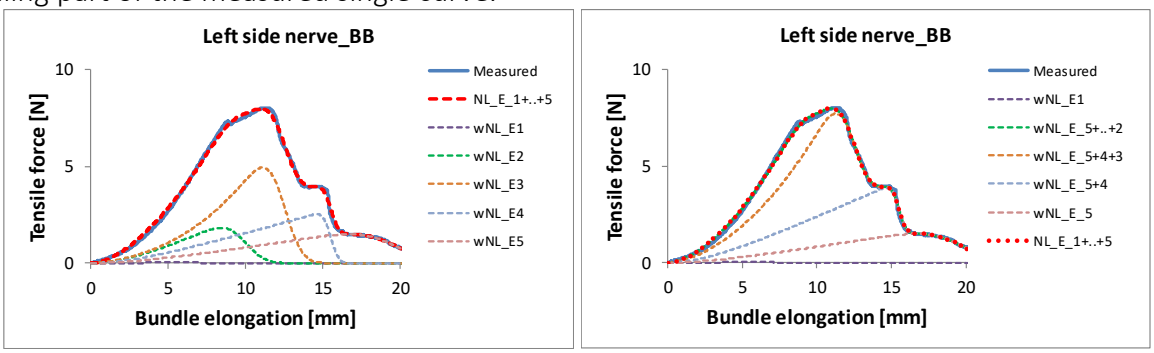

(a) (b)

Figure 4.7 Modeling of the facial nerve Code BB with a series of E-bundles: the weighted component responses (a), and the map obtained by adding them (b)

In this case, decomposition leads to five E-bundle components as can be seen in Fig. 4.7. Their parameters are summarized in Tab. 5. Because of the better approximation, the goodness properties improved significantly (RMSE=1.64%, R^2=0.9974) compared to those of the general FBC model.

Analyzing the data in Tab. 4.5 reveals that the values of parameter b are positive in four cases but it is negative in the case of component 3, meaning a steep exponential tensile characteristic. Moreover, this bundle is dominant because it describes the largest drop in force, thus it has the maximum weight (41%). The use of this kind of bundle is necessary since the initial part of the measured curve has a large curved part (convex from below) and the E-bundles cannot describe that with the fiber tensile characteristic given by Eq. (1.6) if parameter b is positive, in contrast to the general FBC model, which can include an EH-bundle containing wavy or crimped fibers.

Component code	w [%]	a [N]	b [1/mm]	c [N/mm]	K_0 [N/mm]	m [mm]	s [mm]	V [%]
1	3.0	-1.78	0.325	0.58	0	6.0	2.0	33.3
2	30.0	-3.69	0.325	1.20	0	9.8	1.0	10.2
3	41.0	-14.47	-0.095	-1.25	0.13	12.3	0.9	7.3
4	17.0	-4.00	0.325	1.30	0	15.5	0.4	2.6
5	9.0	-4.00	0.325	1.30	0	19.5	1.8	9.2

Table 4.5 Parameters of the E-bundle components

Comparing the component and resultant reliability of the general FBC model (Fig. 4.6) and the E-bundle series model (Fig. 4.8) shows that the significant difference can be observed mainly at larger deformations, where the latter can follow the structured failure process measured.

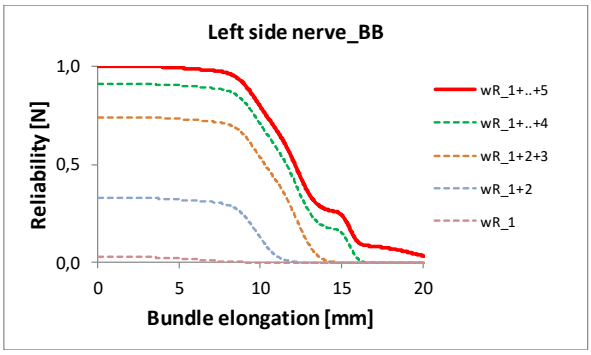

Figure 4.8 Reliability of the E-bundle series model of facial nerve Code BB

Comparing the results of general FBC modeling with those obtained by E-bundle modeling, one can conclude that the former gives a kind of internal description regarding the structural inhomogeneities, while the latter provides a boundary decomposition.

4.4.2. Modeling the tensile behavior of tendons after fatigue

The measured force-elongation curve of the tendon Code 130 has three large bulky peaks, hence we modeled that with the parallel connection of four E-bundles (Fig. 4.9, Tab. 4.6). The good approximation is characterized by RMSE=2.63% and R^2=0.9885.

Three of the components describe the peaks while component 1 models the initial damage and failure events, the scattering of which is the largest (33% in Tab. 4.6). The dominant component is number 2 belonging to the largest peak, hence its weight is 70%. The visible part of the two smaller peaks needed large curved tensile characteristics (Fig. 4.9.b) consequently the *b* values of the corresponding components 3 and 4 became negative (Tab. 4.6).

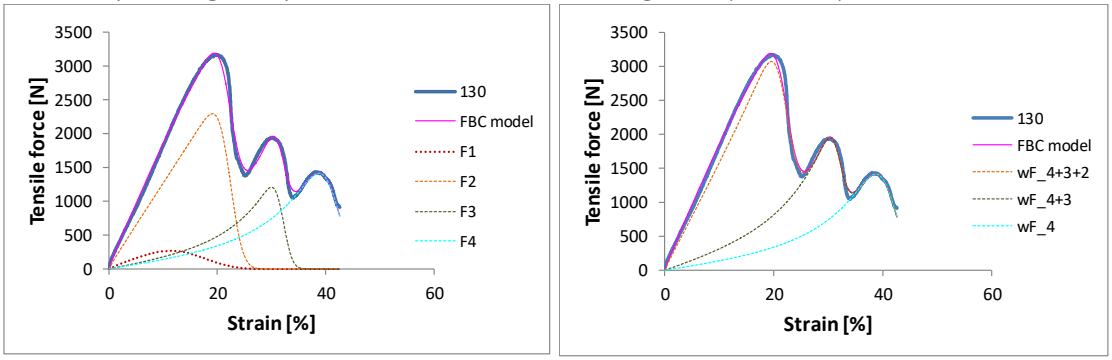

(a) (b)

Figure 4.9 Modeling the tendon Code 130 with a series of E-bundles

Component code	w [%]	a [N]	b [1/%]	c [N/%]	K0 [N/%]	m [%]	s [%]	V [%]
1	16.0	26.5	1.00	28.4	54.9	15.0	5.0	33.3
2	70.0	26.0	1.00	124.4	150.4	22.2	1.8	8.1
3	7.6	-13.5	-0.14	13.5	15.4	31.9	1.3	4.1
4	6.4	-11.4	-0.12	11.4	12.7	41.5	2.4	5.8

Table 4.6 Parameters of the nonlinear E-bundles

Similar relations can be observed regarding component reliabilities (Fig. 4.10). The dominance of component 2 is obvious, while at the same time the last two peaks provide a certain reliability over 25% strain.

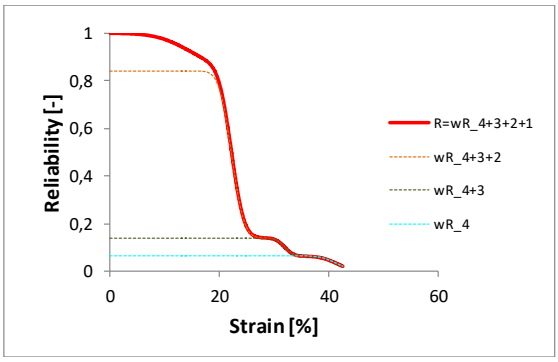

Figure 4.10 The reliability function of tendon Code 130 and its components

4.4.3. Damage spectra of the failure process

The work of viscoelastic structural elements under load without damage or failure can be characterized with the so-called relaxation spectrum (τ), which is a relationship between relaxation time (a sort of reaction time), and the elastic modulus of parallel-connected Maxwell models. This is a kind of density function with a domain of $[0,\infty)$.

Based on the concept established in Chapter 1.4, E-bundle series modeling makes it possible to characterize the damage and failure process of the samples tested, and also the reliability maps, by some relationships of spectrum type that may be called damage spectra. In this case, the mean breaking elongation or strain (m) can play the role of relaxation time according to Eqs. (1.28)-(1.32) while the dependent variable may be the weight (w) or the standard deviation of the breaking strain (s). Nevertheless, it must be taken into account that, all these are based on the conditional expected values and the law of total expectation applied to the tensile force process.

For the sake of comparison, Figs. 4.11-4.13 show together the graphical results of the damage analysis of both human facial nerve BB and tendon Code 130.

The column diagrams in Figs. 4.11 shows the asymptotic tensile stiffness (c) of the fibers characterizing the intact work of the E-bundle components, as well as two damage properties, the mean values (m) and the standard deviation (s) of fiber breaking elongation or strain. The absolute values of facial nerve stiffness (c) increase monotonically (Fig. 4.11.a and Tab. 4.5) with m as opposed to those of the tendon, where the second one is much larger than the others, highlighting its dominance in the tensile force (Fig. 4.11.b). In both cases, the mean breaking elongation or strain increases almost linearly confirming its applicability as independent spectrum variable, while the medium values of standard deviation are smaller than those at the edges (Figs. 4.11.a and 4.11.b).

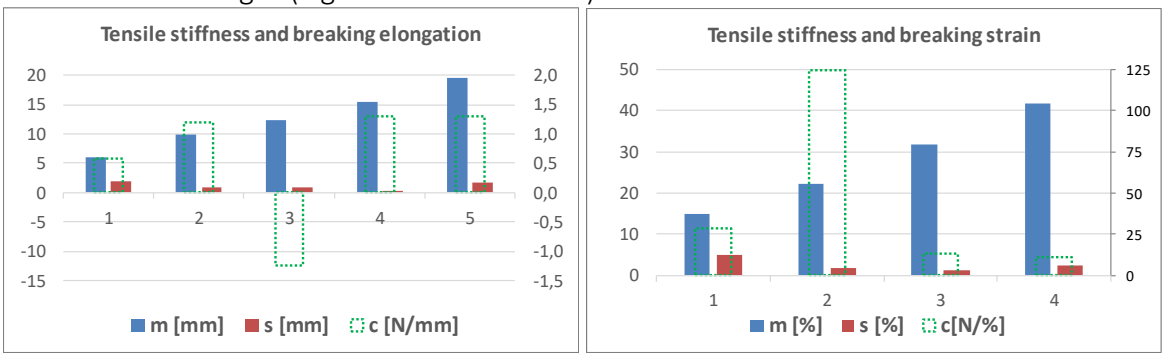

(a) (b)

Figure 4.11 Tensile stiffness (c) and breaking elongation/strain parameters (m, s) of the E-bundle components for facial nerve BB (a) and tendon Code 130 (b)

The latter refers to the form according to the quadratic formula by Eqs. (1.30) and (1.31). Indeed, in Figs. 4.12.a and 4.12.b, the relationship between the mean values and the standard deviation can be seen where the measured values create a discrete line spectrum, which is approximated by a continuous function, $s(m)$, which can be determined by fitting the formula by Eq. (1.30). The minimum point of $s(m)$ belongs to the overall mean value of fiber breaking strain (M). The goodness of fitting was essentially satisfactory (facial nerve: RMSE=11.6%, R^2=0.85; tendon: RMSE=12.2%, R^2=0.82) considering the small amount of data. Also, it can be observed in Fig. 4.12 that the m values can be found about the minimum places or the inflexion point of the derivative of the resultant model tensile force (DF/Du), meaning that they characterize the places of intensive damage.

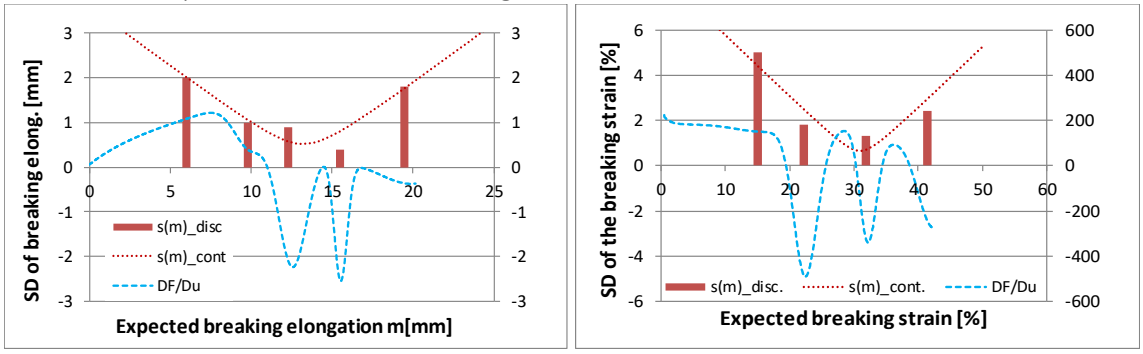

(a) (b)

Figure 4.12 Discrete and continuous damage spectra of facial nerve BB (M=13.22 mm, s_0=0.51 mm, ω^2=0.0723) (a) and tendon Code 130 (M=31 mm, s_0=0.63 mm, ω^2=0.075) (b)

The smaller standard deviation (SD) values are, the steeper changes or drops in the tensile force are modeled by the E-bundle component in question. This can be observed as well when comparing the component density functions of the breaking elongation or strain depicted with dotted lines in Fig. 4.13 to the SD values in Fig. 4.12. These are non-weighted conditional probability density functions that are considered normal with parameters N(m, s^2) and the component weights are indicated by the blue columns. Besides them, in Fig. 4.13, the resultant non-conditional density function, $w(m)$, is plotted with a solid red line, which is assumed to be normal with parameters N(M,S^2). The expected value, M, is the same as in Fig. 4.12, but the standard deviation, S, was estimated to satisfy the next condition related to the mean breaking strain values of the component (m_i):

$$M - 3S < \min_i m_i < \max_i m_i < M + 3S \tag{4.1}$$

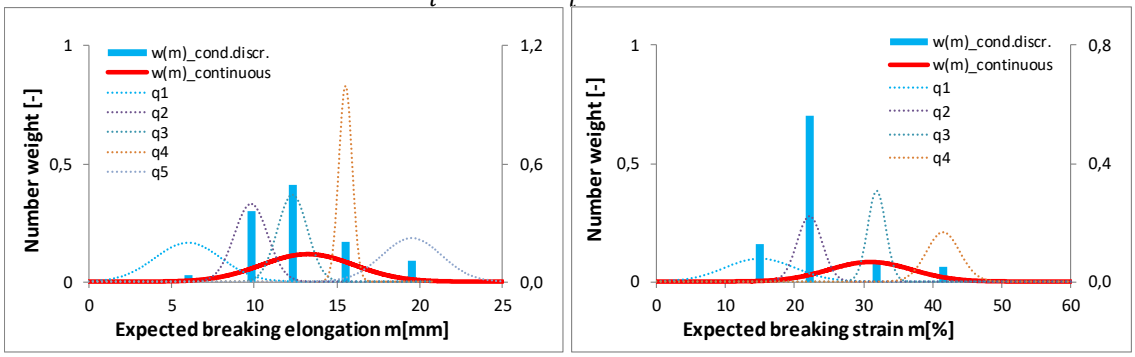

(a) (b)

Figure 4.13 Component weights as well as conditional and resultant number density functions of the fiber breaking strain for facial nerve BB (M=13.22 mm, S=2.8 mm) (a) and tendon Code 130 (M=31 %, S=6 %) (b)

The *S* value estimated in this way can be made more accurate by fitting the integral form according to Eq. (1.29) to the measured force-elongation relationship.

4.5. Conclusions

The idealized statistical fiber-bundle-cells (FBCs) and the modeling method developed are suitable for phenomenological modeling of fibrous structures and make it possible to analyze them on the basis of evaluating measurements and determining the ratio of fibers or their bundles of different geometrical properties. The software FiberSpace uses composite bundles constructed as the parallel connection of FBCs for modeling the tensile load-strain curve of real fibrous structures. The expert system based on Fourier approximation and load-strain curve classes makes it possible to find the best model parameters fast. The system can learn and develop itself by improving mapping and/or establishing new subclasses on the basis of the modeled results.

The two modeling methods developed can be applied as tools in different problems. The use of basic FBCs with the same or different fiber tensile characteristics is based on average mechanical behavior, since in this case, the expected tensile processes are calculated. In this way, the FBC model can reveal some structural details related to statistical inhomogeneities, such as wavy and oblique fibers or weaker connections between fibers and their environment, and the effects of all these problems on mechanical behavior.

However, when a tensile load-strain curve is the result of a single measurement, its modeling and analysis may be performed more advantageously by decomposition based on a series of E-bundles.

The long-range aim of this work would be the application of the statistical FBC model as material law in the finite element simulation of fibrous structures of real geometry, subjected to real mechanical load.

Publications: 1 article submitted to impact factor periodical [P7] and 1-2 other papers are expected to be published in impact factor periodicals.

Related publications and projects: The results have been utilized by 5 Thesis projects [RP6-RP10].

5. Application to FEM Simulations in ANSYS[6] Environment

5.1. Introduction

Up to now the fiber bundles are one or two dimensional structures which are composed of independent theoretical fibers or fiber-like composite elements, hence they are not continuum but discrete models. Therefore, firstly we have derived the properties of the three dimensional fiber bundles and formulated the relationships between the deformations of the fibers and their vicinity including the damages such as slippage and breakage.

Then, we have worked out a continuum layer model where the fibers are embedded into the matrix material and besides the fiber breakage and pull-out or slippage, the stochastic matrix cracks and fiber/matrix debonding can be taken into account as well. In the next period, after testing the embedded FBC model in simple theoretical cases, its applicability to FEM simulation will be verified in the case of tensile testing of human tissues.

[6] https://www.ansys.com/

As the **first results of the cooperation** between the Departments of MOGI and PT, a FEM model was developed for simulating the deformation and fracture process of a human tendon sample based on the concept of the non-linear E-bundle modelling. Because of the problems caused by the decreasing stiffness and the breakages, the rupture was approximated by a **bilinear debonding process** using the Cohesive Zone Method and randomized fiber stiffness. These results were presented at the TDK Conference 2019. In addition, we **showed** that the expected stress-strain process of the non-linear E-bundle is the generalization of the bilinear debonding process hence in the next period an advanced simulation model will be developed. The FBC models used up to now assumed that the strain increases in each bundle and model fiber. However, in a FEM model the damage or failure in an element can cause decreasing or alternating strain in some others having reduced stiffness by earlier damage. Moreover, the FBCs as representative volume element or material model may be subjected to compressive load. We proved that both phenomena can also be described by the non-linear E-bundles when **using minimum-preserving reliability** functions and based on them the nonlinear E-bundle based model can be extended to multiaxial loads as well.

5.2. Elastic and Viscoelastic Anisotropic Material Model for Multiaxial Load

Up to now, the FBCs used in our practice have been built up of linear or nonlinear elastic fibers they have been applied to model the mechanical behavior of simple fibrous samples subjected uniaxial tensile load.

However, in general the polymers and the real human structures behave as viscoelastic materials, on the other hand, they should be treated as 3D structures subjected to multiaxial load as it is needed for FEM simulations. In addition, the real load may alternate with time as well.

The concept of developing material models corresponding to the requirements above are based on the analogy between linear systems and the interpretation of the FBCs as special representative volume elements (RVE).

5.2.1. Analogy between the linear elastic and the linear viscoelastic behaviors

5.2.1.1. Mechanical behavior without damage or failure

In general, the mechanically linear material sample is regarded as a linear input/output system where the relationship between the input as stimulus (X) and the output as response (Y) can be given by a linear operator (A) [E1, E7]:

$$Y(t) = AX(t) \tag{5.1}$$

where X and Y are any of the deformation and stress and they are time dependent functions while A has got an integral form. The system can be given by a linear differential equation (system) as well.

Considering uniaxial tensile or simple shear deformation (ε or γ) or stress (σ or τ) load, the responses of the linear elastic (LE) and the linear viscoelastic (LVE) materials are calculated by using the Hooke's law and the fundamental equations of the linear viscoelastic theory provided by Boltzmann's superposition principle, respectively [E1, F2, F11]:

$$X = \varepsilon;\ \ LE\colon\ \sigma(t) = E\varepsilon(t) \quad \leftrightarrow \quad LVE\colon\ \sigma(t) = E(t) * \dot{\varepsilon}(t) = \int_0^t E(t-t')\,\dot{\varepsilon}(t')dt' \tag{5.2}$$

$$X = \gamma;\ \ LE\colon\ \tau(t) = G\gamma(t) \quad \leftrightarrow \quad LVE\colon\ \tau(t) = G(t) * \dot{\gamma}(t) = \int_0^t G(t-t')\,\dot{\gamma}(u)dt' \tag{5.3}$$

where E and G are the tensile and shear moduli, as well as E(t) and G(t) are the tensile and shear relaxation moduli, respectively, while t' is the running time variable, as well as '$*$' and '$\cdot$' denote the operations of the convolution multiplication and the time derivative, respectively. If E(t) and G(t) are constants the convolution integrals provide the relations of the elastic behavior consequently the viscoelastic equations are the extension of the elastic ones.

Since the formulas by Eqs. (5.2) and (5.3) are true for any elements of the stress or deformation tensors, that are σ_{ij} and ε_{kl} (i,j,k,l∈{1,2,3}), we can apply the analogy also to the multiaxial load based on the general Hooke's law that can be given by a fourth order tensor using the Einstein's convention [F16]:

$$LE:\ \sigma_{ij}(t) = c_{ijkl}\varepsilon_{kl}(t) \quad \leftrightarrow \quad LVE:\ \sigma_{ij}(t) = c_{ijkl}(t) * \dot{\varepsilon}_{kl}(t) \tag{5.4}$$

where c_{ijkl} and $c_{ijkl}(t)$ are the elements of a constant and a time dependent fourth order tensor, respectively. As the deformation and stress tensors are symmetric, the order of indices i and j, and k and l may be exchanged therefore only 36 from the 3^4=81 elements of the fourth order tensors are independent. Accordingly, the relationship between the deformation ($\underline{\varepsilon}$) and stress ($\underline{\sigma}$) vectors created from the 6 independent elements can be given by the next equations:

$$LE:\ \underline{\sigma}(t) = C\underline{\varepsilon}(t) \quad \leftrightarrow \quad LVE:\ \underline{\sigma}(t) = C(t) * \dot{\underline{\varepsilon}}(t) \tag{5.5}$$

where the 6x6 sized C and C(t) are the constant elasticity matrix and the time dependent relaxation matrix, respectively. It is well known that C is symmetric due to the exchangeable partial derivations of an existing elastic potential while in general C(t) is asymmetric.

Similar equations are valid when the stress is the controlled variable:

$$LE:\ \underline{\varepsilon}\ (t) = S\underline{\sigma}(t) \quad \leftrightarrow \quad LVE:\ \underline{\varepsilon}(t) = S(t) * \dot{\underline{\sigma}}(t) \tag{5.6}$$

Laplace transforming the viscoelastic parts of Eqs. (5.5) and (5.6) leads to algebraic products like the elastic ones ($\varepsilon(0)=0$, $\sigma(0)=0$):

$$\tilde{\underline{\sigma}}(s) = \tilde{C}(s)\tilde{\dot{\underline{\varepsilon}}}(s) = s\tilde{C}(s)\tilde{\underline{\varepsilon}}(s) \tag{5.7}$$

$$\tilde{\underline{\varepsilon}}(s) = \tilde{S}(s)\tilde{\dot{\underline{\sigma}}}(s) = s\tilde{S}(s)\tilde{\underline{\sigma}}(s) \tag{5.8}$$

where '~' denotes the Laplace transform and 's' is complex variable. Formulas (5.7) and (5.8) make it possible to use the methods of the linear algebra for calculations.

Also, it is known, that C and S are invertible in the linear elastic case hence they are the inverse of each other. Combining Eqs. (5.7) and (5.8) provides a similar simple implicit relationship between the transformed tensors:

$$\tilde{C}(s)\tilde{S}(s) = \frac{1}{s^2}I \tag{5.9}$$

where 'I' is the suitable unit tensor.

Inverse transforming Eq. (5.9) yields the relationship in time domain in convolution form:

$$LE:\ \ ES = I \quad \leftrightarrow \quad LVE:\ \ E(t) * S(t) = tI \tag{5.10}$$

It should be noted that in some cases certain similarity can be found between the nonlinear elastic and the nonlinear viscoelastic behavior as well. For example, regarding the uniaxial tensile load, and taking the modified Boltzmann's equation based on the so called Boltzmann-Persoz principle [F2] we can compare the relationships for the nonlinear materials given by:

$$X = \varepsilon;\ \ LE:\ \sigma(t) = f\big(\varepsilon(t)\big) \quad \leftrightarrow \quad LVE:\ \sigma(t) = \int_0^t g(\varepsilon(u), t-t')\,\dot{\varepsilon}(t')dt' \tag{5.11}$$

If the integrand function, g, does not depend on the time explicitly then its integral of Stieltjes type can be corresponded to the function f:

$$X = \varepsilon;\ \ LE:\ \sigma(t) = f\big(\varepsilon(t)\big) \quad \leftrightarrow \quad LVE:\ \sigma(t) = \int_0^t g(\varepsilon(t'))\,d\varepsilon(t') \tag{5.12}$$

5.2.1.2. Mechanical behavior with damage and failure

The relations discussed above are related to the flawless behavior of the samples under mechanical load. If a single linear elastic or linear viscoelastic fiber is regarded that breaks at a breaking strain, ε_B, then using the concept of the window function, $\chi(\varepsilon(t),\varepsilon_B)$ [E7, RP2], meaning essentially the implementation of the substitution $\varepsilon(t)\rightarrow\varepsilon(t)\chi(\varepsilon(t),\varepsilon_B)$, Eq. (5.2) can be completed with considering the fiber breakage as well as it follows:

$$LE:\ \sigma(t) = E\varepsilon(t)\chi(\varepsilon(t),\varepsilon_B) \ \leftrightarrow\ LVE:\ \sigma(t) = \int_0^t E(t-t')\frac{d}{dt'}[\varepsilon(t')\chi(\varepsilon(t'),\varepsilon_B)]dt' \tag{5.13}$$

Calculating the expected value yields:

$$LE\colon\ \bar{\sigma}(t) = E\varepsilon(t)R(\varepsilon(t)) \ \leftrightarrow\ LVE\colon\ \bar{\sigma}(t) = \int_0^t E(t-t')\frac{d}{dt'}[\varepsilon(t')R(\varepsilon(t')]dt' \qquad (5.14)$$

Finally, if the fibers are elements of an E-bundle then their deformation ($\boldsymbol{\varepsilon}$(t)) equals that of the bundle (u(t)), that is the stimulus, thus Eq. (5.14) become a bit simpler:

$$LE\colon\ \bar{\sigma}(t) = Eu(t)R(u(t)) \ \leftrightarrow\ LVE\colon\ \bar{\sigma}(t) = \int_0^t E(t-t')\frac{d}{dt'}[u(t')R(u(t')]dt' \qquad (5.15)$$

The LVE equation can be detailed as follows:

$$\bar{\sigma}(t) = \int_0^t E(t-t')R(u(t'))du(t') + \int_0^t E(t-t')u(t')\,dR(u(t')) \qquad (5.16)$$

or taking into account that for E-bundles R=1-Q and Q is the distribution function of the fiber breaking strain yields:

$$\bar{\sigma}(t) = \int_0^t E(t-t')[1-Q(u(t'))]du(t') - \int_0^t E(t-t')q(u(t'))\,du(t') \qquad (5.17)$$

where q is density function.

All this can be applied to the cases of the multiaxial load as well.

5.2.2. Cuboid envelopes as representative volume elements

Based on the concept of the FBC modeling the fibers in a fibrous structure can be classified according to their geometrical and mechanical properties into classes and they are called idealized statistical fiber bundles.

Consider ***a representative element***, a straight or weakly crimped ***fiber*** from one of these fiber bundles and suppose the fiber ends are gripped and one of them coincides into the origin (O) of a Cartesian co-ordinate system (Fig. 1.8). Hence the position vector of the other end ($\overline{OP_0} = \underline{r}_0$) determines the chord of the fiber that is the main diagonal of a cuboid created by the component vectors. At this level, a fiber may be considered *weakly crimped* if it is totally enveloped by this cuboid and its *crimping*, that is the ratio of the arc-length and the chord length of the fiber, is satisfactorily bounded from above.

When the fiber is ***not embedded into matrix material,*** the cuboid can be considered a void in a deformable (e.g. elastic) space. In this case, any deformation of the cuboid may change the position of the fiber end ($P_0 \rightarrow P$) that can be expressed by:

$$\underline{r} = \begin{bmatrix} x \\ y \\ z \end{bmatrix} = \begin{bmatrix} \lambda_1 & 0 & 0 \\ 0 & \lambda_2 & 0 \\ 0 & 0 & \lambda_3 \end{bmatrix}\begin{bmatrix} x_0 \\ y_0 \\ z_0 \end{bmatrix} = \begin{bmatrix} \lambda_1 x_0 \\ \lambda_2 y_0 \\ \lambda_3 z_0 \end{bmatrix} = \Lambda\underline{r}_0 = \underline{r}_0 + U\underline{r}_0 \qquad (5.18)$$

where the extension ratios (λ_i, i=1,2,3) of the cuboid are the ratio of the deformed and initial cuboid sizes and can be expressed by the strains (u_i, i=1,2,3) in the directions of the co-ordinate axes:

$$\lambda_1 = \frac{x}{x_0} = 1 + u_1,\ \lambda_2 = \frac{y}{y_0} = 1 + u_2,\ \lambda_3 = \frac{z}{z_0} = 1 + u_3, \qquad (5.19)$$

Matrix Λ is defined by Eq. (5.18) and the shapes of the resultant deformation matrix is as follows:

$$U = \begin{bmatrix} \lambda_1 - 1 & 0 & 0 \\ 0 & \lambda_2 - 1 & 0 \\ 0 & 0 & \lambda_3 - 1 \end{bmatrix} = \begin{bmatrix} u_1 & 0 & 0 \\ 0 & u_2 & 0 \\ 0 & 0 & u_3 \end{bmatrix} \qquad (5.20)$$

Some of the extension ratios or the finite strains may be controlled deformations or a function of the other ones. Otherwise, sinceλ_i>0 (i=1,2,3), the relationship

$$V = xyz = |\Lambda|V_0 = \lambda_1\lambda_2\lambda_3 V_0 \qquad (5.21)$$

In the case of volume constancy (V=V_0) the next equation stands:

$$\lambda_1\lambda_2\lambda_3 = 1 \qquad (5.22)$$

Some of the extension ratios or the strains may be controlled deformations or a function of the other ones and the matrix $\mathbf{\Lambda}$ is defined by Eq. (5.18).
It should be noted that in the statistical physics based polymer network theory of the elastomers the polymer chains as network branches are treated in the same way as done above [F9, F11].
If *uniaxial load, for example uniaxial extension,* is performed e.g. on axis *x* and Poisson effect occurs that is crosswise contraction then λ_1 is controlled and $\lambda_i=\lambda_i(\lambda_1)$ (i=2, 3) (Fig. 1.8). In FBC modeling the next contraction function is used that is the generalization of Eq. (1.4) (i=2, 3)

$$g_i(\lambda_1) := \lambda_i(\lambda_1) = \frac{1}{[1+c_{a1i}(\lambda_1-1)]^{c_{b1i}}} \sim 1 - c_{a1i}c_{b1i}(\lambda_1 - 1) = 1 - \nu_{1i}u_1 \quad (\lambda_1 \to 1) \tag{5.23}$$

where c_{a1i} and c_{b1i} are non-negative contraction constants while for small deformation the product of them can be regarded as Poisson ratio (i=2,3):

$$\nu_{1i} = c_{a1i}c_{b1i} \quad (u_1 \approx 0) \tag{5.24}$$

The corresponding deformation matrix and its approximation are as follows:

$$U = \begin{bmatrix} \lambda_1 - 1 & 0 & 0 \\ 0 & \lambda_2(\lambda_1) - 1 & 0 \\ 0 & 0 & \lambda_3(\lambda_1) - 1 \end{bmatrix} \approx \begin{bmatrix} u_1 & 0 & 0 \\ 0 & -\nu_{12}u_1 & 0 \\ 0 & 0 & -\nu_{13}u_1 \end{bmatrix} \tag{5.25}$$

Applying *shear* operation(s) to the cuboid distorts into a parallelepiped, which is included by another cuboid determined by the chord of the deformed fiber. Chen and Kaufmann [F13] studied different types of shear operations such as simple shear, 2D beam shear, 2D slice shear, 2D slice-beam shear and 3D beam shear in order to decompose an arbitrary 3D rotation into consecutive shear operations. All that can be represented by a suitable matrix and/or the related co-ordinate mappings.
The *simple shear* is a 1D linear shifting based on a crosswise variable thus there are 6 types of that and they are defined by asymmetric matrices. Denote the initial cuboid, the sheared cuboid, and its envelope cuboid (enc) by C_0, C', and C_1 ($C_0 \to C'$, C_1=enc(C')) respectively. The volume of the sheared cuboid, C', is given by the determinant the transformation matrix, which is the mixed product of the transformed basis vectors, and is obviously smaller than that of the envelope cuboid that is the product of the co-ordinate lengths of the main diagonal (fiber chord). In all cases, the determinant of the shear transformation matrices similar to Eq. (5.22) is equal to 1 thus they realize volume preserving transformations. In some cases, applying two simple shears consecutively gives a matrix of this property as well and it is independent of the order, however, the exchangeability is not true in every case [F8, F13]. Applying two simple shears, not consecutively but simultaneously, provides a matrix that is one of the three *plane shears* (or *in-plane shears*) used commonly in solid mechanics. However, the determinant of this matrix equals 1 only if the shear deformations are small enough [F16].
Corresponding to the definition of the FBCs, the ***fiber bundle*** considered contains fibers of the same properties given by stochastic variables as parameters of the same distribution functions. Each fiber of the ***bundle*** considered is enclosed in its cuboid and is supposed to have a vicinity of the same properties. These requirements make it possible to construct a virtual space where all the fibers with their cuboid are translated so that their origin points coincide for example the yz plane while their end-points coincide another parallel plane at a given distance (x_0 in Figure 1.18.a). The places of the origin points may be given by deterministic geometry or by a suitable stochastic point process. This procedure may provide a special local fiber space where the fibers are in their initial state. The cuboid envelop of those of the single fibers gives a finite volume for the given bundle. If necessary, a suitable affine transformation may lead to a usable ***representative volume element*** (RVE) that provides the properties of the fiber bundle hence it

can be called fiber bundle cell in this sense as well. When the bundle is subjected to mechanical loads acting on the surface of the envelope cuboid the fiber deformation can be calculated from the deformation of the cuboid and so are the forces rising in the fibers determining the resistance forces of the cuboid. Based on the principle of homogenization, this cuboid can be considered as RVE of a solid fiber reinforced polymer material as well.

5.3. FEM Simulation Using Non-linear Hyperelastic Material Model Without Failure

5.3.1. Flawless finite element modeling of human tendons in 2017

As part of this research of Biomechanical Co-operation Research Centre of BUTE, finite element models of biological tissues were performed. The aim of this work is to create a comprehensive data bank that incorporates numerical models of human biological tissues. In the first part of the paper, the literature related to the subject were reviewed, i.e. the anatomy of the tendon, its role in the movement, its structure and mechanical behaviour, the difficulties of modeling the biological tissues and the applied hyper-elastic models. The essence of the task was to process the measurement results of the ***human tendons***, then to prepare the material models in the ANSYS finite element software, and finally to perform the simulation of the tensile test.
The laboratory tensile tests of the tendons were performed by G. Szebényi, in the Materials Testing Laboratory of the Department of Polymer Engineering of the BUTE. The determination of numerical models was based on these tensile tests data and the initial parameters of the specimens provided by the material analysts.
For better clarity and subsequent processing, data was grouped according to the type of biological tissues and the preconditioning. The processed files were named with these corresponding coding. The processed tissues (Achilles, Patella, Peroneus longus, Quadriceps, Semitendinosus+gracilis, Tibialis anterior) were treated separately for the left and right limbs. The preconditioning type was Static and Fatigue Loaded Groups, which included the Normal, Gamma 1 and Gamma 2 irradiation subgroups.
The code for the groups consists of the following elements:

The number of measurements / samples
The first three characters of the type of tendon (Ach, Pat, Per, Qua, Sem, Tib)
Type of preconditioning:

- First character S (Static) or F (Fatigue)
- Second character N (Normal), 1 (Gamma1 Radiation), 2 (Gamma2 Radiation)

Which side limb L (left) or R (right),

so the measurement code 210_Ach_F1_L is a measurement result of a left-footed Achilles tendon that was dynamically loaded and treated with Gamma1 radiation and the sample number is 210.
The force-displacement diagrams from the tensile test were converted to Engineering Stress-strain characteristics by using the available initial parameters (length, width and thickness of the cross-section) (Fig. 5.1). The material models can be created with these data series, and tissues of different sizes are comparable.

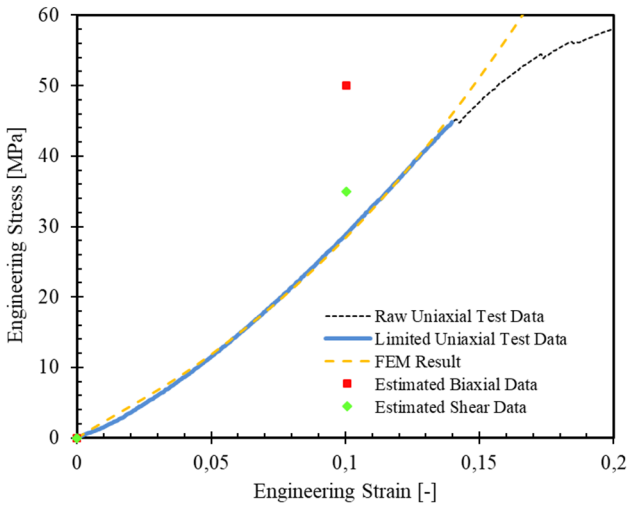

Figure 5.1 Stress-Strain diagram of a specific specimen.

As the tensile curve (Fig. 5.1) includes the breakdown section, separating the elastic section was the next task. Determination of the elastic limit was defined according to the literature („toe region, linear region, failure region"). When the separation of certain fibers was clearly seen in the tensile chart (presence of significant negative slopes) in that case it determined the limit of elastic behavior. The data series of the separated elastic region was used for model fitting. Since elastic elongation in many cases reaches 20-25%, Hyperelastic (also known as Green Materials Models) was used to model material behavior. These models describe the material behavior based on deformation energy density, which allows the modeling of large deformations (more than 100%). At first the identically treated and identical issue types were investigated. But the tensile characteristics in each group showed a large variance, so the models were fitted separately for each sample. Validation of the material models was done by finite element simulation of the tensile tests and by comparison of the obtained result and the original tensile curve. In order to select the appropriate model type, the goodness of fit was examined by squared error. To determine the stability limit of a material model, it is loaded beyond the elasticity limit of the material during the simulation. In the analysis, 1/8-model + symmetry conditions were applied and the tensile test was modeled by displacement.
The material model was created for a total of 197 samples of 5 conditioning classes and 6 tissue types. The model database contains the sample identifier, the type and coefficients of the material model, the strain of the elastic limit of the measurement result and the limit of the stable behavior observed in the finite finite-element analysis, also given by strain.

Related publication: Péter Kerekes (BSc student): Finite element modelling of biological tissue (in Hungarian), Thesis, 2017.

5.3.2. Flawless FE modeling of carpal bones and human tendons in 2018

We have created a pre-test procedure protocol for ***carpal bones***, which includes the cleaning and classification of bones. In the course of our experiments, firstly, we have to know the deformation of carpal bones using a 3D scanner. After the consolidation of the medical bone cement, a 3D scanner was used to make images of the intact bone. After the ***compression tests***, 3D images were taken of the damaged bones to be compared to the intact point clouds.
We have created a model of this complex system based on test results performed on individual constituents and proper geometric characterization. From the obtained results, the material characteristics for FEM modeling were determined and the force-displacement diagram was

used as the input value of the material model. We compared the results of the FEM program with the 3D scanned initial and end images. Further refinement of measurement and FEM model is needed, which will be in the next year. Cyclic test of ***human tendons*** From 57 human cadavers 365 grafts were collected: 73 pieces from: Achilles, quadriceps and peroneus longus (PL); 75 from semitendinosus+gracilis (STG) and 71 from tibialis anterior (TA). We have collected the five types of grafts from human cadavers within 24 hours post mortem. The TA, STG, PL tendons were harvested from the musculotendinous junction. The grafts were divided into four groups. Group A contained 104 fresh and cooled specimens. Another tendon was labelled frozen slowly at -80°C. Group B contained 60 frozen specimens. 200 ligaments of group C were irradiated with a target dose of 21 kGy (this is bactericidal dose). Group D contained the last 200 tendons were irradiated with a target dose of 42 kGy (this is virucidal dose).
Biomechanical parameters were calculated based on measured geometry data, crosshead displacement and ***tensile force-elongation curves*** registered by the tensile tester.
From the results obtained, the material characteristics for FEM modeling were determined and the force-displacement diagram was used as the input value of the material model. The results of the FEM program confirm the results of the measurement.
In addition to the results of the ***dynamic*** measurement, the results of the ***static*** measurement were also processed using FEM software.

5.4. FEM Simulation Using Monte-Carlo Generated Nonlinear E-bundle Fibers

Finite element simulation of the rupture of the tendon
A continuation of the previous Finite Element simulation was performed, which included the failure of the fiber bundle. This was implemented in the ANSYS finite element software, using the Cohesive Zone Method (CZM), to perform the contact debonding (Fig. 5.2) [P5]. Practically speaking, every fiber is already split into two equal length segments, but they are connected with a bonded contact, which at the given time starts to separate, thus mimicking the rupture of the fiber. However, this is a very nonlinear procedure, therefore finding the solution is a difficult task. The same data set was observed, which was also examined in the nonlinear simulation. Because the strongly nonlinear behavior of the fiber makes convergence difficult in itself, it was decided, that a linear material model will be used not to make the solution even more challenging to obtain.
A theoretical equation is used to describe this process. The material model is defined with Hooke's law, and that equation is multiplied with a reliability function, which is expressed with the mean tensile strain and the deviation of this parameter. In practice this means, that bundle is expected to fail when it is stretched to the mean tensile strain, however because of the inhomogeneous nature of the biological tissues, this value differs slightly for each fiber of the bundle. Therefore, this is the complete material model which is used to describe the failure of the bundle, this can be expressed with the three aforementioned parameters: the Young's modulus, the mean tensile strain and its variance. These parameters are constant for the whole bundle. Then this material model is fitted to the data from the measurement, which results in the input parameters for the method. These parameters are then used to generate the individual material model for each fiber. The fibers have the same modulus, but their actual tensile strain is randomized based on the probabilistic parameters. Then this strain value is used to calculate the input parameters for the simulation, basically a transformation of this parameter so that the CZM method can be used. Because of the randomization, each time the

input parameters are generated a slightly different parameter set is created for the model, thus a Monte-Carlo generation is used to create the input parameters (Fig. 5.2.a).
The contact debonding feature uses a bilinear material model for the debonding (Fig. 5.2.b). This means that the two fiber halves are connected and are behaving as one whole body, up until the contact stress is larger than the pre-set parameter. After that, the debonding process starts, which is continuously decreases the contact stiffness linearly until the separation is complete, after which the two halves are behaving as two different body.

Properties of Outline Row 3: cohesive zone

	A	B	
1	Property	Value	
2	Separation-Distance based Debonding		
3	Tangential Slip Under Normal Compression	No	
4	Debonding Interface Mode	Mixed	
5	Maximum Normal Contact Stress	50	MPa
6	Contact Gap at the Completion of Debonding	0.5	mm
7	Maximum Equivalent Tangential Contact Stress	50	MPa
8	Tangential Slip at the Completion of Debonding	0.5	mm
9	Artificial Damping Coefficient	0.001	s

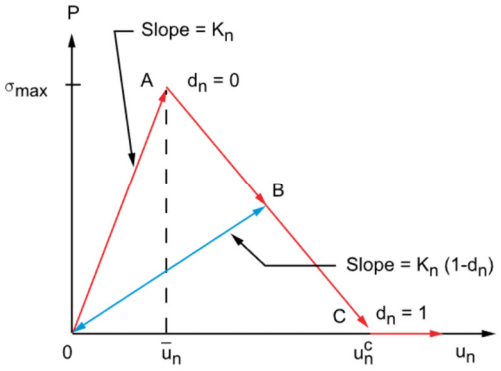

(a) *(b)*

Figure 5.2 Parameters of the debonding, graph of the bilinear approach in action

The model in ANSYS is set up according to the following method. One bundle consists of 25 fibers, which are arranged in a structured manner (Fig. 5.3). Each fiber is split into two halves, therefore 50 bodies are present in this model. The fibers have the same cross section value, in this case the sum of these cross sections is equal to the measured cross section, while the length for each pair of fibers is equal to the measured length. The parametrization of the model is possible, so that in different instances, different lengths and cross section areas can be put in the model, which then can automatically regenerate itself. After the geometry of the model is complete, the simulation must be set up. The halves are connected with the required type of bonded contact, and the cohesive zone method is set up, pairing the right material model to the exact fiber. Then one end of the bundle is fixed, while a displacement is used as a load on the opposite end, with a maximum value similar to the final value of the original measurement (Fig. 5.3). After the simulation is complete, the post-processing of the data can start. The resulting total force and displacement is exported from ANSYS, so that it can be compared to the original measurement and the theoretical model.
This method was used for altogether 120 different measurements. Each simulation result then can be compared to the measurement data. This process uses RMSE calculation and creates an error value and a base variance value. Then from the ratio of these two, the fitting can be described. The smaller the RMSE value is compared to the variance value, the better the simulation fits to the measured data. Despite a few occasions when the simulation did not bring any meaningful results, it can be seen on the graph below (Fig. 5.4), that most of the results have good fits, with the average being R^2=0.78.

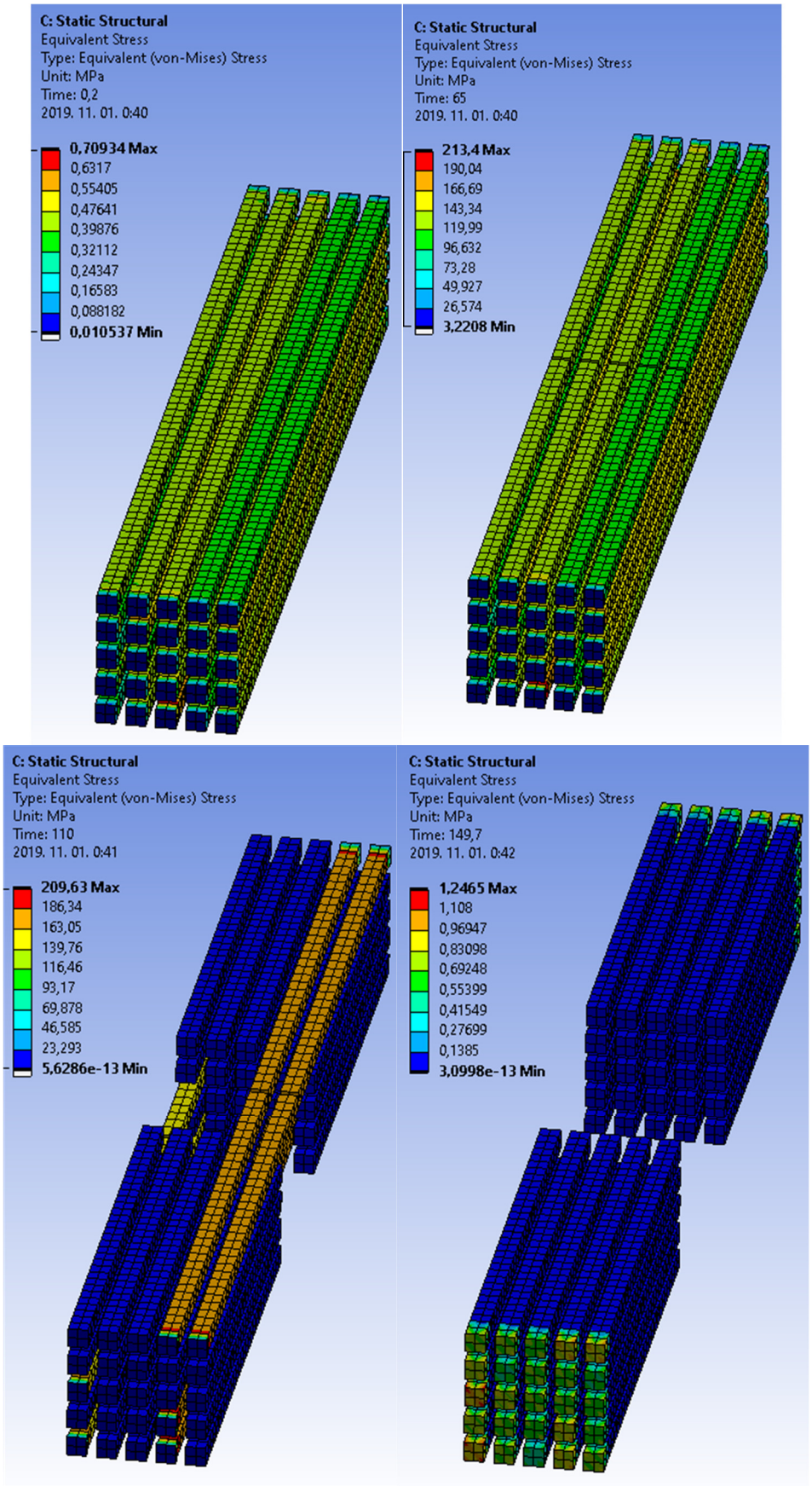

Figure 5.3 Simulation of the failure of the system with fiber debonding visible

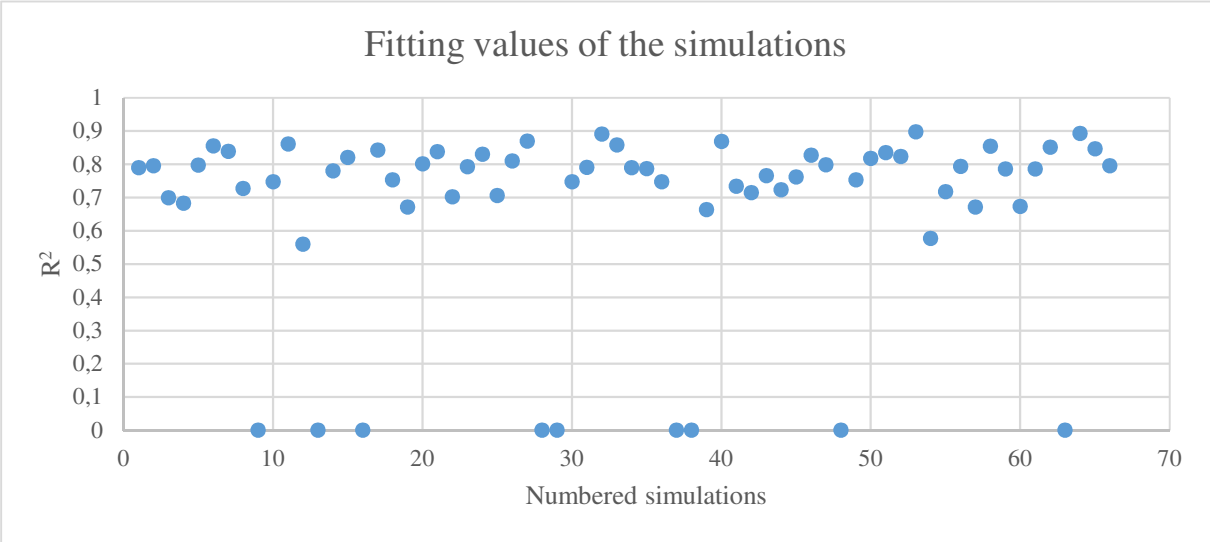

Figure 5.4 Fitting values of the simulations

This method can be used in more complex way as well. Instead of using 1 fiber bundle to describe the behaviour of the tendon, a weighted sum of multiple bundles can be used. This means that instead of having 3 parameters in the theoretical model, each bundle has 3, plus the weight of that bundle. For example, in the case of 4 bundles, 12 material parameters are used with 4 weights, which results in a better fit to the measurement, and consequently better results for the simulation as well. Then the same statistic method can be used to compare the simulation with the measurement, or the complex simulation to the more simplistic one. However, an important drawback is that in this case the model must be multiplied as well, so instead of 50 bodies, there are 200 bodies in the model, creating a 100 different debonding. This significantly increases the solution time, therefore too many bundles are not too efficient to use. Fig. 5.5. shows some results of simulation obtained by different iteration processes.

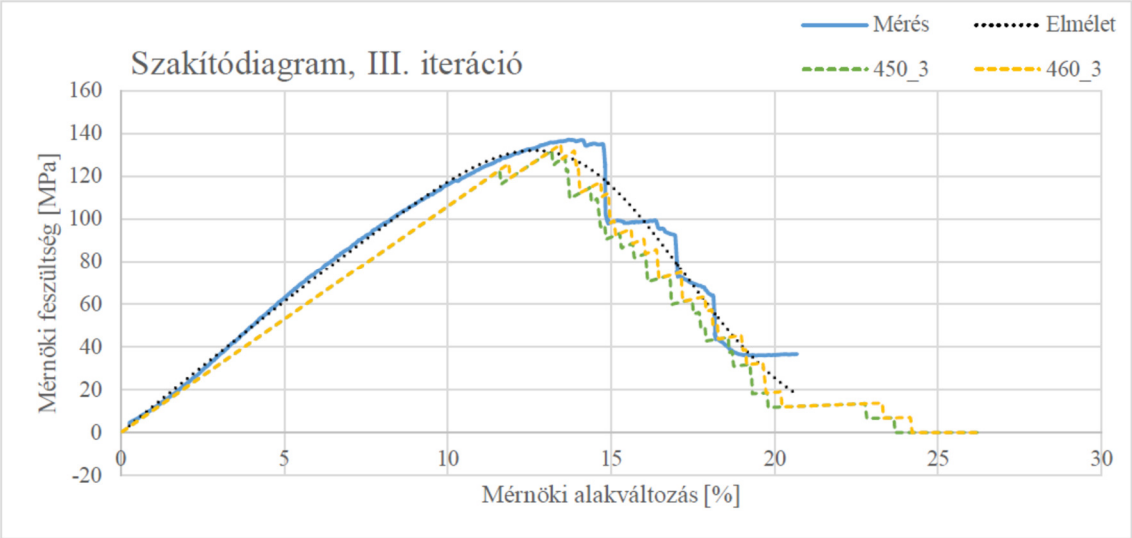

Figure 5.5 Simulation of the failure of the system with fiber debonding visible (measured – solid blue line, theoretical – dotted black line, results of iterative simulations – dotted colored lines)

The method can be used in other areas, such as the examination of ligaments, which possess similar properties, or in the description of the behavior of fiber-reinforced composites.

Related publication: Dániel Takács: FEM Simulation of the Rupture of the Tendon (in Hungarian: Ín szakadásának végeselemes szimulációja) TDK conference paper, BME Budapest 2019. (awarded 1st prize and recommended to OTDK) (supervisors: D. Faragó and A. Poros)

5.5. Extension to Alternating Tensile Load

All the previous studies dealing with FBC modeling discussed such fiber bundles that were subjected to uniaxial constant strain-rate tensile load where the deformation of the fibers monotonic increased. FEM applies meshing in order to create the finite elements of the sample where an element is connected to the neighbor ones hence they realize parallel or serial connections. When every element is considered as a fiber-bundle-cell (FBC) or a network of FBCs thus the serial connected elements create a bundle-chain. A possible fiber breakage taking place in any element of the bundle-chain decreases the resistance or the tensile stiffness of this bundle-element, that can easily be calculated in the linear elastic case, hence its strain increases while the strain of the other chain-element may decrease even if the controlled macrostrain of the sample monotonic increases.

On the basis of this consideration the ***aim of modeling*** should be extended to the development of such FBC based material model that, besides the deformation process observed during the tensile test, is able to describe also the damage and failure process caused locally and/or time-dependent alternating loads and it can be applied in the related FEM simulations as user defined material model. Corresponding to this reformulated aim, the mathematical description of the nonlinear FBCs including the nonlinear E-bundle need further development as well.

5.5.1. Nonlinear E-bundles with value-memory reliability functions

Application of nonlinear FBCs

Let the measured engineering stress-strain curve be $f(u)=F(u)/A_0$ where u, F and A0 are the engineering strain, the measured tensile force and the initial cross section of the specimen, respectively. Using the simplest FBC model, that is the E-bundle, we can determine the expected stress-strain process approximating the measured one that is the weighted sum of those provided by the parallel connected nonlinear E-bundles:

$$f(u) \approx \overline{f}(u) = \sum_{i=1}^{n} w_i \overline{f}_i(u) = \sum_{i=1}^{n} w_i k_i(u) R_i(u), \quad \sum_{i=1}^{n} w_i = 1 \tag{5.26}$$

where n is the number of the E-bundles, f_i and $0 \le w_i \le 1$ are the specific tensile force and the fiber-number-fraction of the i^{th} (i=1,…,n) bundle, respectively. In the case of the E-bundle the expected specific tensile force process is the product of the linear or nonlinear tensile characteristic, $k_i(u)$, representing the flawless functioning and the (expected) reliability function, $R_i(u)$, describing the damage and failure process:

$$\overline{f}_i(u) = k_i(u) R_i(u) = k_i(u)\big(1 - Q_i(u)\big) \tag{5.27}$$

In this case the reliability function is determined by the probability distribution function $Q_i(u)$, of the fiber breaking strain, ε_{Bi}, more preciously, it is equal to the complement distribution function of ε_{Bi}.

It should be noted that Eq. (5.26) may be the finite part of an infinite function series therefore the decomposition into E-bundles is equivalent with a kind of bundle-expansion.

Nonlinear E-bundles for controlled alternating tensile deformation

According to the definition given by Eq. (5.27), the reliability function is a monotonic decreasing function that takes up increasing values again in the case of decreasing deformation. This contradicts to the interpretation of damages and failures namely the failure is ultimate not reversible.

In order to solve this problem firstly let us distinguish the macrostrain u=vt that is the constant rate controlled strain of the bundle model or the sample, where v is the velocity of the mobile grip and t is the time, and the fiber strain, $\varepsilon(t)$, that is identical of that of the E-bundle fibers. On the other hand, we redefine the reliability function by Eq. (5.27) and introduce the so called ***value-memory reliability function*** (VMRF) that can preserve its minimum value reached in interval (0,t):

$$R^*(\varepsilon(t)) = \min_{0\le t'\le t} R(\varepsilon(t')) = \min_{0\le t'\le t}\left(1 - Q(\varepsilon(t'))\right) \tag{5.28}$$

Correspondingly, when alternating tensile load is used the expected specific tensile force of the E-bundles can be calculated similarly to the early way:

$$f^*(\varepsilon(t)) = k(\varepsilon(t))R^*(\varepsilon(t)) \tag{5.29}$$

where, of course, the time increases monotonic while the current fiber strain, $\varepsilon(t)$, may change arbitrarily.

5.5.2. Examples of application

Application examples

As an example let us consider the next sinusoidal strain function (Fig. 5.6) as the deformation stimulus that is normalized by the mean fiber breaking strain (ε_B) and its mean value and amplitude linearly increasing:

$$x = \frac{\varepsilon(t)}{\varepsilon_B} = \frac{c_1}{4}\frac{t}{T}\left(1 - cos\left(2\pi\frac{t}{T}\right) + c_0\right) \tag{5.30}$$

where T is the period time and c_0 and c_1 are constant parameters.

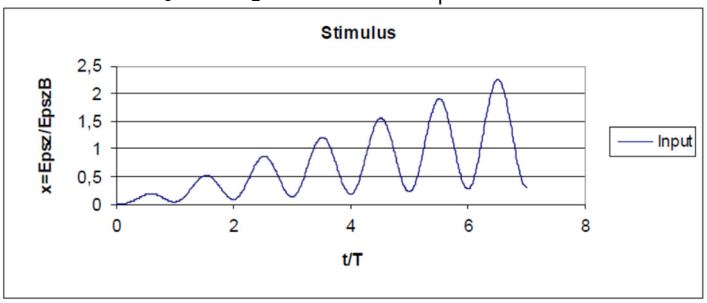

Figure 5.6 Normalized alternating strain function (T=1, c_0=0,3; c_1=0,6)

5.5.2.1. Linear and nonlinear E-bundles

Suppose that the fiber breaking strain, ε_B, is of normal distribution with parameters , the value-memory reliability function (VMRF) according to Eq. (5.28) shows the shape in Fig. 5.7. Accordingly, where the strain $\varepsilon(t)$ decreases the value of the VM reliability function remains at its minimum reached up to that time, t, until the strain exerts its maximum reached up to that time.

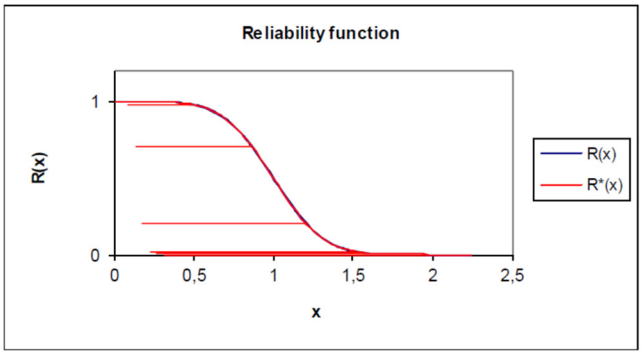

Figure 5.7 Variation of the VM-reliability function in the case of the strain load by Eq. (5.30)

The expected specific tensile force can be obtained by the product according to Eq. (5.29). Using the next relationship for the tensile characteristics of fibers:

$$k(x) = cx + a(1 - e^{-bx}) \tag{5.31}$$

Figure 5.8 shows the corresponding expected tensile force curves for linear (c=1, b=0) and nonlinear (a=-1, b=1, c=1) cases, respectively.

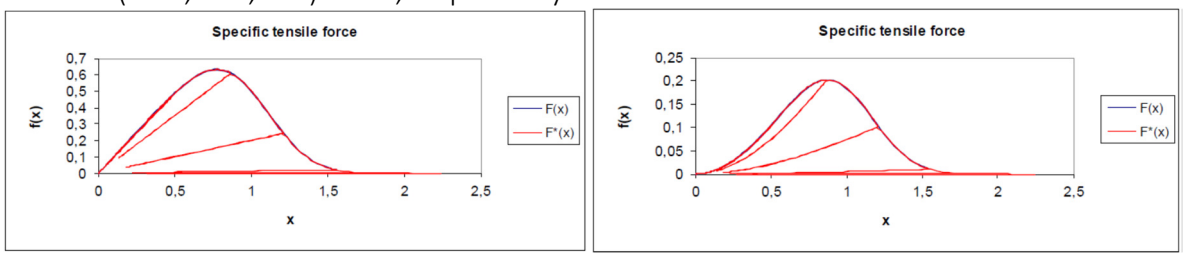

(a) (b)

Figure 5.8 Variation of the expected tensile force in the case of linear (a) and nonlinear (b) tensile characteristics

In both cases it can be well seen that when the value of e(t) decreases the tensile force also but it follows a curve of smaller steep determined by the damages and failures occurred up to that time.

5.5.2.2. Bilinear CZM model as an approximation of a linear E-bundle

The bilinear Cohesive Zone Method (CZM) model that was applied by D. ZS. Takács [P5] in ANSYS environment, after a sharp break caused by the first damage, it follows a linear failure process for determining the tensile stiffness reduced gradually failure by failure. It is obvious that it is a kind of approximation of the expected tensile force process of a linear E-bundle using the initial tangent of the rising part and the inflection tangent of the falling part (Fig. 5.9).

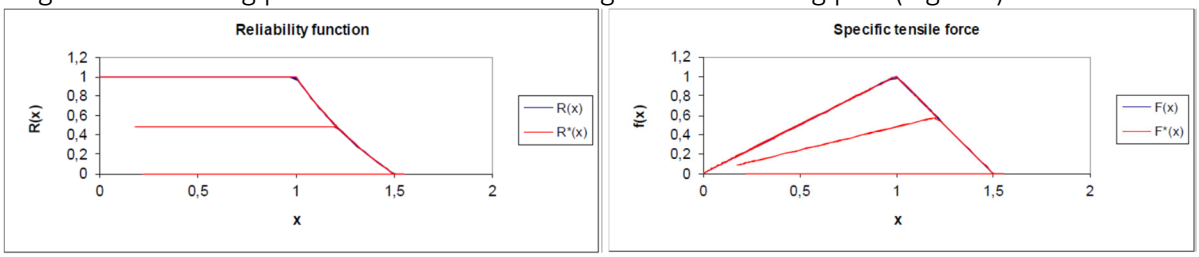

(a) (b)

Figure 5.9 Variation of the VM-reliability function (a) and the specific tensile force (b) in the case of CZM model according to Eq. (5.31) (x_0=1,5; x_1=1)

Of course, this can be given in the form of Eq. (5.27) or (5.30) by using the next single formula for the normal reliability function, R(x):

$$R(x) = \begin{cases} 1, & x = 0 \\ 0; min\left(1; \frac{1}{x}\frac{x - x_0}{x_0 - x_1}\right), & x > 0 \end{cases} \tag{5.32}$$

where x_0 and x_1 are constant parameters. The VM-reliability function, R*(x), (Fig. 5.9.a) can be obtained by the definition according to Eq. (5.28) from Eq. (5.32). Fig. 5.9.b shows the variation of the tensile force as the response to the stimulus by Eq. (5.30).

5.6. Extension to Alternating Tensile and Compressive Load

In the case of compressive load the deformation and failure process can formally be described with the same formula as those for the tensile load such as Eqs. (5.26) and (5.27). Here the question comes up how to use the formula when the sample is subjected to an alternating compressive-tensile load.

5.6.1. Joint reliability function and the expected tensile-compressive force curve

Supposing we know the tensile-compressive characteristic of the elastic fibers that describes flawless functioning and the probability distribution functions $Q_{\varepsilon TB}(u)$ and $Q_{\varepsilon CB}(u)$ of the tensile

and compressive breaking strain, respectively. The compressive deformation can be treated as negative tensile strain and the breaking strains, ε_{TB} and ε_{CB}, are assumed to be independent stochastic variables.

In this case of monotonic controlled deformation starting from zero, it can be proven that the next formula describes the expected tensile and compressive force process of a modified nonlinear E-bundle:

$$\bar{f}(u) = k(u)R_{CT}(u) = k(u)R_C(u)R_T(u) = k(u)Q_{\varepsilon_{CB}}(u)\left(1 - Q_{\varepsilon_{TB}}(u)\right) \tag{5.33}$$

where $R_C(u)$ and $R_T(u)$ are the reliability functions for compressive and tensile load while $R_{CT}(u)$ the joint reliability function valid for both loads.

Taking the distribution function of the tensile and compressive strains (ε_{TB} and ε_{CB}) normal with parameters $N(1; 0{,}25^2)$ and $N(-0{,}7; 0{,}2^2)$, respectively, the reliability function and the expected tensile-compressive force process can be seen in Fig. 5.10.

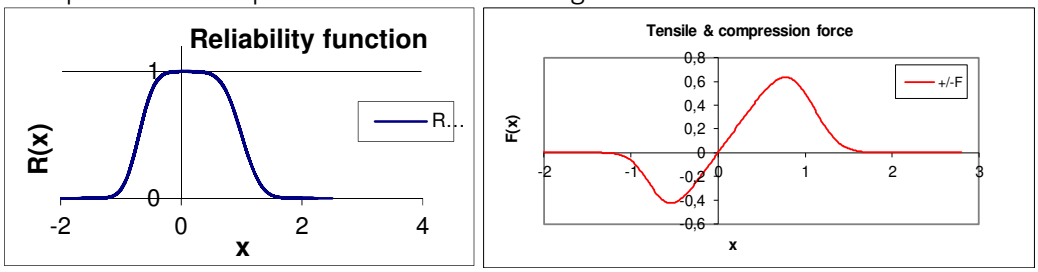

(a) (b)

Figure 5.10 Joint reliability function (a) and the expected force process (b) for tensile-compressive load

5.6.2. Value-memory reliability function and the expected stress-strain curve

Applying the definition by Eq. (5.28), the relationship given by Eq. (5.33) can be extended to alternating tensile-compressive load similarly to the pure tensile load which results in a formula corresponding to Eq. (5.29):

$$f^*(\varepsilon(t)) = k(\varepsilon(t))R^*_{CT}(\varepsilon(t)) = k(\varepsilon(t))R^*_C(\varepsilon(t))R^*_T(\varepsilon(t)) \tag{5.34}$$

where the joint VM-reliability function for both tensile and compressive load is:

$$R^*_C(\varepsilon(t)) = \min_{0\le t'\le t} R_C(\varepsilon(t')) = \min_{0\le t'\le t} Q_{\varepsilon_{CB}}(\varepsilon(t')) \tag{5.35}$$

5.6.3. Application example

For graphical representation we use the deformation stimulus in Fig. 5.11.

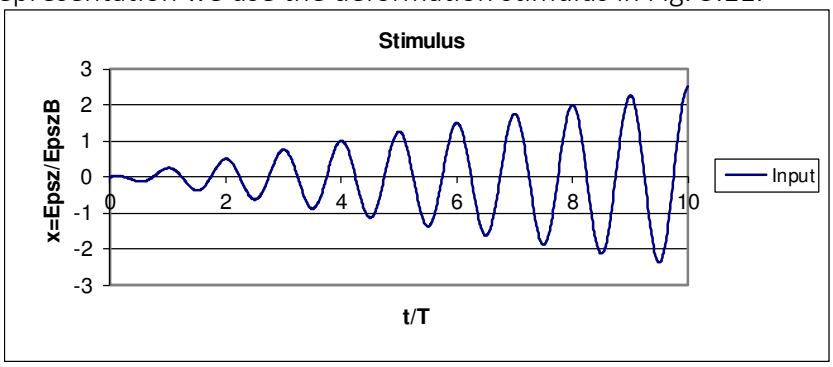

Figure 5.11 Periodical tensile-compressive deformation

The functioning of the joint VM-reliability function and the expected response of the linear E-bundle given to the stimulus in Fig. 5.11 can be seen in Fig. 5.12. Fig. 5.12 shows well the effect of interaction of the accumulating damages and failures caused by the sinusoidal alternating tensile-compressive load with increasing mean value and, as a result, the increasing and increasing steep of the current force-deformation characteristic.

For example, applying this type of fiber bundles extended to both tensile and compressive load, in the case of 3P bending, the failure process not only for the stretched layers can be described as it is in [E2, E3] but that for the compressed layers as well.

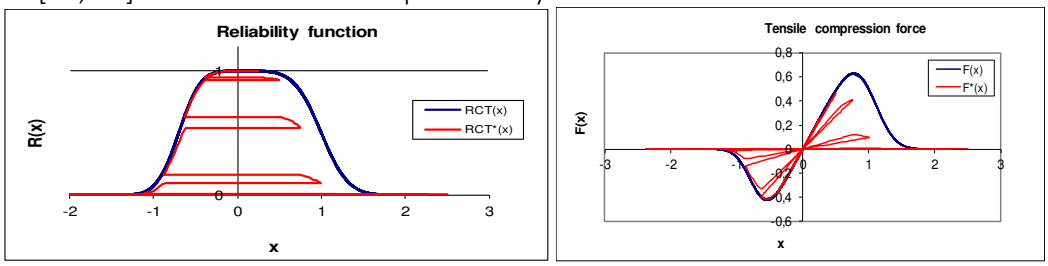

(a) (b)

Figure 5.12 Reliability function (a) and expected force process (b) for alternating tensile-compressing load

5.7. Extension to Anisotropic 3D Material Subjected to Alternating Multiaxial Load

Curiskis and Carnaby G.A. [F8] made an attempt to treat a fiber bundle subjected to multiaxial loads by using the linear elastic material approach. They proposed a relation where the stiffness matrix is not necessarily symmetric. We are going to make use of this approach completing with describing the damage process based on the E-bundles with extended functioning.

5.7.1. Deformation of the single fibers with their vicinity subjected to multiaxial load

In this general case Eq. (5.18) is to be used but it should be taken into consideration that all the deformation components may be controlled or at least they are known loads when $\lambda_{ii}=1+u_i$, $\lambda_{ij}=u_{ij}$ ($i\neq j$) are deformation variables, however $\lambda_{ii}\neq\lambda_i$. Because of the well determined displacements that act simultaneously, hence it is supposed that Poisson effect cannot occur in any axis direction. The deformation matrix $U=\Lambda-I$ can be decomposed into 9 parts to realize a 9 termed linear combination of the deformation variables:

$$U=\begin{bmatrix}\lambda_{11}-1 & \lambda_{12} & \lambda_{13}\\ \lambda_{21} & \lambda_{22}-1 & \lambda_{23}\\ \lambda_{31} & \lambda_{32} & \lambda_{33}-1\end{bmatrix}=\begin{bmatrix}u_1 & u_{12} & u_{13}\\ u_{21} & u_2 & u_{23}\\ u_{31} & u_{32} & u_3\end{bmatrix} \tag{5.36}$$

On the other hand, when the controlled deformations λ_{ii} (i=1,2,3) act consecutively they may imply Poisson effect, but the result may depend on their order. Consequently, the extension ratio of the fiber is given by:

$$\Lambda=\begin{bmatrix}\lambda_{11}(\lambda_{22},\lambda_{33}) & \lambda_{12} & \lambda_{13}\\ \lambda_{21} & \lambda_{22}(\lambda_{11},\lambda_{33}) & \lambda_{23}\\ \lambda_{31} & \lambda_{32} & \lambda_{33}(\lambda_{11},\lambda_{22})\end{bmatrix} \tag{5.37}$$

Using the hyperbolic function form (g) by Eq. (5.23) and neglecting the multiplicative increase effect at calculating the contraction leads to the next matrix:

$$\Lambda\approx\begin{bmatrix}\lambda_{11}g_{21}(\lambda_{22})g_{31}(\lambda_{33}) & \lambda_{12} & \lambda_{13}\\ \lambda_{21} & \lambda_{22}g_{12}(\lambda_{11})g_{32}(\lambda_{33}) & \lambda_{23}\\ \lambda_{31} & \lambda_{32} & \lambda_{33}g_{13}(\lambda_{11})g_{23}(\lambda_{22})\end{bmatrix} \tag{5.38}$$

that gives the extension ratio of the fiber:

$$\lambda=\lambda_0\frac{\sqrt{(\lambda_{11}g_{21}g_{31}x_0+\lambda_{12}y_0+\lambda_{13}z_0)^2+(\lambda_{21}x_0+\lambda_{22}g_{12}g_{32}y_0+\lambda_{23}z_0)^2+(\lambda_{31}x_0+\lambda_{32}y_0+\lambda_{33}g_{13}g_{23}z_0)^2}}{\sqrt{x_0^2+y_0^2+z_0^2}} \tag{5.39}$$

When c_{aij}=1 stands for every $i\neq j$ then the components in the main diagonal become products of the power of λ_{ii}:

$$\Lambda \approx \begin{bmatrix} \lambda_{11}\lambda_{22}^{-c_{b21}}\lambda_{33}^{-c_{b31}} & \lambda_{12} & \lambda_{13} \\ \lambda_{21} & \lambda_{22}\lambda_{11}^{-c_{b12}}\lambda_{33}^{-c_{b32}} & \lambda_{23} \\ \lambda_{31} & \lambda_{32} & \lambda_{33}\lambda_{11}^{-c_{b13}}\lambda_{22}^{-c_{b23}} \end{bmatrix} \tag{5.40}$$

that gives the extension ratio of the fiber in the next form:

$$\lambda = \lambda_0 \frac{\sqrt{\left(\frac{\lambda_{11}x_0}{\lambda_{22}^{c_{b21}}\lambda_{33}^{c_{b31}}}+\lambda_{12}y_0+\lambda_{13}z_0\right)^2+\left(\lambda_{21}x_0+\frac{\lambda_{22}y_0}{\lambda_{11}^{c_{b12}}\lambda_{33}^{c_{b32}}}+\lambda_{23}z_0\right)^2+\left(\lambda_{31}x_0+\lambda_{32}y_0+\frac{\lambda_{33}z_0}{\lambda_{11}^{c_{b13}}\lambda_{22}^{c_{b23}}}\right)^2}}{\sqrt{x_0^2+y_0^2+z_0^2}} \tag{5.41}$$

5.7.4. Expected stress-strain relationship of linear elastic damageable continuum cuboids

Expansion to anisotropic material subjected to multiaxial alternating load

The formula according to Equation (5.34) valid for tensile-compressive load can be interpreted for pure shear in the same form. Moreover, the interpretation can formally be extended for the usual stresses as well. Based on this and the known relationships in composite mechanics the extension can be implemented for the anisotropic materials subjected to multiaxial load.

When the linear elastic material is loaded by uniaxial tensile-compressive load the Eq. (5.34) has got the next shape:

$$\sigma^*(\varepsilon(t)) = \sigma(\varepsilon(t))R_{CT}^*\big(\varepsilon(t)\big) = E\varepsilon(t)R_{CT}^*(\varepsilon(t)) \tag{5.42}$$

where σ is the normal stress, ε is the related strain, and E is the tensile modulus. The flawless functioning is expressed by:

$$\sigma(\varepsilon(t)) = E\varepsilon(t) \tag{5.43}$$

Eq. (5.42) can be interpreted for pure shear in a similar form:

$$\tau^*(\gamma(t)) = \tau(\gamma(t))R_S^*\big(\gamma(t)\big) = G\gamma(t)R_S^*(\gamma(t)) \tag{5.44}$$

where τ is the shear stress, γ is the related shear deformation, and G is the shear modulus, as well as the flawless relation is:

$$\tau(\gamma(t)) = G\gamma(t) \tag{5.45}$$

In both cases the time-dependent variation of the deformation-stimuli $\varepsilon(t)$ and $\gamma(t)$ are known. In the case of multiaxial load, let D and F be the matrices of the deformation and stress tensors, respectively:

$$D = \left[\varepsilon_{ij}\right]_{i,j=1}^{3} \qquad F = \left[\sigma_{ij}\right]_{i,j=1}^{3} \tag{5.46}$$

It is well known for linear elastic materials the general Hooke's law describes the relationship between the deformation and stress components that can be given by a tensor C of fourth order (i,j,k,l∈{1,2,3}):

$$\sigma_{ij} = C_{ijkl}\varepsilon_{kl} \tag{5.47}$$

Tensor C has got 3^4=81 constant elements, however, taking into account the symmetries (matrices D and F are symmetric and because of the existence of the elastic potential the order of the indices ij and kl can be exchanged) leads to only 21 independent elements. On the basis of this consideration, ordering the 6-6 independent deformation and stress components into vectors $\underline{\varepsilon}$ and $\underline{\sigma}$, the relationship between them can be given by a 6x6 elastic matrix E:

$$\underline{\sigma} = E\underline{\varepsilon} \tag{5.48}$$

Eq. (5.48) describes the flawless behavior for arbitrary multiaxial load.

Deformation controlled failure process

When deformation-stimulus is used, the description corresponding to Eqs. (5.42) and (5.44) including the failure can be obtained by reforming the deformation vector:

$$\underline{\varepsilon}^* = \begin{bmatrix} \varepsilon_{11}^* \\ \varepsilon_{22}^* \\ \varepsilon_{33}^* \\ \varepsilon_{12}^* \\ \varepsilon_{13}^* \\ \varepsilon_{23}^* \end{bmatrix} = \begin{bmatrix} R_{11}^* \varepsilon_{11} \\ R_{22}^* \varepsilon_{22} \\ R_{33}^* \varepsilon_{33} \\ R_{12}^* \varepsilon_{12} \\ R_{13}^* \varepsilon_{13} \\ R_{23}^* \varepsilon_{23} \end{bmatrix} = \begin{bmatrix} R_{11}^* & 0 & 0 & 0 & 0 & 0 \\ 0 & R_{22}^* & 0 & 0 & 0 & 0 \\ 0 & 0 & R_{33}^* & 0 & 0 & 0 \\ 0 & 0 & 0 & R_{12}^* & 0 & 0 \\ 0 & 0 & 0 & 0 & R_{13}^* & 0 \\ 0 & 0 & 0 & 0 & 0 & R_{23}^* \end{bmatrix} \begin{bmatrix} \varepsilon_{11} \\ \varepsilon_{22} \\ \varepsilon_{33} \\ \varepsilon_{12} \\ \varepsilon_{13} \\ \varepsilon_{23} \end{bmatrix} = R^* \underline{\varepsilon} \tag{5.49}$$

where R^* is the general reliability matrix the elements of which are the component reliability functions. The special value of R^* is equal to the unit matrix over the total range of the flawless functioning. On the other hand, the determinant of R^* denoted by R_G^* characterizes the scalar global reliability corresponding to the given load combination:

$$0 \leq R_G^* = detR^* = \prod_{i \leq j} R_{ij}^* \leq 1 \tag{5.50}$$

Being aware of the deformation-components of the linear elastic material, we can write the general relationship between the deformation and stress into the form of Eq. (5.48) that includes the failure as well:

$$\underline{\sigma}^* = E\underline{\varepsilon}^* = ER^*(\underline{\varepsilon})\underline{\varepsilon} \tag{5.51}$$

The reliability matrix is a multivariable function ~~of~~ every element of which is the function of the related deformation-components. The detailed 2D form of Eq. (5.51) is as follows:

$$\underline{\sigma}^* = \begin{bmatrix} \sigma_{11}^* \\ \sigma_{22}^* \\ \sigma_{12}^* \end{bmatrix} = \begin{bmatrix} \sigma_{11}\bar{R}_{11}^* \\ \sigma_{22}\bar{R}_{22}^* \\ \sigma_{12}\bar{R}_{12}^* \end{bmatrix} = \begin{bmatrix} E_{11} & E_{12} & 0 \\ E_{21} & E_{22} & 0 \\ 0 & 0 & G_{12} \end{bmatrix} \begin{bmatrix} R_{11}^* & 0 & 0 \\ 0 & R_{22}^* & 0 \\ 0 & 0 & R_{12}^* \end{bmatrix} \begin{bmatrix} \varepsilon_{11} \\ \varepsilon_{22} \\ \varepsilon_{12} \end{bmatrix} = E\underline{\varepsilon}^* \tag{5.52}$$

where E12 and E21 are the components of matrix without any details regarding e.g. the Poisson factors. Hence, in the case of controlled deformation, the controlling reliability functions belonging to the deformation-components are these:

$$\underline{\sigma}^* = \begin{bmatrix} \sigma_{11}^* \\ \sigma_{22}^* \\ \sigma_{12}^* \end{bmatrix} = \begin{bmatrix} \sigma_{11}\bar{R}_{11}^* \\ \sigma_{22}\bar{R}_{22}^* \\ \sigma_{12}\bar{R}_{12}^* \end{bmatrix} = \begin{bmatrix} R_{11}^* E_{11}\varepsilon_{11} + R_{22}^* E_{12}\varepsilon_{22} \\ R_{11}^* E_{21}\varepsilon_{11} + R_{22}^* E_{22}\varepsilon_{22} \\ R_{12}^* G_{12}\varepsilon_{12} \end{bmatrix} = \begin{bmatrix} E_{11}R_{11}^* & E_{12}R_{22}^* & 0 \\ E_{21}R_{11}^* & E_{22}R_{22}^* & 0 \\ 0 & 0 & G_{12}R_{12}^* \end{bmatrix} \begin{bmatrix} \varepsilon_{11} \\ \varepsilon_{22} \\ \varepsilon_{12} \end{bmatrix} \tag{5.53}$$

The reliability factors, R_{ij}^*, of the deformation-components are functions depending on ~~them~~ the related deformation component only while the reliability factors, $\bar{R}_{ij}^*$, of the stress-components are weighted averages, for example:

$$\bar{R}_{11}^*(\varepsilon_{11}, \varepsilon_{22}) = \frac{\sigma_{11}^*}{\sigma_{11}} = \frac{R_{11}^* E_{11}\varepsilon_{11} + R_{22}^* E_{12}\varepsilon_{22}}{E_{11}\varepsilon_{11} + E_{12}\varepsilon_{22}} = \frac{E_{11}R_{11}^*(\varepsilon_{11})\varepsilon_{11} + E_{12}R_{22}^*(\varepsilon_{22})\varepsilon_{22}}{E_{11}\varepsilon_{11} + E_{12}\varepsilon_{22}} \tag{5.54}$$

Otherwise, on the basis of Eq. (5.53) it can be seen that although the matrix E is symmetric but the product matrix ER is not namely in general $R_{11}^* \neq R_{22}^*$. The 3D form of Eq. (5.51) is as follows:

$$\underline{\sigma}^* = \begin{bmatrix} \sigma_{11}^* \\ \sigma_{22}^* \\ \sigma_{33}^* \\ \sigma_{12}^* \\ \sigma_{13}^* \\ \sigma_{23}^* \end{bmatrix} = \begin{bmatrix} \sigma_{11}\bar{R}_{11}^* \\ \sigma_{22}\bar{R}_{22}^* \\ \sigma_{33}\bar{R}_{33}^* \\ \sigma_{12}\bar{R}_{12}^* \\ \sigma_{13}\bar{R}_{13}^* \\ \sigma_{23}\bar{R}_{23}^* \end{bmatrix} = E \begin{bmatrix} R_{11}^* \varepsilon_{11} \\ R_{22}^* \varepsilon_{22} \\ R_{33}^* \varepsilon_{33} \\ R_{12}^* \varepsilon_{12} \\ R_{13}^* \varepsilon_{13} \\ R_{23}^* \varepsilon_{23} \end{bmatrix} = E \begin{bmatrix} R_{11}^* & 0 & 0 & 0 & 0 & 0 \\ 0 & R_{22}^* & 0 & 0 & 0 & 0 \\ 0 & 0 & R_{33}^* & 0 & 0 & 0 \\ 0 & 0 & 0 & R_{12}^* & 0 & 0 \\ 0 & 0 & 0 & 0 & R_{13}^* & 0 \\ 0 & 0 & 0 & 0 & 0 & R_{23}^* \end{bmatrix} \begin{bmatrix} \varepsilon_{11} \\ \varepsilon_{22} \\ \varepsilon_{33} \\ \varepsilon_{12} \\ \varepsilon_{13} \\ \varepsilon_{23} \end{bmatrix} \tag{5.55}$$

This interpretation can be extended to nonlinear elastic and linear viscoelastic material behavior as well.

Stress controlled failure process

The case of controlled stress can be treated in a similar way, however, the place in the order in Eq. (5.51) will change and the stress dependent element of the reliability matrix will change as

well. It should be taken into consideration that, in this case, the failure may be catastrophic when reaching the maximum resistance of the given volume element.

5.8. Application of FBCs Based Material Models in FEM Simulations

5.8.1. Difficulties and possibilities of modeling failure processes in FEM environment

The damage and failure processes are essentially of dynamic nature that are connected with local stability loss. Hence, considering the difficulties, their modeling is, to a certain degree, similar to the simulation of the so called post-buckling phenomenon [P9, RP8]. For the FEM simulation of the post-buckling type process, in general, two different approaches, the so called implicit and explicit solvers, are used.

The widely used ***implicit solver*** such as ANSYS Mechanical APDL or LS-DYNA implicit has been developed mainly for static mechanical problems. The implicit solvers, in every time-step, calculate the discretized displacement field in each node of the meshed object using variation-calculus completed with force-balance analysis. Therefore, they are rather slow. Another problem, that the stability loss as a phenomenon or process takes place in a very short time hence its numerical simulation needs very small time-steps the realization of which can hardly be implemented in the practice. In addition, if some elements fail during the simulation the continuation needs re-meshing. Consequently, in general, the implicit solver is applied to simulate buckling problems when:

-checking the odds of the stability loss (bifurcation analysis) using suitable criteria, or

-studying the initial part of the buckling process supposing there are no significant geometrical distortion and inertial effects, and mainly no damage or failure.

These problems and drawbacks can be eliminated by using ***explicit solver*** such as ANSYS Explicit Dynamics or LS-DYNA explicit that is a numerically treatable and stable option [P9, RP8]. The explicit solver solves the classical second order dynamic differential equation in discretized form for each node displacement vectors in every time step. It uses the theory of the finite deformations so it can treat the large deformation yet the numerical calculations are easier.

Nowadays, every significant commercial FEM software has got both implicit and explicit solvers. In general, all the engineering problems related to dynamic effects (impact test, dart test, catastrophic phenomena, fracture,…) are investigated in FEM environment using explicit solver [RP8]. Correspondingly, the explicit solver makes it possible to use much more complex material models including the failure than that in the case of the implicit solver.

As an intermediate solution, using the cohesive zone method (CZM) connected to the implicit solver, cohesive elements can be defined at given places, for example as an interface layer, that can model damage phenomena.

5.8.2. Steps of application development based on the results achieved

Considering the theoretical and experimental results and experiences of the investigations regarding the FBC based and FEM material models, the development of FBC applications to FEM simulations may reasonably carried out in the next steps.

(1) Improving the standard bilinear CZM model for tensile load by making use of the related VM-reliability function created from Eqs. (5.28) and (5.32). Let us denote that by CZM*.
(2) Extending the bilinear CZM* model by using linear and nonlinear E-bundles with VM-reliability function and denote them by ECZM* and nECZM*, respectively.
(3) Extending the linear ECZM* and the nonlinear nECZM* models for tensile and compressive loads and denote them by ETC and nETC, respectively.
(4) Extending the linear ETC model for multiaxial load.

All that needs to find the FEM environment where these application can be realized. Up to now, this environment means the use of explicit solvers and the necessary related tools.

5.8.3. Developing material model for causality-connected failures

Failure modes of unembedded fibers

When the fibers are not embedded into any matrix material, but they are gripped at both ends or there is adhesion connection between the fibers, they or their force transmitting may failure by the breakage or the slippage out of the fibers given gripping, respectively (Fig. 5.13). These events are not in casual relation since they depend on their orientation and the load level.

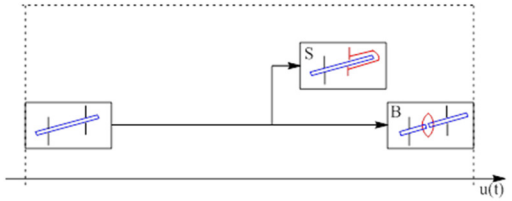

Figure 5.13 Failure modes of an unembedded fiber (S=slippage, B=breakage)

Failure modes of the matrix and the embedded fibers

In general, when the fibers are embedded into the matrix the composite creates an inhomogeneous continuum that may contain different types of defects or flaws such as structural inhomogeneity (I3) or inclusions (I) such as air-bubbles (I1) and contaminations(I4) in the matrix, air-inclusions about fibers(I1) (Fig. 5.14). In such case, the damages such as craze (C), microcrack (mC) and failures such as macrocrack (MC), fiber/matrix debonding (D), fiber slippage (S), fiber breakage (B) do not come into being independent of each other but one type of damage may be the condition or requirement for the other type (Fig. 5.14).

Consequently, ***damage induced damage and failure chains*** or causality-connected event-network as complex failure processes are realized in the polymer composite material (Fig.5.14). These significantly stochastic processes need more investigations so that they could be used for developing more accurate and effective material models for the numerical simulations.

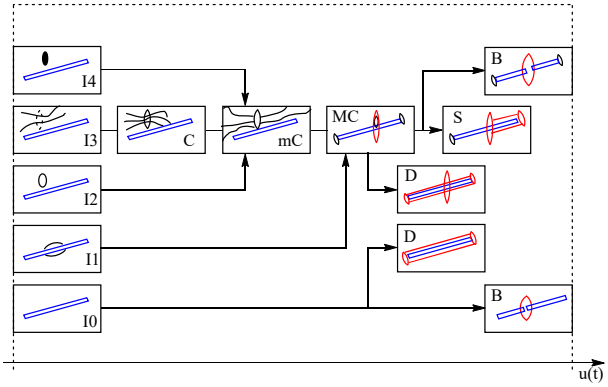

Figure 5.14 Flow chart of the causality-connected damage and failure processes in fiber reinforced composites (I0 = no inhomogeneity or inclusion)

5.9. Conclusions

The main conclusion drawn from the results regarding the applicability of the FBCs may be that they make it possible to develop material models representing statistical defects, damage and failure phenomena that may be applied for FEM numerical simulations.

Based on these results, for example, the next objectives for further research may be set:

(1) Novel FBCs based linear laminate theory can be developed that may use stochastic fiber orientations different in each lamina (ply) and does not need to use the fracture criteria because of the built-in expected failure processes.
(2) On the basis of the fundamental equation of the FBC modeling, Eq. (1.8), the statistical window-function technique makes it possible to treat the matrix R^* defined by Eq. (5.55) as the expected value of a window-function matrix hence using the statistical methods of the data matrices [F18] its covariance characteristics can be calculated and analyzed and suitable confidence intervals can be constructed.
(3) Development of novel FBCs based linear viscoelastic laminate theory as an extension the linear one.
(4) Development of the damage induced damage chain theory makes it possible to create novel FEM simulation models of much more accuracy that would be able to predict damage events and post-damage behavior.
(5) Development of novel FEM simulation models for human bones, tendons, muscles, and arms, hand, legs, etc.
(6) Development of novel software packages in available FEM software environments.

Publications: 1 BSc Thesis [P1], 1 TDK conference paper (1st prize) [P5], 1 article submitted [P7], 1 article before submission [P8] and 2-3 other papers are expected to be published in impact factor periodicals (one of them will based on [P9]).
Related publications and projects: Some of the results have been utilized by 5 PhD Thesis projects [RP6-RP10].

References and Publications

Earlier own publications in the FCB topic

E1 Bodor G., Vas L.M.: Structure and Properties of Polymers (in Hungarian: Polimer anyagszerkezettan), Műegyetemi Kiadó, Bp. 2000.
E2 Vas, L.M., Rácz, Zs.: Modeling and Testing the Fracture Process of Impregnated Carbon Fiber Roving Specimens During Bending Part I. Fiber Bundle Model, Journal of Composite Materials 38(20), 1757-1785 (2004)
E3 Vas L.M., Rácz Zs., Nagy P.: Modeling and Testing the Fracture Process of Impregnated Carbon Fiber Roving Specimens During Bending Part II. Experimental Studies, Journal of Composite Materials 38(20), 1787-1801 (2004)
E4 Vas L.M.: Strength of Unidirectional Short Fiber Structures as a Function of Fiber Length, Journal of Composite Materials 40(19), 1695-1734 (2006)
E5 Vas L.M.: Statistical Modeling of Unidirectional Fiber Structures, Macromolecular Symposia. Special Issue: Advanced Polymer Composites and Technologies 239(1), 159-175 (2006)
E6 Vas L. M. and Tamás P.: Fiber-Bundle-Cells Method and its Application to Modeling Fibrous Structures, GÉPÉSZET 2006, 5th Conf. on Mech. Eng. Budapest, May 25-26, 2006. Proceedings (CD – Full-text) ISBN 963 593 465 3 (2006)
E7 Vas L.M.: Idealized statistical fiber-bundle-cells and their application to (in Hungarian: Idealizált statisztikus szálköteg-cellák és alkalmazásuk szálas szerkezetek, kompozitok modellezésére) DSc Thesis Hungarian Academy of Sciences, Budapest 2007. http://pt.bme.hu/~vas/HAS_DSc_Thesis/HAS-DSc_Thesis_VasLM_2007.pdf

E8 Vas L.M., Tamás P.: Modelling Method Based on Idealised Fiber Bundles. Plastics, Rubber and Composites (IF=0.412, 2004) 37(5/6) 233-239 (2008)
E9 Tamás P., Vas L. M.: Modelling Fibrous Structures by FiberSpace Using Fourier Transformation Based Expert Program. GÉPÉSZET 2008, 6th Conf. on Mech. Eng. Budapest, May 28-29, 2008. Proceedings (CD – Full-text) ISBN 978 963 420 947 8 (2008)
E10 Tamás P., Vas L. M.: Fiber Bundle Based Modeling Software, ITC&DC Magic World of Textiles IV. International Textile, Clothing & Design Conference Oct. 5-8, 2008 Dubrovnik. Book of Proceedings 892-897, ISBN 978-953-7105-26-6 (2008)
E11 Vas L.M., Ronkay F., Czigány T.: Active fiber length distribution and its application to determine the critical fiber length. Polymer Testing 28 (2009) 752-759
E12 Vas L.M., Tamás P.: Modelling Size Effects of Fibrous Materials Using Fiber-Bundle-Cells., ECCM-14 14th European Conference on Composite Materials. Budapest, 7-10 June, 2010. Proceedings Paper ID-705, 1-11. ISBN: 978-963-313-008-7. (2010)
E13 Molnár K., Vas L.M., Czigány T.: Determination of tensile strength of electrospun single nanofibers through modeling tensile behavior of the nanofibrous mat. Composites Part B-Engineering 43:(1) pp. 15-21. (2012)
E14 Vas L. M., Göktepe F., Tamás P., Halász M., Özdemir D., Kokas Palicska L.: Modeling and Analysing the Tensile Behavior of Fabric Samples, Acta Polytechnica Hungarica, Volume 10, Issue Number 3, 79-95, 2013.

Foreign publications as source

F1 Daniels, H.E.: The Statistical Theory of the Strength of Bundles of Threats. Proceedings of the Royal Society of London. Vol. A183. (1945) 405-435.
F2 Persoz B. (edited by): Introduction à l'Etude de la Rheologie, Dunod, Paris, 1960.
F3 Feller W.: An introduction to probability theory and its applications, 3rd ed., John Wiley & Sons Inc., New York, 1968.
F4 Bolotin V.V.: Statistical Methods in the Structural Mechanics (in Hungarian: Statisztikai módszerek a szerkezetek mechanikájában), Műszaki Könyvkiadó Budapest, 1970.
F5 Harlow, D.G. & Phoenix, S.L.: The Chain-of-Bundles Probability Model For the Strength of Fibrous Materials I: Analysis and Conjectures. Journal of Composite Materials 12(6) (1978) 195-214. II: A Numerical Study of Convergence. 12(7) (1978) 314-334.
F6 Cleary J.G.: Analysis of an Algorithm for Finding Nearest-neighbors in Euclidean Space, ACM Transactions on Mathematical Software, 5(2) (1979) 183-192.
F7 Phoenix, S.L.: Statistical Models for the Tensile Strength of Yarns and Cables, In: Mechanics of Flexible Fiber Assemblies (edited by Hearle J.W.S. et al.) NATO Advanced Study Institutes Series, Series E: Applied Sciences No.38, Sijthoff & Nordhoff, Alphen aan de Rijn, The Netherlands; Germantown, ML USA (1980), 113-141.
F8 Curiskis J.I., Carnaby G.A.: Continuum Mechanics of the Fiber Bundle. Textile Research Journal 55 (1985) 334-344.
F9 Halász L., Zrínyi M.: Introduction to Polymer Physics (in Hungarian: Bevezetés a polimerfizikába), Műszaki Könyvkiadó Budapest, 1989.
F10 Nordin M, Frankel VH: Basic Biomechanics of the Musculoskeletal System. 2nd Ed., Williams & Wilkins, Pennsylvania, 1989.
F11 Strobl G.R.: The Physics of Polymers - Concepts for Understanding their Structures and Behavior, Springer Verlag, Berlin 1996.
F12 Moore K.L., Dalley A.F., Clinically Oriented Anatomy. 4th Ed., Lippincott Williams & Wilkins, Maryland, 1999.

F13 Chen B. and Kaufman A.:3D Volume Rotation Using Shear Transformations. Graphical Models 62 (2000), 308–322.
F14 Pan N., Lin Y., Wang X., Posle R.: An Oblique Fiber Bundle Test and Analysis. Textile Research Journal 70(8) (2000) 671-674.
F15 Paris F.: A Study of Failure Criteria of Fibrous Composite Materials, Final report NASA/CR-2001-210661, 2001, https://ntrs.nasa.gov/archive/.../20010035883.pdfKollár L., Springer G.S.: Mechanics of Composite Materials. Cambridge University Press, Cambridge UK, 2003.
F16 Kollár L., Springer G.S.: Mechanics of Composite Materials. Cambridge University Press, Cambridge UK, 2003.
F17 He W.W., Wang X.: Modeling the Tensile Behavior of Fiber Bundles with Irregular Constituent Fibers, Journal of Applied Polymer Science, Vol. 93, 2664–2668 (2004) DOI 10.1002/app.20852 (www.interscience.wiley.com)
F18 Bolla M., Krámli A.: Theory of Statistical Inferences (in Hungarian: Statisztikai következtetések elmélete), Typotex Kiadó, Budapest, 2005.
F19 Pollintine P., Luo J., Offa-Jones B., Dolan P., Adams M.A.: Bone creep can cause progressive vertebral deformity, Bone 45 (2009) 466–472.
F20 Tunák M., Linka A., Volf P.: Load-sharing and Monte Carlo models of defects in a bundle of fibers. Composites Science and Technology 69 (2009) 1417-1421.
F21 Salviato M., Bazant Z.P.: The asymptotic stochastic strength of bundles of elements exhibiting general stress-strain laws. Probabilistic Engineering Mechanics 36 (2014) 1-7.
F22 Hader A., Achik I., Lahyani A., Sbiaai K., Boughaleb Y.: Characterization of the failure process in composite materials by the Fiber Bundle Model. Superlattices and Microstructures 71 (2014) 30-37.
F23 Hao W., Yao X., Ma Y., Yuan Y.: Experimental study on interaction between matrix crack and fiber bundles using optical caustic method. Engineering Fracture Mechanics 134 (2015) 354-367.
F24 Tian W., Qi L., Su Ch., Liang J., Zhou J.: Numerical evaluation on mechanical properties of short-fiber-reinforced metal matrix composites: Two-step mean-field homogenization procedure. Composite Structures 139 (2016) 96-103.
F25 Fletcher J.: Fiber Bundle Modeling for Nacre Fracture Simulation http://www.csm.ornl.gov/Internships/rams_06/abstracts/j_fletcher.pdf (downloaded: 19.08.2018.)

Publications

Publication results of developing material models for the human tissues

P1 Kerekes Péter: Finite element modelling of biological tissue (in Hungarian: Biológiai szövetminta végeselemes szimulációja), BSc Thesis, MOGI BUTE Budapest, 2017. (supervisor: A. Bojtos),
P2 Vas L.M., Kocsis Z., Czigány T., Tamás P., Romhány G.: Novel Evaluation Method Of Acoustic Emission Data Based On Statistical Fiber Bundle Cells. Journal of Composite Materials 53(17) (2019) 2429–2446 https://doi.org/10.1177/0021998319826666
P3 Virág Á. D.: Testing the applicability of the FBC model in the case of different glass fiber woven fabrics (in Hungarian: Az FBC modell alkalmazhatóságának vizsgálata különböző üvegszövetek esetén), TDK conference paper, BME, Budapest (2018). (supervisors: M. Halász, L.M. Vas, P. Bakonyi)

P4 Virág Á.D.: FBC Based Modelling of the Deformation and Failure of Glass Fiber Reinforced Composite Sheets (in Hungarian: Üvegszövet erősítésű kompozit lapok deformációjának és tönkremenetelének szálkötegcella-alapú modellezése). TDK conference paper, BUTE Budapest 2019. (awarded 1st prize and recommended to OTDK) (supervisors: M. Halász, L.M. Vas, P. Bakonyi)

P5 Takács D.: FEM Simulation of the Rupture of the Tendon (in Hungarian: Ín szakadásának végeselemes szimulációja) TDK conference paper, BME Budapest 2019. (awarded 1st prize and recommended to OTDK) (supervisors: D. Faragó and A. Poros)

P6 Virág Á.D.: Testing the possibility of modeling fabric-reinforced composite sheets by using fiber-bundle-cells (in Hungarian: Szöveterősítésű kompozit lapok szálkötegcella-alapú modellezési lehetőségének vizsgálata) MSc Thesis PT BUTE Budapest, 2019. (supervisors: M. Halász, P. Bakonyi, L.M. Vas)

P7 Vas L.M., Tamás P., Bognár E., Nagy P., Késmárszky R.P., Pap K., Szebényi G.: Nonlinear Fiber-Bundle-Cells Based Modeling of Human Tissue Samples. 2020. (pp. 1-27) Submitted to: Journal of the Mechanical Behavior of Biomedical Materials (accepted after minor revision)

P8 Vas L.M., Tamás P. Faragó D., Poros A., Takács D.: FEM application of CZM modified by simulated fiber bundle. (under work before submission)

P9 Kovács L., Takács L.: Possibilities of Fiber-Bundle-Cells Based Material Modeling in LS-DYNA Environment with Taking into Account the Damages (In Hungarian: Nemlineáris szálkötegcella alapú anyagmodellezési lehetőségek LS-DYNA környezetben károsodás figyelembe vételével) Power Point presentation, Dept. of Polymer Engineering, BUTE, Budapest, 29 October, 2020.

Related publications and projects regarding the FBC and FEM material models

RP1 Hangody Gy., Szebényi G., Abonyi B., Kiss R., Hangody L., Pap K.: Does a different dose of gamma irradiation have the same effect on five different types of tendon allografts?: A biomechanical study, International Orthopaedics 41(2) (2017), 357-365. https://link.springer.com/article/10.1007%2Fs00264-016-3336-7

RP2 Vas L.M.: Idealized statistical fiber-bundle-cells and their application (in Hungarian: Idealizált statisztikus szálköteg-cellák és alkalmazásuk), GlobeEdit, OmniScriptum GmbH & Co. KG, Saarbrücken, Deutschland; Beau Bassin, Mauritius, 2017. ISBN 978-620-2-48604-0

RP3 Szebényi G., Faragó D., Kiss R.M., Pap K.: Stiffening effect of human tendons during strain controlled fatigue loading. Biomechanica Hungarica, XI(2) (2018), 61-68.

RP4 Virág Á. D., Halász M., Vas L. M., Bakonyi P.: Modelling of the yarn-pull out process for the characterization of reinforcing woven fabrics. in 'FEMS Junior EUROMAT 2018 Budapest. 2018.07.08.-2018.07.12,1 (2018)

RP5 Virág Á.D., Vas L.M., Bakonyi P., Halász M.: Analysing of the Yarn Pull-out Process for the Characterization of Reinforcing Woven Fabrics. Fibers and Polymers, Vol.20. No.9. (2019) 19975-1982, DOI 10.1007/s12221-019-8978-9

RP6 Faragó D.: PhD Thesis project, MOGI BUTE, Budapest, 2018-2021. (supervisor: R. Kiss) (Under work)

RP7 Takács L.: Decomposition and bonding of polymer composite constructions (in Hungarian: Polimer kompozit szerkezet alkatrészekre bontása és kötése), PhD Thesis project, PT BUTE, Budapest, 2018-2021. (supervisor: F. Szabó) (Under work)

RP8 Kovács L.: Effects of manufacturing defects of composite materials on their stiffness and strength properties (in Hungarian: Kompozit anyagok gyártási hibáinak hatása azok merevségi és szilárdsági tulajdonságaira), PhD Thesis project, PT BUTE, Budapest, 2018-2021. (supervisor: G. Romhány) (Under work); Report on PhD project 19 May, 2020.

RP9 Marino S.G.: Development of high performance pseudo-ductile hybrid composites, PhD Thesis project, PT BUTE, Budapest, 2018-2021. (supervisor: G. Czél) (Under work)

RP10 Virág Á.D.: Structural and phenomenological modeling of shape-memory polymers (in Hungarian: Alakemlékező polimerek szerkezeti és fenomenológiai modellezése), PhD Thesis project, PT BUTE, Budapest, 2020-2024. (supervisor: K. Molnár) (Under work)